

Old Dominion University

ODU Digital Commons

Mechanical & Aerospace Engineering Theses & Dissertations

Mechanical & Aerospace Engineering

Spring 1980

Analytic and Experimental Studies of a True Airspeed Sensor

Joseph Yao-Cheng Shen
Old Dominion University

Follow this and additional works at: https://digitalcommons.odu.edu/mae_etds



Part of the [Aeronautical Vehicles Commons](#), and the [Mechanical Engineering Commons](#)

Recommended Citation

Shen, Joseph Y.. "Analytic and Experimental Studies of a True Airspeed Sensor" (1980). Doctor of Philosophy (PhD), Dissertation, Mechanical & Aerospace Engineering, Old Dominion University, DOI: 10.25777/4ej7-0484
https://digitalcommons.odu.edu/mae_etds/285

This Dissertation is brought to you for free and open access by the Mechanical & Aerospace Engineering at ODU Digital Commons. It has been accepted for inclusion in Mechanical & Aerospace Engineering Theses & Dissertations by an authorized administrator of ODU Digital Commons. For more information, please contact digitalcommons@odu.edu.

ANALYTIC AND EXPERIMENTAL STUDIES
OF A TRUE AIRSPEED SENSOR

By

Joseph Yao-Cheng Shen
B.S. June 1970, Chung Yuan Christian College of
Science and Engineering
M.E. August 1975, Old Dominion University

A Dissertation Submitted to the Faculty of Old Dominion
University in Partial Fulfillment of the Requirements
for the Degree of

DOCTOR OF PHILOSOPHY
MECHANICAL ENGINEERING

OLD DOMINION UNIVERSITY
May 1980

Approved by:

~~Gene L. Goglia (Director)~~

~~JU M. Kuhlman~~

~~S. N. Tiwari~~

~~C. H. Cooke~~

~~R. F. Hellbaum~~

ABSTRACT

ANALYTIC AND EXPERIMENTAL STUDIES OF A TRUE AIRSPEED SENSOR

Joseph Yao-Cheng Shen
Old Dominion University, 1980
Director: Dr. Gene L. Goglia

The objective of this study was to analyze and design a true airspeed sensor which will replace the conventional pitot-static pressure transducer. This sensor should have the following characteristics: the flow phenomenon is vortex precession, or the "vortex whistle", it should have no moving parts, and also is to be independent of temperature, density, altitude or humidity changes. This sensor has been designed mainly for small commercial aircraft with the airspeed up to 321.9 km/hr (200 mph).

In an attempt to model the complicated fluid mechanics of the vortex precession, three-dimensional, inviscid, unsteady, incompressible fluid flow was studied by using the hydrodynamical linearized stability theory. The temporal stability approach was used to derive the relationship between the true airspeed and frequency response. The results show that the frequency response is linearly proportional to the airspeed.

The designed sensor basically consists of a vortex tube, a swirler, and a pick up system. When air passed

through the swirler, a precessional flow was generated at the region before and after the sudden enlargement area. Also an audible vortex whistle is generated. The signal is picked by the microphone and the frequency response is shown in a frequency counter. The measurement for both closed conduit tests and wind tunnel tests were recorded.

A computer program was developed for obtaining the numerical solution to the theoretical model. The parameters described the sensor geometry were introduced into the calculation. Computational results for various combinations of vortex tubes and swirlers have been obtained.

For a specific flow rate or airspeed, the larger the exit swirler angle, the greater the frequency response. For a smaller cross-sectional area at the precessional flow region, the frequency response is higher. It was observed that as the airspeed was increased the Strouhal number remained constant for a fixed design. The Strouhal number was found to be only dependent on the exit angle on swirler.

In some cases, the experimental results were found to be in reasonable agreement with the inviscid theoretical predictions. Viscous effects on the performance of the sensor was believed to be appreciable when experiment and theory differed.

ACKNOWLEDGMENTS

It is with pleasure that the author acknowledges the support and guidance of the individuals and organizations whose technical and financial assistance made completion of this study possible. In particular, the author would like to extend his sincerest thanks to the following:

Dr. Gene L. Goglia, the dissertation committee chairman, for his constant encouragement, advice, suggestions, criticism and moral support throughout the study,

The author's dissertation committee members: Dr. John M. Kuhlman, Dr. Surendra N. Tiwari, Dr. Charlie H. Cooke, and Mr. Richard F. Hellbaum, who generously provided valuable advice and assistance,

National Aeronautics and Space Administration for their financial support, without which this study would have been virtually impossible,

The administrators of the NASA Langley Research Center for the privilege of using their facilities to conduct much of the investigation,

The personnel of the instrument shops of the Langley Research Center for their aid in design of the equipment,

Mr. Richard F. Hellbaum for his indispensable advice, suggestions, and guidance.

And, finally, to my wife Esther, for her patience, understanding, and sacrifices.

TABLE OF CONTENTS

	Page
ACKNOWLEDGMENTS	ii
LIST OF TABLES	vi
LIST OF FIGURES	vii
LIST OF SYMBOLS	xvi
 Chapter	
1. INTRODUCTION	1
2. THEORY	10
3. NUMERICAL RESULTS AND DISCUSSION	22
3.1 Relationship between Flow Rate and Frequency Response	22
3.2 Effect of Exit Angle on Swirler	24
3.3 Effect of Wavenumber	24
3.4 Effect of Flutes on Swirler	54
3.5 Effect of Swirler Core Size, D_2	54
3.6 Effect of the Cross-sectional Size of the Precessional Flow Region	61
3.7 Relationship between the Mean Axial Velocity, W_c , and Airspeed	61
3.8 Relationship between Reynolds Number and Strouhal Number	72

	Page
4. APPARATUS AND TESTS	79
4.1 General Description	79
4.2 Visualization	80
4.3 Closed Conduit Test	85
4.4 Wind Tunnel Test	90
5. EXPERIMENTAL RESULTS AND DISCUSSION	94
5.1 Closed Conduit Test	97
5.2 Wind Tunnel Test	104
SUMMARY AND CONCLUSION	121
REFERENCES	124
APPENDIXES	
A. NUMERICAL ANALYSIS AND SOLUTIONS	130
B. THE DERIVATION OF THE UPSTREAM FLUID ANGULAR VELOCITY, ω_0 , AND THE CONSTANT MEAN AXIAL FLOW VELOCITY, w_c	139
C. COMPUTING PROCEDURE AND PROGRAMMING	145
D. ERROR ANALYSIS	157
E. THE CONSTRUCTION OF FIGURES 72 THROUGH 83	177

LIST OF TABLES

Table	Page
1. Different combinations of vortex tube and swirler	23
2. The working ranges of the sensors with the swirlers having four flutes and different exit angles	103

LIST OF FIGURES

Figure	Page
1. Designed cross-sectional view and description of true airspeed sensor	11
2. Flow rate versus frequency response for Sensor 1 with swirlers having two flutes and various exit angles	25
3. Flow rate versus frequency response for Sensor 1 with swirlers having three flutes and various exit angles	26
4. Flow rate versus frequency response for Sensor 1 with swirlers having four flutes and various exit angles	27
5. Flow rate versus frequency response for Sensor 2 with swirlers having four flutes and various exit angles	28
6. Flow rate versus frequency response for Sensor 3 with swirlers having four flutes and various exit angles	29
7. Flow rate versus frequency response for Sensor 4 with swirlers having four flutes and various exit angles	30

Figure	Page
8. Flow rate versus frequency response for Sensor 5 with swirlers having four flutes and various exit angles	31
9. Flow rate versus frequency response for Sensor 6 with swirlers having four flutes and various exit angles	32
10. True airspeed versus frequency response for Sensor 1 with two flutes swirlers and wavenumber $k = 1$	33
11. True airspeed versus frequency response for Sensor 1 with three flutes swirlers and wavenumber $k = 1$	34
12. True airspeed versus frequency response for Sensor 1 with four flutes swirlers and wavenumber $k = 1$	35
13. True airspeed versus frequency response for Sensor 1 with four flutes swirlers and wavenumber $k = 3$	36
14. True airspeed versus frequency response for Sensor 1 with four flutes swirlers and wavenumber $k = 5$	37
15. True airspeed versus frequency response for Sensor 1 with four flutes swirlers and wavenumber $k = 7$	38

Figure	Page
16. True airspeed versus frequency response for Sensor 2 with swirlers having two flutes and various exit angles	39
17. True airspeed versus frequency response for Sensor 2 with swirlers having three flutes and various exit angles	40
18. True airspeed versus frequency response for Sensor 2 with swirlers having four flutes and various exit angles	41
19. True airspeed versus frequency response for Sensor 3 with swirlers having two flutes and various exit angles	42
20. True airspeed versus frequency response for Sensor 3 with swirlers having three flutes and various exit angles	43
21. True airspeed versus frequency response for Sensor 3 with swirlers having four flutes and various exit angles	44
22. True airspeed versus frequency response for Sensor 4 with swirlers having two flutes and various exit angles	45
23. True airspeed versus frequency response for Sensor 4 with swirlers having three flutes and various exit angles	46

Figure	Page
24. True airspeed versus frequency response for Sensor 4 with swirlers having four flutes and various exit angles	47
25. True airspeed versus frequency response for Sensor 5 with swirlers having two flutes and various exit angles	48
26. True airspeed versus frequency response for Sensor 5 with swirlers having three flutes and various exit angles	49
27. True airspeed versus frequency response for Sensor 5 with swirlers having four flutes and various exit angles	50
28. True airspeed versus frequency response for Sensor 6 with swirlers having two flutes and various exit angles	51
29. True airspeed versus frequency response for Sensor 6 with swirlers having three flutes and various exit angles	52
30. True airspeed versus frequency response for Sensor 6 with swirlers having four flutes and various exit angles	53
31. True airspeed versus frequency response for Sensor 1 with swirlers having 45 ^o exit angle and various flutes	55

Figure	Page
32. True airspeed versus frequency response for Sensor 1 with swirlers having 60° exit angle and various flutes	56
33. True airspeed versus frequency response for Sensor 1 with swirlers having 75° exit angle and various flutes	57
34. True airspeed versus frequency response for Sensor 2 with swirlers having 45° exit angle and various flutes	58
35. True airspeed versus frequency response for Sensor 2 with swirlers having 60° exit angle and various flutes	59
36. True airspeed versus frequency response for Sensor 2 with swirlers having 75° exit angle and various flutes	60
37. Comparison of the variation of the size of the precessional flow region, D_3 , with four flutes and exit angle 45° swirler . . .	62
38. Comparison of the variation of the size of the precessional flow region, D_3 , with four flutes and exit angle 60° swirler . . .	63
39. Comparison of the variation of the size of the precessional flow region, D_3 , with four flutes and exit angle 75° swirler . . .	64

Figure	Page
40. True airspeed versus mean axial velocity for Sensor 1 with swirlers having four flutes and various exit angles	65
41. True airspeed versus mean axial velocity for Sensor 2 with swirlers having four flutes and various exit angles	66
42. True airspeed versus mean axial velocity for Sensor 3 with swirlers having four flutes and various exit angles	67
43. True airspeed versus mean axial velocity for Sensor 4 with swirlers having four flutes and various exit angles	68
44. True airspeed versus mean axial velocity for Sensor 5 with swirlers having four flutes and various exit angles	69
45. True airspeed versus mean axial velocity for Sensor 6 with swirlers having four flutes and various exit angles	70
46. Relationship between mean axial velocity and frequency response for Sensor 1 with swirlers having four flutes and various exit angles	71
47. Reynolds number versus Strouhal number for Sensor 1	73
48. Reynolds number versus Strouhal number for Sensor 2	74

Figure	Page
49. Reynolds number versus Strouhal number for Sensor 3	75
50. Reynolds number versus Strouhal number for Sensor 4	76
51. Reynolds number versus Strouhal number for Sensor 5	77
52. Reynolds number versus Strouhal number for Sensor 6	78
53. Vortex tube for flow visualization	81
54. Setup for water model	82
55. Fluid flow phenomenon-precession	83
56. Fluid flow phenomenon-precession	84
57. The dimensions of the vortex tube	86
58. The dimensions of the vortex tube with abrupt enlargement in the rear	87
59. The design and dimensions of the swirler	88
60. Setup for experimental test	89
61. Schematic diagram for input amplifier	91
62. The description of electric condenser micro- phone made by Radio Shack	92
63. 15.24 cm by 15.24 cm wind tunnel	93
64. The actual flute width h on swirler used in the experimental test	95
65. Comparison of designed and actual areas of different swirlers with four flutes	96

Figure	Page
66. The position of the microphone used in experimental test	98
67. The experimental data for Sensor 1 with swirlers having four flutes and various exit angles	99
68. The experimental data for Sensor 2 with swirlers having four flutes and various exit angles	100
69. The experimental data for Sensor 3 with swirlers having four flutes and various exit angles	101
70. The experimental data for Sensor 4 with swirlers having four flutes and various exit angles	102
71. Modified version of vortex tube for wind tunnel test	105
72. The performance of Sensor 1 with swirler having four flutes and exit angle 45° . . .	107
73. The performance of Sensor 1 with swirler having four flutes and exit angle 60° . . .	108
74. The performance of Sensor 1 with swirler having four flutes and exit angle 75° . . .	109
75. The performance of Sensor 2 with swirler having four flutes and exit angle 45° . . .	110
76. The performance of Sensor 2 with swirler having four flutes and exit angle 60° . . .	111

Figure	Page
77. The performance of Sensor 2 with swirler having four flutes and exit angle 75° . . .	112
78. The performance of Sensor 3 with swirler having four flutes and exit angle 45° . . .	113
79. The performance of Sensor 3 with swirler having four flutes and exit angle 60° . . .	114
80. The performance of Sensor 3 with swirler having four flutes and exit angle 75° . . .	115
81. The performance of Sensor 4 with swirler having four flutes and exit angle 45° . . .	116
82. The performance of Sensor 4 with swirler having four flutes and exit angle 60° . . .	117
83. The performance of Sensor 4 with swirler having four flutes and exit angle 75° . . .	118
B.1 The description and cross-sectional view of vortex tube and swirler	140
B.2 The cross-sectional view of section A-A . . .	141
C.1 Flow diagram for calculating the frequency at various true airspeed	147
C.2 Flow diagram for getting the plots	148
D.1 Flow diagram for the error analysis in the Bessel functions	165
E.1 Types of data line taken at closed conduit test	178
E.2 The scales for flow rate at right hand side .	179
E.3 The performance line of a specific sensor . .	180

LIST OF SYMBOLS

C	constant, defined as in equation (52)
c_1, c_2	arbitrary constants
D_1	diameter of swirler generation region, as defined in Fig. 1, cm
D_2	diameter of swirler, as defined in Fig. 1, cm
D_3	diameter of precessional flow region, as defined in Fig. 1, cm
f	function of radius r , amplitude of preliminary complex solution in r -direction
F	frequency response, KHz
g	function of radius r , amplitude of preliminary complex solution in θ -direction
h	function of radius r , amplitude of preliminary complex solution in z -direction
k	wavenumber, a real number
K	parameter, as defined in equation (40)
n	integer
p	actual fluid pressure, kg/cm^2
p'	pressure fluctuation, kg/cm^2
\hat{p}'	preliminary complex solution in pressure
\bar{p}	mean pressure, kg/cm^2

q	function of radius r , amplitude of preliminary complex solution in pressure
Q	flow rate, m^3/min
r	radius, or radial coordinate, cm
R	radius of precessional flow region, as defined in Fig. 1, cm
Re	Reynolds number based on mean axial velocity and D_3
St	Strouhal number based on mean axial velocity and D_3
t	time, sec
u	actual fluid radial velocity, km/hr
u'	velocity fluctuation in r -direction, km/hr
\hat{u}'	preliminary complex solution in r -direction, km/hr
U	true airspeed, km/hr
v	actual fluid tangential velocity, km/hr
v'	velocity fluctuation in θ -direction, km/hr
\hat{v}'	preliminary complex solution in θ -direction, km/hr
\bar{v}	mean velocity in θ -direction, km/hr
w	actual fluid axial velocity, km/hr
w'	velocity fluctuation in z -direction, km/hr
\hat{w}'	preliminary complex solution in z -direction, km/hr
\bar{w}	mean velocity in z -direction, km/hr
W_c	constant mean axial velocity, km/hr

Z	axial coordinate
α	exit swirler angle, as defined in Fig. 59
θ	θ -coordinate
ρ	fluid density, g/cm ³
ω	angular velocity, a constant complex number
ω_0	constant upstream fluid angular velocity
*	complex conjugate of preliminary complex solution

1. INTRODUCTION

At the present time, there are two types of airspeed instruments which might be used on aircraft: the differential-pressure type and the true airspeed meter. The pitot-static instrument, which is of the differential-pressure type, is however exclusively used. This indicator is calibrated in terms of airspeed at a standard air density. In order to obtain the actual airspeed at other densities, a correction must be made. The performance of the pitot-static tube is greatly affected by installation location. One must therefore find a location for the pitot-static openings that will be free from structural interference effects.

The true airspeed sensor is the conventional type of meter with rotating surfaces, such as propellers, which gives readings independent of air density. The sensor is usually used in making measurements of airspeeds in the lower ranges. One kind of true airspeed sensor used by the United States Navy on airships is known as the commutator-condensor type.

The idea of designing a true airspeed sensor originated from the discovery of vortex whistle and the flow phenomenon-precession, which is different from that of

vortex shedding. The understanding of the origin of the sound or whistle was studied by a few investigators [1-3]* from different points of view. Also, the vortex shedding problems associated with the aerolian tones and edgetones were studied and observed experimentally by many researchers [4-12]. Very few people worked on the vortex whistle and precessional flow problems. Bernard Vonnegut [13] in 1954 was the first to discover and investigate the vortex whistle. In his laboratory, they were conducting an experiment on a vortex creating housing for aircraft thermometers. During their experiments, they observed a sound that was generated when the rotating air escaped from the open end of the tube. They also found that the frequency of this sound increased with increasing rates of air flow. In addition, the frequency that was produced decreased as the length of the tube in which the vortex rotates was increased. Vonnegut suggested that the vortex instability leaving the tube caused the whistle. Vonnegut developed an empirical formula describing the performance of his whistle.

In 1955, Irving Michelson [14] published a paper which was the first analytical work on the theory of a vortex whistle. He considered the flow throughout the whistle to be two-dimensional unsteady, inviscid and isentropic. He introduced the parameters s , u' , and v' where s was a non-dimensional density perturbation. By this method, he was

*Numbers in brackets indicate references.

able to arrive at linearized simultaneous equations. A secular equation was then derived with one root of particular interest being noted. From the solution and the secular equation, he noted the occurrence of a frequency that was proportional to the flow speed U . When he introduced the isentropic flow relationship, he was able to express the frequency in terms of pressure drop and reservoir sound speed C_1 . Michelson's theory compares very favorable with Vonnegut's empirical formula.

In 1957, J. P. Nicklas [15] reported his work on the investigation of a vortex tube acoustic true airspeed sensor conducted at the Cornell Aeronautical laboratory. He investigated the feasibility of measuring true aircraft airspeed by measuring the frequency of the sound produced in a vortex tube mounted on an airplane. Nicklas, however, concentrated his efforts on the single tangential nozzle vortex tube. His data revealed that the fundamental sound frequency of a vortex tube could be considered a linear function of true airspeed in the subsonic speed range. He indicated that the altitude and temperature sensitivities of the vortex tube could be reduced by proper design. In his conclusion, he also mentioned that no significant improvement in signal quality was obtained by modifying the tube shape. Nicklas also studied the effect the angle of attack had on frequency response.

In 1960, M. Suzuki [16] studied and investigated the

vortex tube with an objective of finding a method of eliminating the whistle occurring in the vortex tube. In his analysis he assumed both a free and forced vortex region of velocity distribution. Suzuki, using the boundary conditions at the wall and at the interface between free and forced vortex, derived a linearly proportional relationship between the peculiar frequency and the angular velocity of the forced vortex. In his derivation, the density and velocity components were separated into mean and fluctuation terms. Suzuki introduced a number of assumptions and restrictions to enable him to obtain the Bessel's equation and its solution. Although Suzuki did not present either numerical or quantitative results, he did, however, report and discuss his experimental data. In addition to the linear relationship, Suzuki found that no sound was produced at small flow rates, and that when the value of L_c/D_c was less than unity, no distinct frequency could be observed. L_c was the length of cold tube in his model, whereas the D_c was the diameter of the outlet.

In 1963, Robert C. Chanaud [17] converted Vonnegut's data into Reynolds and Strouhal numbers, and found that the air and water data were almost coincident, suggesting that dynamic similarity might occur. The perturbation of a two-dimensional inviscid vortex flow was investigated. Chanaud derived a linear relationship between perturbation frequency and fluid angular velocity for neutrally stable oscillations of an inviscid flow. His results support the

investigations and conclusions reported by Vonnegut and Michelson. He confirmed that the precessional frequency is the same as the sound frequency and that the fluid angular velocity is simply related with the precession frequency of the unstable motion. In his conclusion, he mentioned that "high speed" was not necessary to generate the whistle, as velocities of five feet per second were found sufficient. He, as others did, explained that the instability which occurred was due to the sudden area change at the tube exit. Chanaud's results show that the amplitude of oscillation within the tube depends on how the area changes; a gradual area increase permits larger amplitude flow oscillations whereas an abrupt area change reduces the magnitude of the flow oscillation within the tube. He mentioned that this may be the reason Vonnegut did not detect the sound with a flared tube. He also stated that no quantitative information on the nature of the instability had been obtained.

Powell [18] in 1964 published a paper discussing the origin of the sound. He showed and explained in detail from a physical point of view how aerodynamic sound in an unsteady fluid flow was generated as a result of the movement of vortices, or of vorticity.

In 1965, Chanaud [19] published a paper describing the experimental study in certain swirling flows. One of the swirling flows was studied by Talbot [20]. The experimental results show that the periodic motion in both a vortex whistle and a cyclone separator can be described in terms

of a hydrodynamic oscillator where the frequency is closely related to the angular velocity of the flow. Chanaud also mentioned that the two important parameters, the Reynolds number and the Strouhal number, are both of such magnitude that it appears no important simplifications can be made in the equations of motion to solve the problem analytically. The energy of the oscillator is derived from the hydrodynamic instability of the fluid within a reversed-flow region on the swirl axis. No quantitative information is available on the condition of a steady reversed-flow region. Chanaud, however, mentioned that the experimental results suggest that the two-dimensional perturbation analysis may prove of some value in describing the amplifier part of the oscillator.

Rodely, et al [21] found that the oscillative motion began only beyond certain Reynolds numbers. He also observed that the oscillative motion was accompanied by the reversal of flow near the tube axis. Gove and Ranz [22] in their paper explained in detail this reversal of flow. The reversal of flow was caused by the sudden area enlargement at the tube exit. In the better swirler designs the Rossby number could be held constant for various Reynolds numbers. This indicates that the frequency is linearly related to the flow rate. However, below some Reynolds number, due to viscous effects, there were deviations from the constant value.

Chanaud again in 1970 [23] suggested that in the aerodynamic whistle the vibrating system is the air itself. This is in contrast to nonaerodynamic devices such as a drum or loud speaker, where sound is generated when a mechanical system vibrates and disturbs the air. Chanaud showed that due to the instability of the system a small disturbance in the stream flowing through the aerodynamic whistle was amplified, and that kinetic energy was converted to oscillatory energy. Part of the energy of the amplified disturbance is fed back upstream, where the flow is most unstable, and, if the right frequency and amplitude exists, it interacts with the original disturbance to maintain the process. After a few cycles the feedback controls the input completely. A whistle is produced when the flow speed is high enough and the frequency is in the audible range.

As mentioned in [21, 24-29], there is one common feature that introduces the concept of "no moving parts" in fluidic devices. In contrast to this concept is the device with moving parts as in [30]. Fluidic devices have been widely researched in the past 19 years. Simplicity, reliability and easy maintenance make fluidic devices attractive. A quote from the text Design Theory of Fluidic Components [31], worthy of mention is:

Although present theory gives results sufficiently accurate for engineering design, it is not possible to justify all the assumptions used. Thus in a scientific sense the theory is not

always satisfying, but in an engineering design sense the theory does seem to be satisfactory.

In this investigation fluidic models were designed and then tested in both water and air. Flow visualization tests in a water model were undertaken in order to actually see the flow phenomenon of precession. Smaller models were subsequently made for testing with compressed air and in a wind tunnel. A complete analytical analysis was provided in this study. The physical models were simulated and used in computer calculation. The numerical solutions involved true airspeeds up to 321.89 km (200 miles) per hour. Six different combinations of vortex tubes and swirlers were used both in computer calculations as well as in experimental tests.

The objective of this study was two-fold. The first objective was to analyze and design a true airspeed sensor which will replace the conventional pitot-static pressure transducer for small commercial aircraft. The desired features of this sensor should include the flow phenomenon-precession, vortex whistle and have no moving parts. In addition this sensor should not be affected by temperature, density, altitude, and humidity changes. The second objective was to obtain a numerical solution and predict the frequency response which is generated by the vortex whistle at a certain airspeed. Prior to this study, theoretical results were never presented quantitatively to enable a comparison with experimental data. Thus this study will

present a general solution to the problem and also provide specific analytical results for comparison purposes. A correction factor for viscous effects will later be introduced to enable a correlation between theoretical results and experimental data.

2. THEORY

For this study, the flow is assumed to be three-dimensional, inviscid, unsteady and incompressible. The analysis presented here is based on the hydrodynamical linearized stability theory. The hydrodynamical linearized stability theory as mentioned in [32-38] has been used in a variety of problems. In the application of this theory for the temporal stability approach, the frequency was considered a constant complex quantity, and the wavenumber k a real number. Later it will be observed that when the imaginary part of the frequency is greater than zero, the disturbance grows exponentially in time and is termed a temporally unstable disturbance. This disturbance when amplified to a certain degree gives a definite whistle at a frequency which is linearly proportional to the true airspeed. The initial effort will be devoted to the study of the disturbance caused by sudden enlargement in the rear end of the vortex tube as shown in Fig. 1. Notice that the variable fluid properties, compressibility effects and viscous effects were neglected throughout in this study.

For the flow described above, the continuity and momentum equations expressed in cylindrical coordinates

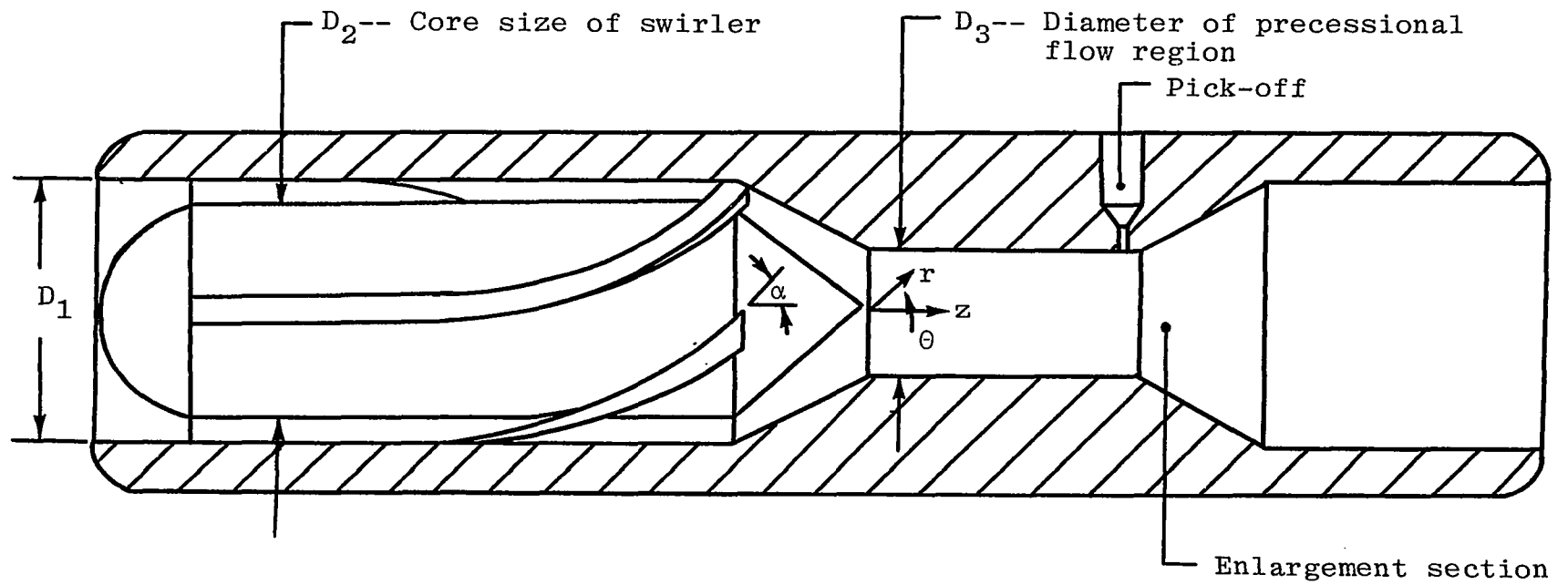


Fig. 1 Designed cross-sectional view and description of true airspeed sensor.

are as follows:

continuity

$$\frac{1}{r} \frac{\partial}{\partial r} (ru) + \frac{1}{r} \frac{\partial v}{\partial \theta} + \frac{\partial w}{\partial z} = 0 \quad (1)$$

r-momentum

$$\frac{\partial u}{\partial t} + u \frac{\partial u}{\partial r} + \frac{v}{r} \frac{\partial u}{\partial \theta} + w \frac{\partial u}{\partial z} - \frac{v^2}{r} = - \frac{1}{\rho} \frac{\partial p}{\partial r} \quad (2)$$

θ -momentum

$$\frac{\partial v}{\partial t} + u \frac{\partial v}{\partial r} + \frac{v}{r} \frac{\partial v}{\partial \theta} + w \frac{\partial v}{\partial z} + \frac{uv}{r} = - \frac{1}{\rho r} \frac{\partial p}{\partial \theta} \quad (3)$$

z-momentum

$$\frac{\partial w}{\partial t} + u \frac{\partial w}{\partial r} + \frac{v}{r} \frac{\partial w}{\partial \theta} + w \frac{\partial w}{\partial z} = - \frac{1}{\rho} \frac{\partial p}{\partial z} \quad (4)$$

where u , v and w denote respectively the actual fluid radial velocity V_r , tangential velocity V_θ and axial velocity V_z .

It is the purpose here to derive the equations that control the small disturbances of a swirling and steady mean flow. This is accomplished in three steps: separation of fluctuations, linearization and recourse to complex functions.

According to the first step the velocities are separated into a mean value and a fluctuation from the mean. It is assumed that in the absence of fluctuations the flow is laminar and can be specified as follows:

$$u = 0, \quad v = \bar{V}(r), \quad w = \bar{W}(r), \quad p = \bar{P}(r), \quad (5)$$

where the r component mean velocity is assumed to be zero, and the fluid beyond the swirling flow generator consists

of a forced vortex flow, or solid body rotation. The mean flow in the θ -direction, the axial mean flow and the pressure terms are assumed to be functions of radius only. If u' , v' and w' denote respectively the fluctuations in the r , θ and z directions, and p' denotes the fluctuations in the pressure then the following relationships can be used to express the instantaneous velocity components and pressure:

$$u = u'(r, \theta, z, t) \quad (6)$$

$$v = \bar{V}(r) + v'(r, \theta, z, t) \quad (7)$$

$$w = \bar{W}(r) + w'(r, \theta, z, t) \quad (8)$$

$$p = \bar{P}(r) + p'(r, \theta, z, t) \quad (9)$$

It should be noted that the mean flow, i.e., \bar{V} , \bar{W} and \bar{P} must satisfy the governing equations (1) through (4).

Therefore, if equations (6) through (9) are introduced into equations (1) through (4), and the mean flow subtracted from these, one obtains:

the continuity disturbance equation,

$$\frac{\partial u'}{\partial r} + \frac{u'}{r} + \frac{1}{r} \frac{\partial v'}{\partial \theta} + \frac{\partial w'}{\partial z} = 0; \quad (10)$$

the r -momentum disturbance equation,

$$\begin{aligned} \frac{\partial u'}{\partial t} + u' \frac{\partial u'}{\partial r} + \frac{1}{r} (\bar{V} \frac{\partial u'}{\partial \theta} + v' \frac{\partial u'}{\partial \theta}) + (\bar{W} \frac{\partial u'}{\partial z} + w' \frac{\partial \bar{W}}{\partial z} + \\ w' \frac{\partial w'}{\partial z}) - 2 \frac{\bar{V} v'}{r} + \frac{v'^2}{r} = - \frac{1}{\rho} \frac{\partial p'}{\partial r}; \end{aligned} \quad (11)$$

the θ -momentum disturbance equation,

$$\begin{aligned} \frac{\partial v'}{\partial t} + u' \frac{\partial \bar{v}}{\partial r} + u' \frac{\partial v'}{\partial r} + \bar{v} \frac{\partial v'}{\partial \theta} + \frac{v'}{r} \frac{\partial \bar{v}}{\partial \theta} + \frac{v'}{r} \frac{\partial v'}{\partial \theta} + \\ \bar{w} \frac{\partial v'}{\partial z} + w' \frac{\partial \bar{v}}{\partial z} + w' \frac{\partial v'}{\partial z} + \frac{\bar{v}u'}{r} + \frac{u'v'}{r} = - \frac{1}{\rho r} \frac{\partial p'}{\partial \theta} ; \end{aligned} \quad (12)$$

and the z-momentum disturbance equation,

$$\begin{aligned} \frac{\partial w'}{\partial t} + u' \frac{\partial \bar{w}}{\partial r} + u' \frac{\partial w'}{\partial r} + \bar{v} \frac{\partial w'}{\partial \theta} + \frac{v'}{r} \frac{\partial \bar{w}}{\partial \theta} + \frac{v'}{r} \frac{\partial w'}{\partial \theta} + \\ \bar{w} \frac{\partial w'}{\partial z} + w' \frac{\partial \bar{w}}{\partial z} + w' \frac{\partial w'}{\partial z} = - \frac{1}{\rho} \frac{\partial p'}{\partial z} \end{aligned} \quad (13)$$

In the above equations the product terms such as $u' \cdot \frac{u'}{r}$ correspond to an effect of one fluctuation on another. Retention of these product terms prohibits an easy solution to the equations. However, these difficulties are eliminated should it be assumed that the fluctuations and their derivatives have small amplitudes with respect to mean flow quantities. This indeed is a reasonable assumption and will be invoked. Thus all products and powers (higher than the first) of the fluctuations are neglected and only those terms which are linear in them are retained. This procedure of linearization leads to the following linearized equations:

r-momentum

$$\frac{\partial u'}{\partial t} + \frac{\bar{v}}{r} \frac{\partial u'}{\partial \theta} + \bar{w} \frac{\partial u'}{\partial z} + w' \frac{\partial \bar{w}}{\partial \theta} - 2 \frac{\bar{v}v'}{r} = - \frac{1}{\rho} \frac{\partial p'}{\partial r} ; \quad (14)$$

θ-momentum

$$\begin{aligned} & \frac{\partial v'}{\partial t} + u' \frac{\partial \bar{V}}{\partial r} + \frac{\bar{V}}{r} \frac{\partial v'}{\partial \theta} + \frac{v'}{r} \frac{\partial \bar{V}}{\partial \theta} + \bar{W} \frac{\partial v'}{\partial z} + w' \frac{\partial \bar{V}}{\partial z} + \frac{\bar{V}u'}{r} \\ & = - \frac{1}{\rho r} \frac{\partial p'}{\partial \theta} \quad ; \end{aligned} \quad (15)$$

z-momentum

$$\begin{aligned} & \frac{\partial w'}{\partial t} + u' \frac{\partial \bar{W}}{\partial r} + \frac{\bar{V}}{r} \frac{\partial w'}{\partial \theta} + \frac{v'}{r} \frac{\partial \bar{W}}{\partial \theta} + \bar{W} \frac{\partial w'}{\partial z} + w' \frac{\partial \bar{W}}{\partial z} = \\ & - \frac{1}{\rho} \frac{\partial p'}{\partial z} \quad . \end{aligned} \quad (16)$$

For simplicity, the axial mean flow, \bar{W} , is assumed to be a constant, and since the mean flow in the θ -direction is a function of radius only, the above continuity and momentum disturbance equations can then be written as:

the continuity disturbance equation,

$$\frac{\partial u'}{\partial r} + \frac{u'}{r} + \frac{1}{r} \frac{\partial v'}{\partial \theta} + \frac{\partial w'}{\partial z} = 0 \quad ; \quad (10)$$

the r-momentum disturbance equation,

$$\frac{\partial u'}{\partial t} + \frac{\bar{V}}{r} \frac{\partial u'}{\partial \theta} + \bar{W} \frac{\partial u'}{\partial z} - 2 \frac{\bar{V}u'}{r} = - \frac{1}{\rho} \frac{\partial p'}{\partial r} \quad ; \quad (17)$$

the θ -momentum disturbance equation,

$$\frac{\partial v'}{\partial t} + u' \frac{\partial \bar{V}}{\partial r} + \frac{\bar{V}}{r} \frac{\partial v'}{\partial \theta} + \bar{W} \frac{\partial v'}{\partial z} + \frac{\bar{V}u'}{r} = - \frac{1}{\rho r} \frac{\partial p'}{\partial \theta} \quad ; \quad (18)$$

and the z-momentum disturbance equation,

$$\frac{\partial w'}{\partial t} + \frac{\bar{V}}{r} \frac{\partial w'}{\partial \theta} + \bar{W} \frac{\partial w'}{\partial z} = - \frac{1}{\rho} \frac{\partial p'}{\partial z} \quad . \quad (19)$$

Finally, the linearity of the above equations enables one to obtain periodic solutions in terms of complex

functions. Thus the system of partial differential equations (10), (17), (18) and (19) can be converted into ordinary differential equations.

The various parameters, describing the perturbation, have a (z, θ, t) -dependence assumed to be given by

$$e^{i(kz + n\theta - \omega t)} \quad (20)$$

where k is the wavenumber of the disturbance in the z -direction, n is an integer (which can only be positive, zero or negative), and ω is a constant (which can be complex). In this analysis, it is assumed that k be considered a real number and ω a complex number that will be determined later. Furthermore, if $f(r)$, $g(r)$, $h(r)$ and $q(r)$ were to denote the amplitudes of the respective perturbations u' , v' , w' and p' whose (z, θ, t) -dependence is governed by equation (20), then one could expect to find solutions of the type:

$$\hat{u}' = i f(r) e^{i(kz + n\theta - \omega t)} \quad (21)$$

$$\hat{v}' = g(r) e^{i(kz + n\theta - \omega t)} \quad (22)$$

$$\hat{w}' = h(r) e^{i(kz + n\theta - \omega t)} \quad (23)$$

$$\text{and } \hat{p}' = q(r) e^{i(kz + n\theta - \omega t)} \quad (24)$$

The superscript $\hat{}$ denotes a preliminary complex solution which ultimately leads to a real solution. In other words, one can obtain a set of solutions which are the complex conjugates of the preliminary solutions. The pure real solutions can then be constructed as follows:

$$u' = \frac{1}{2} (\hat{u}' + \hat{u}'^*) \quad (25)$$

$$v' = \frac{1}{2} (\hat{v}' + \hat{v}'^*) \quad (26)$$

$$w' = \frac{1}{2} (\hat{w}' + \hat{w}'^*) \quad (27)$$

$$\text{and } p' = \frac{1}{2} (\hat{p}' + \hat{p}'^*) \quad (28)$$

where the superscript * denotes a conjugate of the preliminary solution.

Substituting the above expressions (21) through (24) into equations (10), (17), (18) and (19), and cancelling the common expression, $\exp(i(kz + n\theta - \omega t))$, one obtains the following equations:

continuity

$$\frac{df}{dr} + \frac{f}{r} + \frac{n}{r} g + k h = 0 \quad (29)$$

r-momentum

$$(\omega - \frac{n}{r} \bar{V} - k \bar{W}) f - 2 \frac{\bar{V}}{r} g = - \frac{1}{\rho} \frac{dq}{dr} \quad (30)$$

θ -momentum

$$\left(\frac{d\bar{V}}{dr} + \frac{\bar{V}}{r} \right) f + \left(n \frac{\bar{V}}{r} - \omega + k \bar{W} \right) g = - \frac{n}{\rho r} q \quad (31)$$

z-momentum

$$\left(n \frac{\bar{V}}{r} - \omega + k \bar{W} \right) h = - \frac{k}{\rho} q \quad (32)$$

Since the flow at the section of radius R is a forced vortex, or solid body rotation, the mean flow velocity in θ -direction \bar{V} can be written as

$$\bar{V} = r \omega_0, \quad (33)$$

where ω_0 is the upstream fluid angular velocity. However,

with

$$\frac{d\bar{V}}{dr} + \frac{\bar{V}}{r} = 2 \omega_0 , \quad (34)$$

and the axial mean flow velocity \bar{W} considered a constant W_c , equations (29) through (32) become:

continuity

$$\frac{df}{dr} + \frac{f}{r} + \frac{n}{r} g + k h = 0 ; \quad (35)$$

r-momentum

$$(\omega - n\omega_0 - k W_c) f - 2 \omega_0 g = - \frac{1}{\rho} \frac{dq}{dr} ; \quad (36)$$

θ -momentum

$$2 \omega_0 f - (\omega - n\omega_0 - k W_c) g = - \frac{n}{\rho r} q ; \quad (37)$$

z-momentum

$$(\omega - n\omega_0 - k W_c) h = \frac{k}{\rho} q. \quad (38)$$

It can be shown from the above that

$$f(r) = \frac{k}{K} \left(\frac{dh}{dr} - \frac{2 n \omega_0}{\omega - n\omega_0 - k W_c} \frac{h}{r} \right) \quad (39)$$

where the parameter K , a function of (k, ω) , is defined as

$$K^2 = \frac{k^2 [4 \omega_0^2 - (\omega - n \omega_0 - k W_c)^2]}{(\omega - n \omega_0 - k W_c)^2} . \quad (40)$$

Substituting equation (39) into equation (36) the following expression for g is obtained,

$$g(r) = \frac{k}{K^2} \left[\left(1 + \frac{K^2}{k^2} \right) \frac{\omega - n \omega_0 - k W_c}{2 \omega_0} \frac{h}{r} - n \frac{h}{r} \right]. \quad (41).$$

It is interesting to observe that equations (39), (40) and (41) are exactly the same as Suzuki's equations (197), (198) and (198').

Substituting equations (39) and (41) into the continuity equation (35), produces the following Bessel's equation of order n in cylindrical coordinates

$$\frac{d^2 h}{dr^2} + \frac{1}{r} \frac{dh}{dr} + \left(K^2 - \frac{n^2}{r^2} \right) h = 0. \quad (42)$$

The general solution of this equation is of the form,

$$h(r) = c_1 J_n(rK) + c_2 Y_n(rK). \quad (43)$$

where c_1 and c_2 are arbitrary constants. It should be noted that in the above development no restrictions were necessary and therefore the analysis should be simpler and less restrictive.

Because the value Y_n tends to infinity as r approaches zero, it is necessary to force the constant c_2 to zero. Equation (43) becomes

$$h(r) = c_1 J_n(rK). \quad (44)$$

The wall boundary condition stipulates no radial velocity, i.e.,

$$f(r) = 0 \quad \text{at } r = R.$$

Hence from equations (39) and (44), one obtains

$$f(r = R) = 0 = \frac{k}{K^2} \left\{ \frac{d}{dr} (c_1 J_n(rK)) \right\} - \frac{2n\omega_0}{\omega - n\omega_0 - kW_c} \cdot$$

$$\left. \frac{c_1 J_n(rK)}{r} \right\} r = R \quad . \quad (45)$$

Evaluation of the derivative of the Bessel function

$$\frac{dJ_n(rK)}{dr} = K \left[J_{n-1}(rk) - \frac{n}{rK} J_n(rK) \right] \quad (46)$$

and inclusion in equation (45), produces

$$\begin{aligned} \frac{c_1 k}{K^2} \left\{ K J_{n-1}(RK) - \frac{n}{R} J_n(RK) - \frac{2 n \omega_o}{(\omega - n\omega_o - kW_c)R} J_n(RK) \right\} \\ = 0. \end{aligned} \quad (47)$$

From equation (40), however, it can readily be shown that

$$\omega = \left(n + \frac{2}{1 + \frac{K^2}{k^2}} \right) \omega_o + k W_c \quad . \quad (48)$$

It should be noted that if $k = 0$, equation (47) is automatically satisfied, and equation (48) becomes

$$\omega = n \omega_o \quad (49)$$

This shows that the angular velocity ω is linearly related to the constant upstream fluid angular velocity ω_o . The angular velocity ω can be simply related to the sound frequency as $\omega = 2 \pi F$, where F is the frequency response in kiloHertz (KHz). The upstream fluid angular velocity ω_o is in reality another form of the true airspeed which can be derived easily. Therefore, equation (49) indicates that the vortex whistle frequency response is linearly proportional to the true airspeed for $k = 0$.

If, however, k is not equal to zero, and since c_1 cannot be zero, then the bracketed quantity of equation (47) must be zero, or

$$K J_{n-1}(RK) - \frac{n}{R} \left(1 + \frac{2 \omega_o}{\omega - n \omega_o - kW_c} \right) J_n(RK) = 0. \quad (50)$$

By rearranging equation (50), ω can be expressed as

$$\omega = C \omega_o + k W_c \quad (51)$$

where

$$C = n + \frac{2}{\frac{RK}{n} \frac{J_{n-1}(RK)}{J_n(RK)} - 1} \quad (52)$$

Equation (51), therefore, is the desired general solution showing a linear relation between the frequency response of the vortex whistle and true airspeed. This, however, is only the situation, as long as the values of the parameters ω_o , k , W_c , α and K are known.

Although equation (51) appears simple the complex values for angular velocity ω and parameter K must be recognized. For this reason it is difficult to obtain a quantitative solution. Fortunately, a numerical procedure as described in Appendix A can be used to obtain the desired solution. The derivation of the expression for the upstream fluid angular velocity ω_o as well as the constant mean axial velocity W_c are included in Appendix B.

3. NUMERICAL RESULTS AND DISCUSSION

It has been suggested and subsequently theoretically proven that the sensor frequency response is linearly proportional to the airspeed under various conditions. The different combinations of vortex tubes and swirlers used are tabulated in Table 1. The results from computer calculations will be presented later. The quantitative results which are derived in Appendix A prove that the analytic theory works well for all combinations of vortex tubes and swirlers tested in the current work. It should be noted that the procedure of calculation presented applied only to those geometries similar to the ones discussed in this study. For other designs the procedure of calculation would have to be modified. The quantitative results and discussions of the theoretical work can be summarized as follow.

3.1 Relationship between Flow Rate and Frequency Response

Basically, the flow rate versus frequency response has the same relationship as airspeed versus frequency response, i.e., the flow rate is linearly proportional to the frequency response. For the swirlers with the same exit angle

Table 1 Different combinations of vortex tube and swirler.

Sensor No. Size		1	2	3	4	5	6
		D_1	cm (in)	1.892 (0.745)	1.892 (0.745)	1.892 (0.745)	1.892 (0.745)
D_2	cm (in)	1.588 (0.625)	1.588 (0.625)	1.524 (0.600)	1.524 (0.600)	0.953 (0.375)	0.953 (0.375)
D_2	cm (in)	0.953 (0.375)	0.635 (0.250)	0.953 (0.375)	0.635 (0.250)	0.953 (0.375)	0.635 (0.250)

Note: D_1 , D_2 and D_3 are shown in Fig. 1.

but different flutes, the theoretical frequency responses are the same as shown in Figs. 2-9. Under the specified condition and configuration, the frequency response changes dramatically as the cross-sectional size of the precessional flow region changes. For example, the frequency response for Sensor 2 is approximately 3.5 times greater than that of Sensor 1. The frequency response is higher with larger exit angle swirlers. It is expected that these sensors can be utilized as an instrument for measurement of flow rates in the industrial and research areas.

3.2 Effect of Exit Angle on Swirler

In general, under the same conditions, the higher the exit angle, the higher the frequency response. This is true because at higher exit angles the tangential component of flow is higher. The higher exit angles generate higher angular velocities or revolutions which in turn produce higher frequencies. A comparison of the results is possible by reference to Figs. 10-30.

3.3 Effect of Wavenumber

The results for Sensor 1 with wavenumber one, three, five and seven are shown in Figs. 12, 13, 14 and 15 respectively. When the results are compared each to the other there appears no difference. This quantitative result therefore proves that the frequency response does not depend on the wavenumber. This also indicates that the

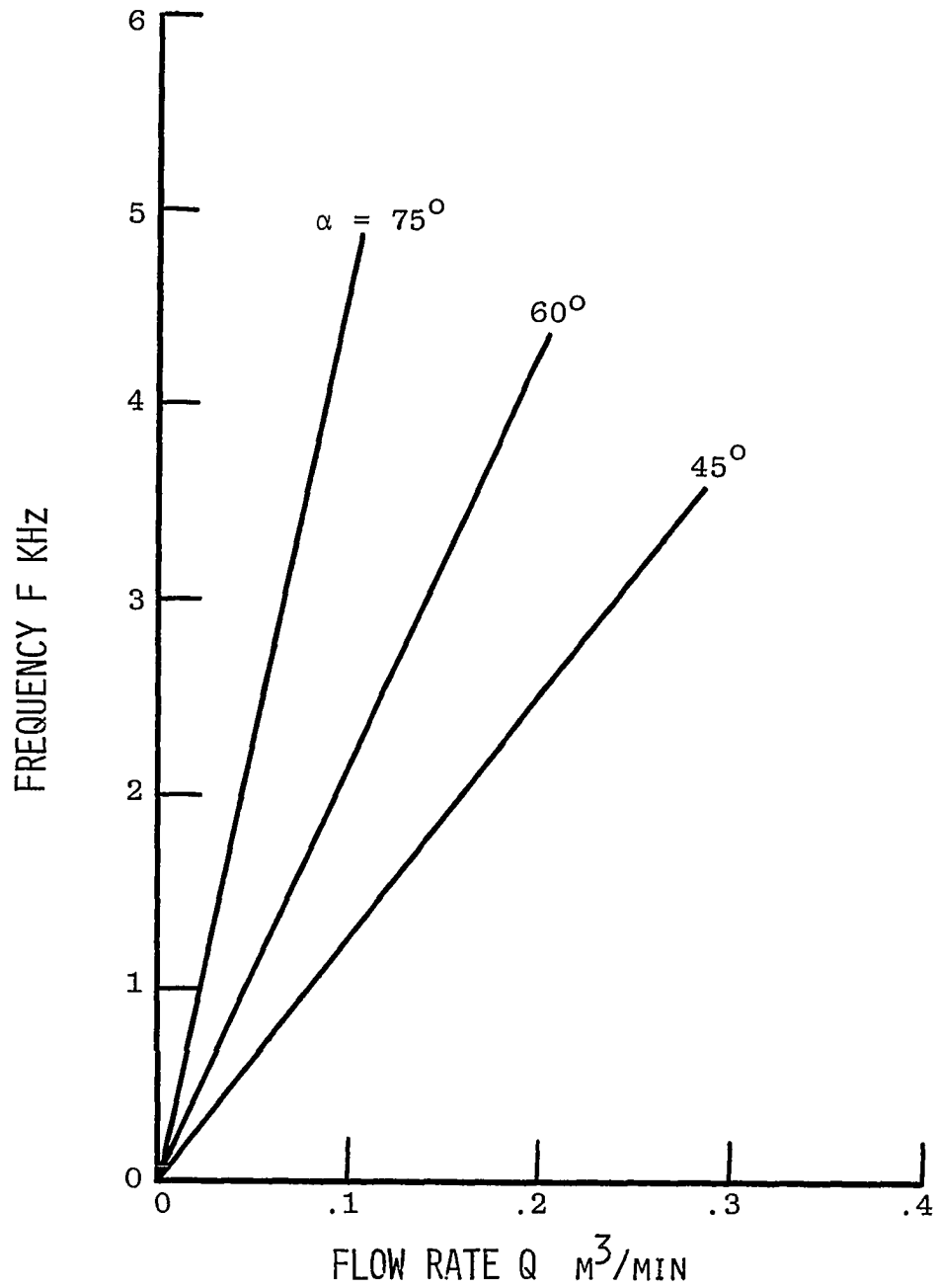


Fig. 2 Flow rate versus frequency response for Sensor 1 with swirlers having two flutes and various exit angles.

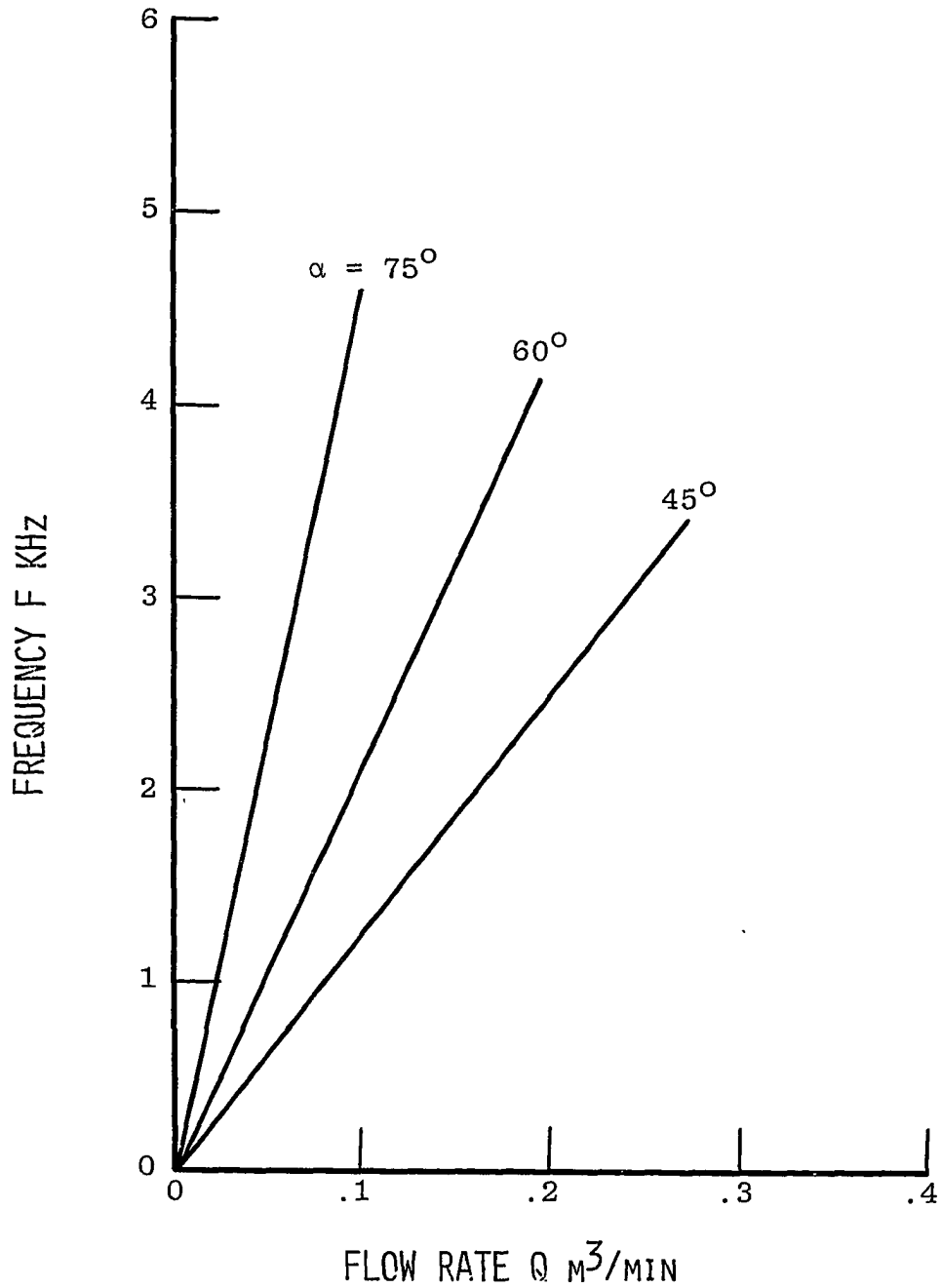


Fig. 3 Flow rate versus frequency response for Sensor 1 with swirlers having three flutes and various exit angles.

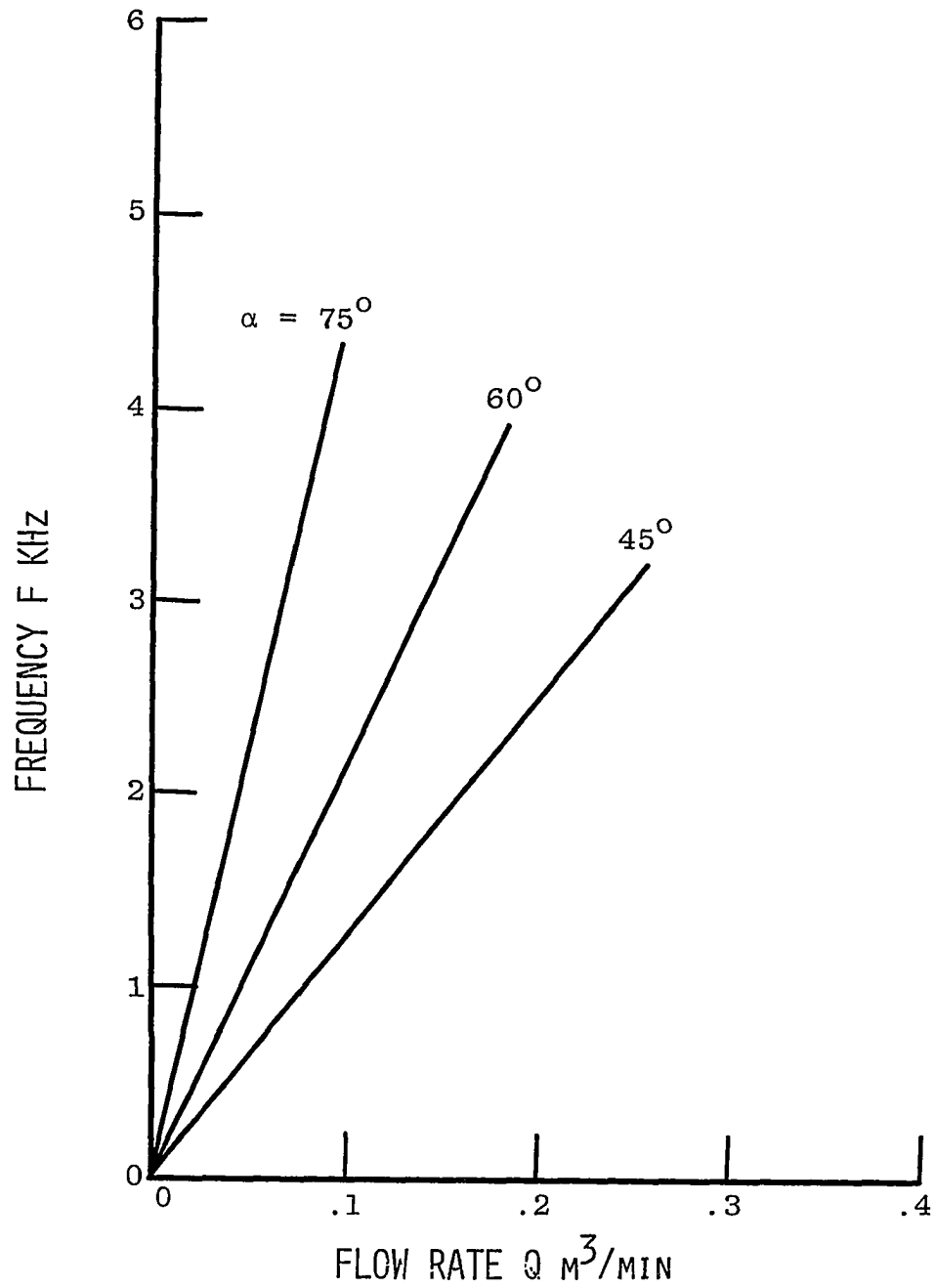


Fig. 4 Flow rate versus frequency response for Sensor 1 with swirlers having four flutes and various exit angles.

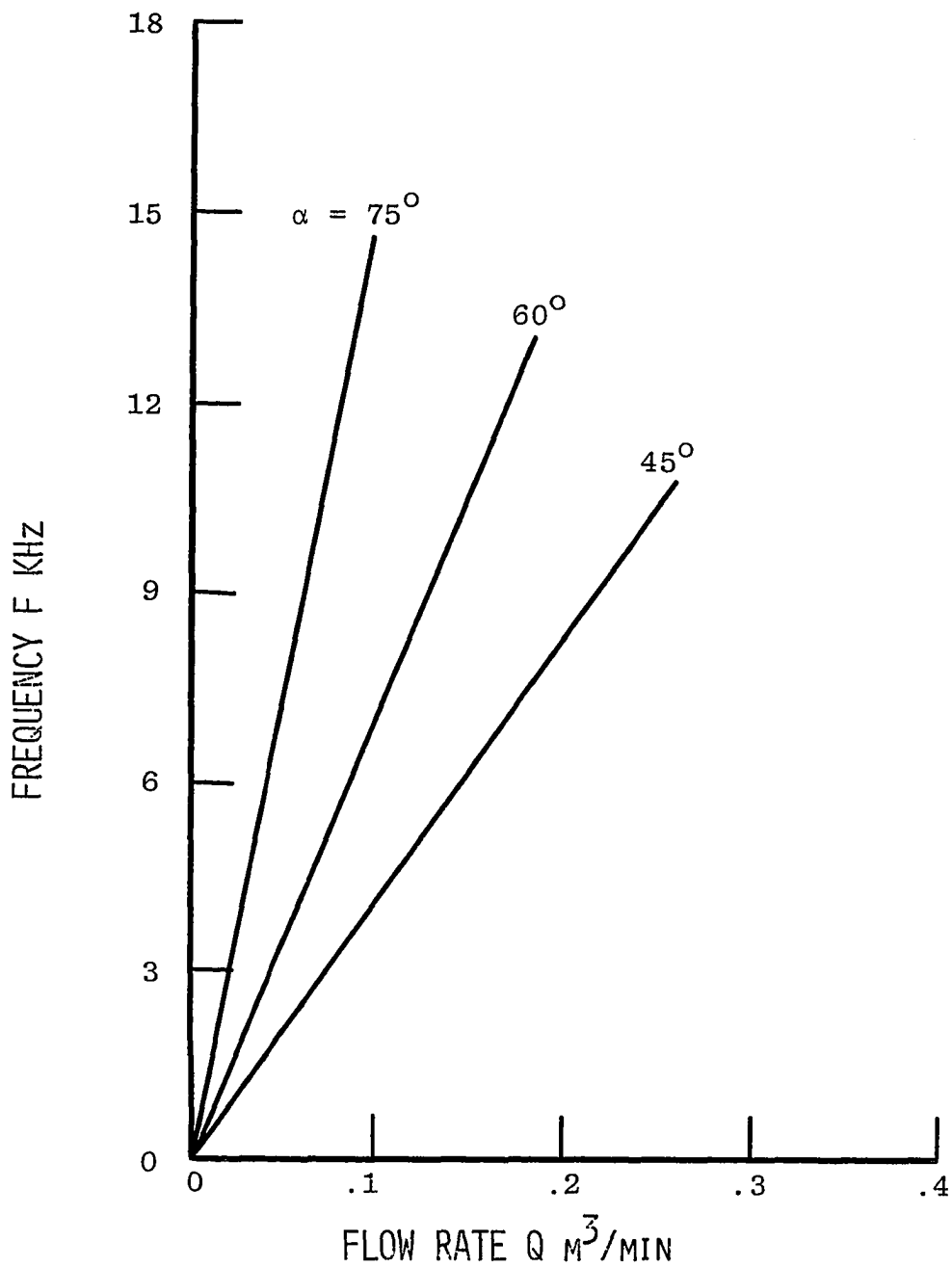


Fig. 5 Flow rate versus frequency response for Sensor 2 with swirlers having four flutes and various exit angles.

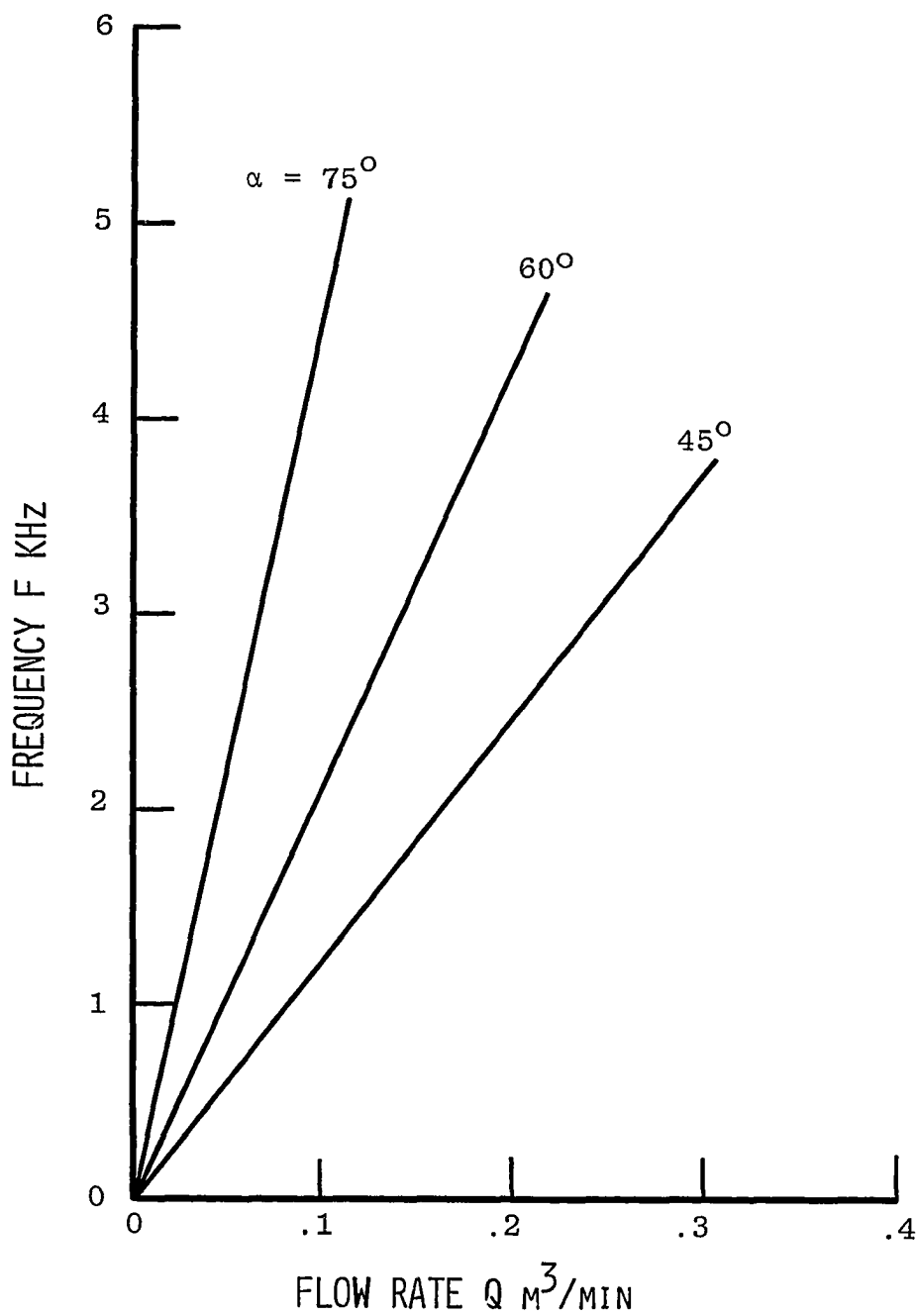


Fig. 6 Flow rate versus frequency response for Sensor 3 with swirlers having four flutes and various exit angles.

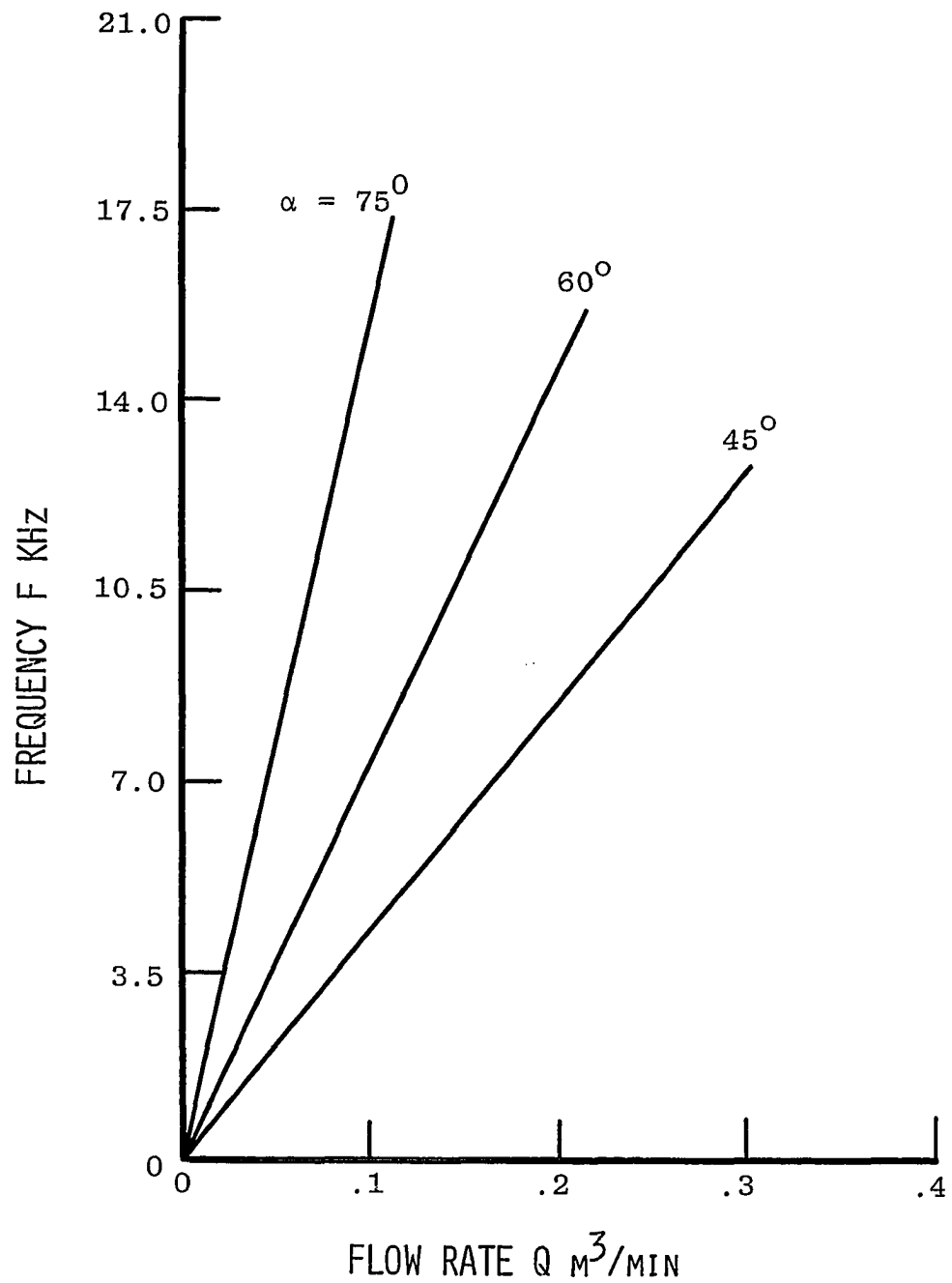


Fig. 7 Flow rate versus frequency response for Sensor 4 with swirlers having four flutes and various exit angles.

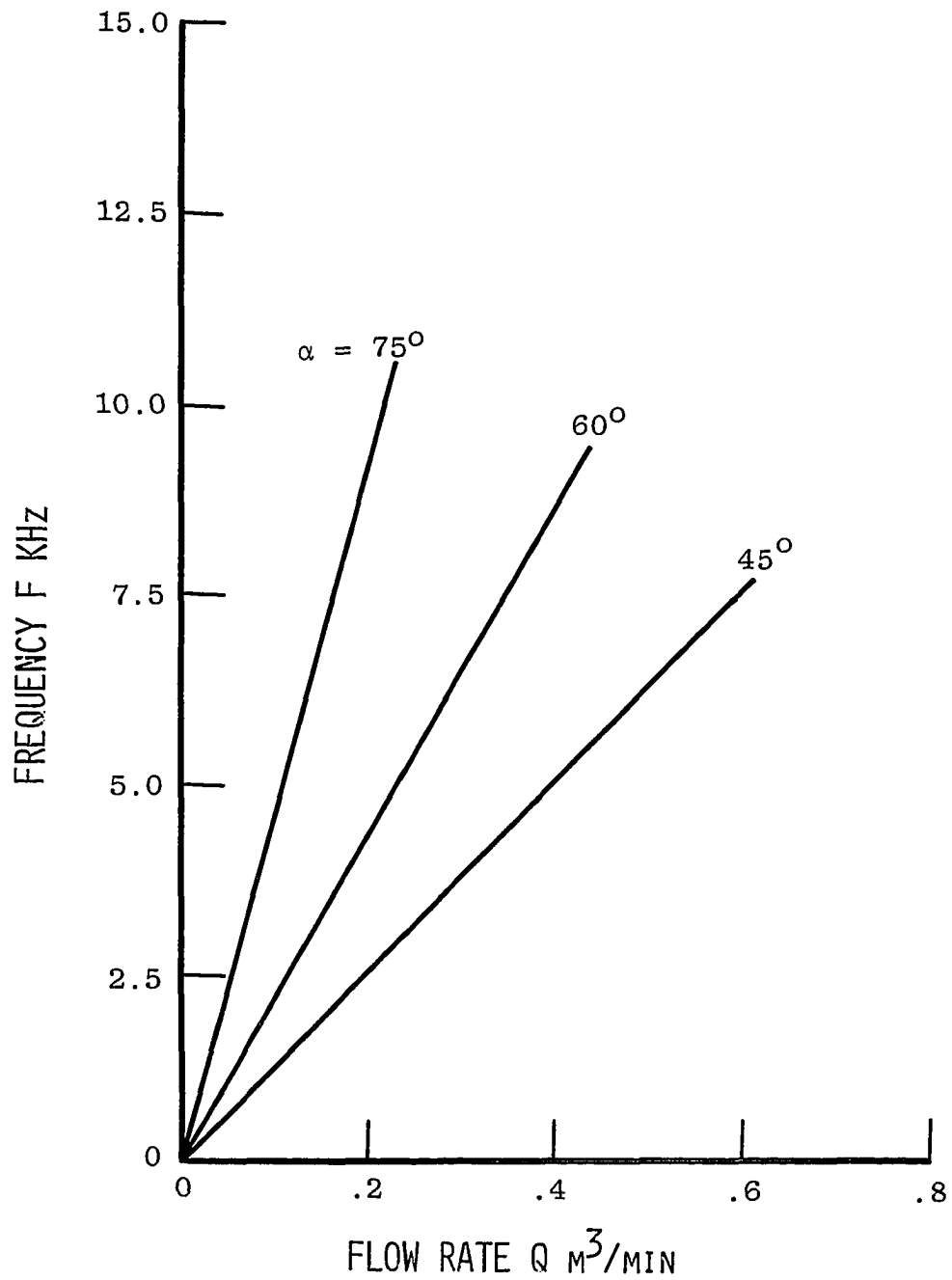


Fig. 8 Flow rate versus frequency response for Sensor 5 with swirlers having four flutes and various exit angles.

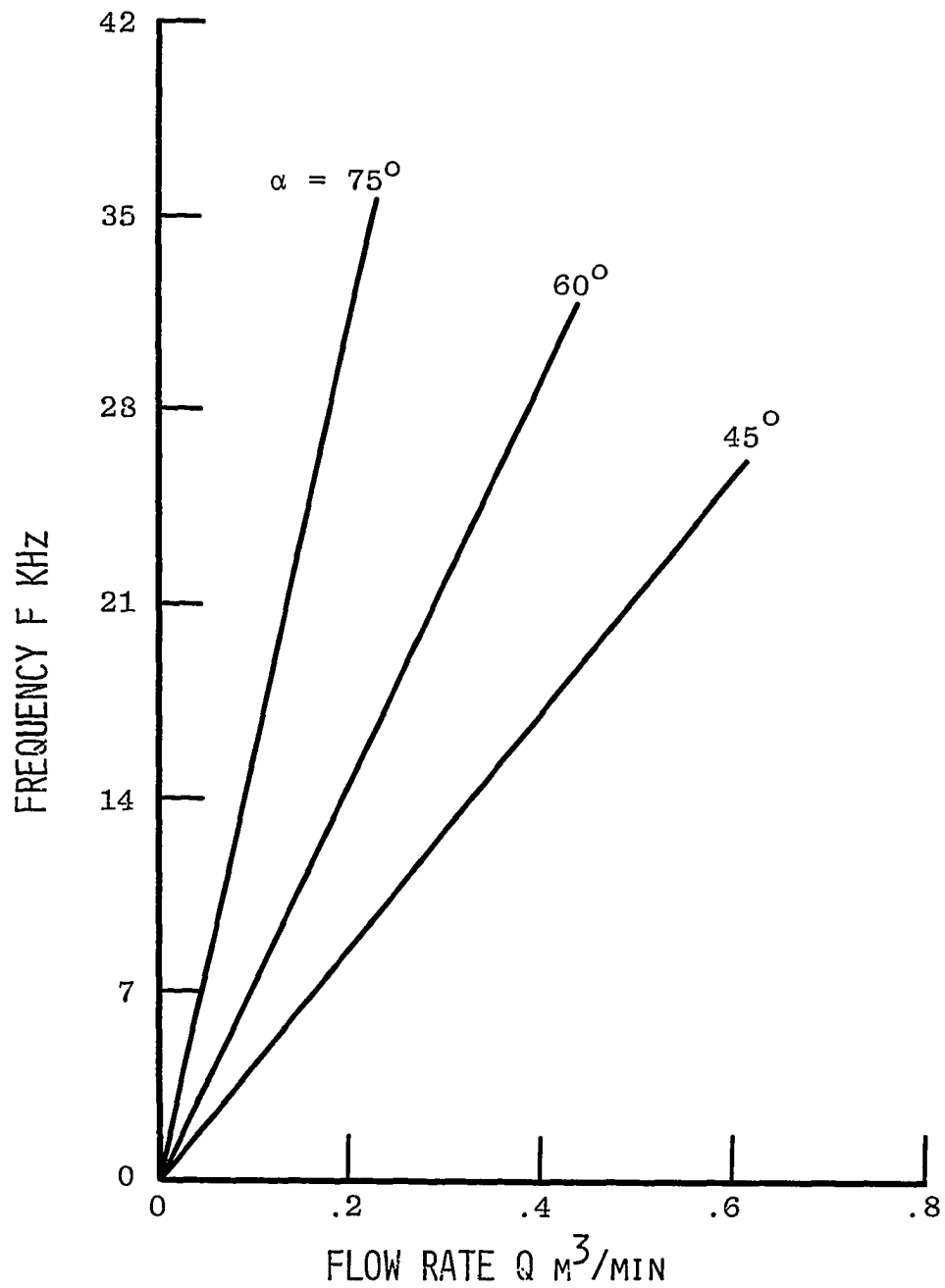


Fig. 9 Flow rate versus frequency response for Sensor 6 with swirlers having four flutes and various exit angles.

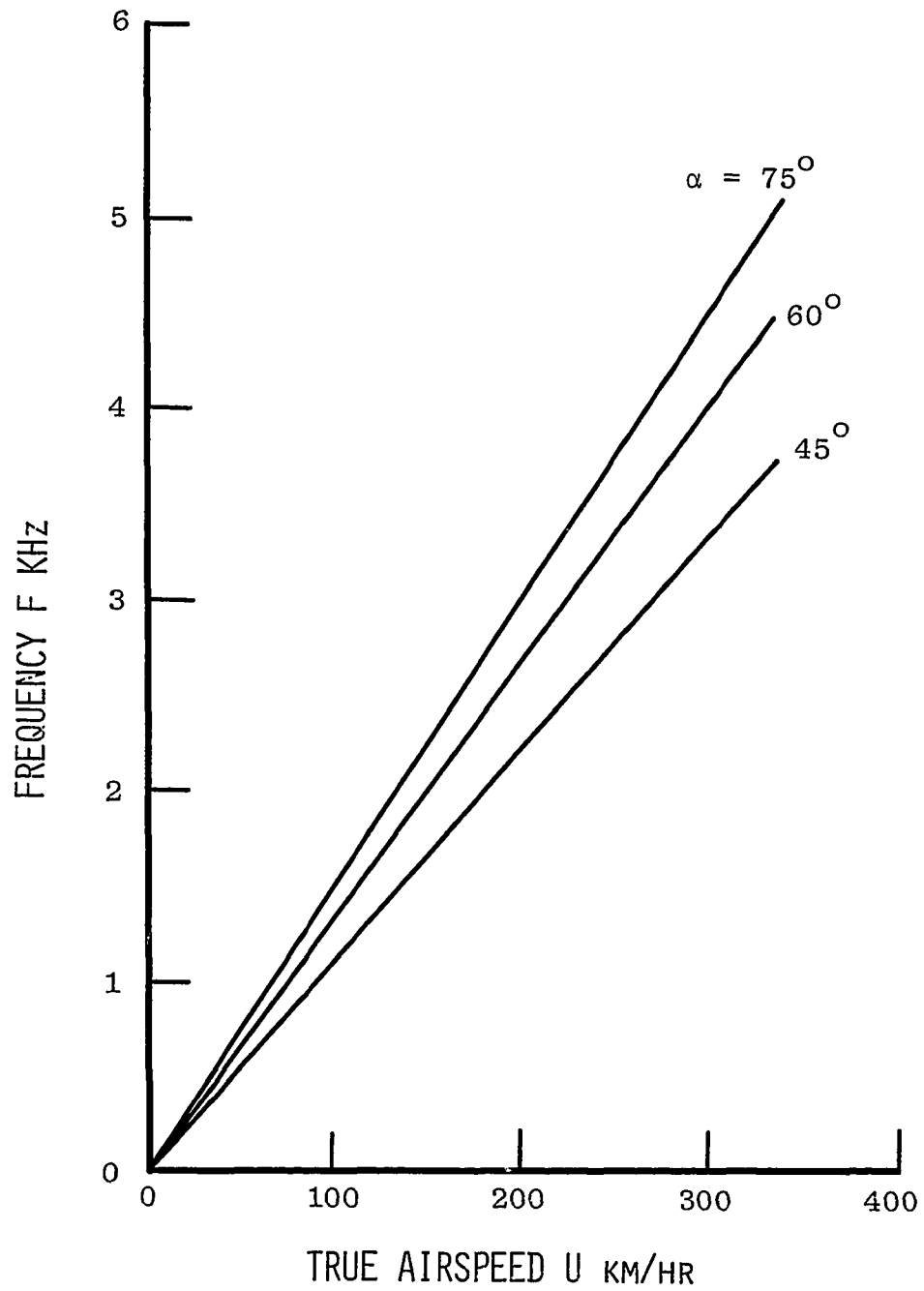


Fig. 10 True airspeed versus frequency response for Sensor 1 with two flutes swirlers and wavenumber $k = 1$.

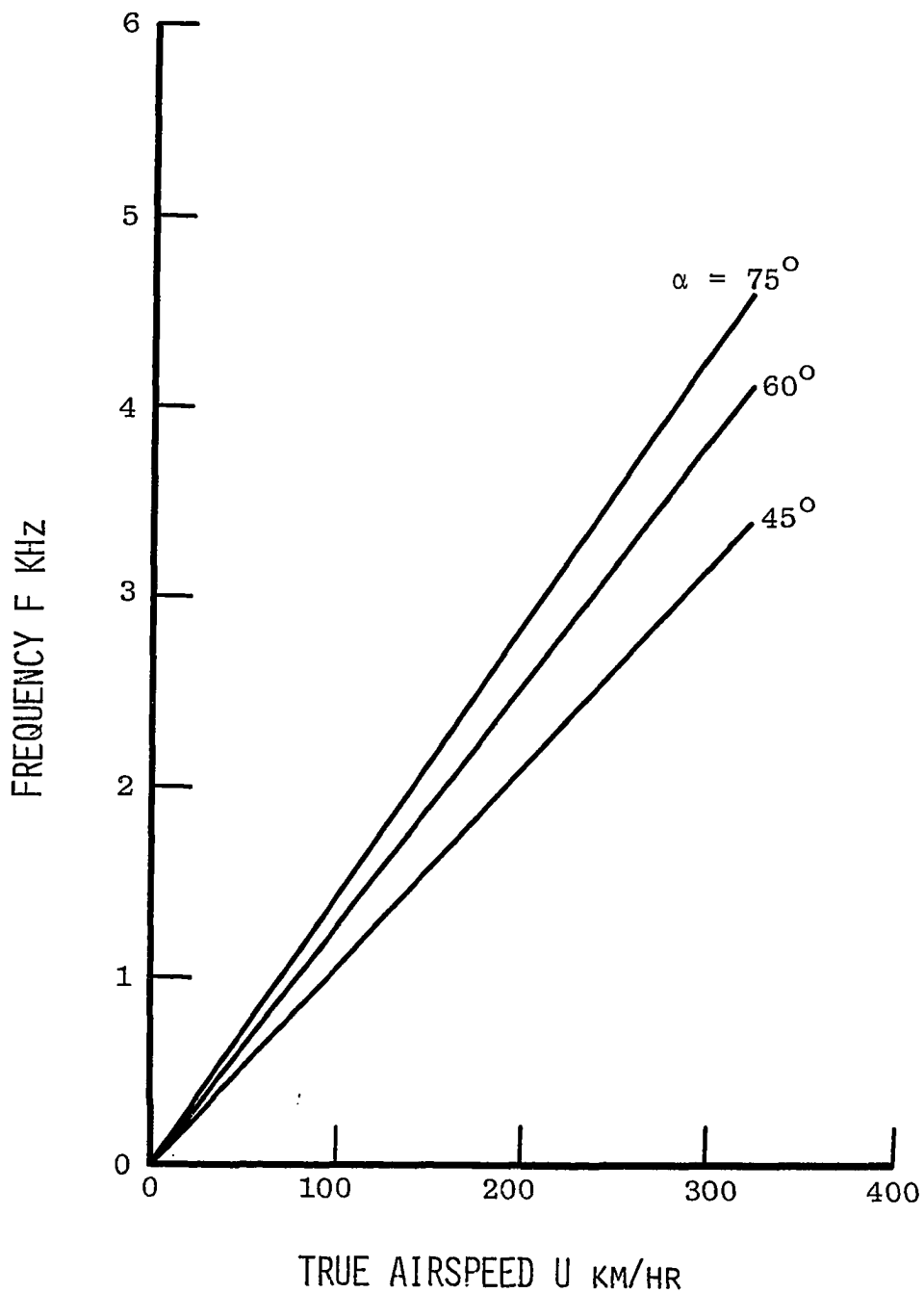


Fig. 11 True airspeed versus frequency response for Sensor 1 with three flutes swirlers and wavenumber $k = 1$.

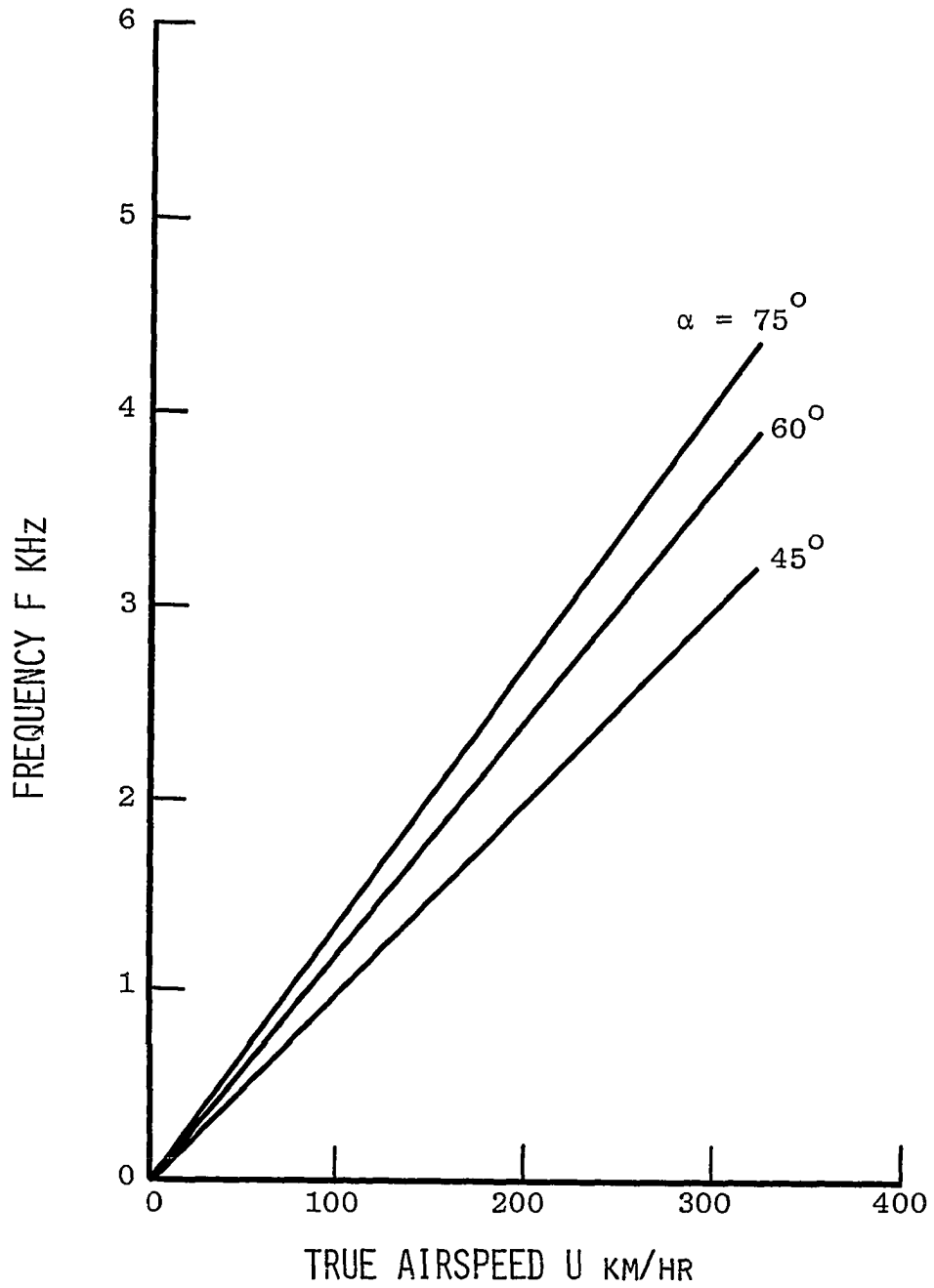


Fig. 12 True airspeed versus frequency response for Sensor 1 with four flutes swirlers and wavenumber $k = 1$.

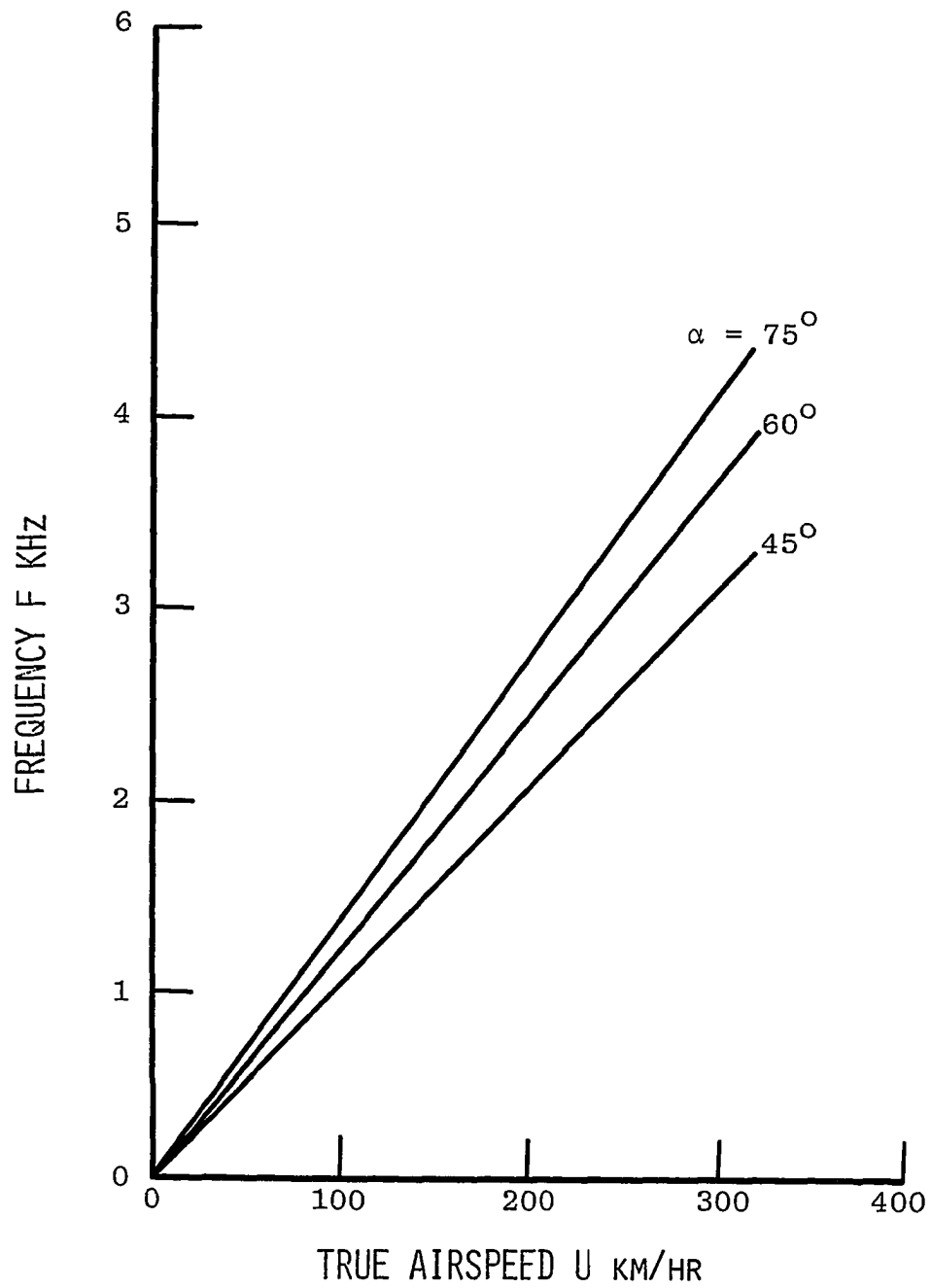


Fig. 13 True airspeed versus frequency response for Sensor 1 with four flutes swirlers and wavenumber $k = 3$.

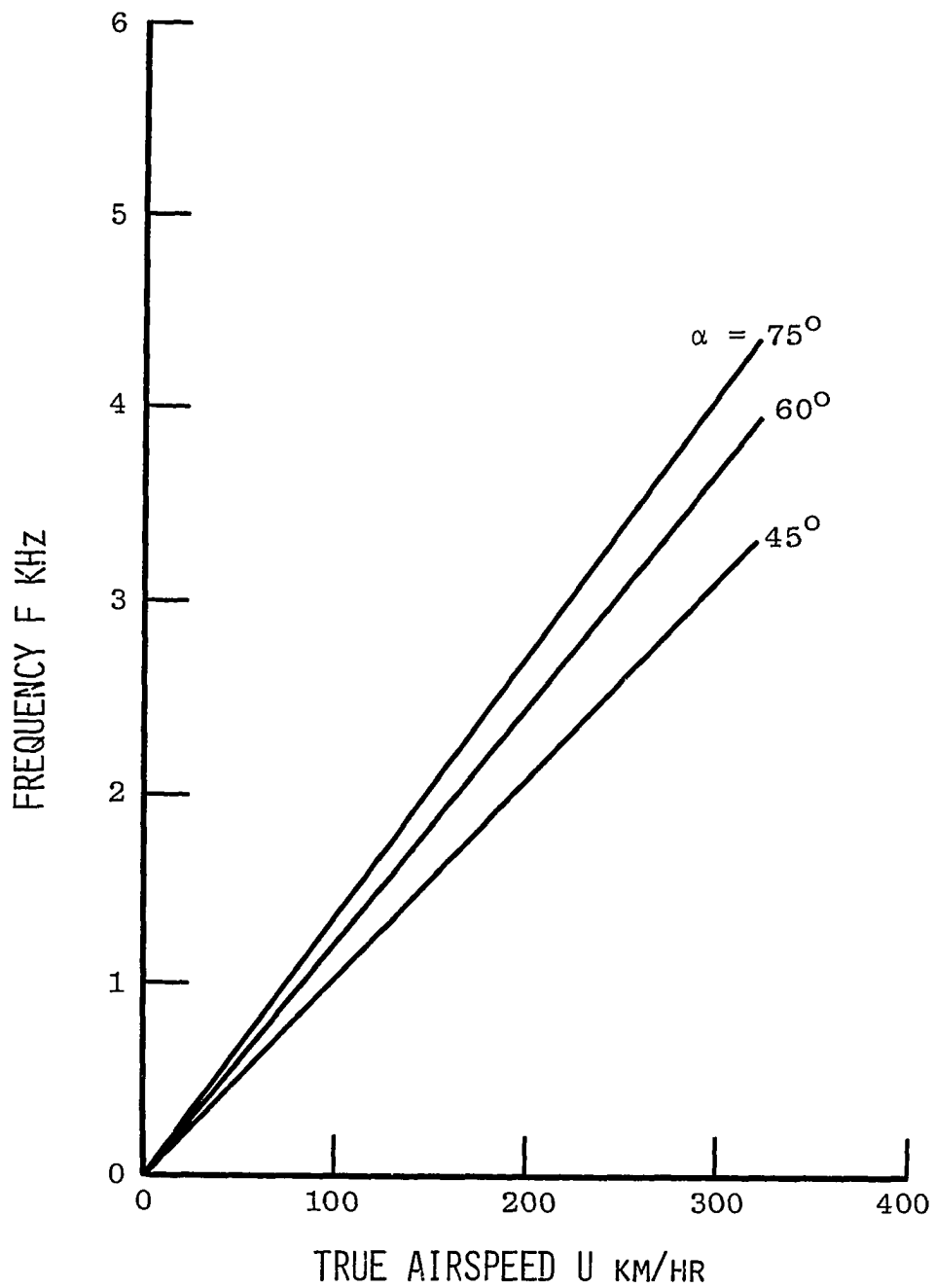


Fig. 14 True airspeed versus frequency response for Sensor 1 with four flutes swirlers and wavenumber $k = 5$.

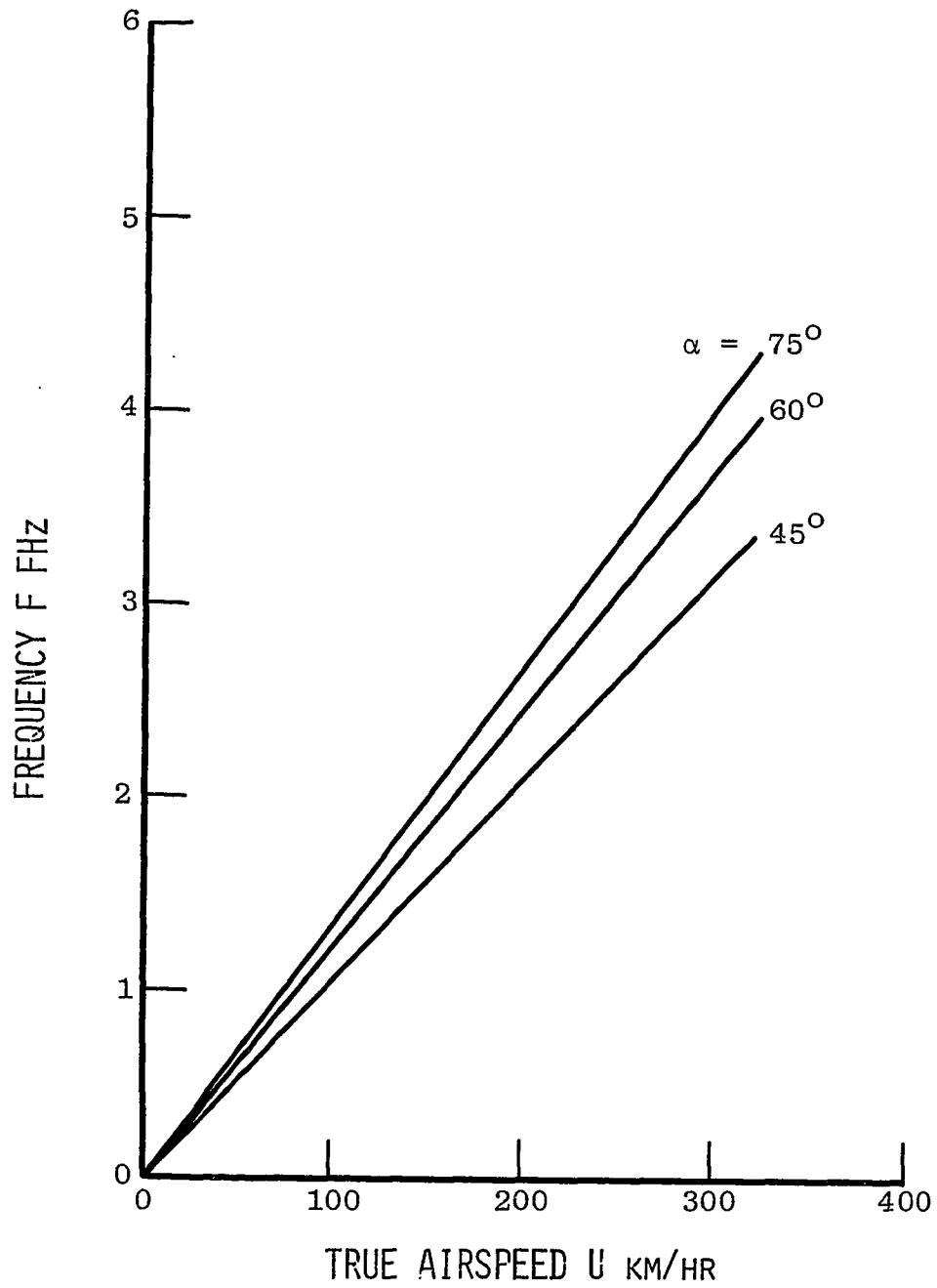


Fig. 15 True airspeed versus frequency response for Sensor 1 with four flutes swirlers and wavenumber $k = 7$.

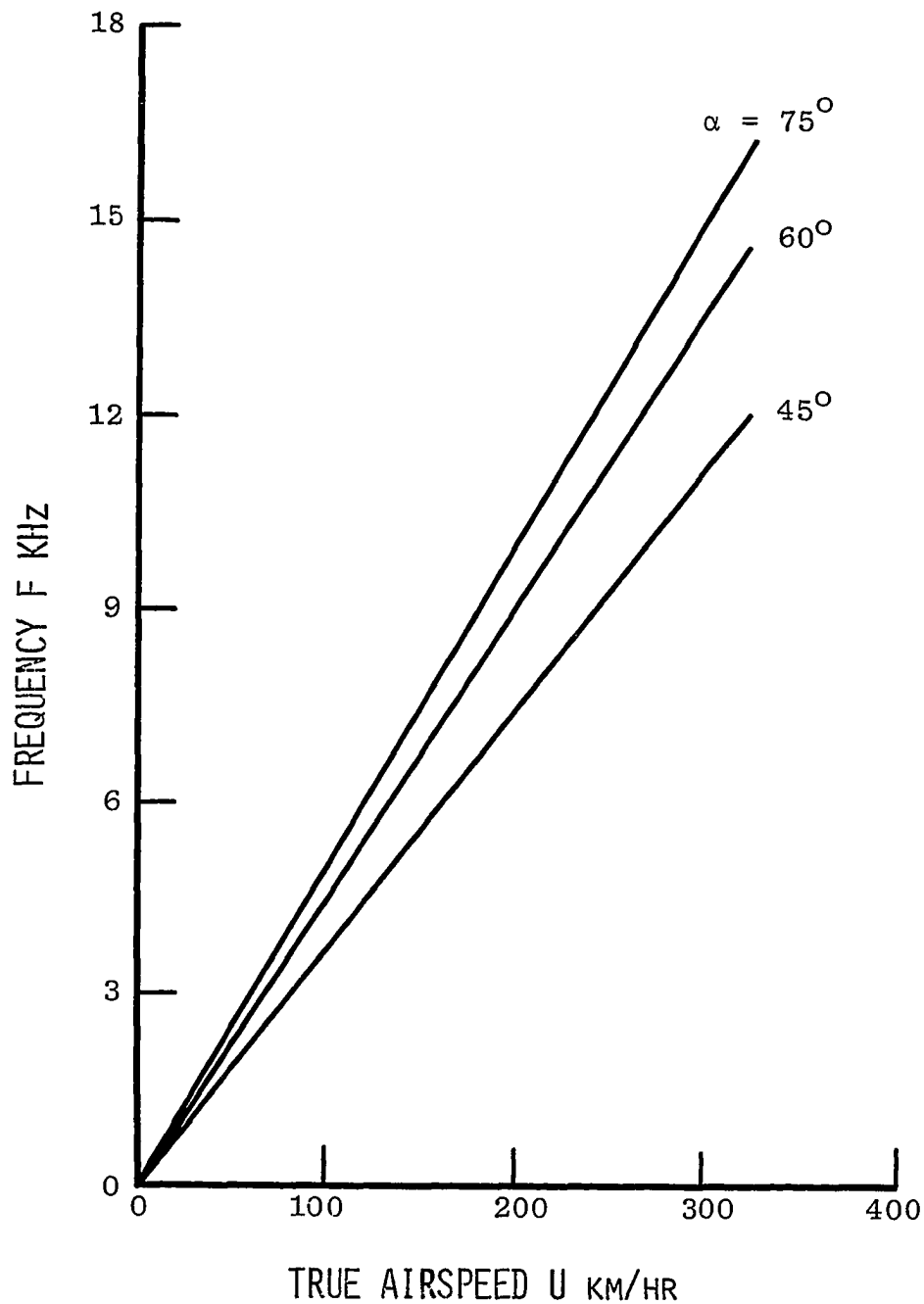


Fig. 16 True airspeed versus frequency response for Sensor 2 with swirlers having two flutes and various exit angles.

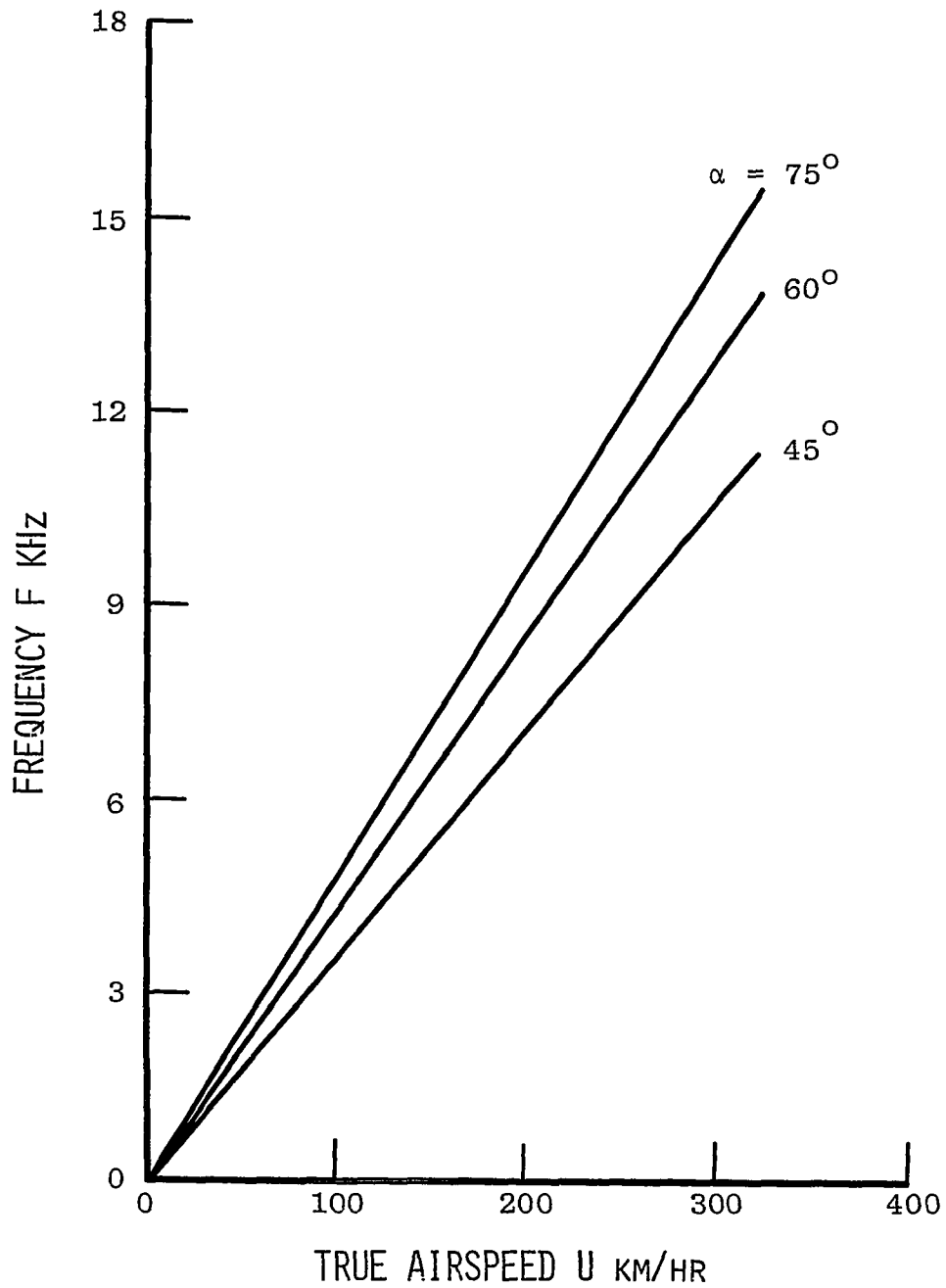


Fig. 17 True airspeed versus frequency response for Sensor 2 with swirlers having three flutes and various exit angles.

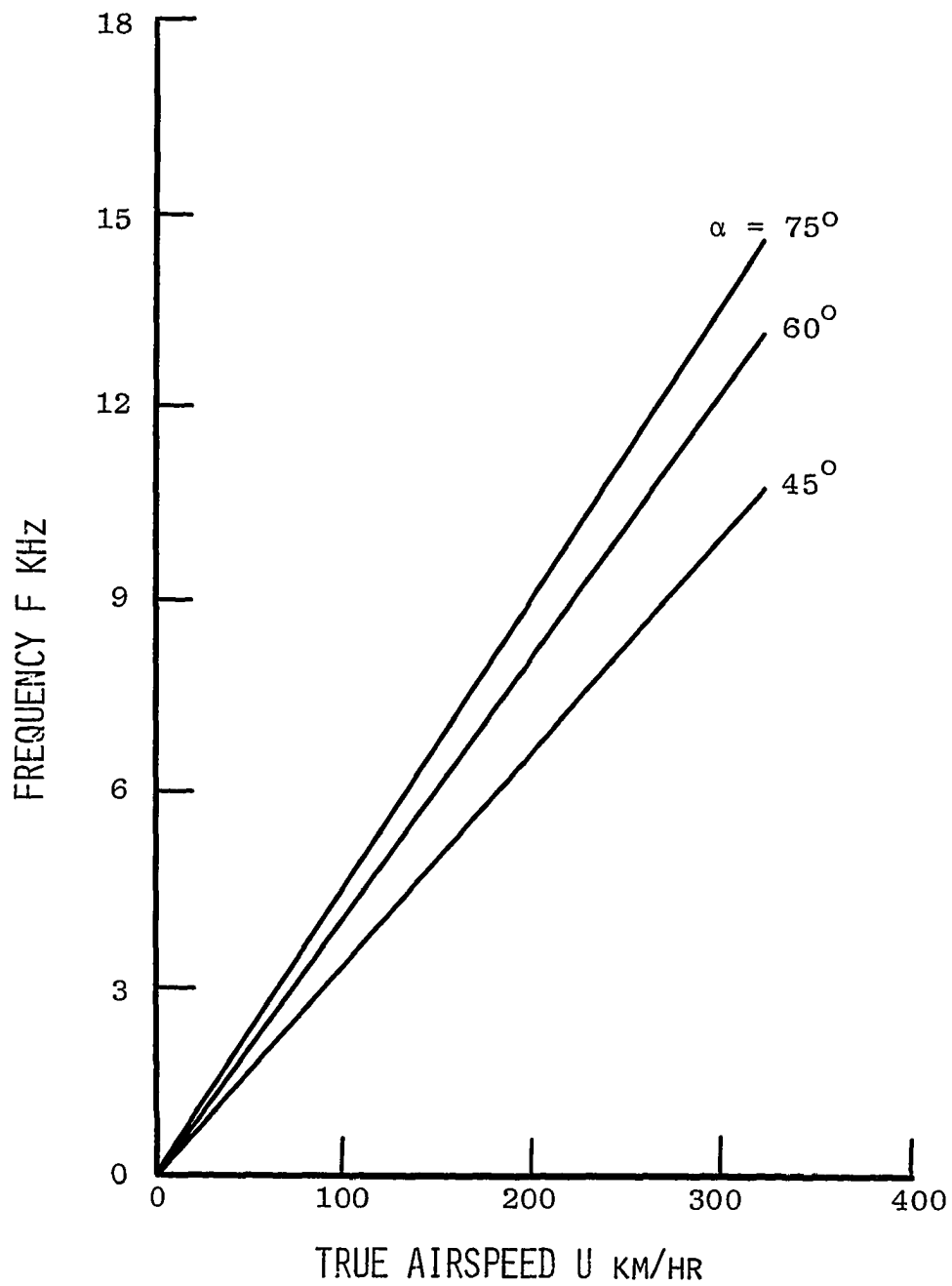


Fig. 18 True airspeed versus frequency response for Sensor 2 with swirlers having four flutes and various exit angles.

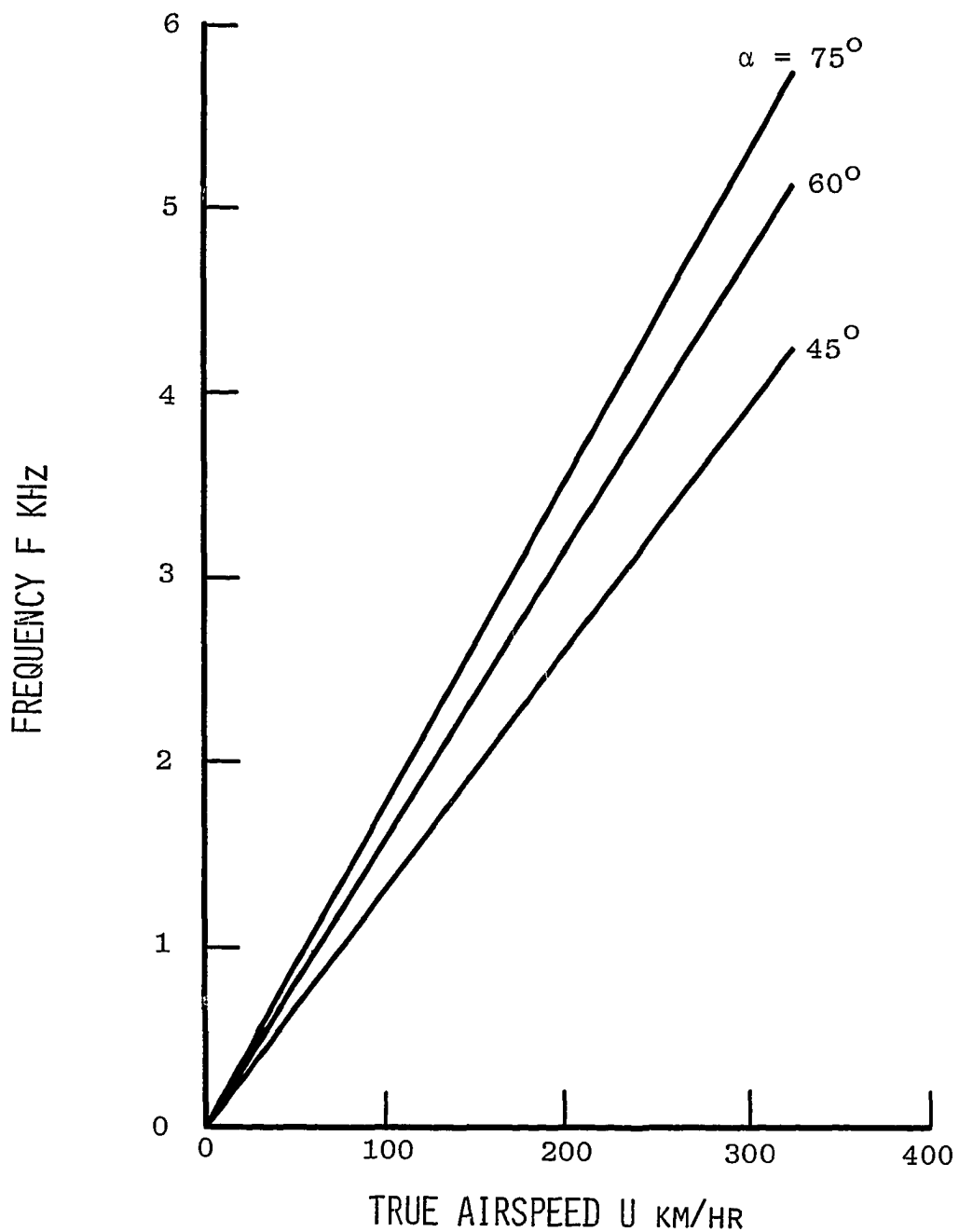


Fig. 19 True airspeed versus frequency response for Sensor 3 with swirlers having two flutes and various exit angles.

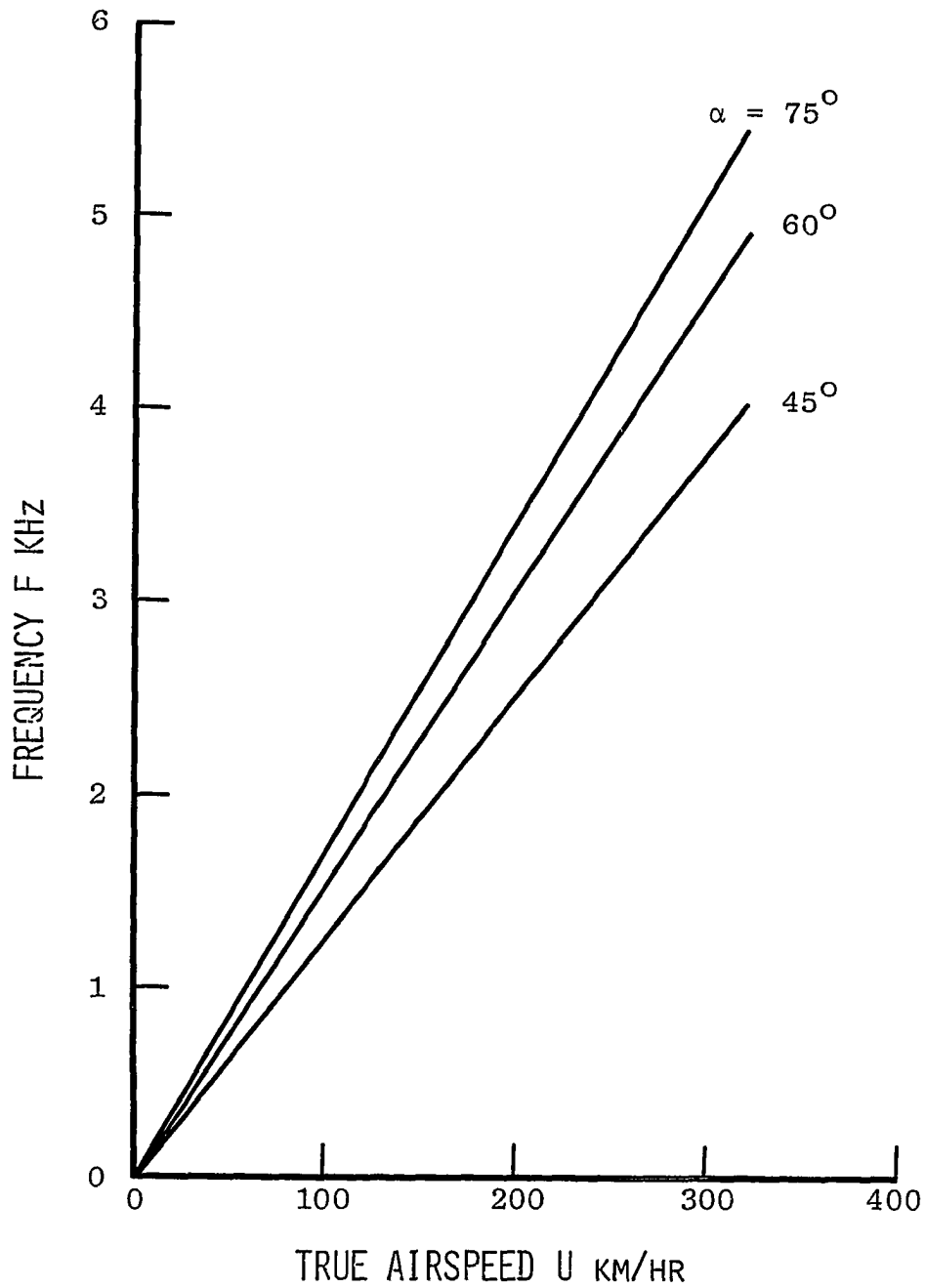


Fig. 20 True airspeed versus frequency response for Sensor 3 with swirlers having three flutes and various exit angles.

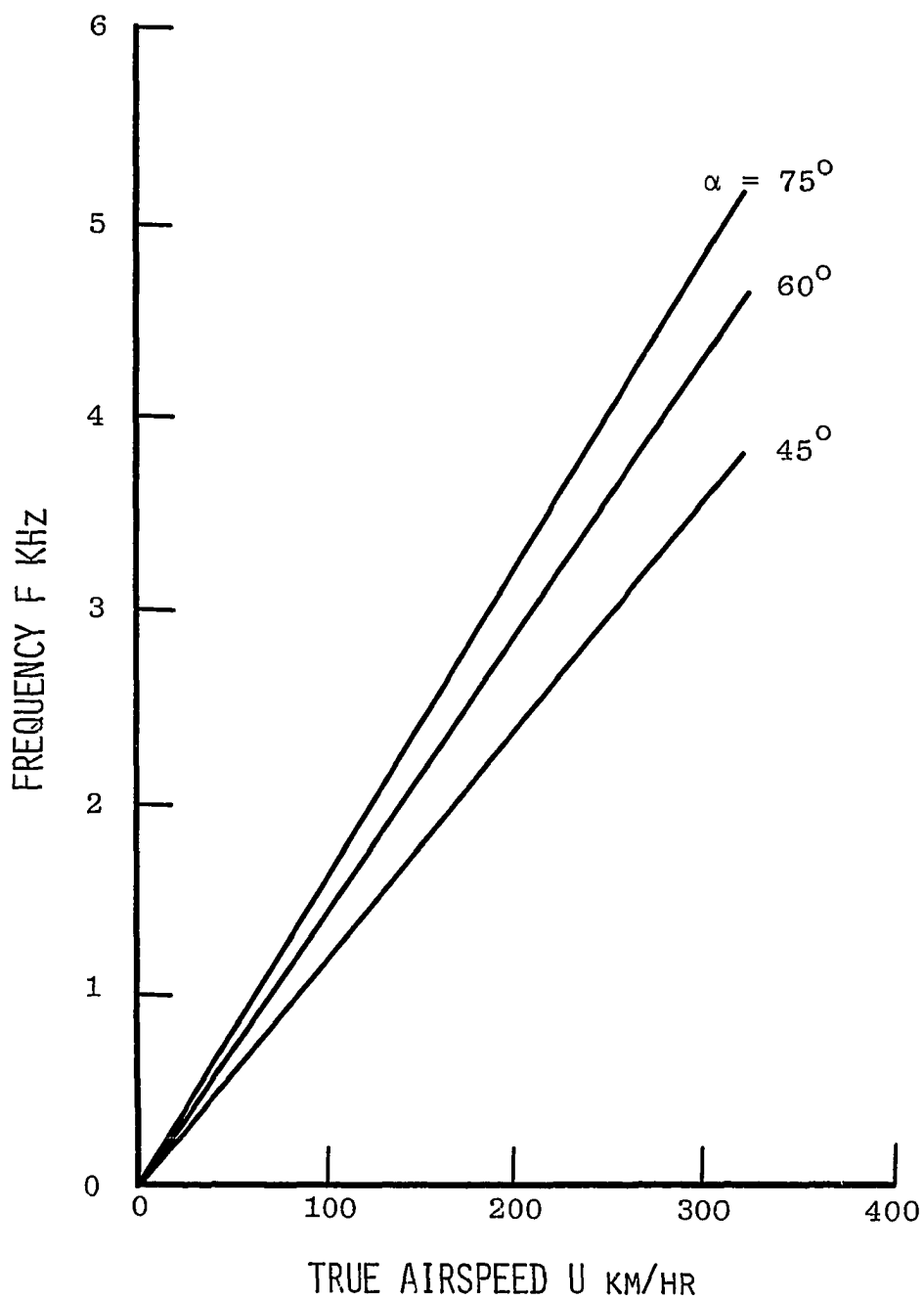


Fig. 21 True airspeed versus frequency response for Sensor 3 with swirlers having four flutes and various exit angles.

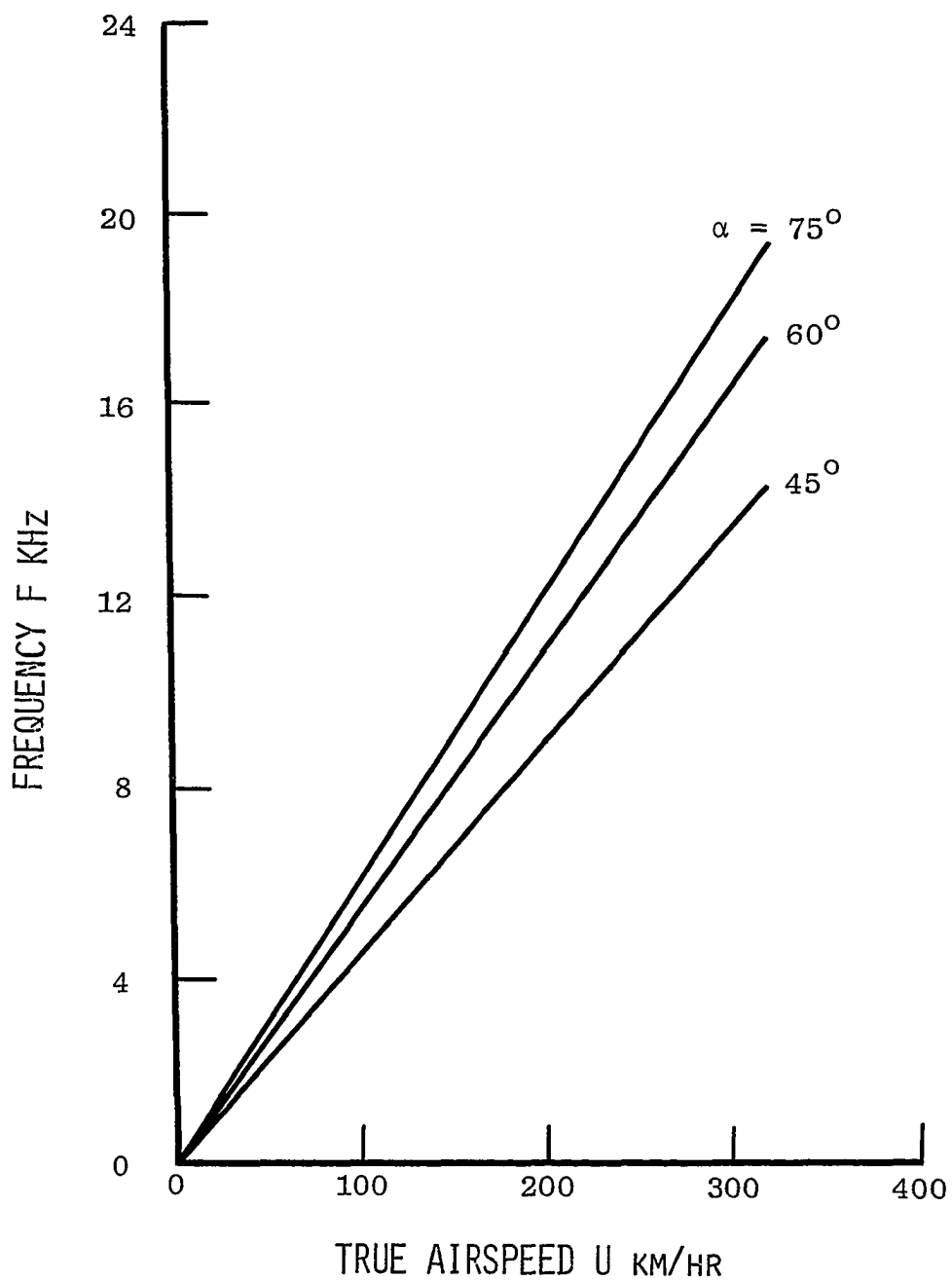


Fig. 22 True airspeed versus frequency response for Sensor 4 with swirlers having two flutes and various exit angles.

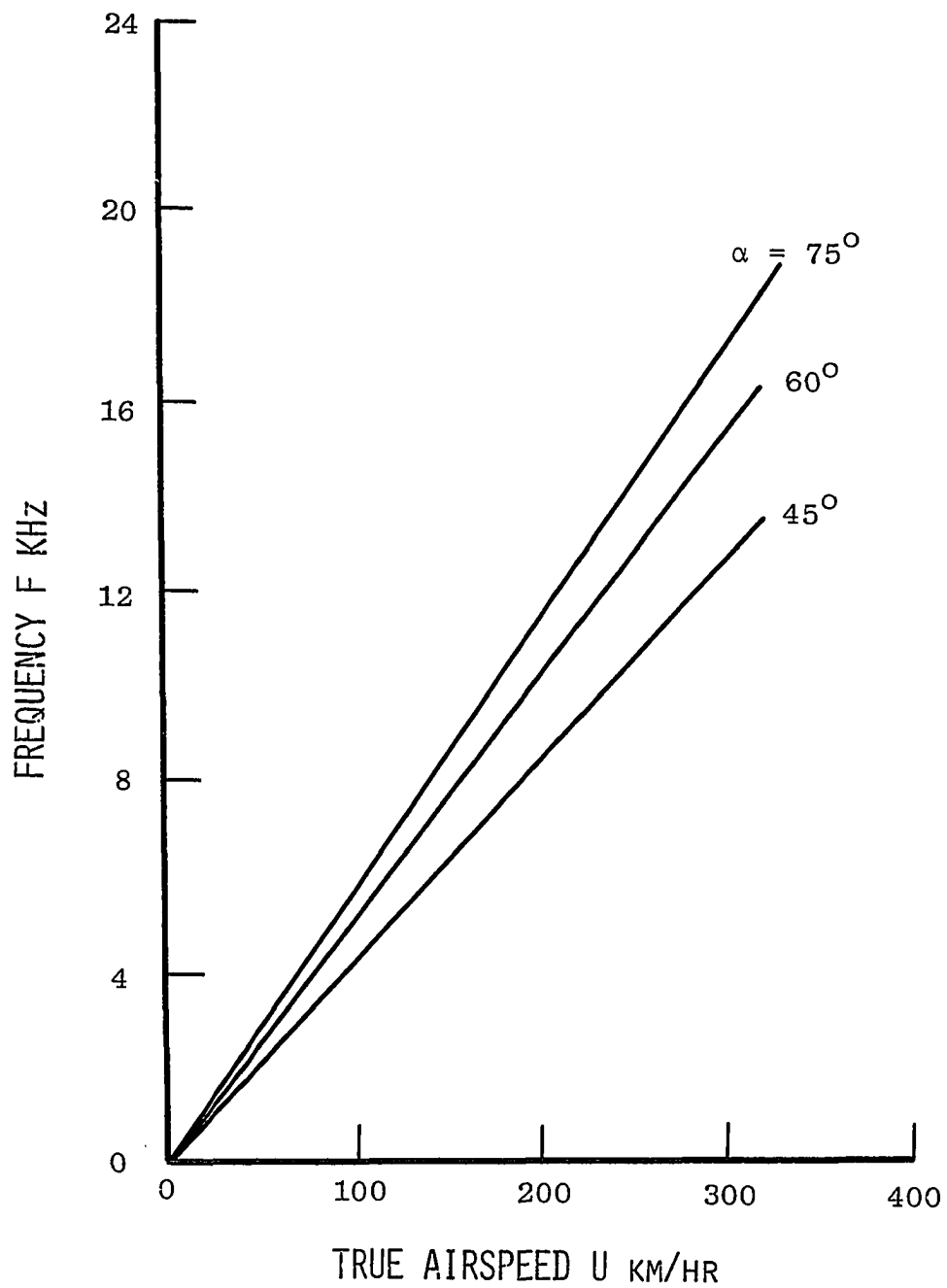


Fig. 23 True airspeed versus frequency response for Sensor 4 with swirlers having three flutes and various exit angles.

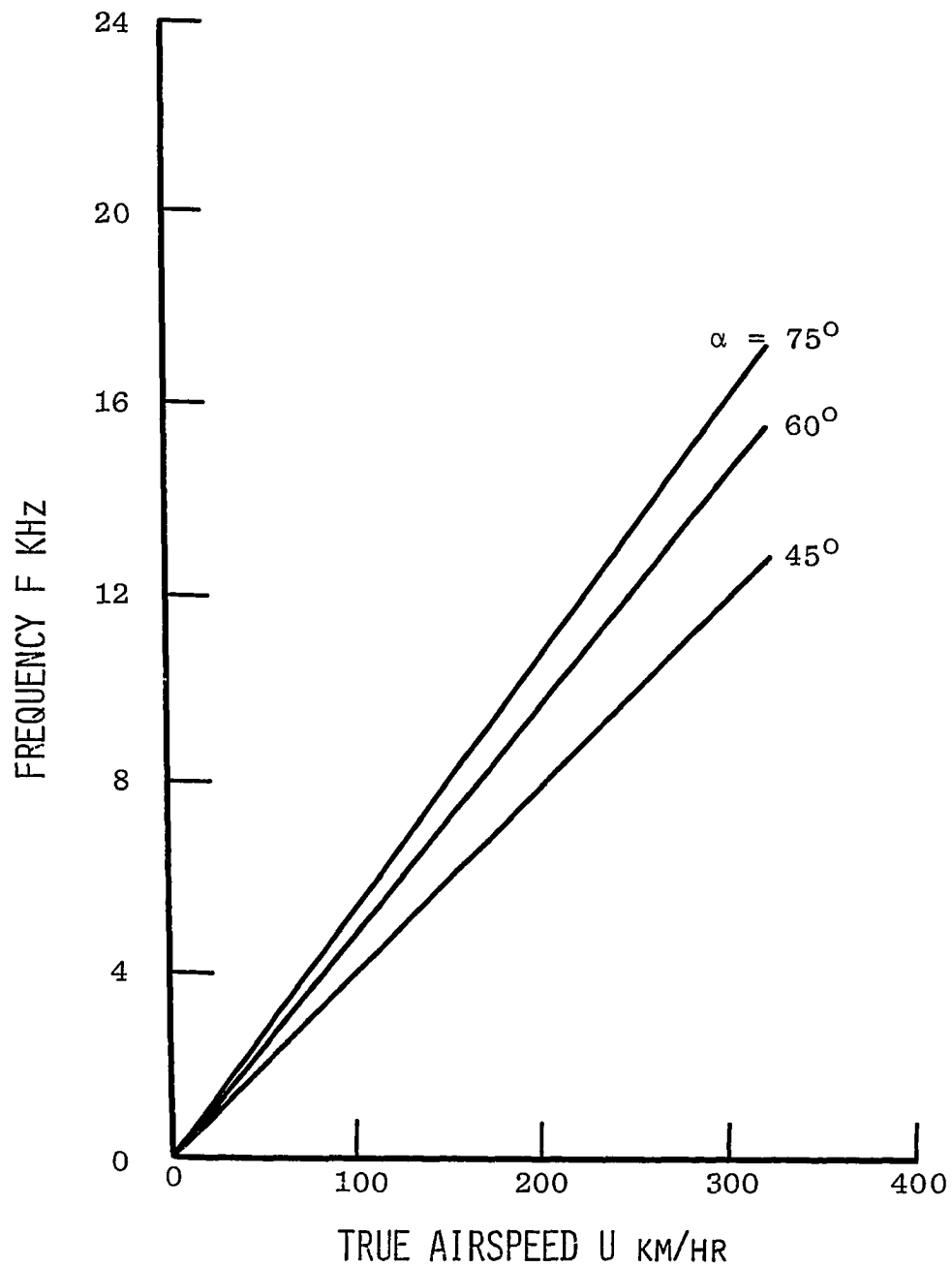


Fig. 24 True airspeed versus frequency response for Sensor 4 with swirlers having four flutes and various exit angles.

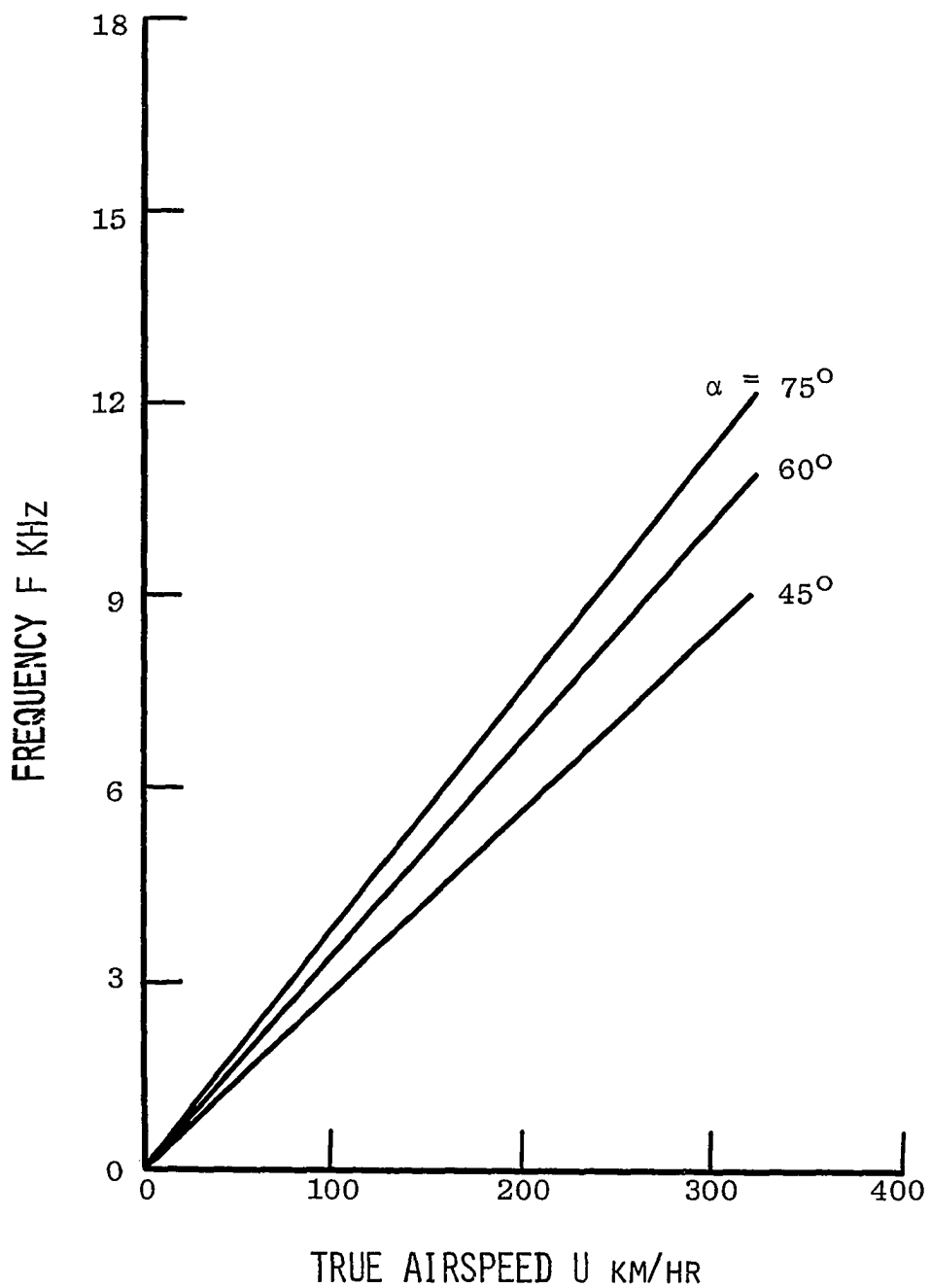


Fig. 25 True airspeed versus frequency response for Sensor 5 with swirlers having two flutes and various exit angles.

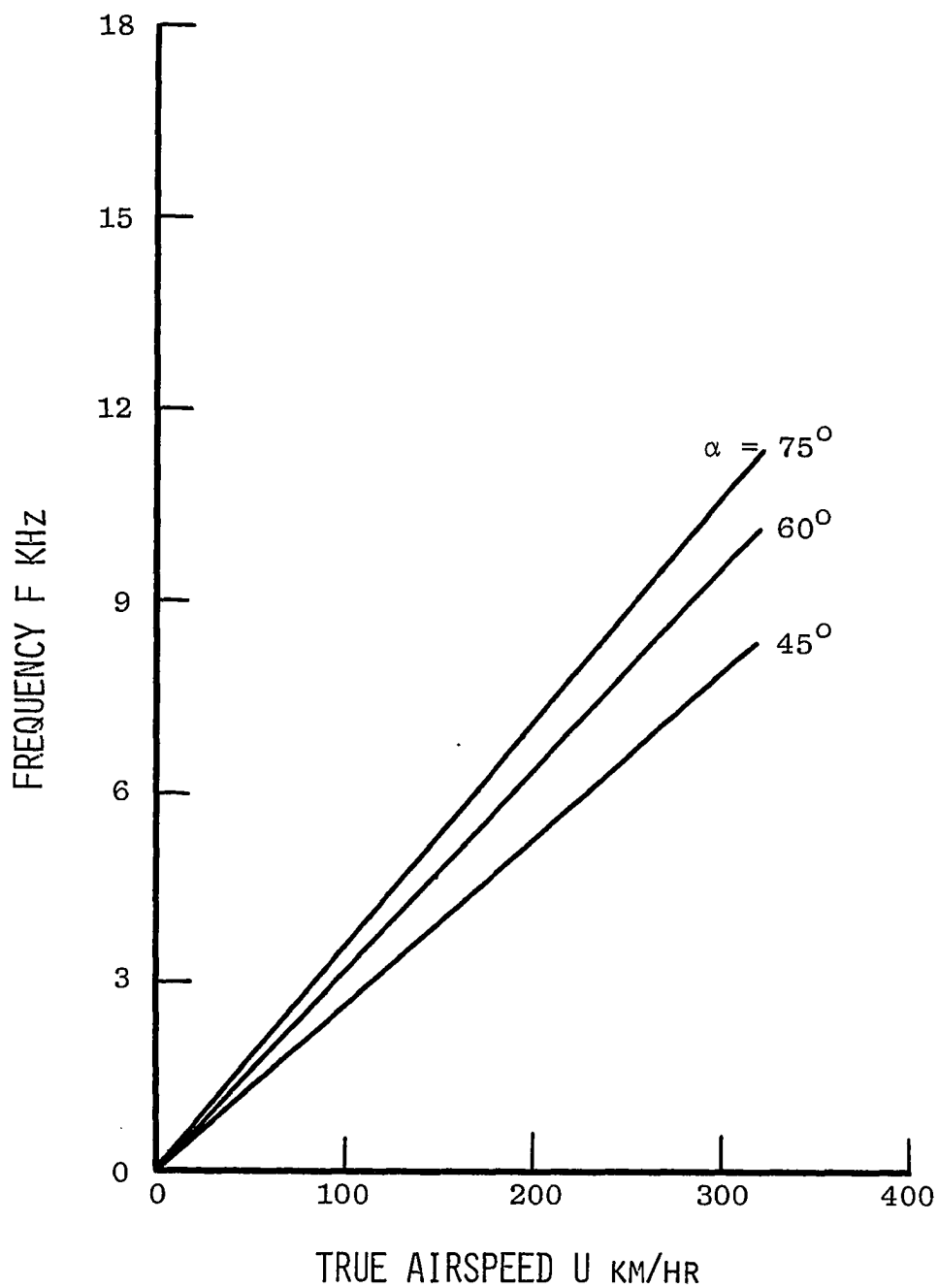


Fig. 26 True airspeed versus frequency response for Sensor 5 with swirlers having three flutes and various exit angles.

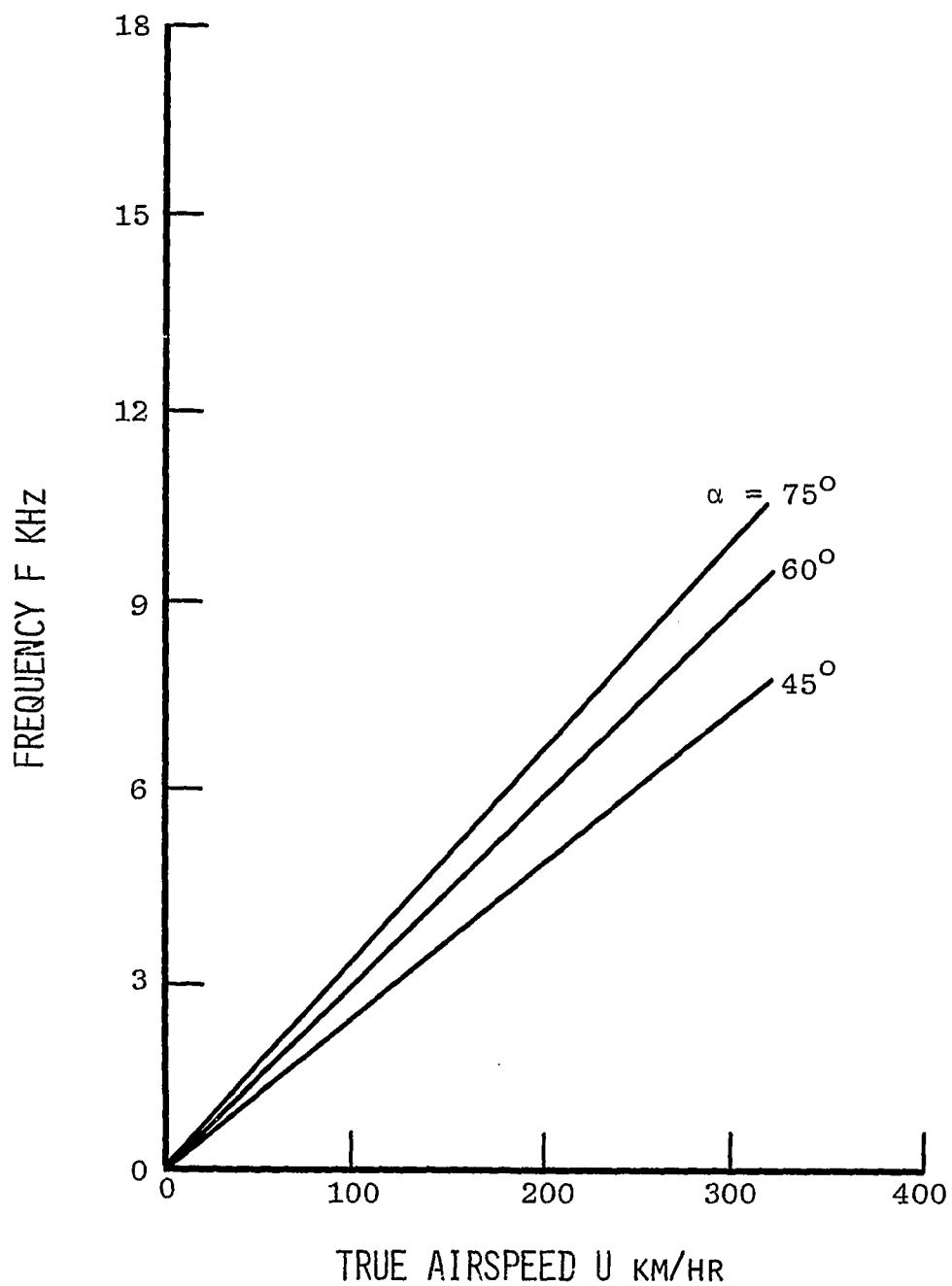


Fig. 27 True airspeed versus frequency response for Sensor 5 with swirlers having four flutes and various exit angles.

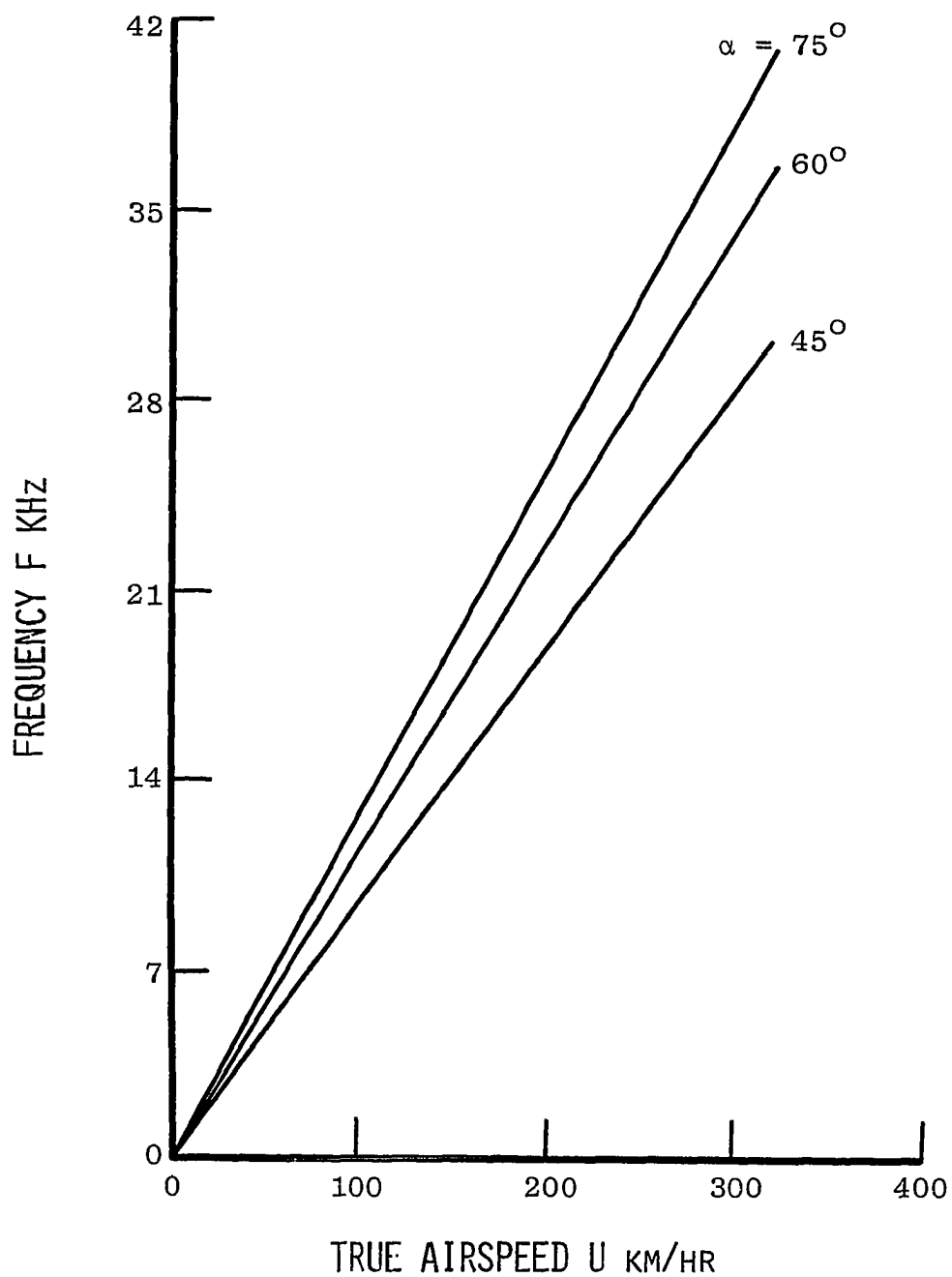


Fig. 28 True airspeed versus frequency response for Sensor 6 with swirlers having two flutes and various exit angles.

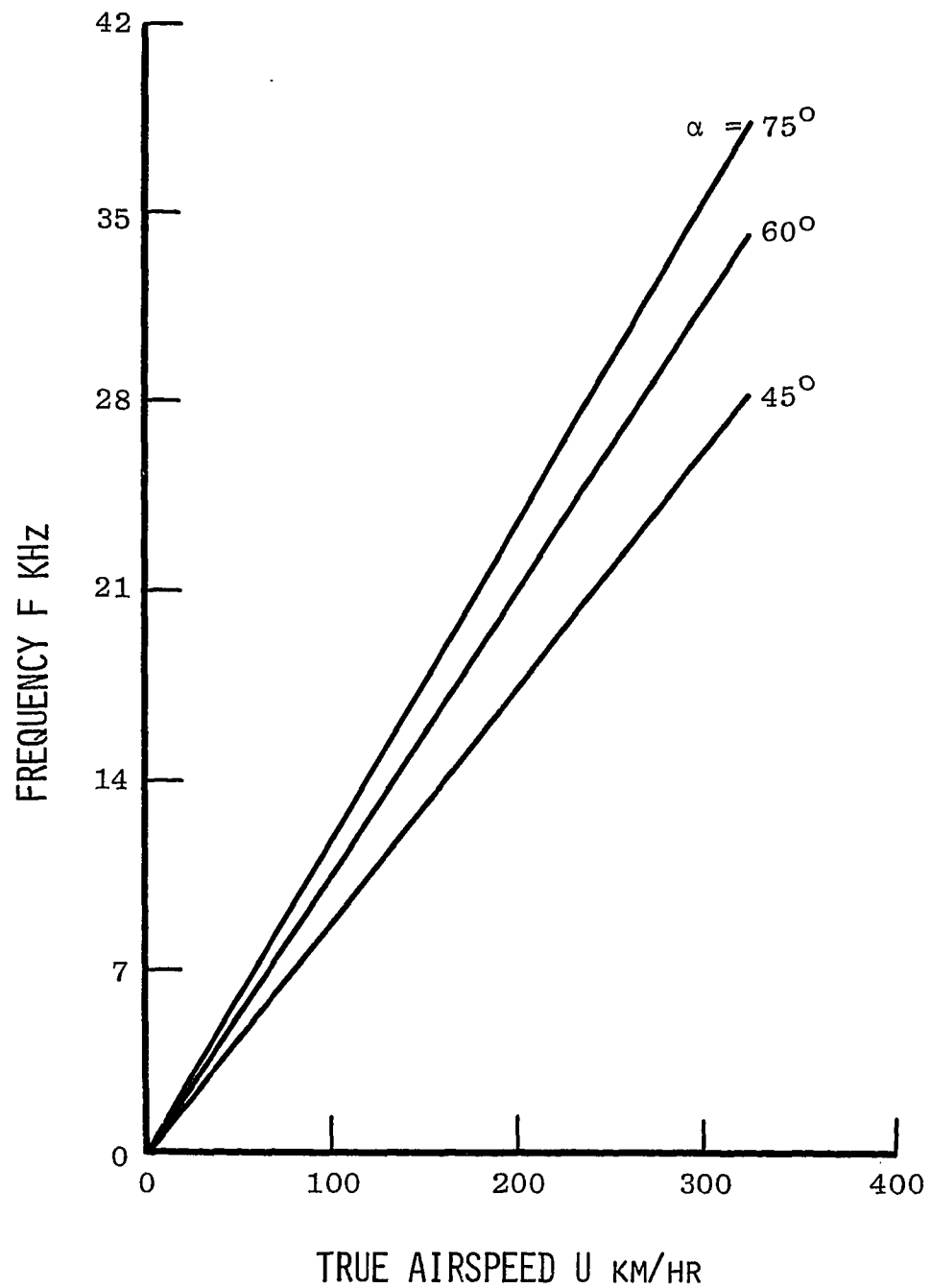


Fig. 29 True airspeed versus frequency response for Sensor 6 with swirlers having three flutes and various exit angles.

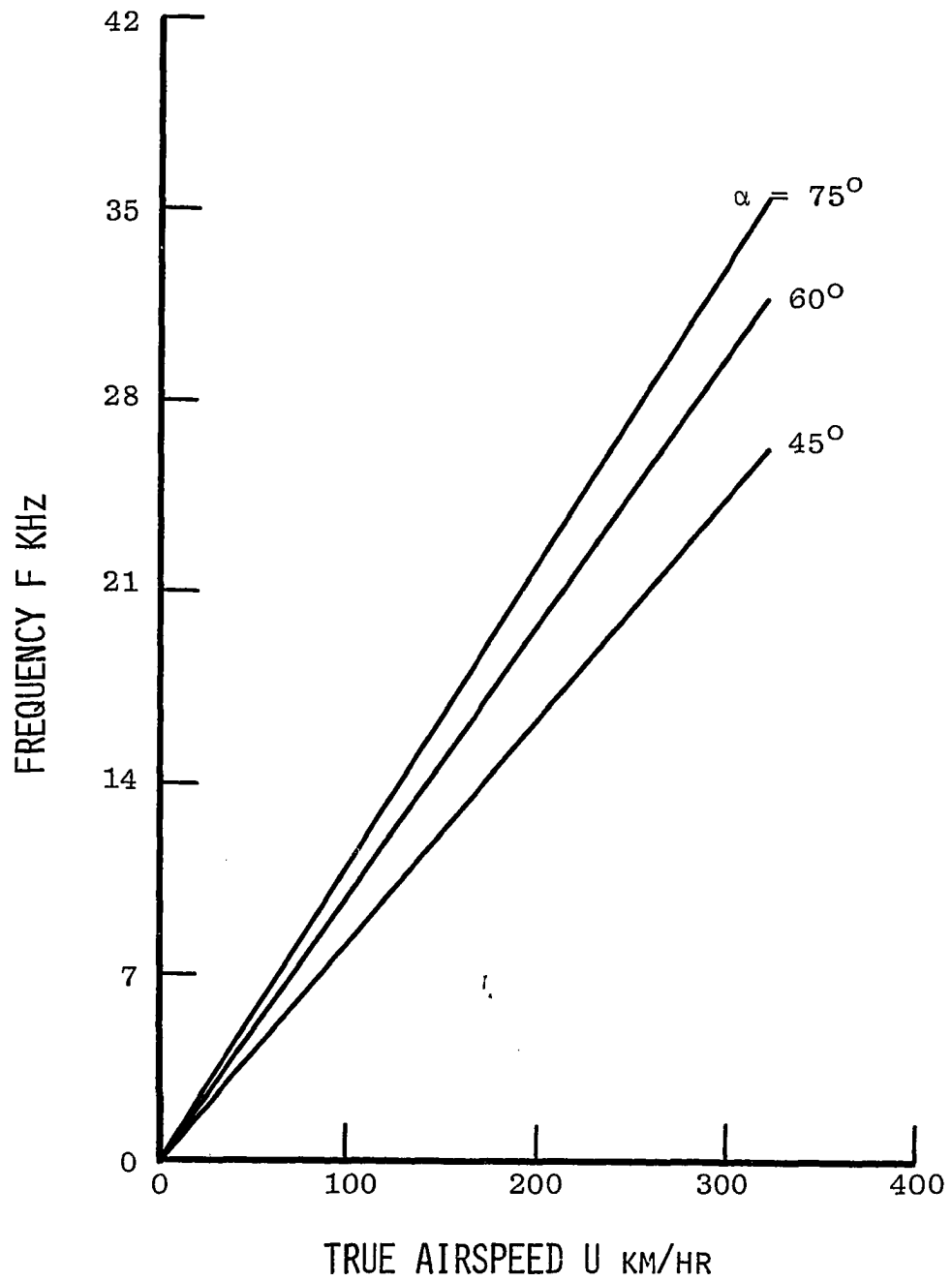


Fig. 30 True airspeed versus frequency response for Sensor 6 with swirlers having four flutes and various exit angles.

assumption of one for the wavenumber in the computing results is justified.

3.4 Effect of Flutes on Swirler

The effect of flutes imposed on the swirler is shown in the Figs. 31-36. As the number of flutes on the swirler is increased, the intake flow decreases as does the frequency response. For the same frequency, the airspeed sensor designed as a four flute swirler needs approximately 12 per cent more flow or speed than that of a two flute swirler. Although the two flute swirler would be the more economical one, the decision as to how many flutes be in the swirler should be determined from both design and performance qualities.

3.5 Effect of Swirler Core Size D_2

As observed from Figs. 12, 21 and 27 the frequency response is higher in the small core size of swirler. Specifically, the frequency response for the 1.588 and 1.524 cm core size swirlers is much lower than for the 0.953 cm swirler. (See Table 1, page 23, for the dimensions of each configuration.) In the experiments for the 0.953 cm core size diameter swirler with three flutes whose exit angles are each 45 degrees, a whistle was generated. As mentioned in [39], some swirlers would not generate a distinct whistle as expected. The idea range for the swirler core size D_2 when expressed in terms of

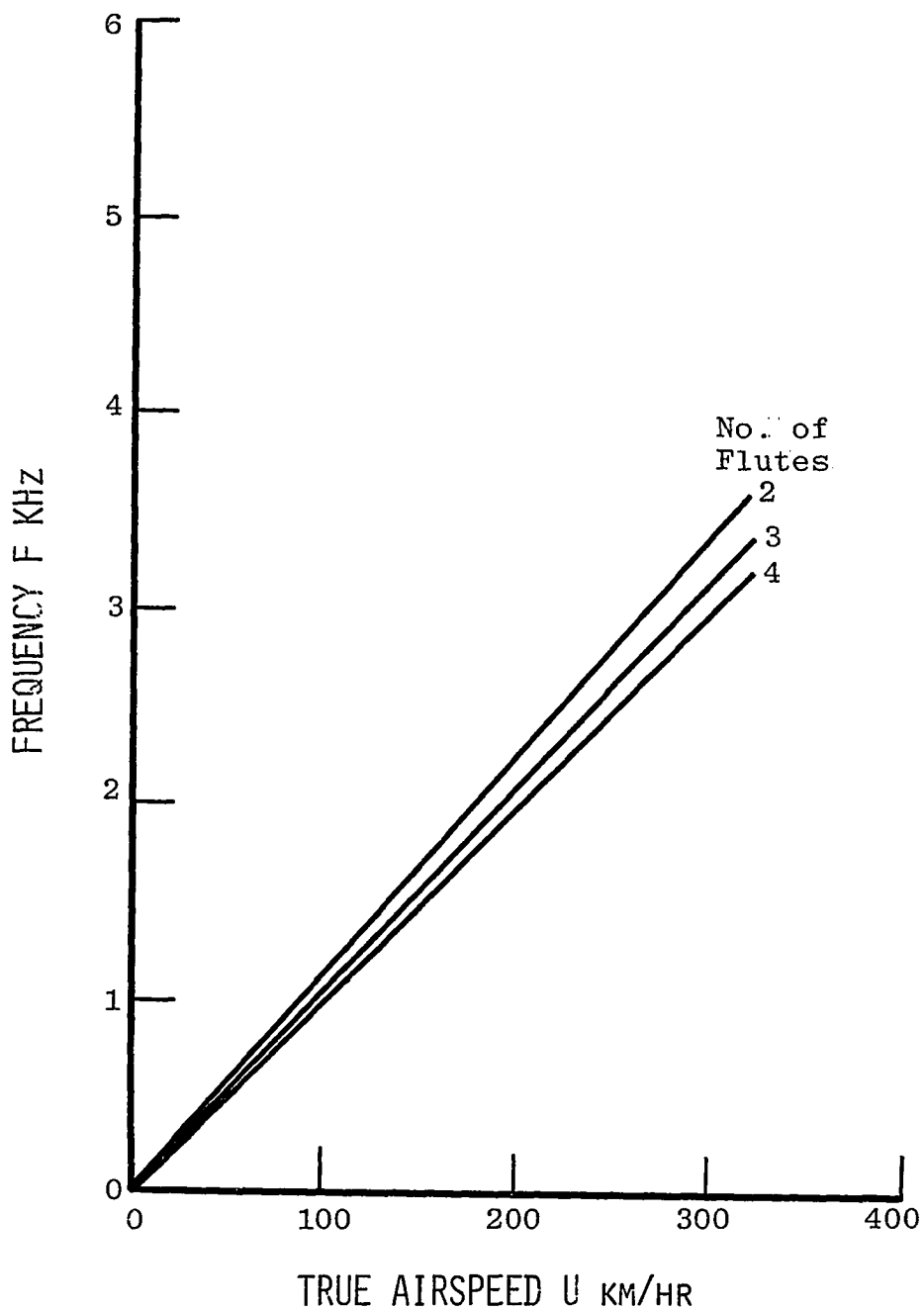


Fig. 31 True airspeed versus frequency response for Sensor 1 with swirlers having 45° exit angle and various flutes.

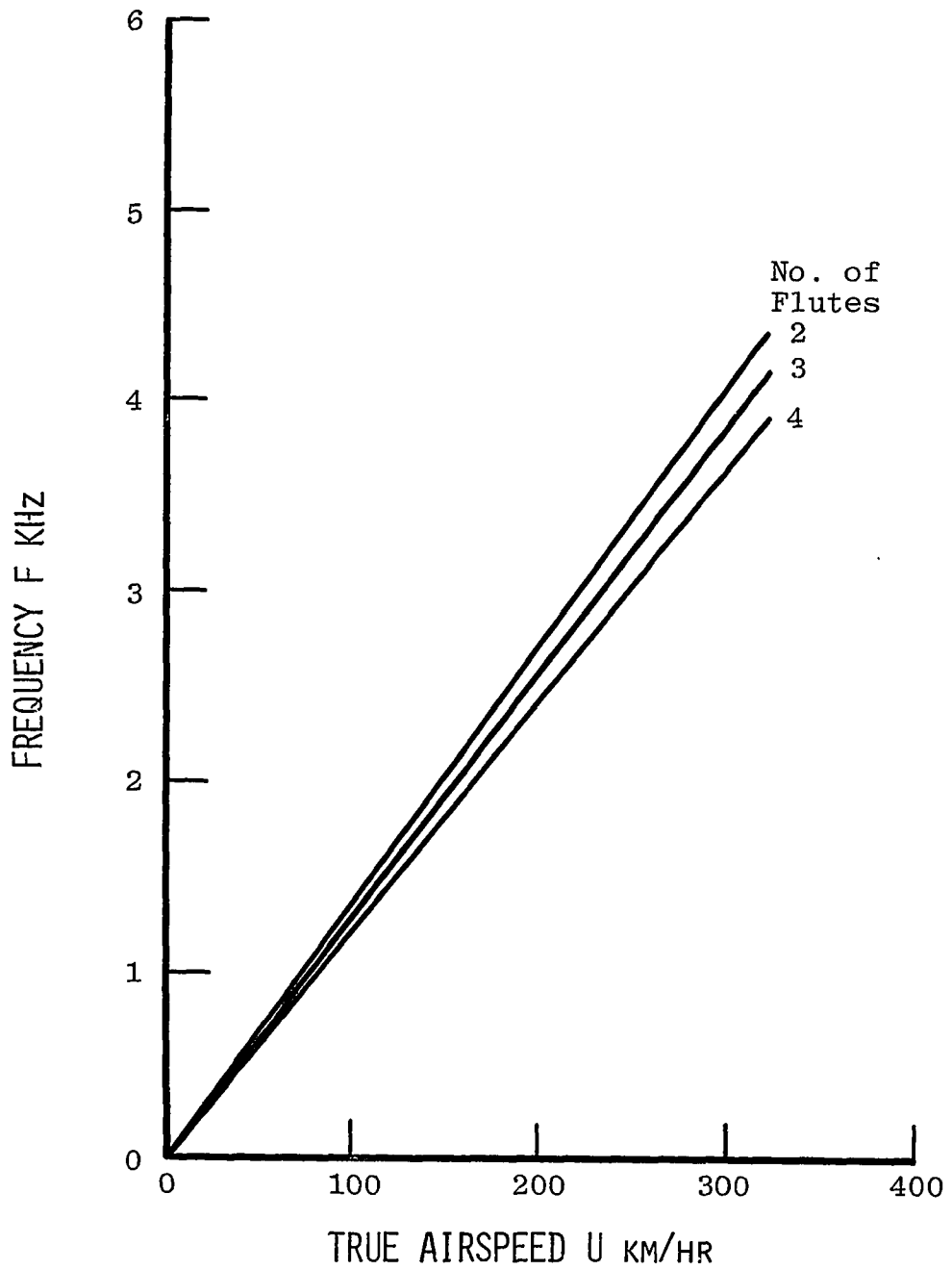


Fig. 32 True airspeed versus frequency response for Sensor 1 with swirlers having 60° exit angle and various flutes.

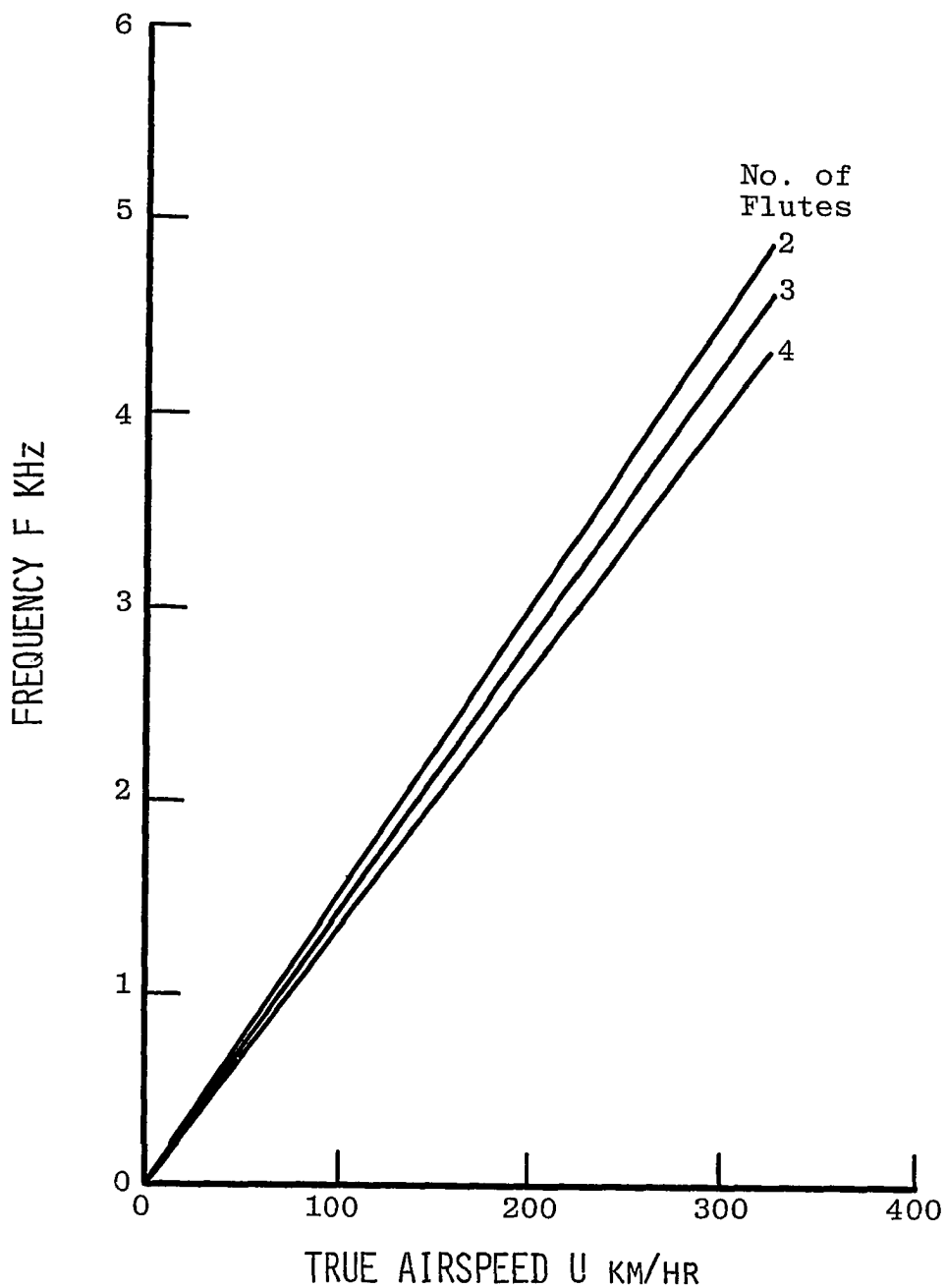


Fig. 33 True airspeed versus frequency response for Sensor 1 with swirlers having 75° exit angle and various flutes.

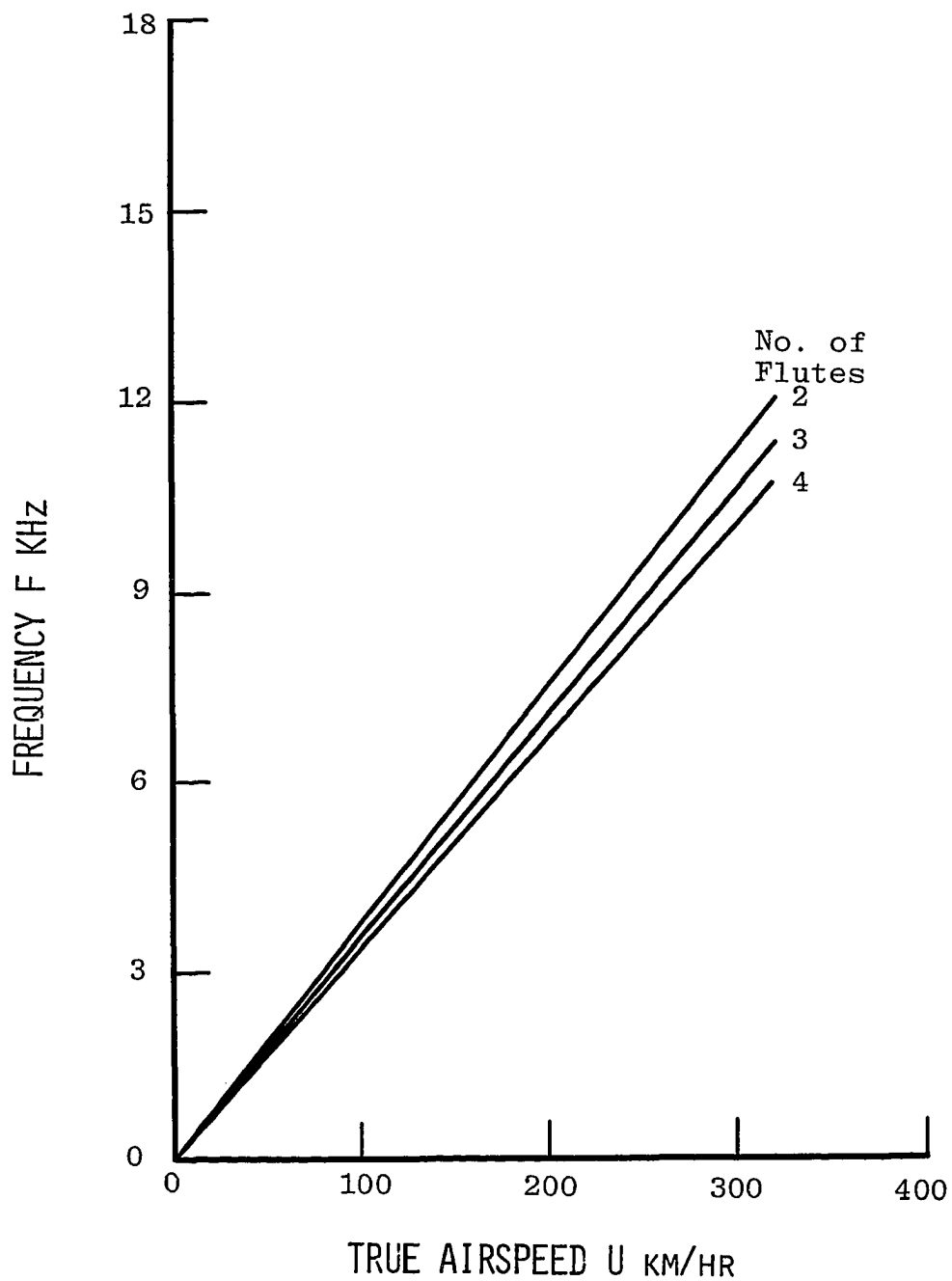


Fig. 34 True airspeed versus frequency response for Sensor 2 with swirlers having 45° exit angle and various flutes.

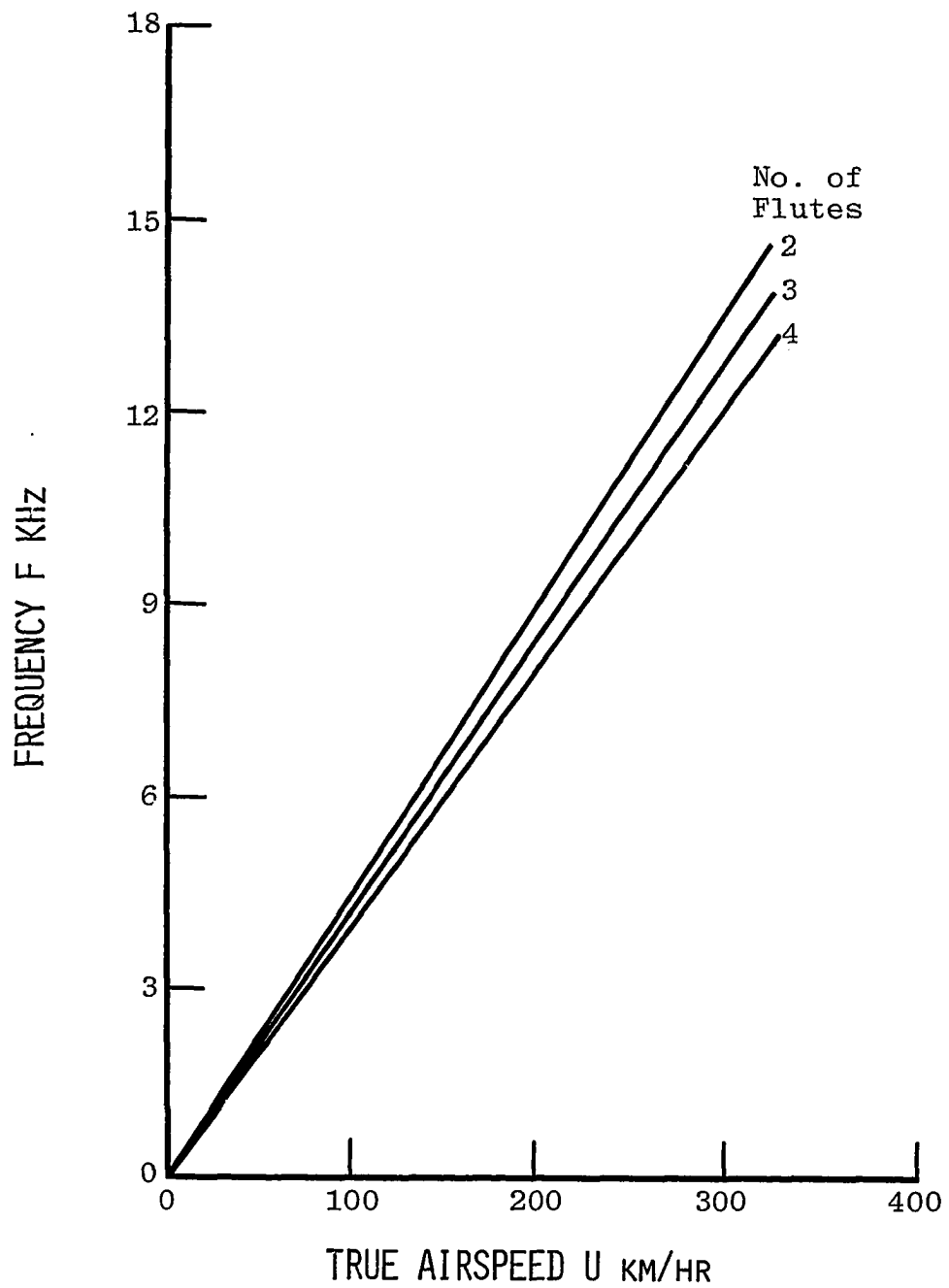


Fig. 35 True airspeed versus frequency response for Sensor 2 with swirlers having 60° exit angle and various flutes.

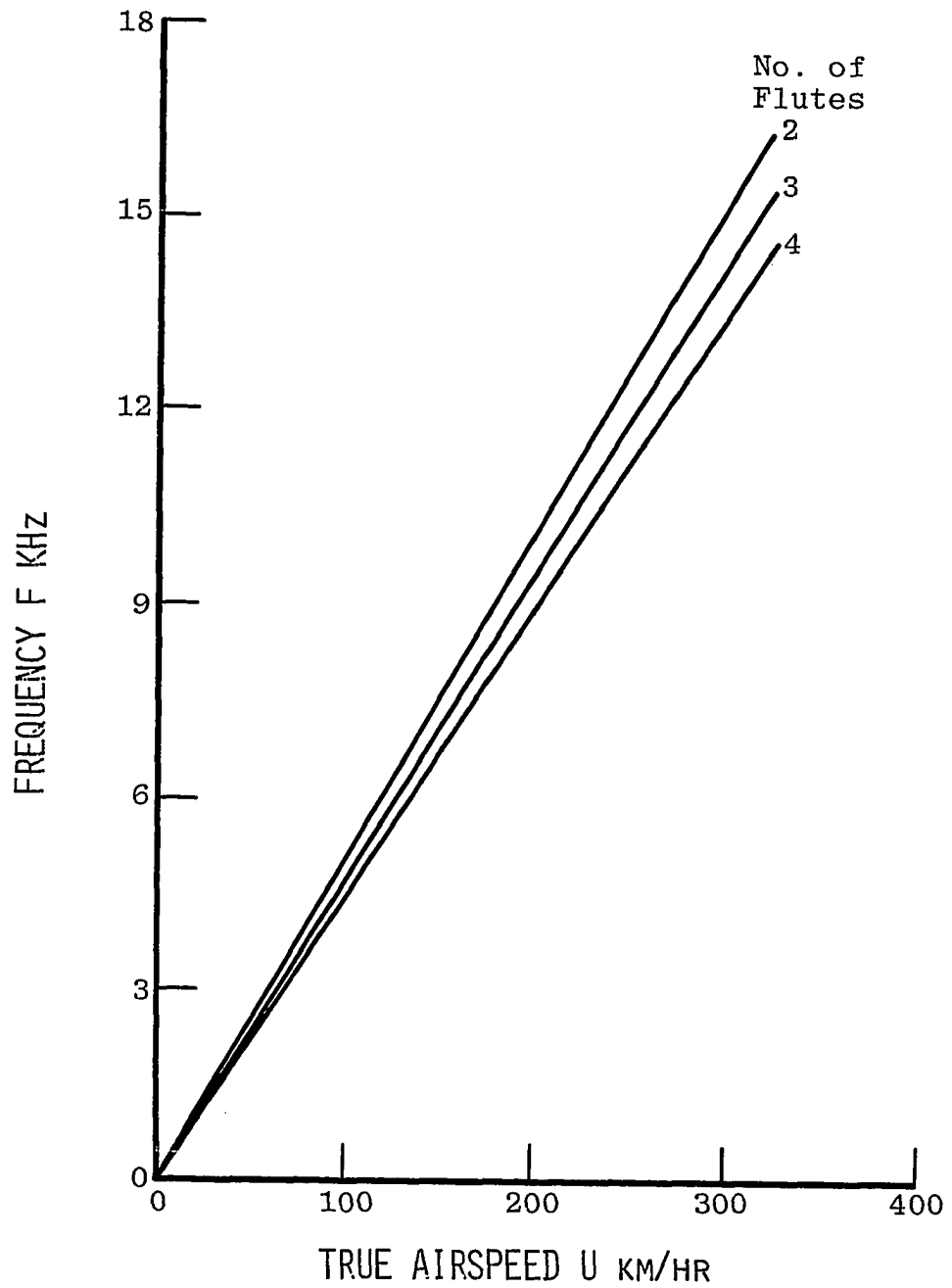


Fig. 36 True airspeed versus frequency response for Sensor 2 with swirlers having 75° exit angle and various flutes.

the ratio of D_2/D_1 is between 0.81 and 0.67.

3.6 Effect of the Cross-sectional size of the Precessional Flow Region

The cross-sectional size of the precessional flow region proved to be a significant parameter in the design of the vortex tube. The frequency responses were much higher for the smaller diameter precessional flow regions. Figures 37-39 clearly show that much higher frequency responses occurred in Sensors 2, 4 and 6 than was experienced respectively in Sensors 1, 3 and 5. Again, refer to Table 1, page 23, and Fig. 1, page 11, for dimensions of Sensors 1 through 6. The 0.635 cm diameter precessional flow region produced a frequency response approximately three times that of the 0.953 cm one. It should be noted that the diameter size of the precessional flow region can be adjusted to obtain a desired frequency response range.

3.7 Relation between the Mean Axial Velocity W_c and Airspeed

From equation (B10) as in Appendix B, it is concluded that the mean axial velocity W_c is linearly related to the airspeed. Theoretical data for different indicators are plotted in Figs. 40-45. The theoretical results show the mean axial velocity for the higher exit angle swirlers. Figure 46 reveals the frequency response to be linearly proportional to the mean axial velocity.

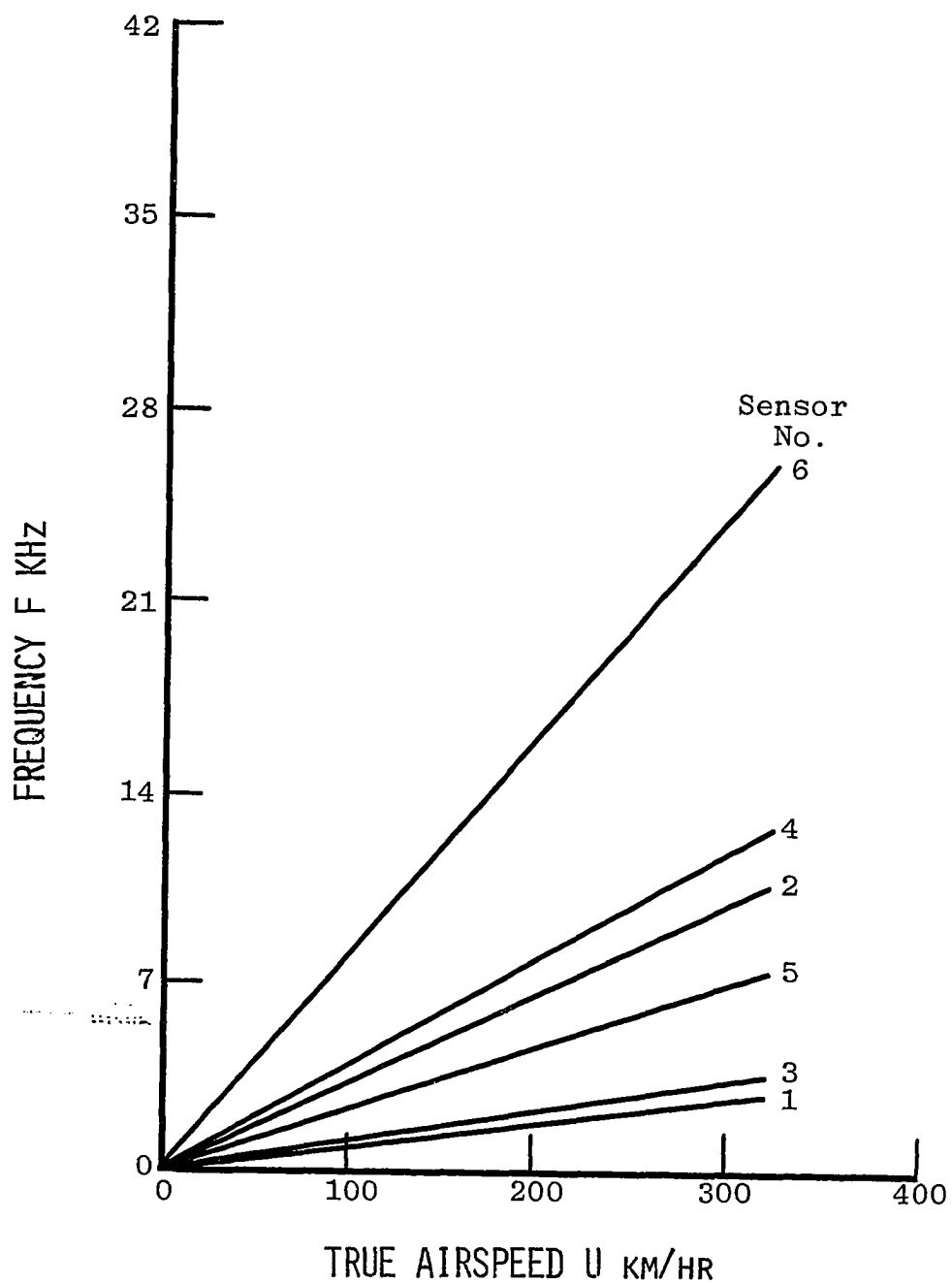


Fig. 37 Comparison of the variation of the size of the precessional flow region, D_3 , with four flutes and exit angle 45° swirler.

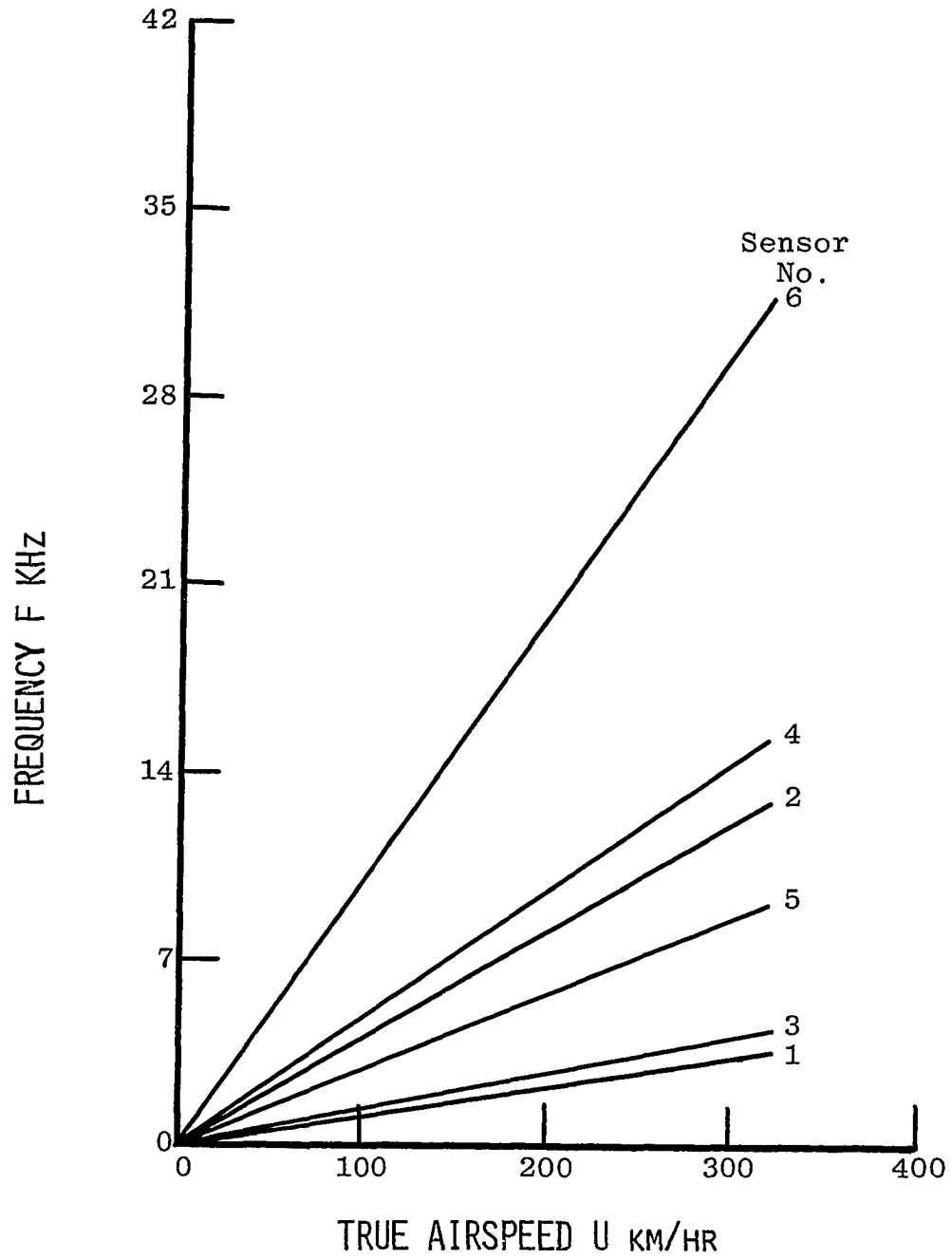


Fig. 38 Comparison of the variation of the size of the precessional flow region, D_3 , with four flutes and exit angle 60° swirler.

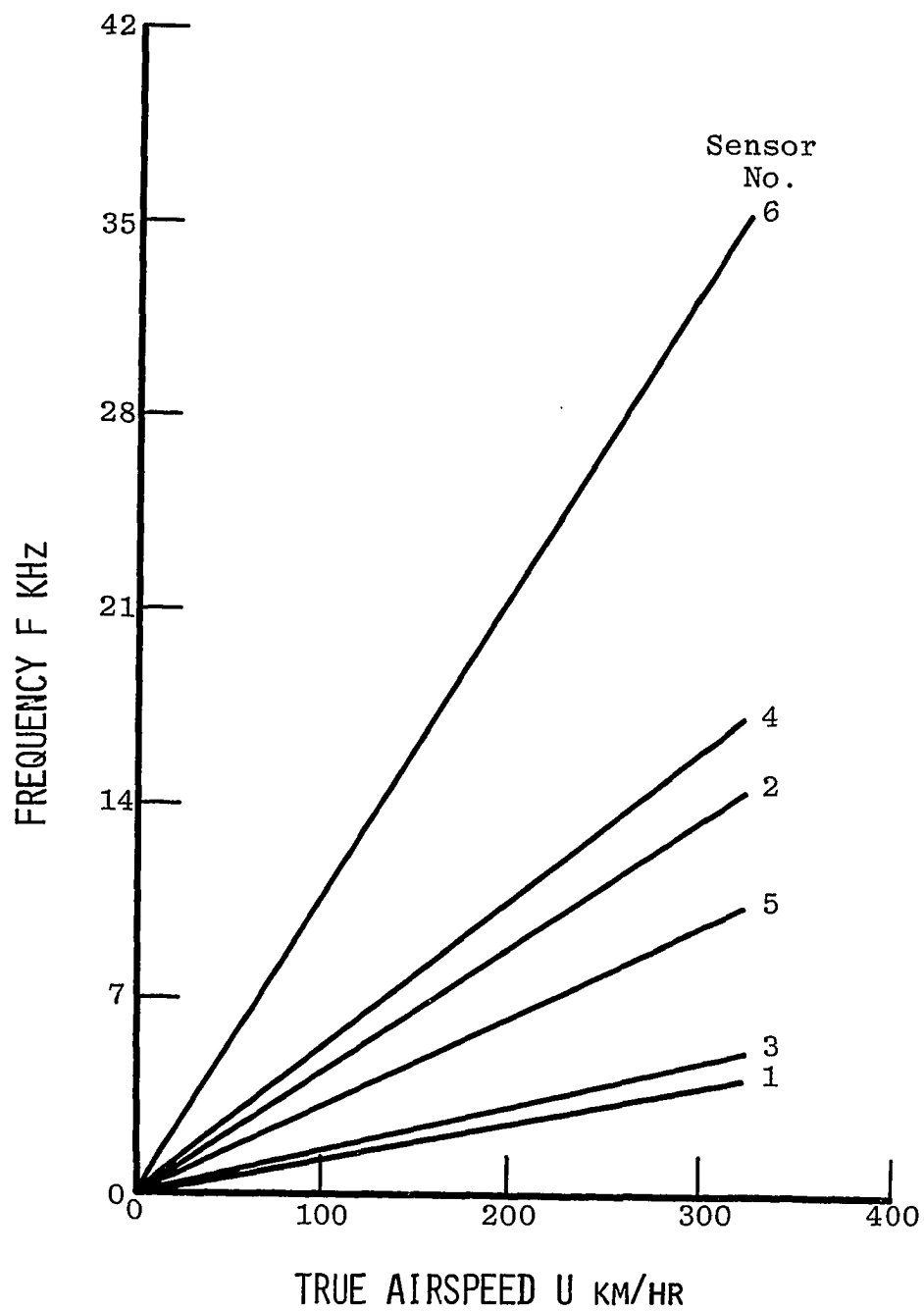


Fig. 39 Comparison of the variation of the size of the precessional flow region, D_3 , with four flutes and exit angle 75° swirler.

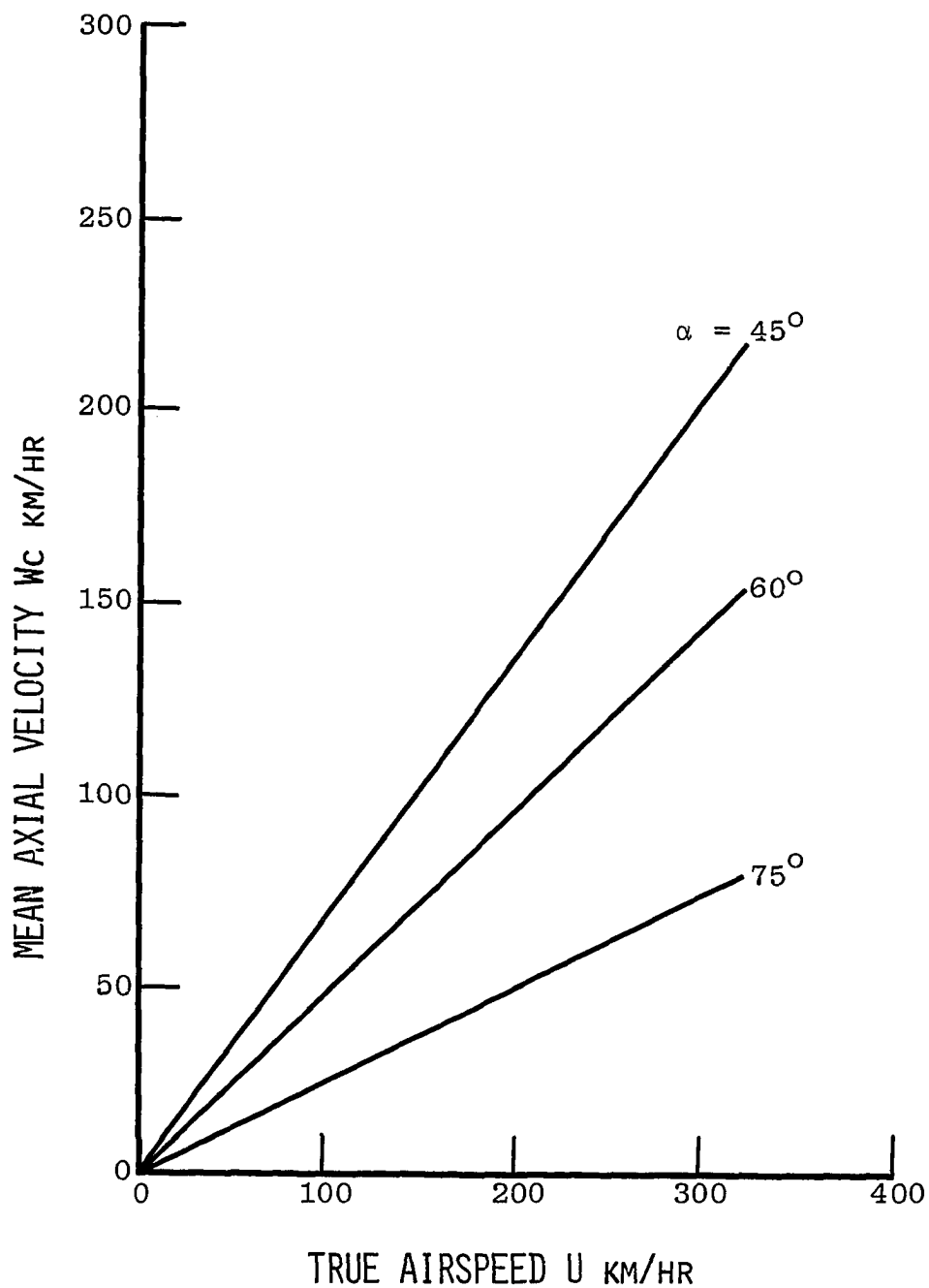


Fig. 40 True airspeed versus mean axial velocity for Sensor 1 with swirlers having four flutes and various exit angles.

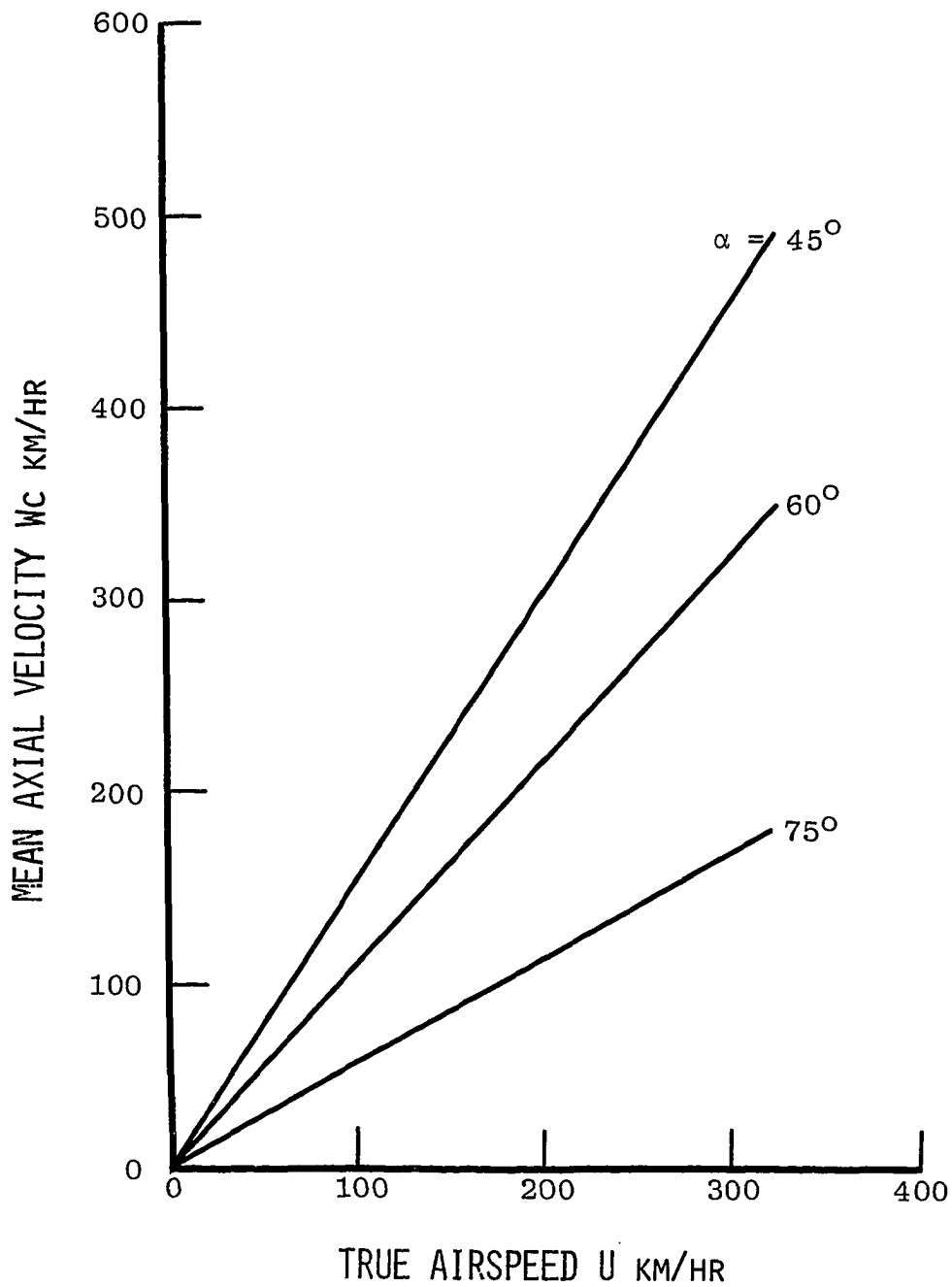


Fig. 41 True airspeed versus mean axial velocity for Sensor 2 with swirlers having four flutes and various exit angles.

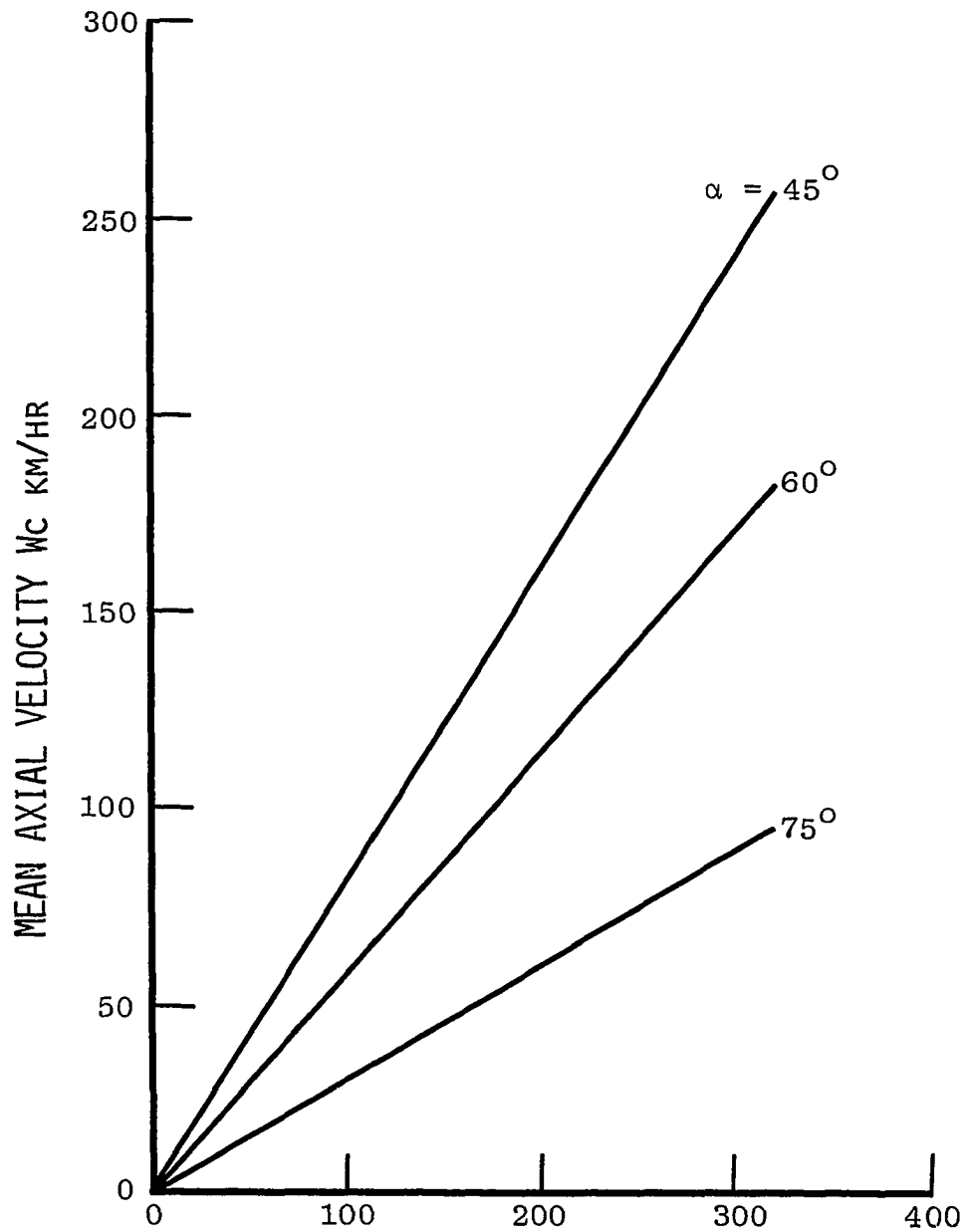


Fig. 42 True airspeed versus mean axial velocity for Sensor 3 with swirlers having four flutes and various exit angles.

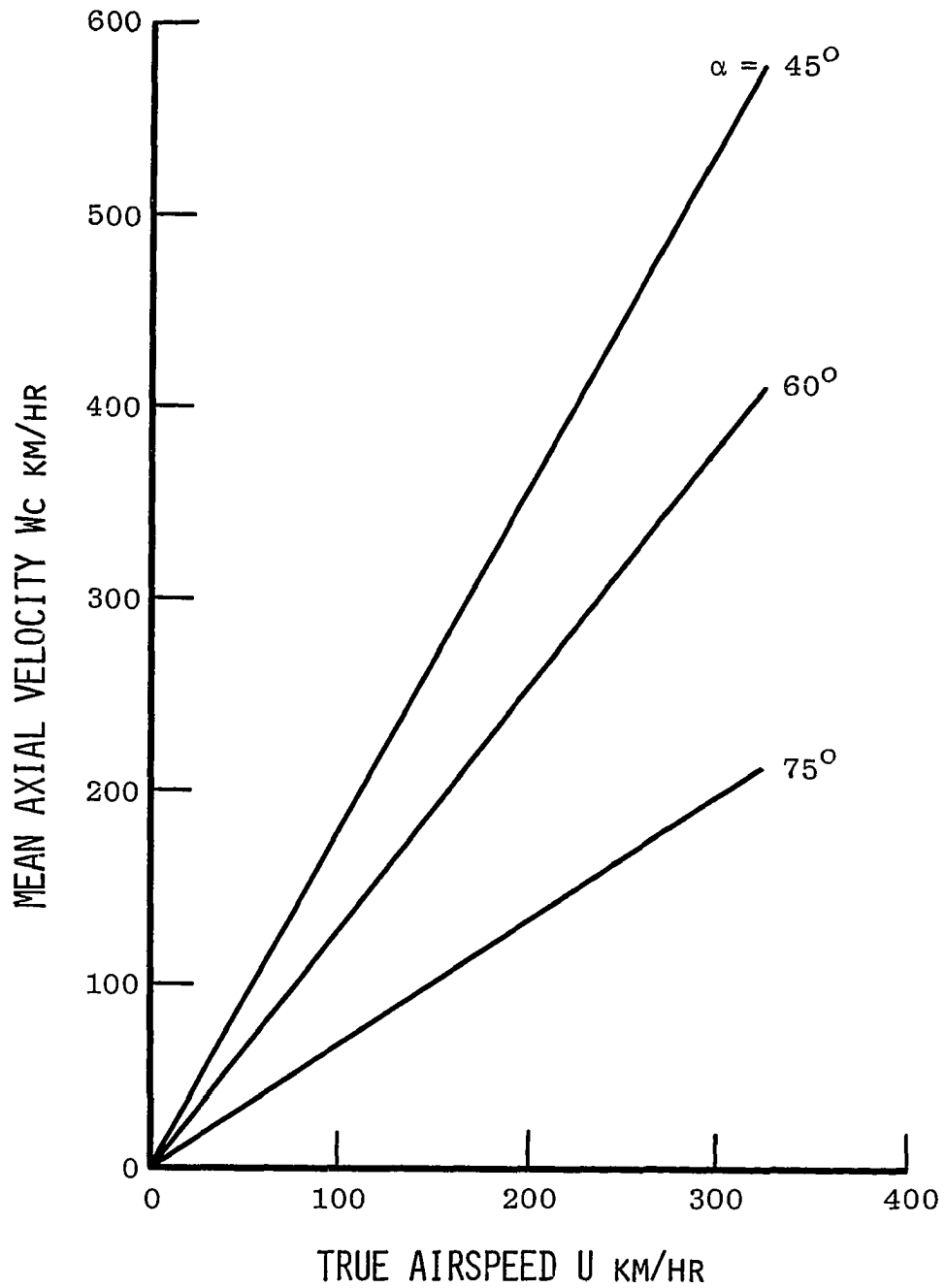


Fig. 43 True airspeed versus mean axial velocity for Sensor 4 with swirlers having four flutes and various exit angles.

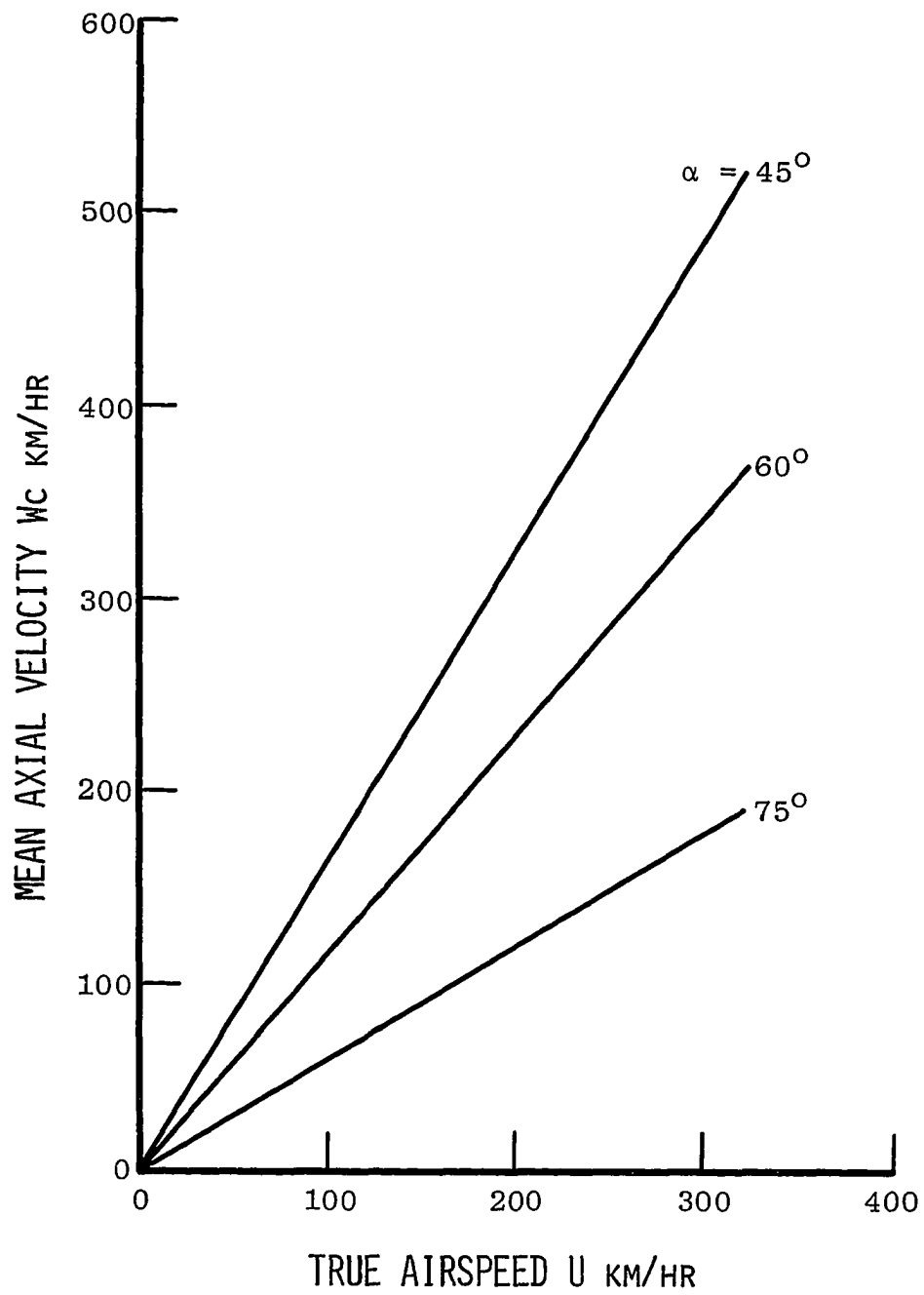


Fig. 44 True airspeed versus mean axial velocity for Sensor 5 with swirlers having four flutes and various exit angles.

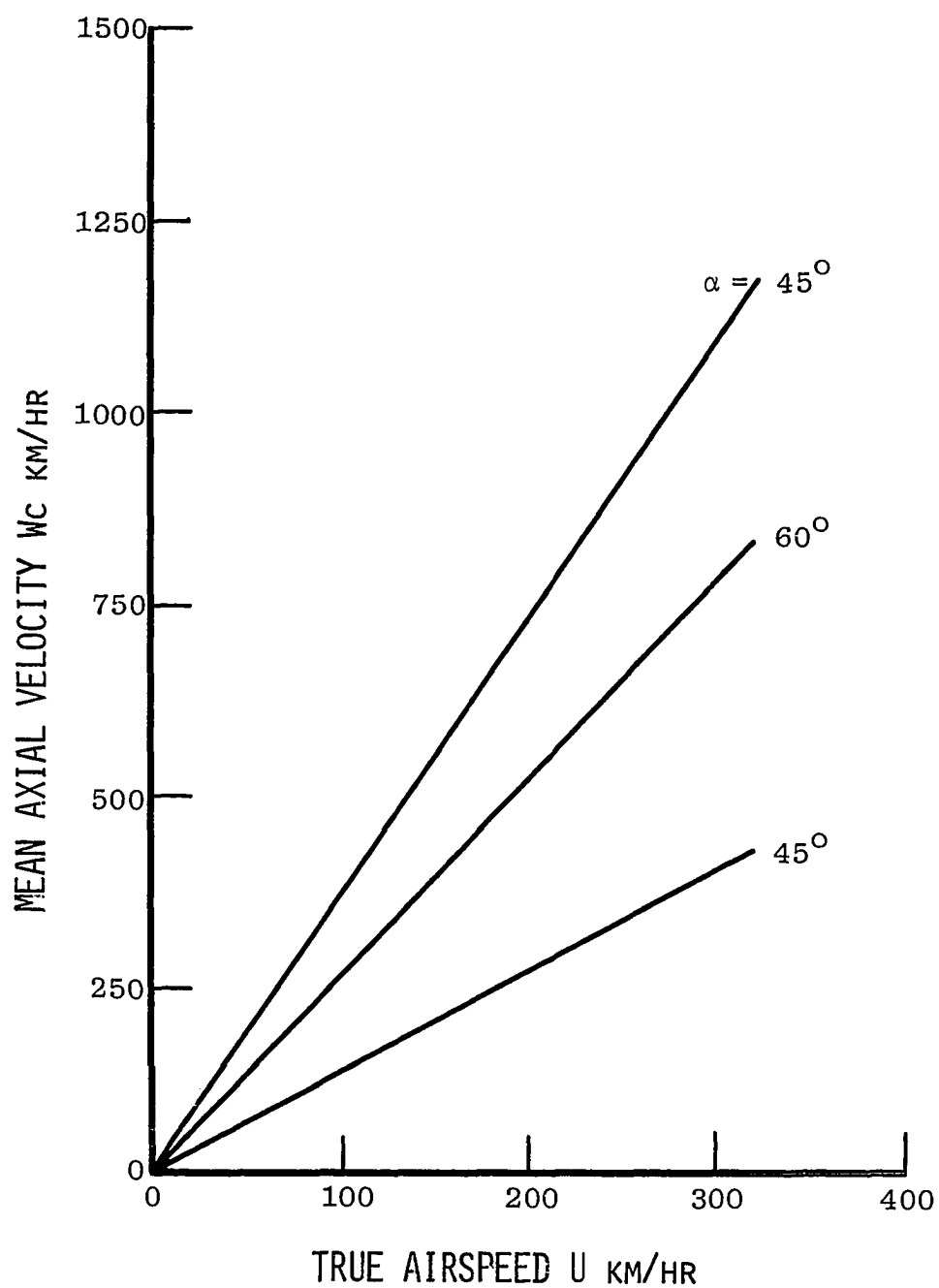


Fig. 45 True airspeed versus mean axial velocity for Sensor 6 with swirlers having four flutes and various exit angles.

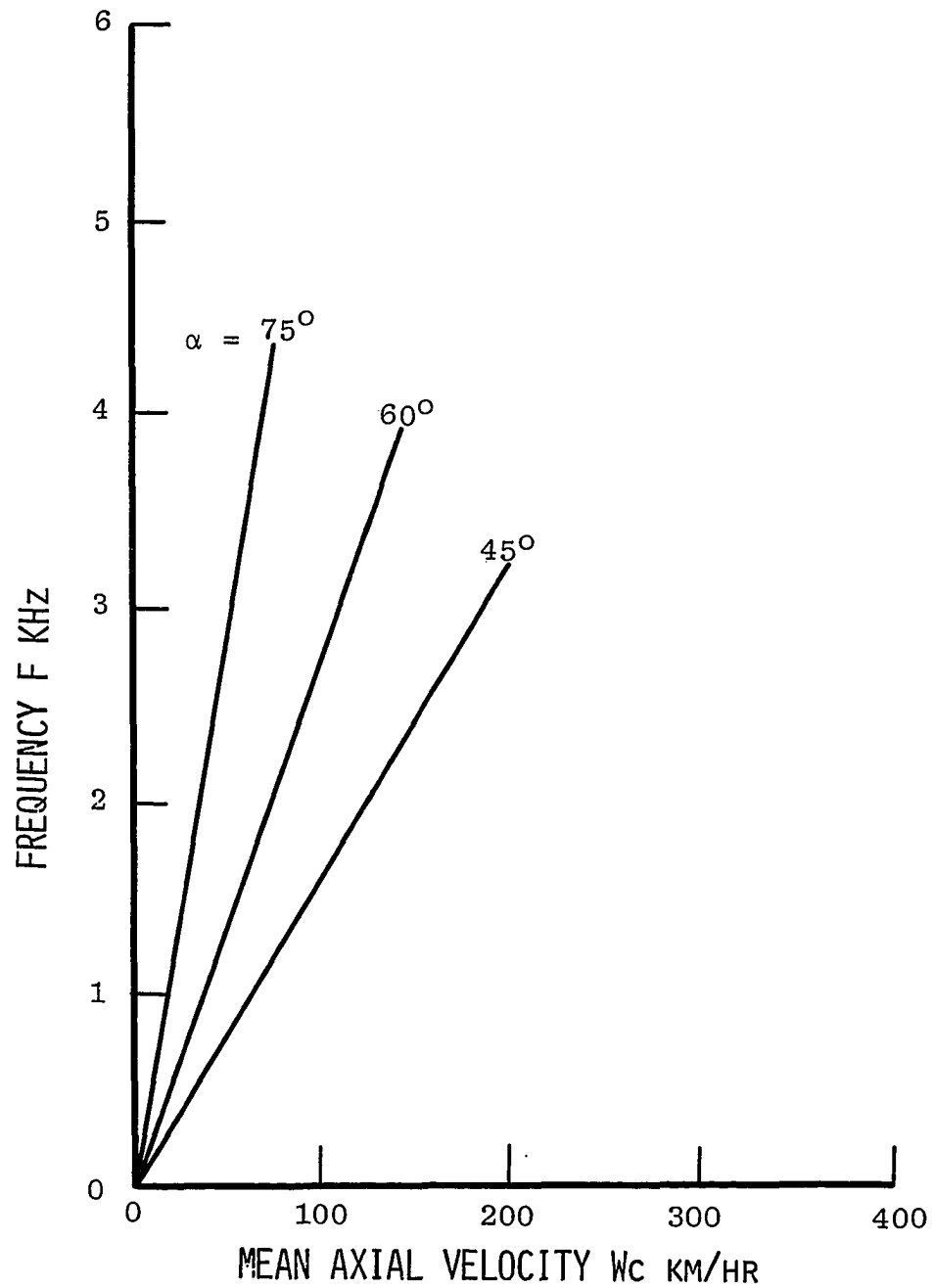


Fig. 46 Relationship between mean axial velocity and frequency response for Sensor 1 with swirlers having four flutes and various exit angles.

3.8 Relationship between Reynolds Number and Strouhal Number

Both Reynolds number, Re , and Strouhal number, St , are defined in terms of the axial velocity W_c and diameter of precessional flow region, D_3 . Except for the singular point at zero airspeed, the predicted Strouhal numbers remained constant as the airspeed was increased. It should be noted that for a given exit angle the Strouhal number is a constant regardless of the number of flutes in the swirler. The data for six different indicators are plotted in Figs. 47-52. When the sensors with the same swirler exit angles are compared one finds the Strouhal numbers are the same. Therefore it is reasonable to conclude that the Strouhal number is dependent only on α , the swirler exit angle. The approximate values of Strouhal number for 45° , 60° and 75° swirlers are respectively 0.51, 0.88 and 1.88.

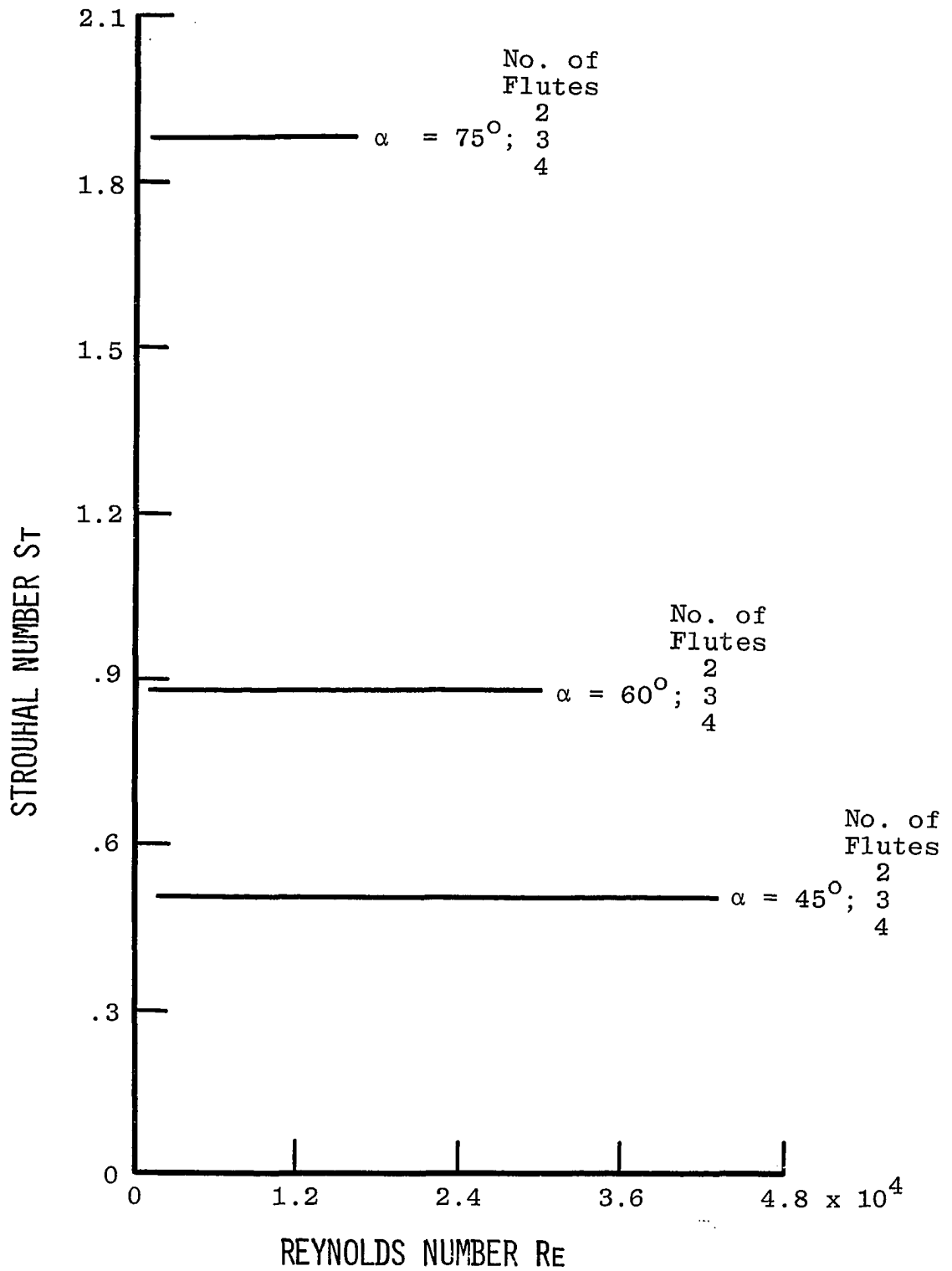


Fig. 47 Reynolds number versus Strouhal number for Sensor 1.

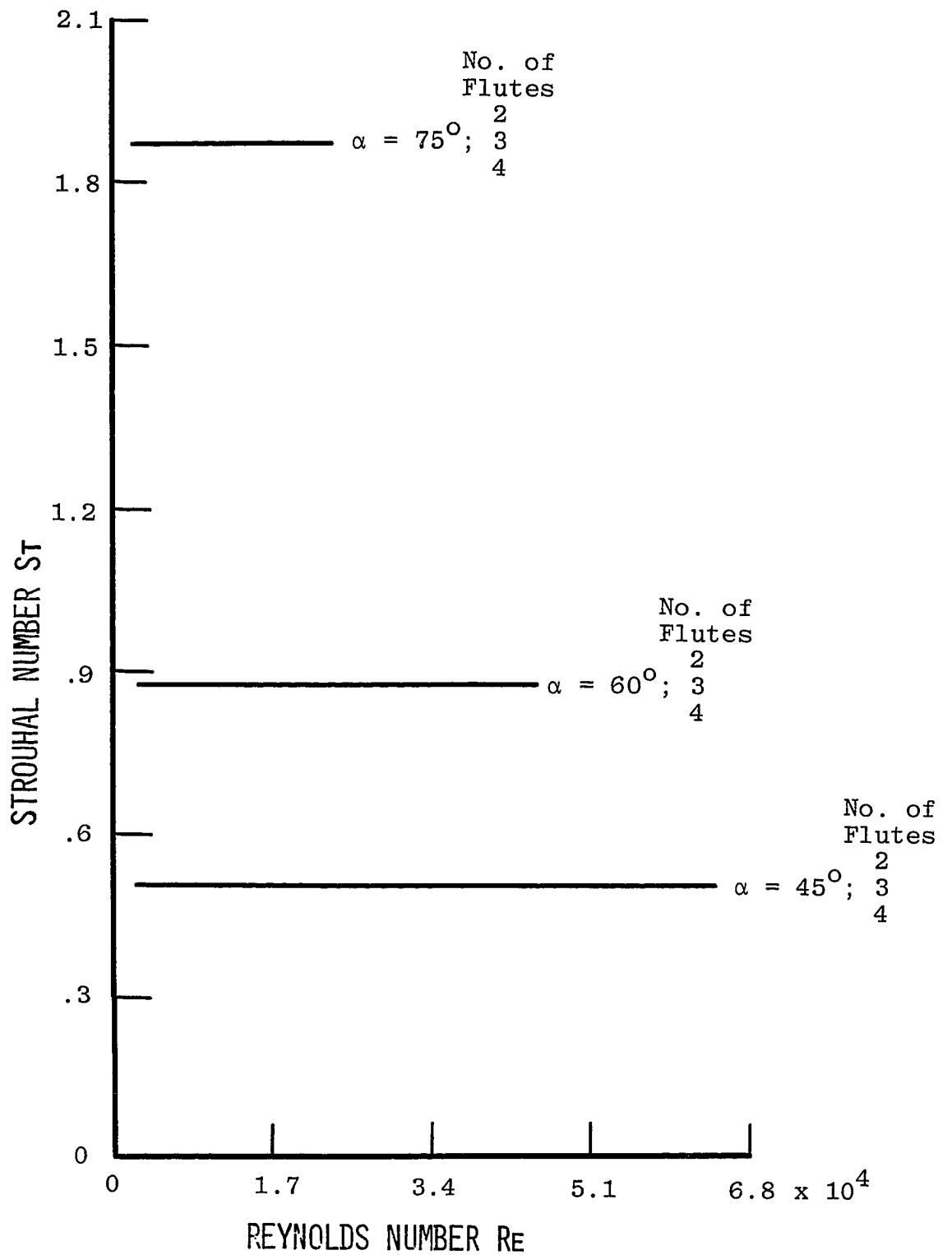


Fig. 48 Reynolds number versus Strouhal number for Sensor 2.

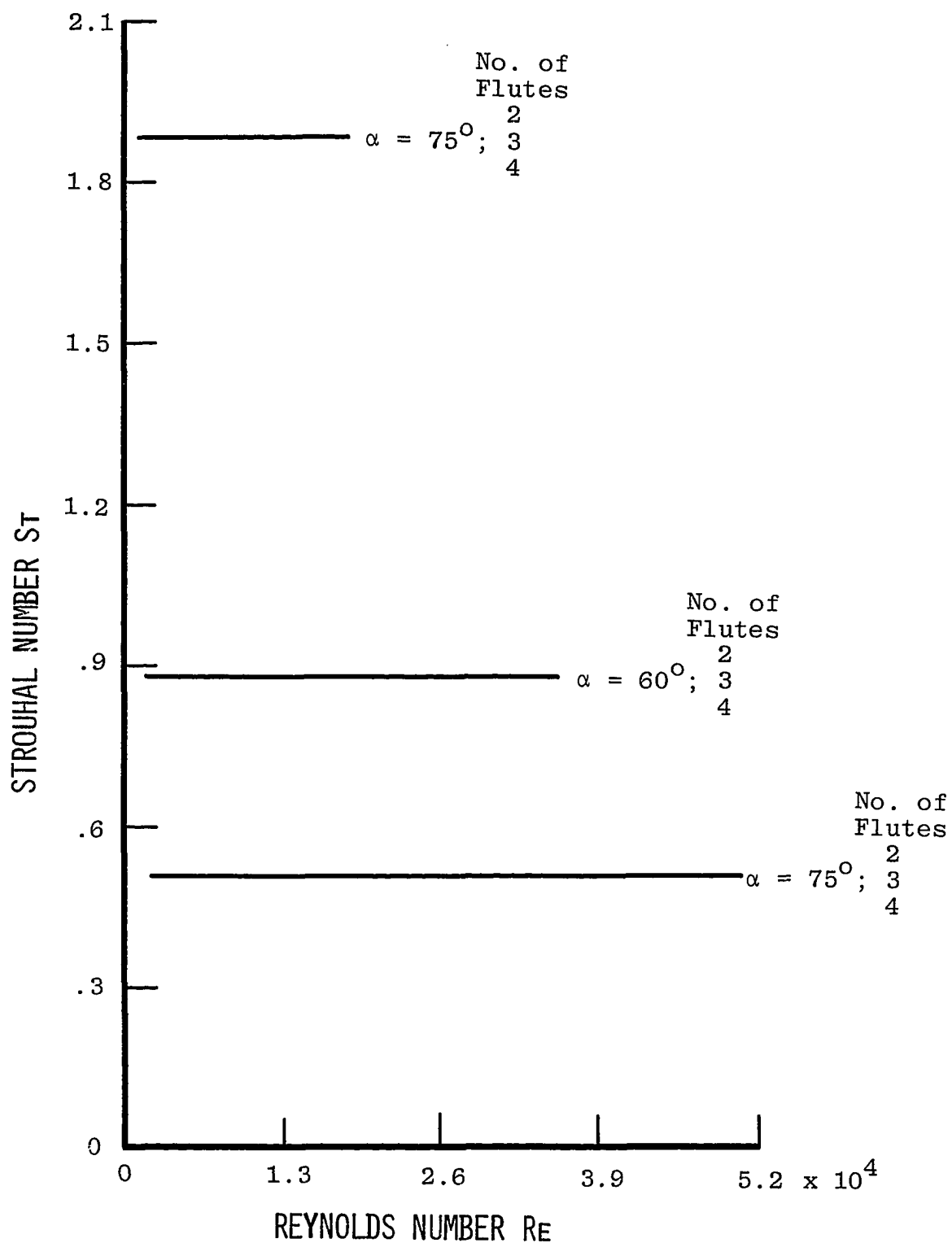


Fig. 49 Reynolds number versus Strouhal number for Sensor 3.

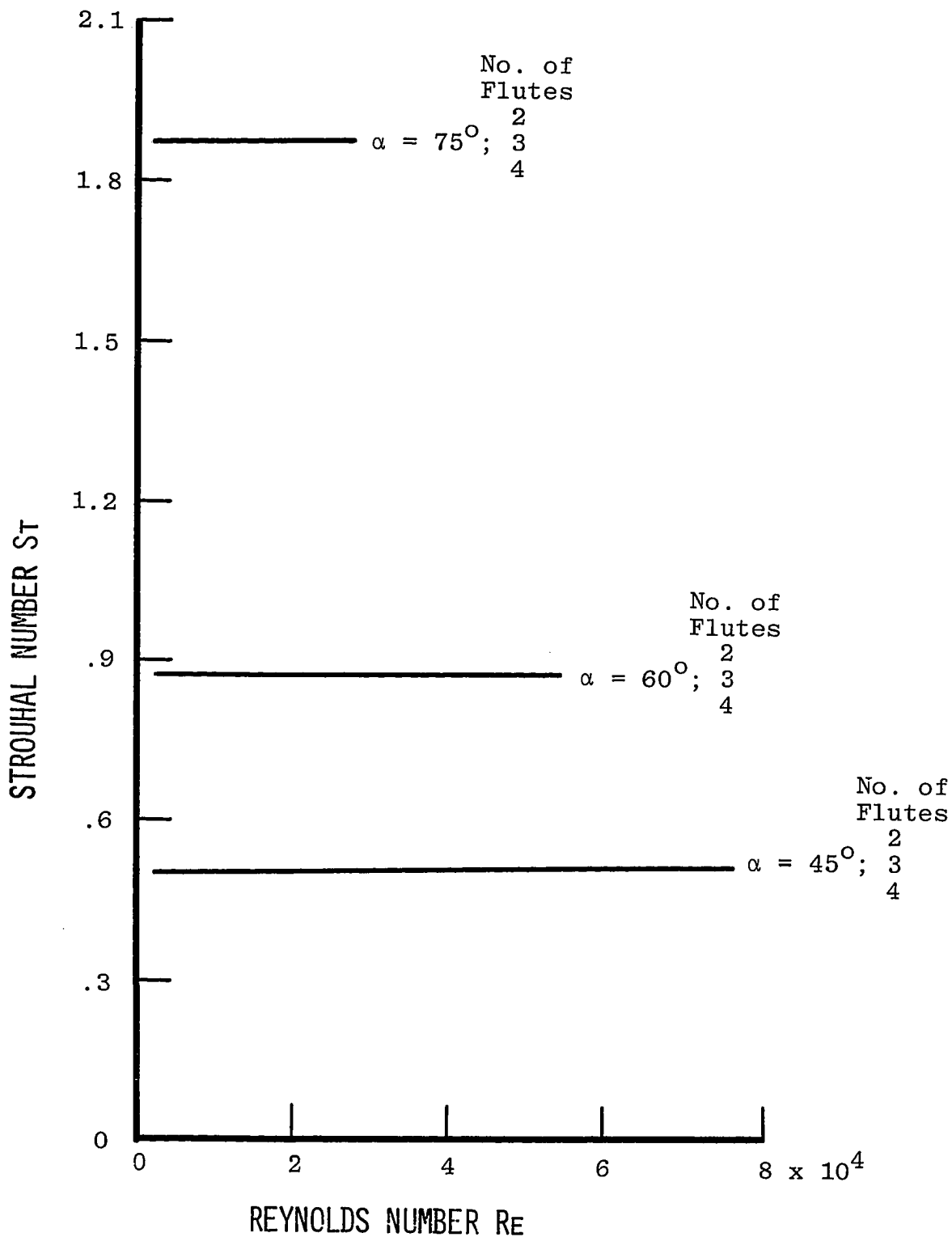


Fig. 50 Reynolds number versus Strouhal number for Sensor 4.

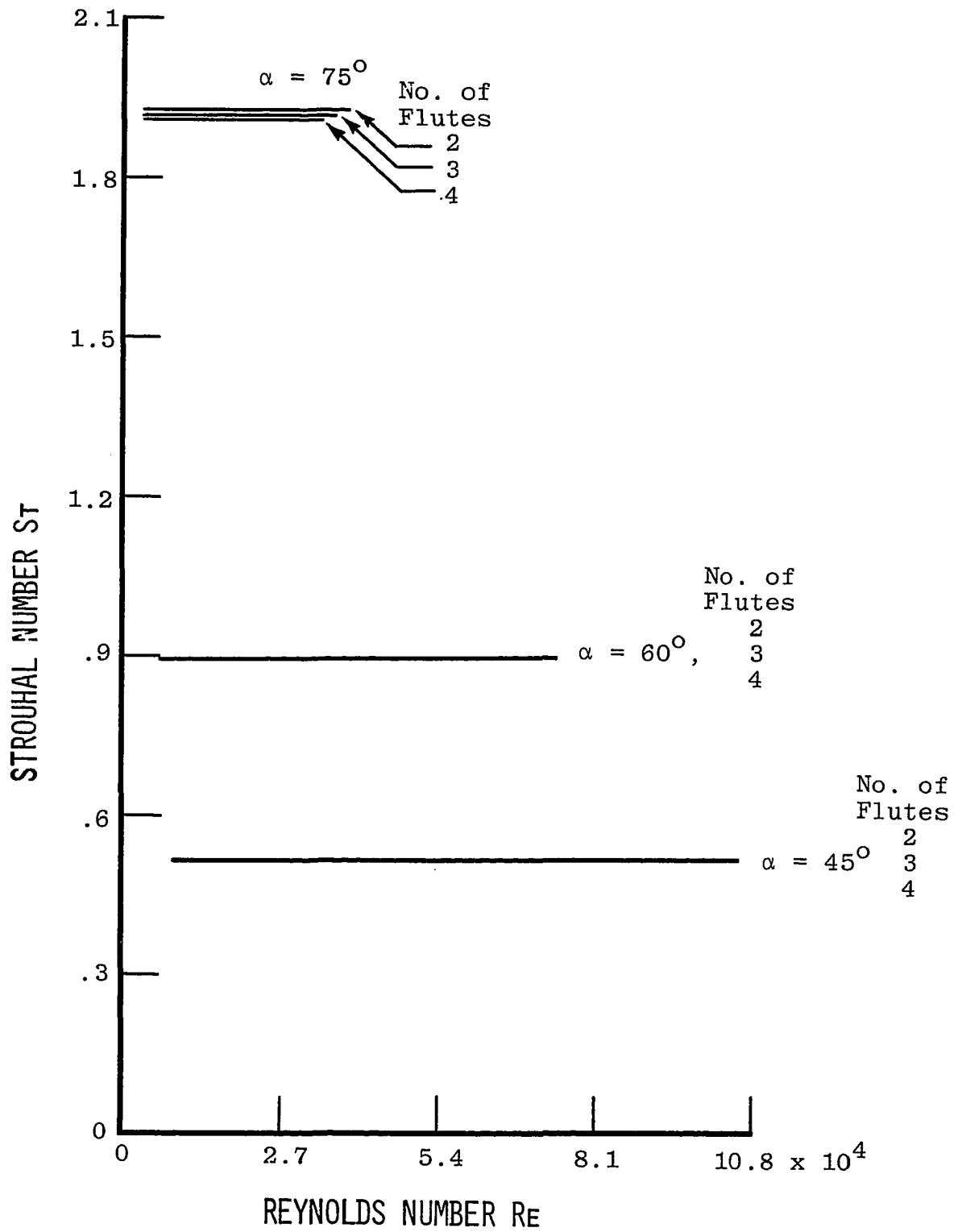


Fig. 51 Reynolds number versus Strouhal number for Sensor 5.

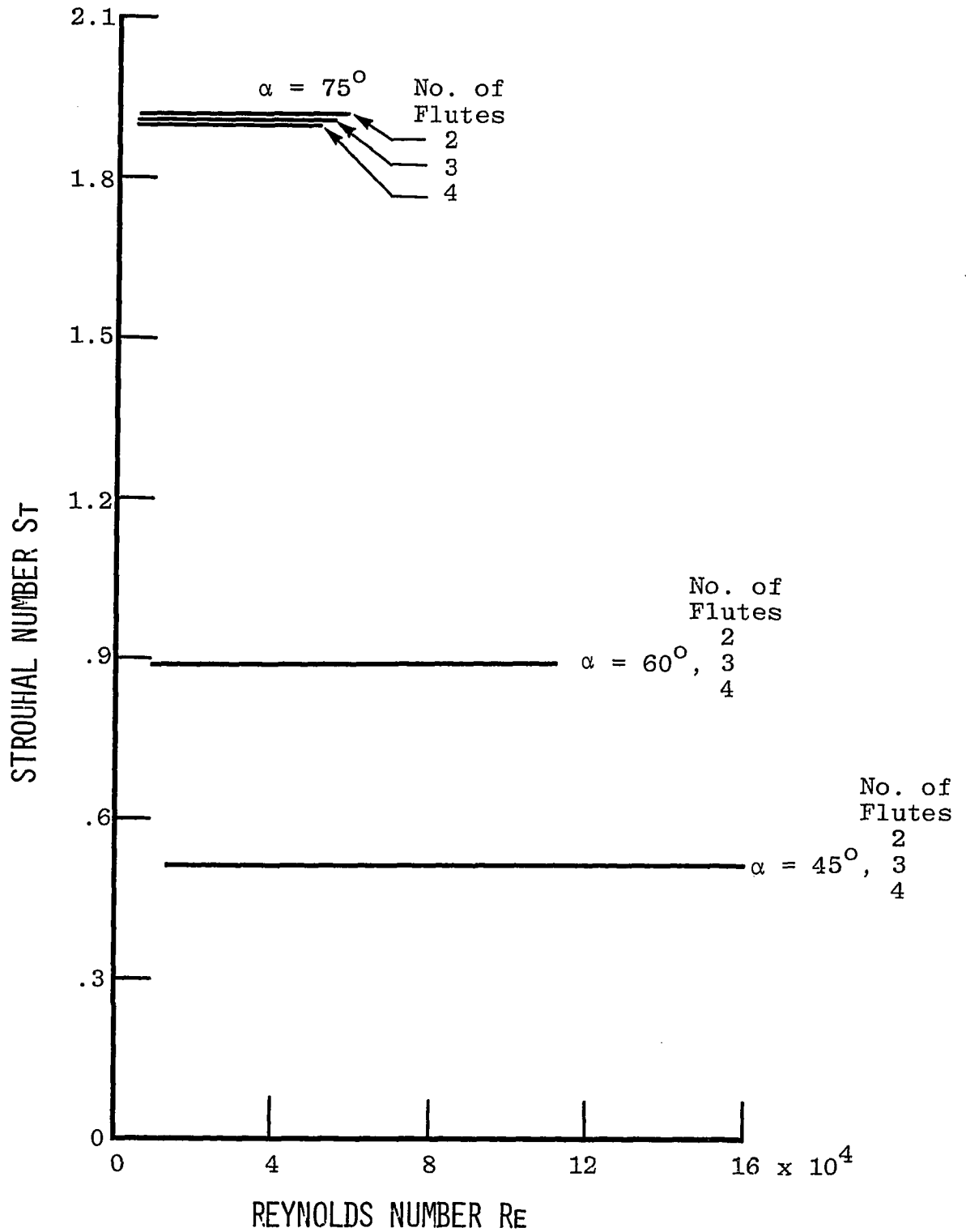


Fig. 52 Reynolds number versus Strouhal number for Sensor 6.

4. APPARATUS AND TESTS

4.1 General Description

In order to understand the operation and performance of the true airspeed sensor, visualization, closed conduit and wind tunnel tests were undertaken. The purpose of the visualization test was to carefully examine the fluid flow phenomenon-precession, and observe how the flow velocity affects the precessional motion. Another objective was to observe and locate a suitable position for picking up the signal. The closed conduit test (flow rate versus frequency response) provided information as to how the flow rate could be related to the frequency response. These sensors can certainly be compared with commercially available flow meters. Finally, the wind tunnel test or actual flight test was conducted to supply the actual data for the relationship between the true airspeed and the frequency response. It is anticipated that additional research will be undertaken to improve the design of the sensor in the latter two stages. The complete descriptions of the sensor, setup and test procedures follows.

4.2 Visualization

In the earlier stage of investigation, a water model apparatus was set up for observing the fluid flow phenomenon-precession. The descriptions of vortex tube geometry and experimental arrangement were shown in Figs. 53 and 54. In Fig. 53, sections I and II, which were made of brass, were used for generating the swirling flow. Axial flow was injected at section I while eight tangential jet flows were brought into the stream at section II. Both the axial and tangential flows were regulated by separate valves so as to produce the desired swirling flow pattern. To provide the necessary space for the occurrence of precessional flow, section III was made of transparent plexiglass and constructed as a Venturi-like converging-diverging nozzle. Small air bubbles were brought into the main stream from the tangential flow inlet. The air bubbles collected in the lowest pressure region. The movement of the low-pressure air bubbles stream revealed the precessional flow for some definite flow rate. It was clearly shown that the higher the flow rate, the higher the number of revolutions of the air bubble stream about the axis of the tube. For investigation and observation purposes, four rolls of high speed movies and some slides were taken from different angles. Some of the pictures are shown in Figs. 55 and 56. It was clearly shown from the pictures that the precessional flow whirled around as it left the central part or as it

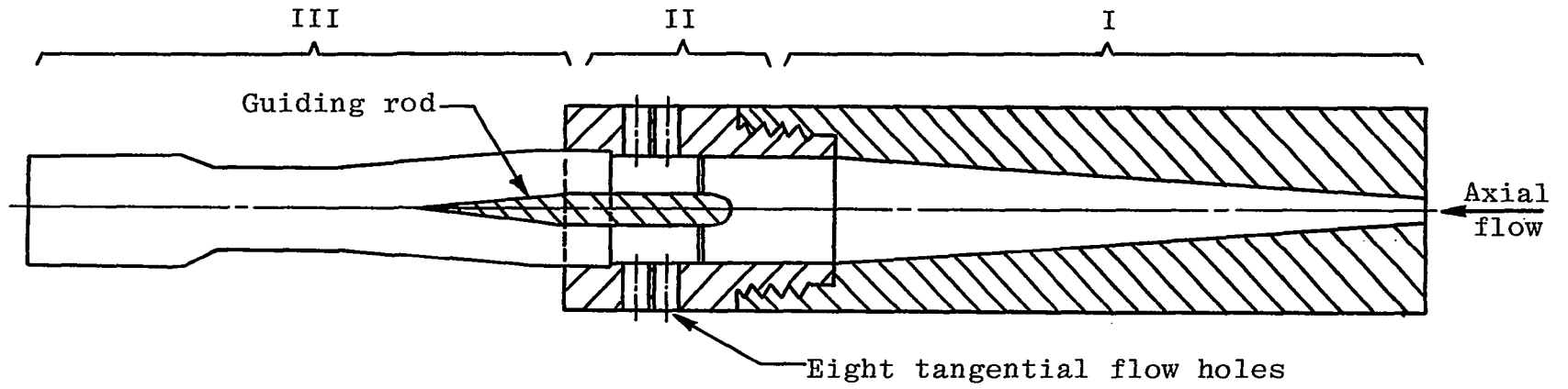


Fig. 53 Vortex tube for flow visualization.

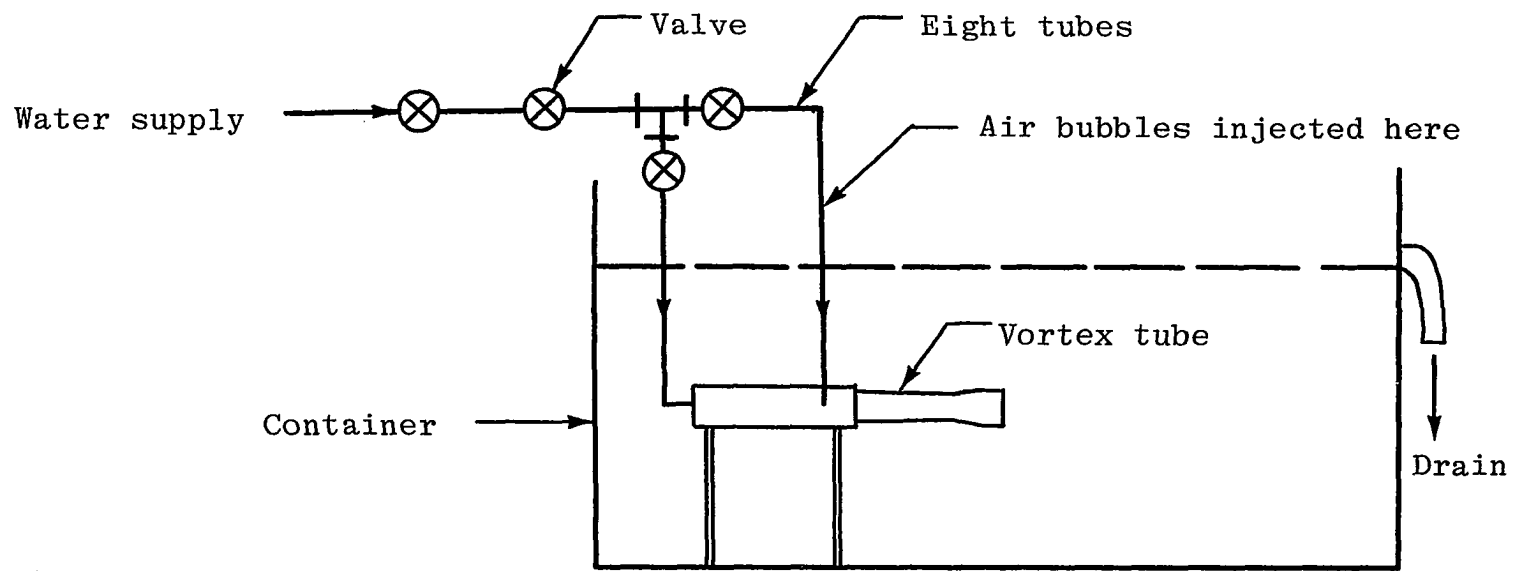


Fig. 54 Setup for water model.



Fig. 55 Fluid flow phenomenonon-precession.



Fig. 56 Fluid flow phenomenon-precession.

entered the enlargement (divergement) section.

4.3 Closed Conduit Test

There are many different types of gas flow meters currently in use. Some of the meters make use of either the vortex shedding principle or the vortex precession principle. Such meters are usually used for low flow rates. The indicator designed during this project could also be considered as a potential flow meter. It was therefore considered desirable to investigate the relationships between the flow rate and the frequency response. It was also anticipated that the results from this test could be compared with data from wind tunnel tests.

The initial designs for the vortex tubes and swirlers are shown in Figs. 57-59. The vortex tube in Fig. 58 was used to investigate the effect of the enlargement exit section wall and to note whether a gradual or abrupt enlargement made any difference. Swirlers with four flutes and with 45° , 60° or 75° exit angles were considered. The vortex tubes were made of plexiglass while the swirlers were made of aluminium. The test apparatus is shown in Fig. 60. The VOL-O-FLO flow meter (product of National Laboratories Instrument Inc. Model 50) with 0.283 m^3 (10 ft^3) per minute capacity was used for the measurement of flow rate. The flow rate could be read and recorded through a voltmeter and converted to the equivalent flow rate unit, cubic meter per minute. The sound or whistle signals were

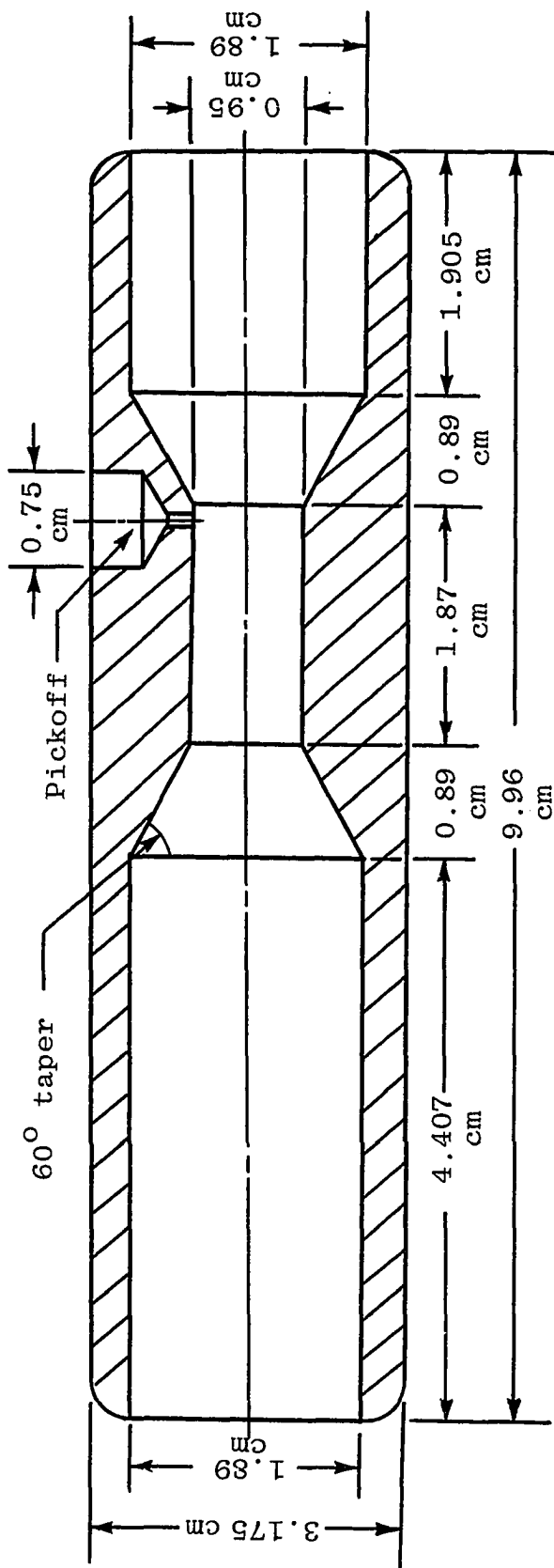


Fig. 57 The dimensions of the vortex tube.

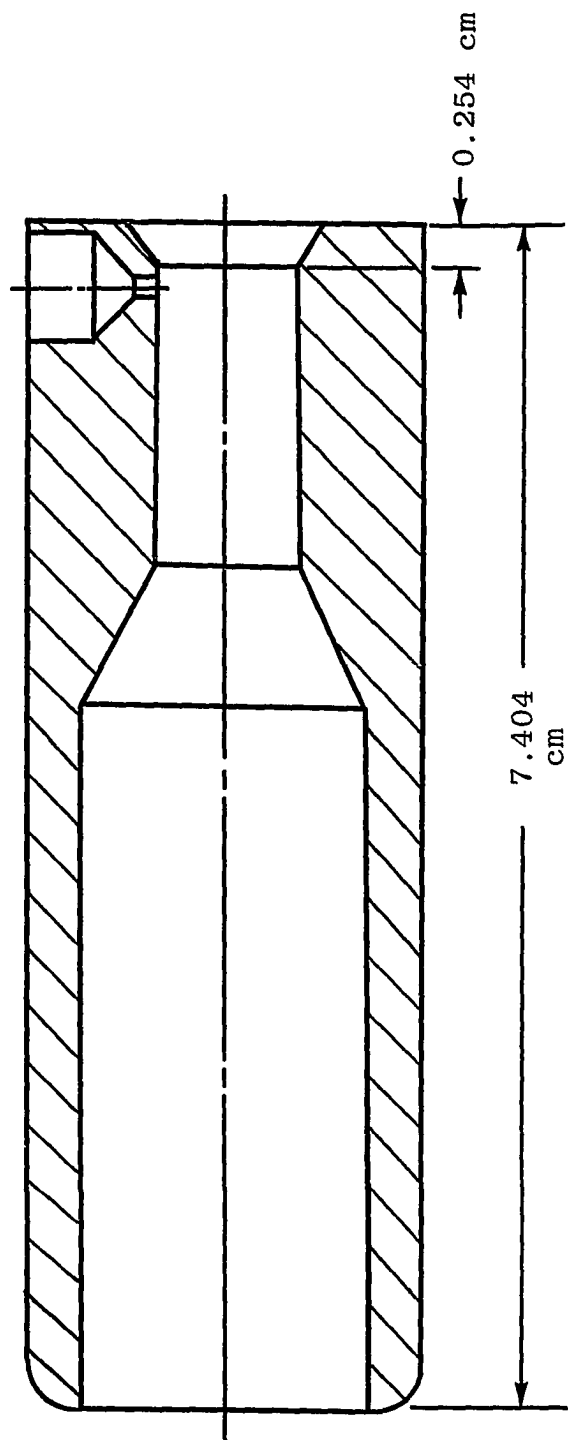
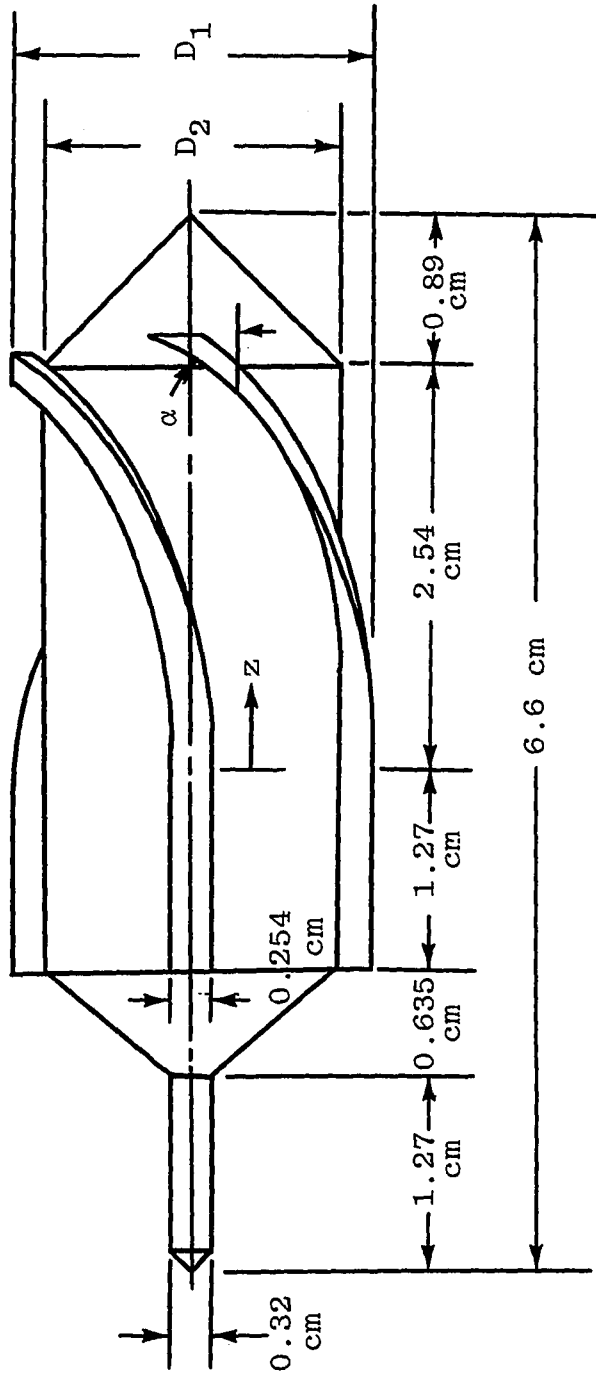


Fig. 58 The dimensions of the vortex tube with abrupt enlargement in the rear.



For $\alpha = 45^\circ$, $\theta = 76.9 z^2$ degree

For $\alpha = 60^\circ$, $\theta = 133.2 z^2$ degree

For $\alpha = 75^\circ$, $\theta = 191.4 z^2$ degree

Fig. 59 The design and dimensions of the swirller.

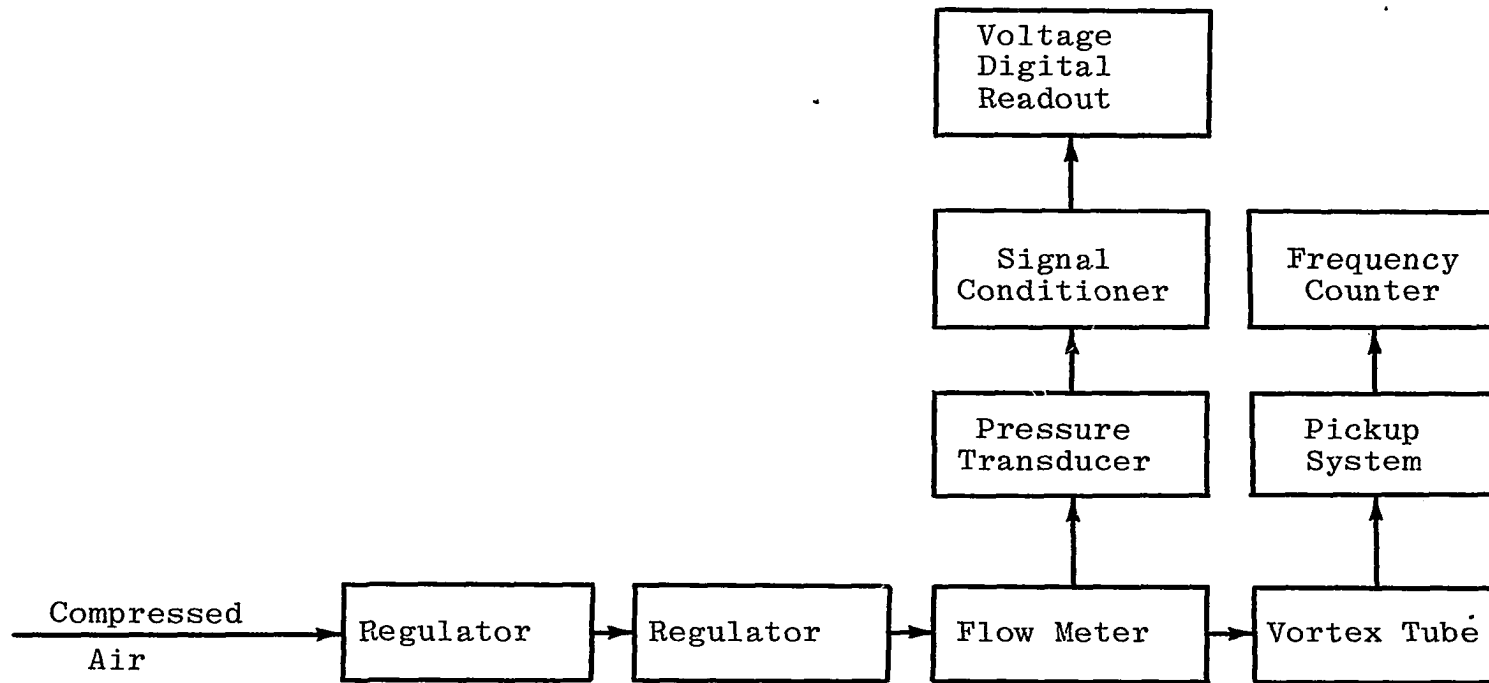
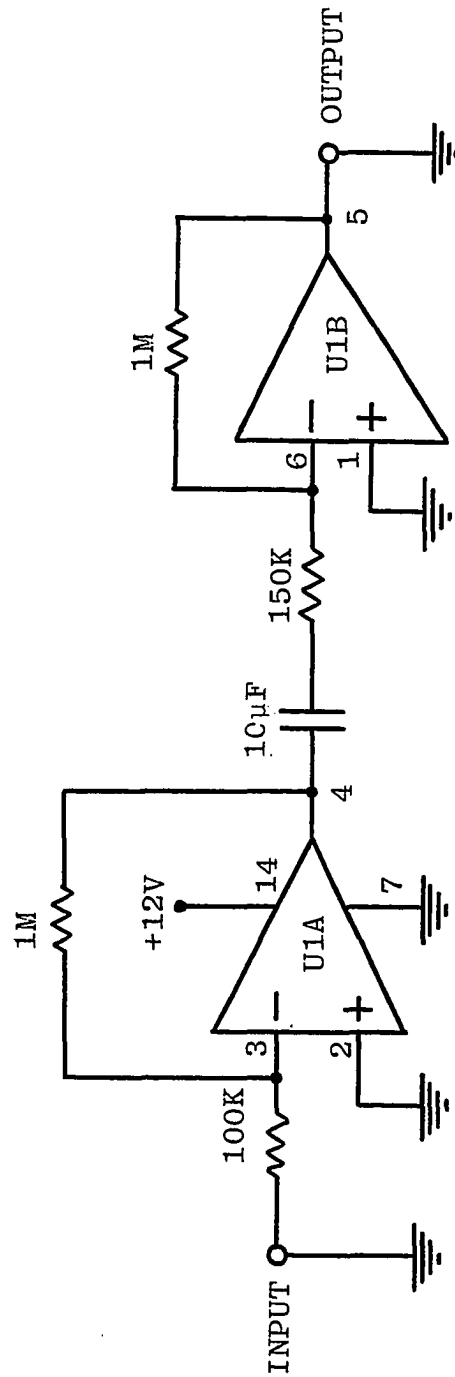


Fig. 60 Setup for experimental test.

picked up by an electric condenser microphone and passed through an amplifier which was connected to either an oscilloscope or a frequency counter. The schematic diagram of the signal amplifier is shown in Fig. 61. Also the description of the electric condenser microphone used in this test is shown in Fig. 62. It is expected that the flow rate is also linearly proportional to the frequency response.

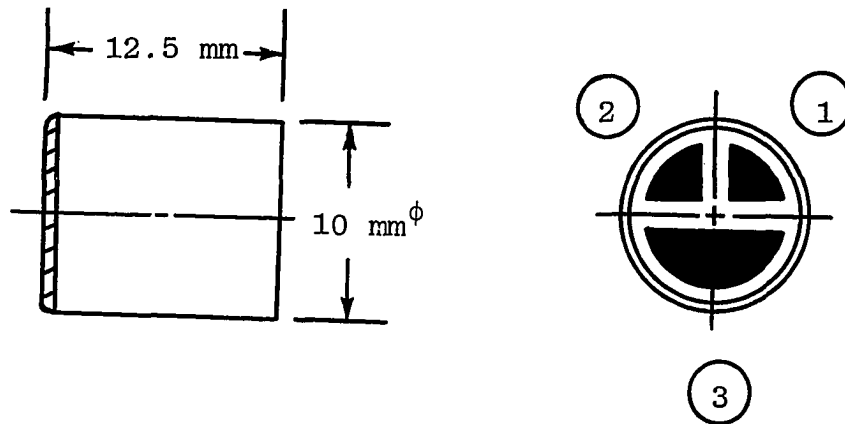
4.4 Wind Tunnel Test

A small but well designed wind tunnel was available for testing. This wind tunnel is shown in Fig. 63. The test area is 15.24 cm by 15.24 cm (6 in by 6 in). An honey comb type screen, 2.54 cm by 2.54 cm grid, was placed in front of the tunnel in order to assure uniform flow at the test section. The speed was measured by a pitot-static tube which was aligned with the entrance plane of the vortex tube being tested. The frequency responses were also picked up by the electric condenser microphone. The arrangement is the same as in closed conduit test. Different combinations of vortex tubes and swirlers are arranged for testing. Their dimensions are given in Table 1.

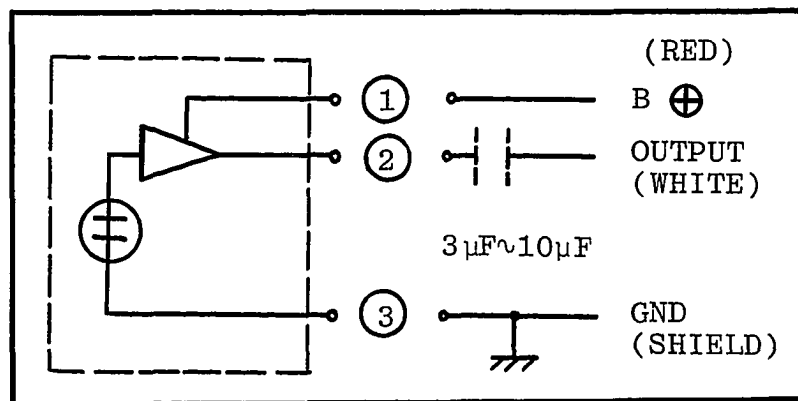


* U1 CA3401E

Fig. 61 Schematic diagram for input amplifier.



CIRCUIT DIAGRAM



ELECTRICAL CHARACTERISTICS

Sensitivity: $-65\text{dB} \pm 4\text{dB}$ (OdB REF 1V/ μbar at 1 KHz)

Output Impedance: 600 Ohms

Omni-directional Response

Supply Voltage: 2.0 V Min., 10 V Max.

Nominal Supply: 4.5 V

Current Drain: 0.5 mA Max.

Fig. 62 The description of electric condenser microphone made by Radio Shack.

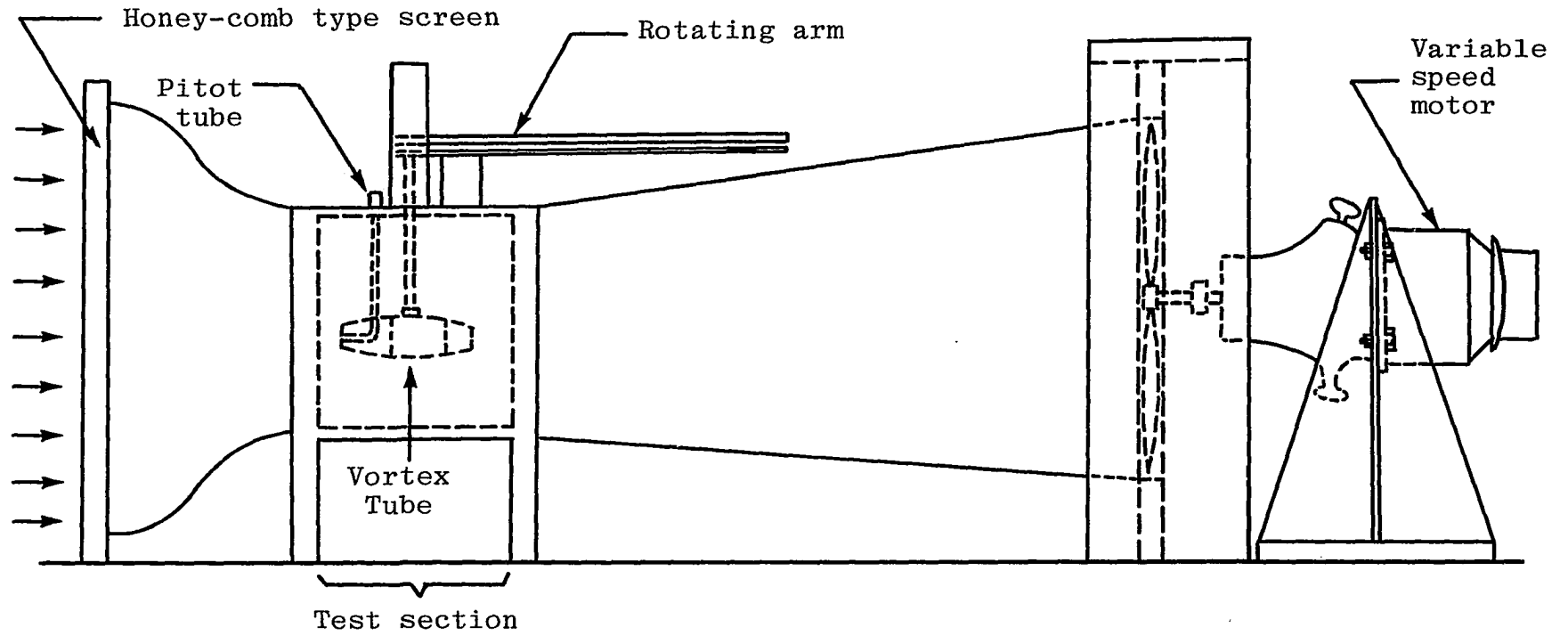
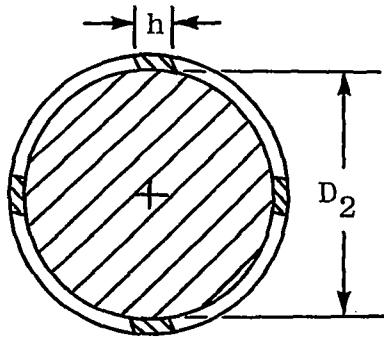


Fig. 63 15.24 cm by 15.24 cm wind tunnel.

5. EXPERIMENTAL RESULTS AND DISCUSSION

The experimental results, obtained from both the closed conduit tests and the wind tunnel tests, did reveal a linear relationship between the true airspeed/flow rate and the frequency response. All swirlers used in these tests had four flutes with an exit angle either 45° , 60° or 75° . The actual dimension h on the swirler shown in Fig. B.2 (in Appendix B) is shown in Fig. 64. The comparison between the designed (used in the numerical calculations) and actual cross-sectional areas for flow passage at section A-A shown in Fig. B.1 (in Appendix B) is also shown in Fig. 65. Past investigators had difficulty eliminating noise from the signal. A discovery that was made during these tests was that the proper positioning of the microphone was critical in obtaining the desired frequency response. This inevitably resulted in eliminating noise interference and thus produced a stable and clean signal. This breakthrough made measurements possible. It was observed that a definite minimum airspeed value had to be reached first for the frequency response to be stable. The reasons were due to the unstable precessional flow at low airspeed as well as the low amplitude signals. The



Swirler type D_2 Diameter	4 Flutes 45°	4 Flutes 60°	4 Flutes 75°
1.5875 cm (0.625 in)	0.3429 cm (0.135 in)	0.5080 cm (0.200 in)	0.6096 cm (0.240 in)
1.5240 cm (0.600 in)	0.3429 cm (0.135 in)	0.5080 cm (0.200 in)	0.6096 cm (0.240 in)

Fig. 64 The actual flute width h on swirler used in the experimental test.

Type of Swirlers	Areas	Desired Area A_d cm ²	Actual Area A_a cm ²	Ratio of A_a/A_d
$D_2=1.5875$ cm	45°	0.7096	0.6532	0.9205
	60°	0.7096	0.5483	0.7727
	75°	0.7096	0.4838	0.6818
$D_2=1.5240$ cm	45°	0.8325	0.7648	0.9186
	60°	0.8325	0.6390	0.7675
	75°	0.8325	0.5616	0.6745

Fig. 65 Comparison of designed and actual areas of different swirlers with four flutes.

minimum airspeed value was obtained by either lifting or lowering the microphone. It was therefore necessary to maintain this microphone position for all measurements, as the signal would have otherwise deteriorated. The arrangement and position of the microphone is shown in Fig. 66. The results obtained from both the closed conduit test and wind tunnel test are shown and discussed as follows.

5.1 Closed Conduit Test

The first step is to test the sensor with compressed air. The results for Sensors 1 through 4 are shown in Figs. 67-70. The flow rate is recorded and calculated according to the calibration sheet provided with the flow meter used in this test. When calibrated at atmospheric pressure, the formula for flow rate is

$$Q = F_1 \cdot P$$

where Q is the flow rate of the air (cubic feet per minute), P is the differential pressure (inches of water), and F_1 is the constant 5.23. The flow rate, Q , is then converted to the metric system units.

As observed from the figures, the frequency response for each sensor with different swirlers was linearly proportional to the flow rate over a definite range. The working ranges for each sensor with a special swirler are tabulated in Table 2. It was noted that Sensors 2 and 4 had wider ranges of frequency response than for Sensors 1 and 3. The minimum flow rate for generating a stable

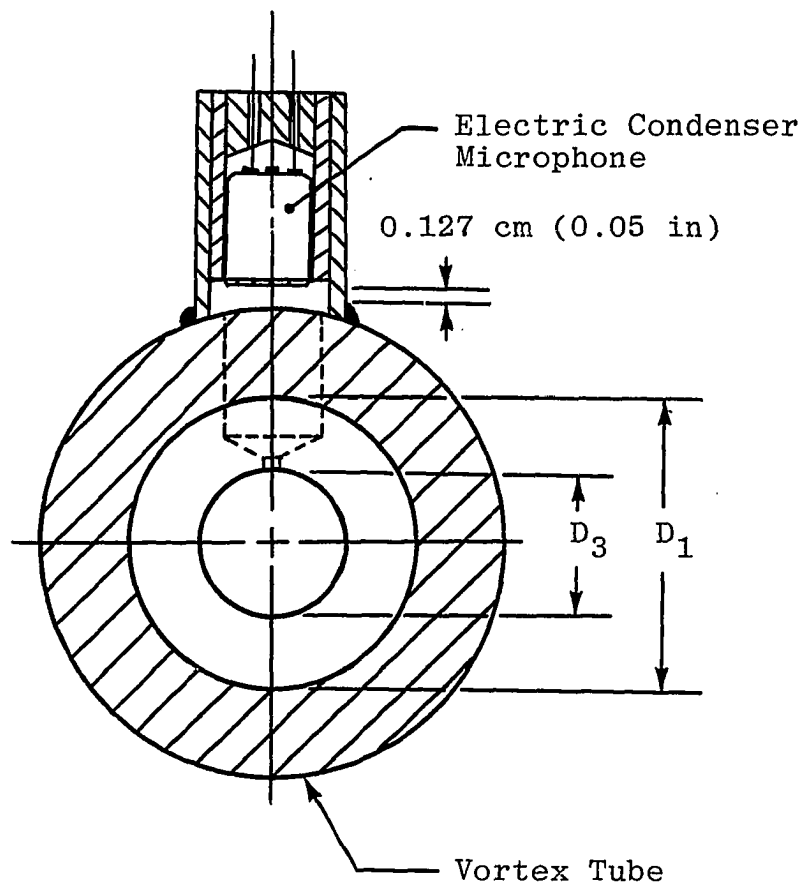


Fig. 66 The position of the microphone used in experimental test.

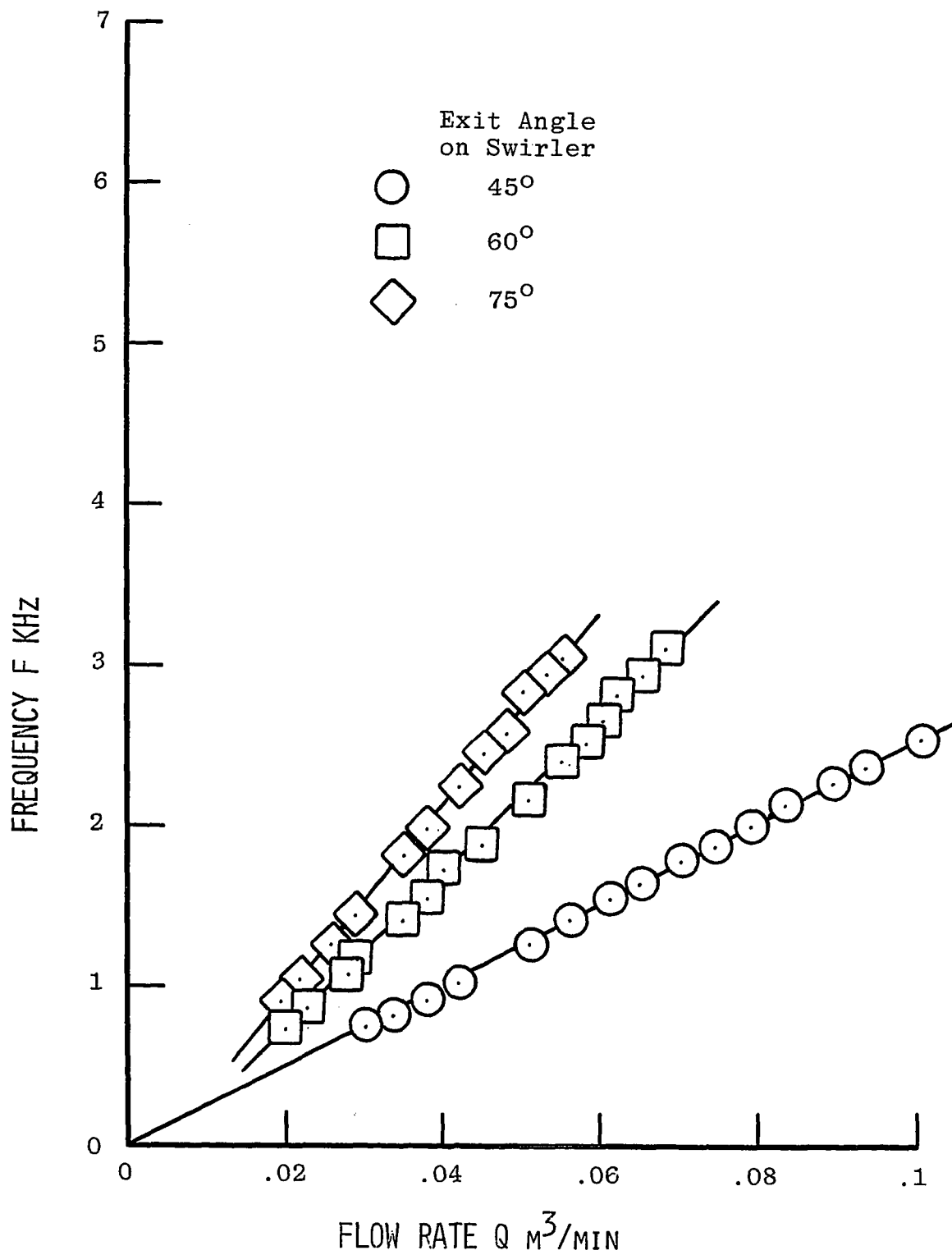


Fig. 67 The experimental data for Sensor 1 with swirlers having four flutes and various exit angles.

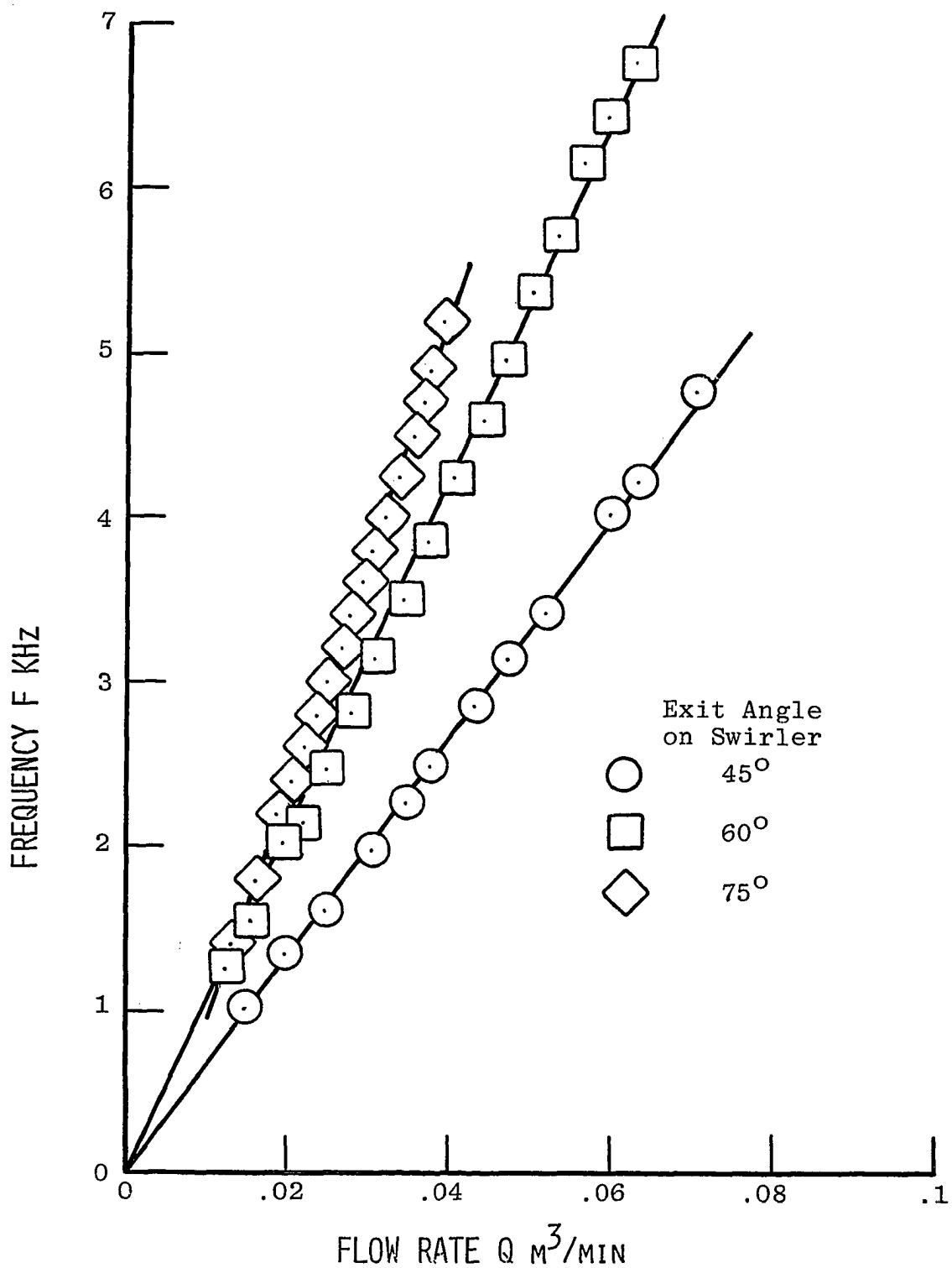


Fig. 68 The experimental data for Sensor 2 with swirlers having four flutes and various exit angles.

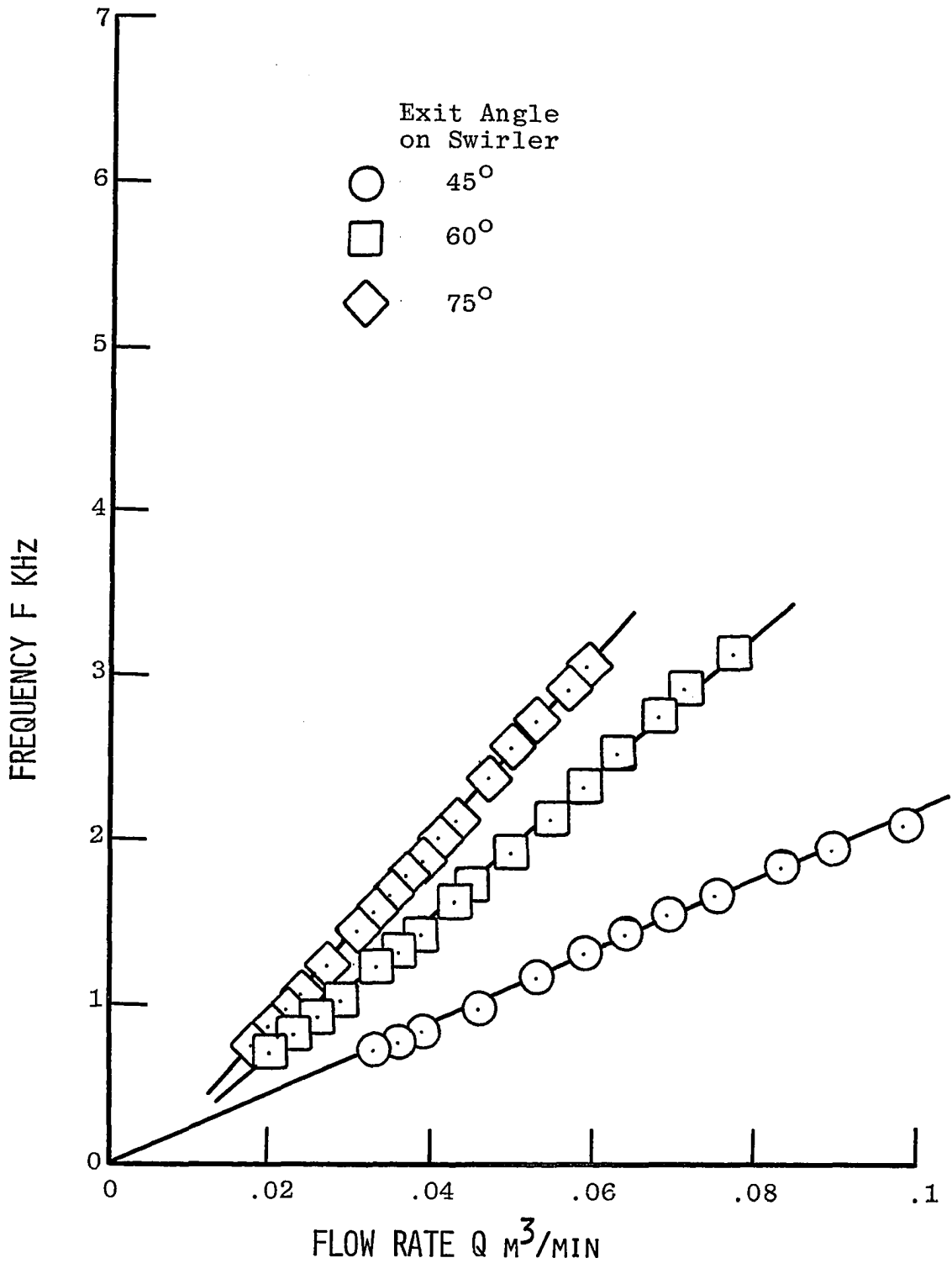


Fig. 69 The experimental data for Sensor 3 with swirlers having four flutes and various exit angles.

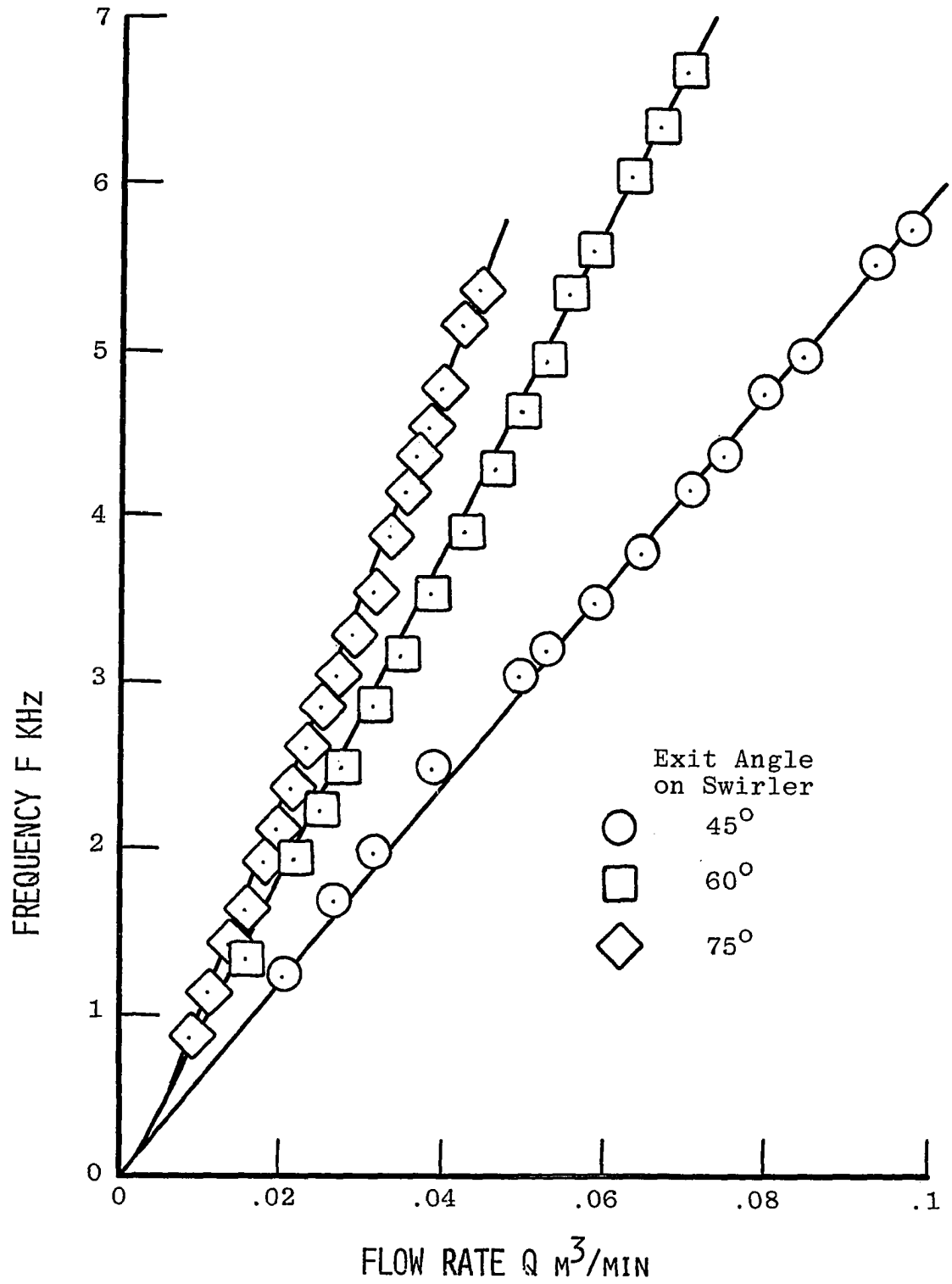


Fig. 70 The experimental data for Sensor 4 with swirlers having four flutes and various exit angles.

Table 2 The working ranges of the sensors with the swirlers having four flutes and different exit angles.

Flow rate ranges Type of Combination		MINIMUM		MAXIMUM	
		Q m ³ /min	F KHz	Q m ³ /min	F HKz
Sensor 1	45°	0.0304	0.72	0.1150	2.98
	60°	0.0200	0.72	0.0680	3.10
	75°	0.0200	0.89	0.0550	3.05
Sensor 2	45°	0.0152	1.03	0.0713	4.75
	60°	0.0127	1.23	0.0698	7.50
	75°	0.0090	0.85	0.0400	5.20
Sensor 3	45°	0.0330	0.70	0.1570	3.30
	60°	0.0200	0.69	0.0770	3.10
	75°	0.0180	0.74	0.0590	3.05
Sensor 4	45°	0.0206	1.20	0.1200	7.00
	60°	0.0158	1.30	0.0702	6.65
	75°	0.0090	0.84	0.0450	5.35

signal was $0.009 \text{ m}^3/\text{min}$, and this occurred in Sensors 2 and 4 with an exit swirler angle of 75 degrees. The minimum frequency response picked up by the microphone was 0.70 KHz, and this was observed in Sensor 3 which had an exit swirler angles of either 45 or 60 degrees. The maximum flow rate working linear range was noted to be $0.157 \text{ m}^3/\text{min}$ and this was observed with Sensor 3 having an exit swirler angle of 45 degrees. As predicted in the numerical calculations, it was found that the higher the exit swirler angle, the higher the frequency response. The best performance among those sensors was for the one with an exit swirler angle of 45 degrees. In general the sensors with the smaller cross-sectional precessional flow areas, had quicker responses at the lower flow rates. This smaller cross-sectional precessional flow area produced a more stable precessional flow and a more pronounced whistle. Below the minimum flow rate, the signal was random, and also the noise level was high. Beyond the maximum point, the frequency response declined. It will be shown later that the working ranges listed in Table 2 will indeed cover the maximum desired airspeed of 321.9 km/hr.

5.2 Wind Tunnel Test

Unlike the closed conduit test, when a sensor was tested in the wind tunnel, a much higher airspeed was needed to generate a stable frequency response. Due to this reason, as shown in Fig. 71, a modified model for the

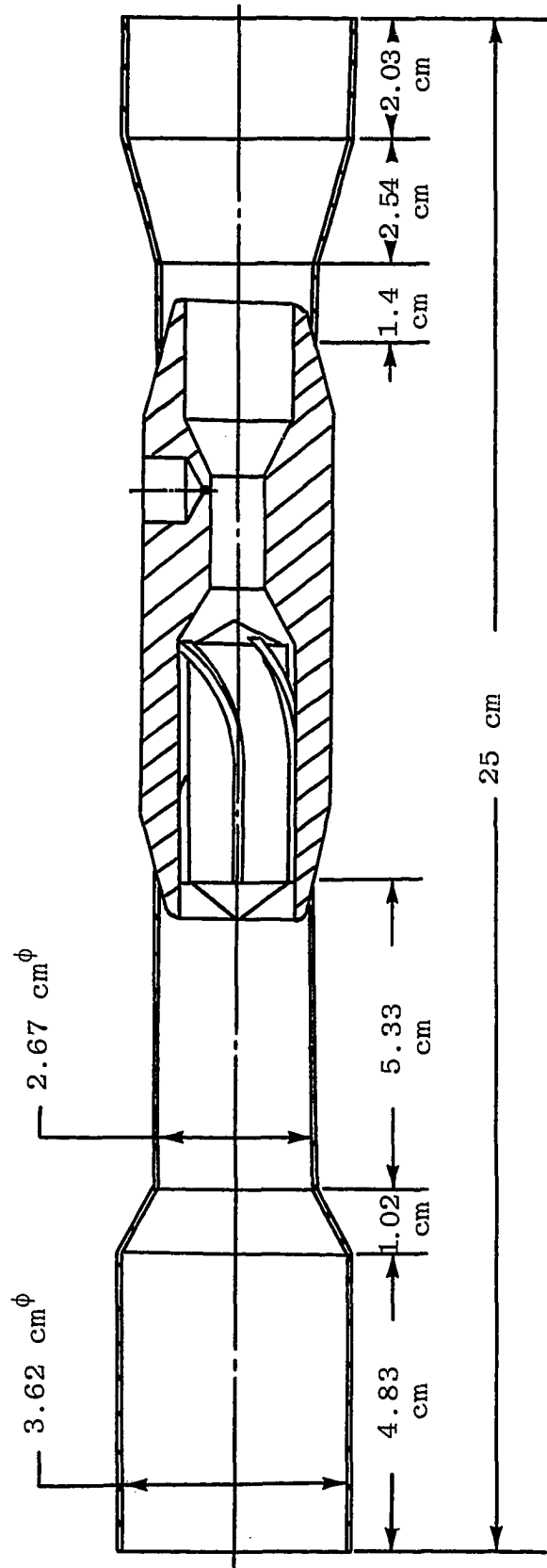


Fig. 71 Modified version of vortex tube for wind tunnel test.

vortex tube was made. A convergent nozzle was placed in front of the vortex tube. This enabled the airspeed to reach a higher value at the entrance to the vortex tube. When compared with the original sensor, this modified model was able to generate a higher angular velocity and more stable precessional flow. Also, a divergent nozzle was placed in the back of the vortex tube in order to minimize the outside influence on the back flow region. Such an arrangement, another breakthrough, contributed to making the measurements possible. A pitot-static tube was placed in front of the convergent nozzle so as to measure the airspeed. It was anticipated that a stable frequency response would not be possible until the minimum frequency response as noted in the closed conduit test with a specified sensor was reached. Based on this test the minimum airspeed to obtain a stable signal was 70 km/hr (43.5 mph).

Due to wind tunnel limitations described in Fig. 63, only a few measurements were made. However, through correlation of flow rates, airspeeds and frequency responses additional data can be extrapolated to higher airspeeds. The combinations of test results for true airspeed, flow rate and frequency response are shown in Figs. 72-83 for the individual sensors with a specified swirler. The procedure used to obtain these figures is described in Appendix E.

It should be mentioned that for a specified sensor and

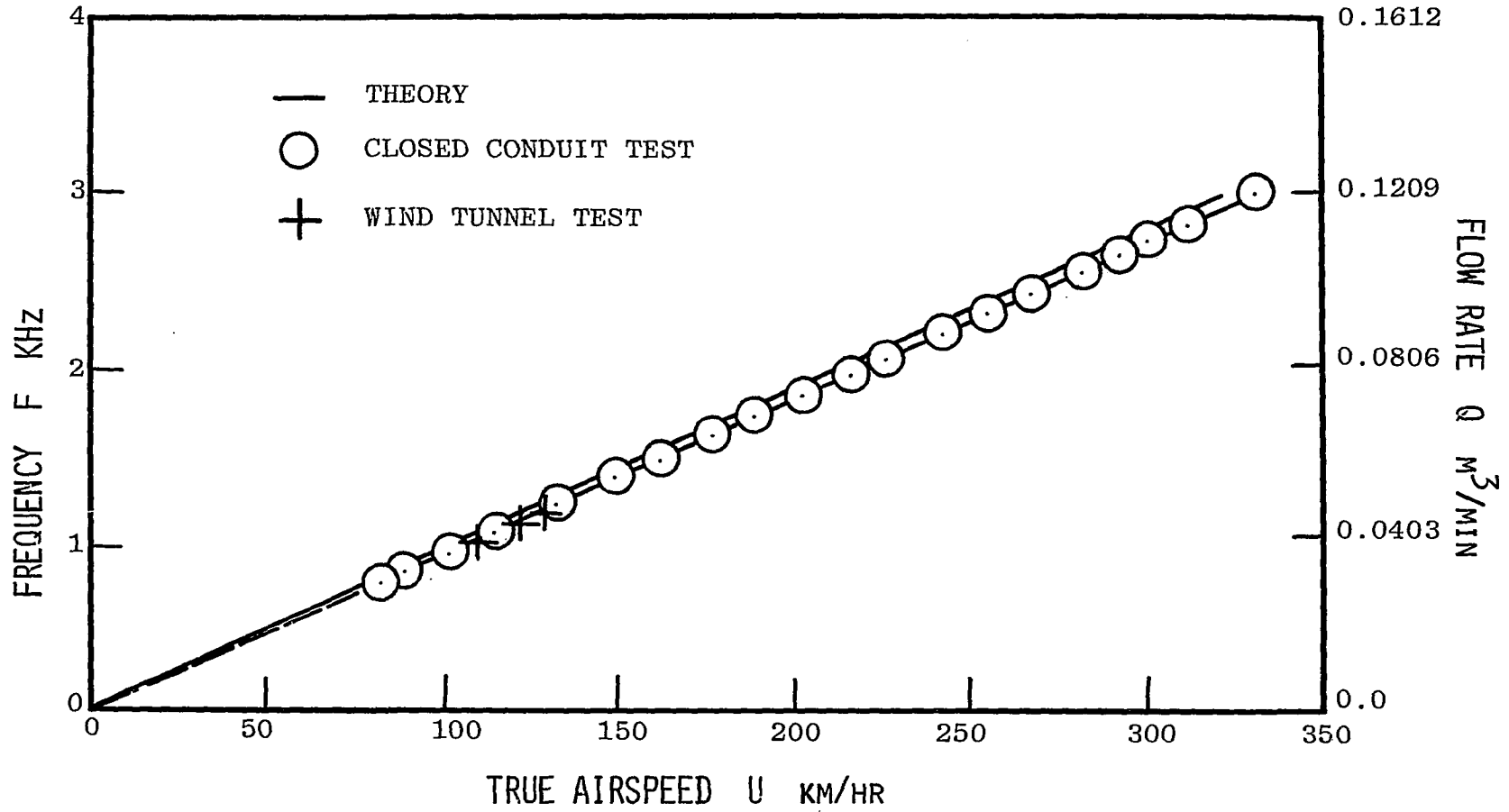


Fig. 72 The performance of Sensor 1 with swirler having four flutes and exit angle 45°.

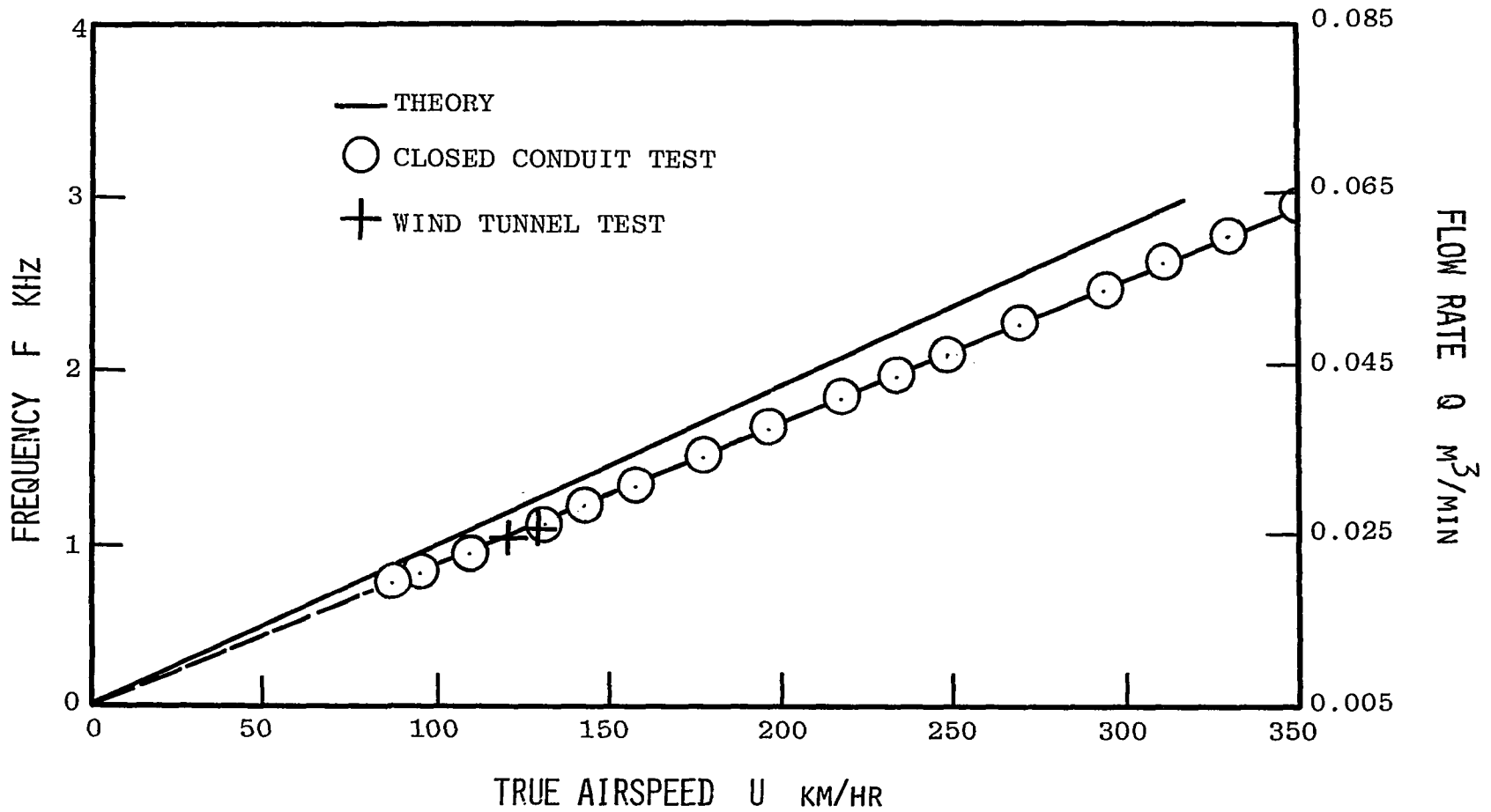


Fig. 73 The performance of Sensor 1 with swirler having four flutes and exit angle 60° .

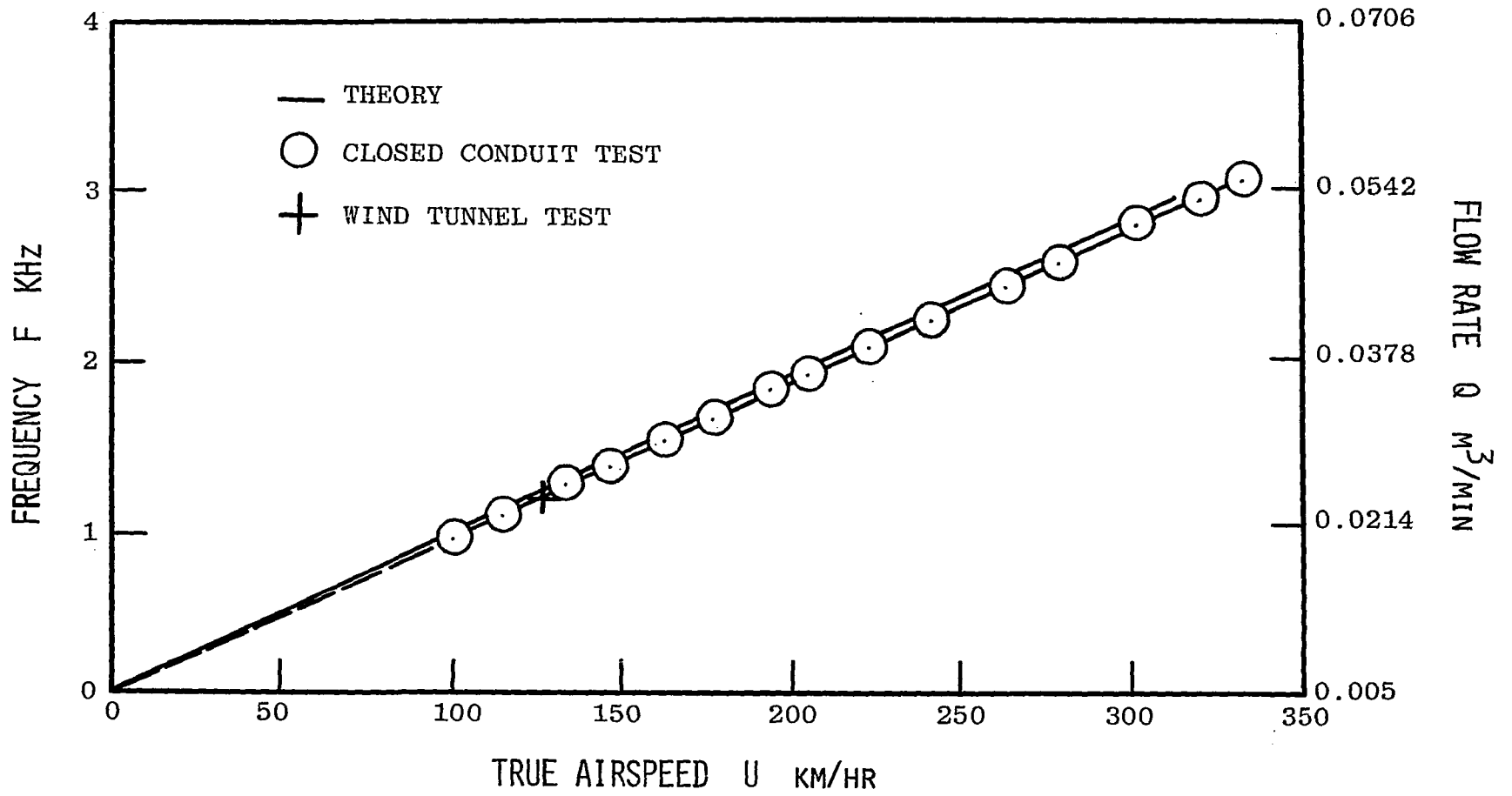


Fig. 74 The performance of Sensor 1 with swirler having four flutes and exit angle 75°.

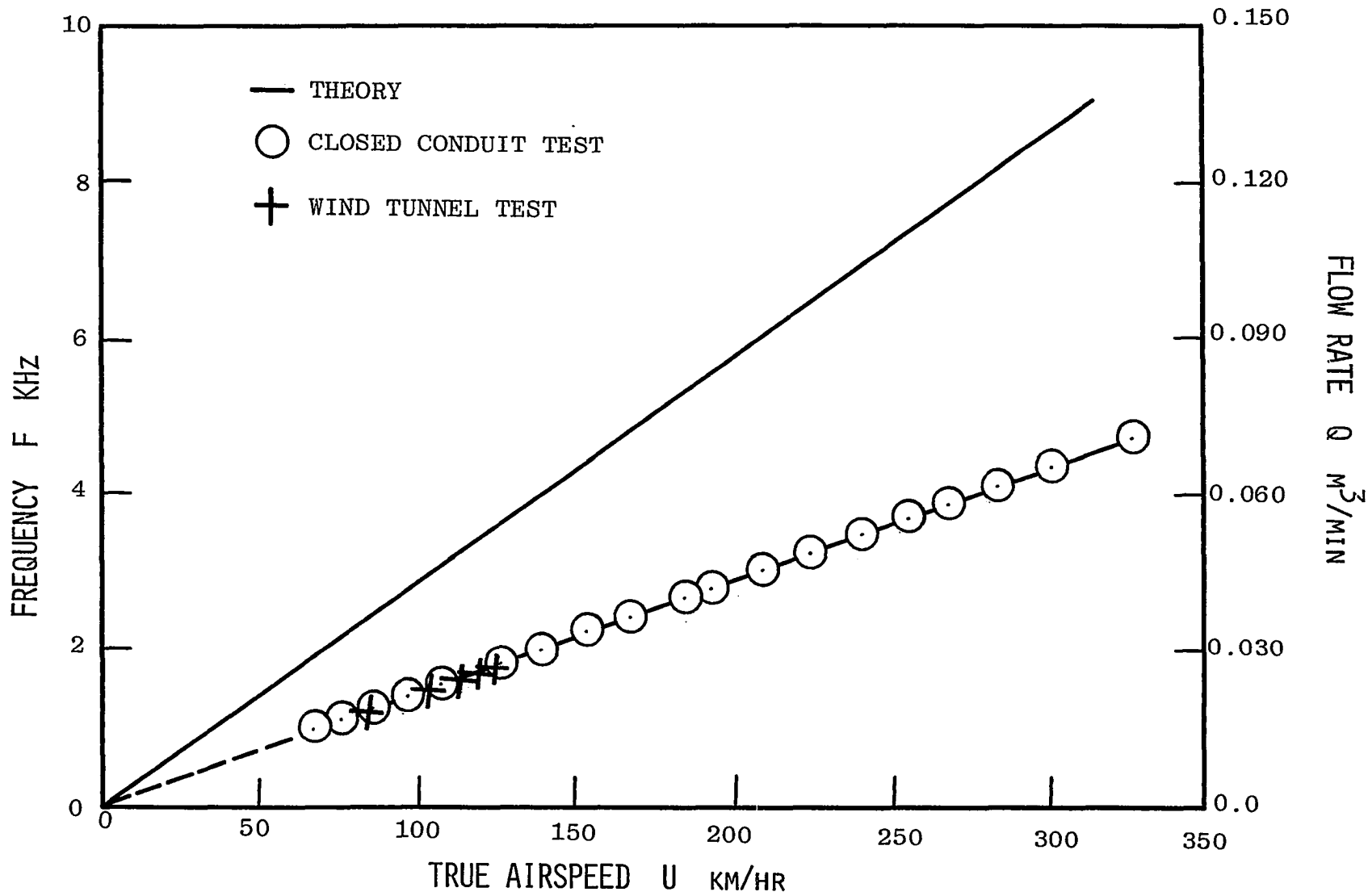


Fig. 75 The performance of Sensor 2 with swirler having four flutes and exit angle 45°.

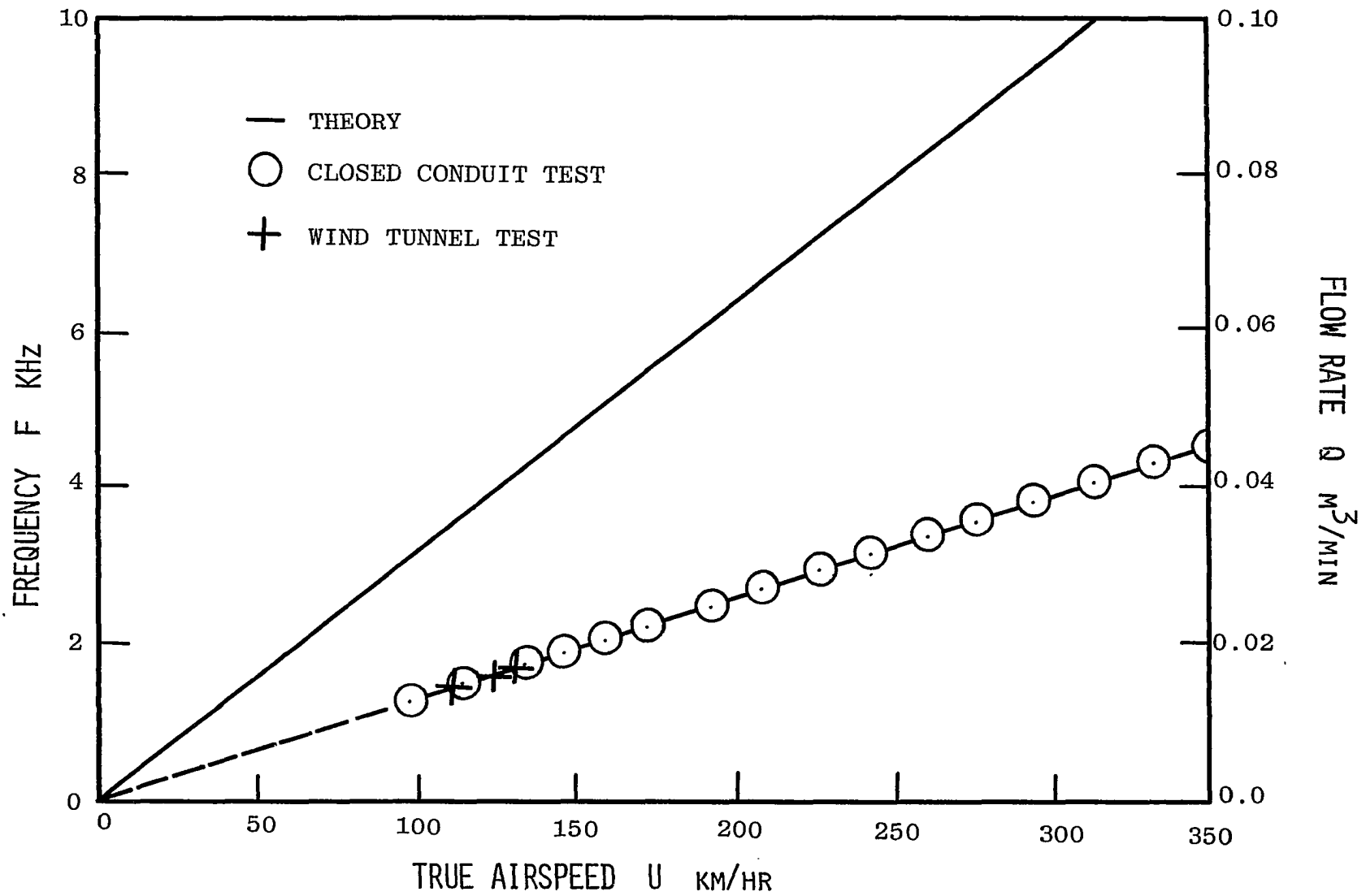


Fig. 76 The performance of Sensor 2 with swirler having four flutes and exit angle 60°.

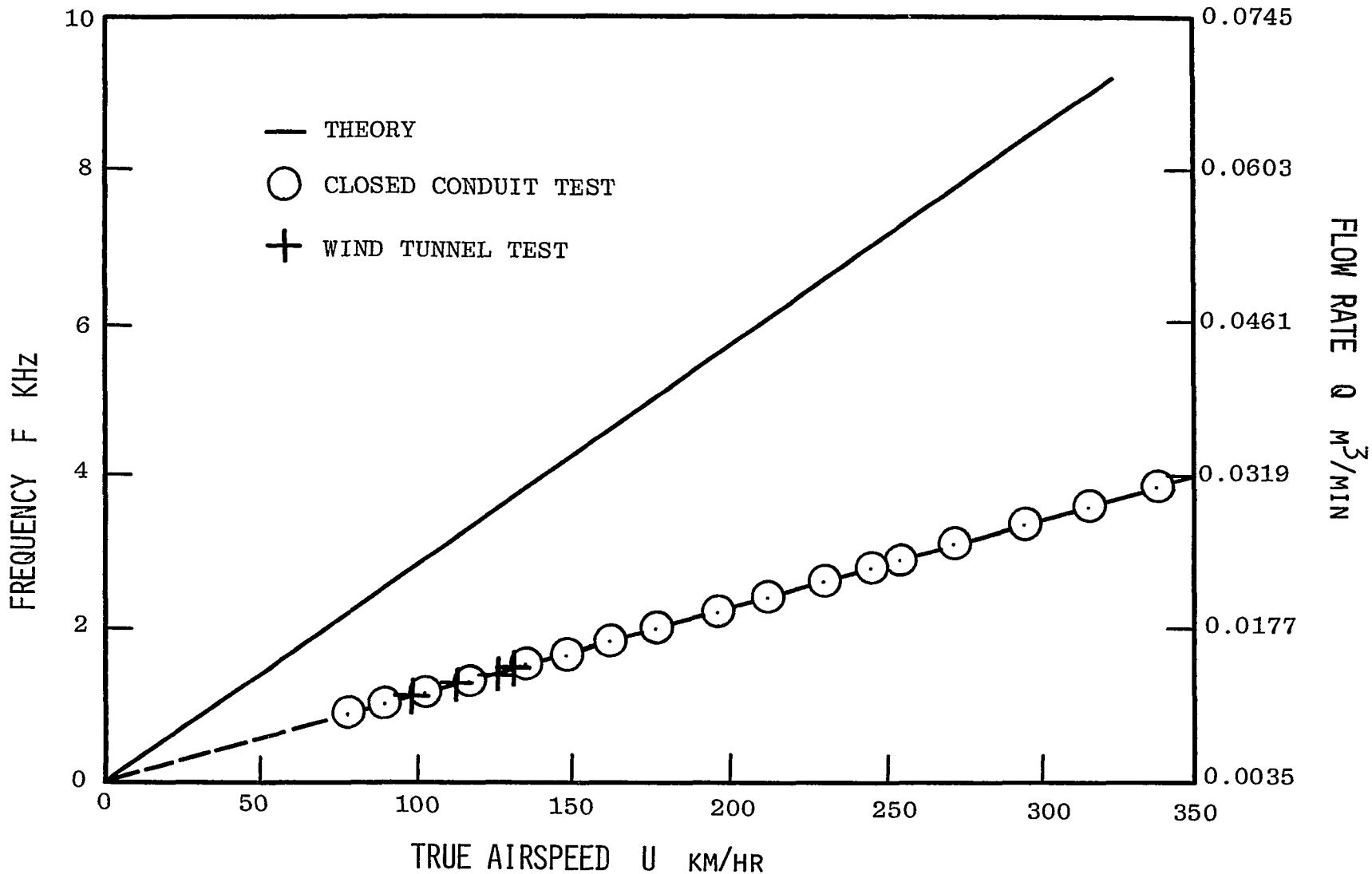


Fig. 77 The performance of Sensor 2 with swirler having four flutes and exit angle 75°.

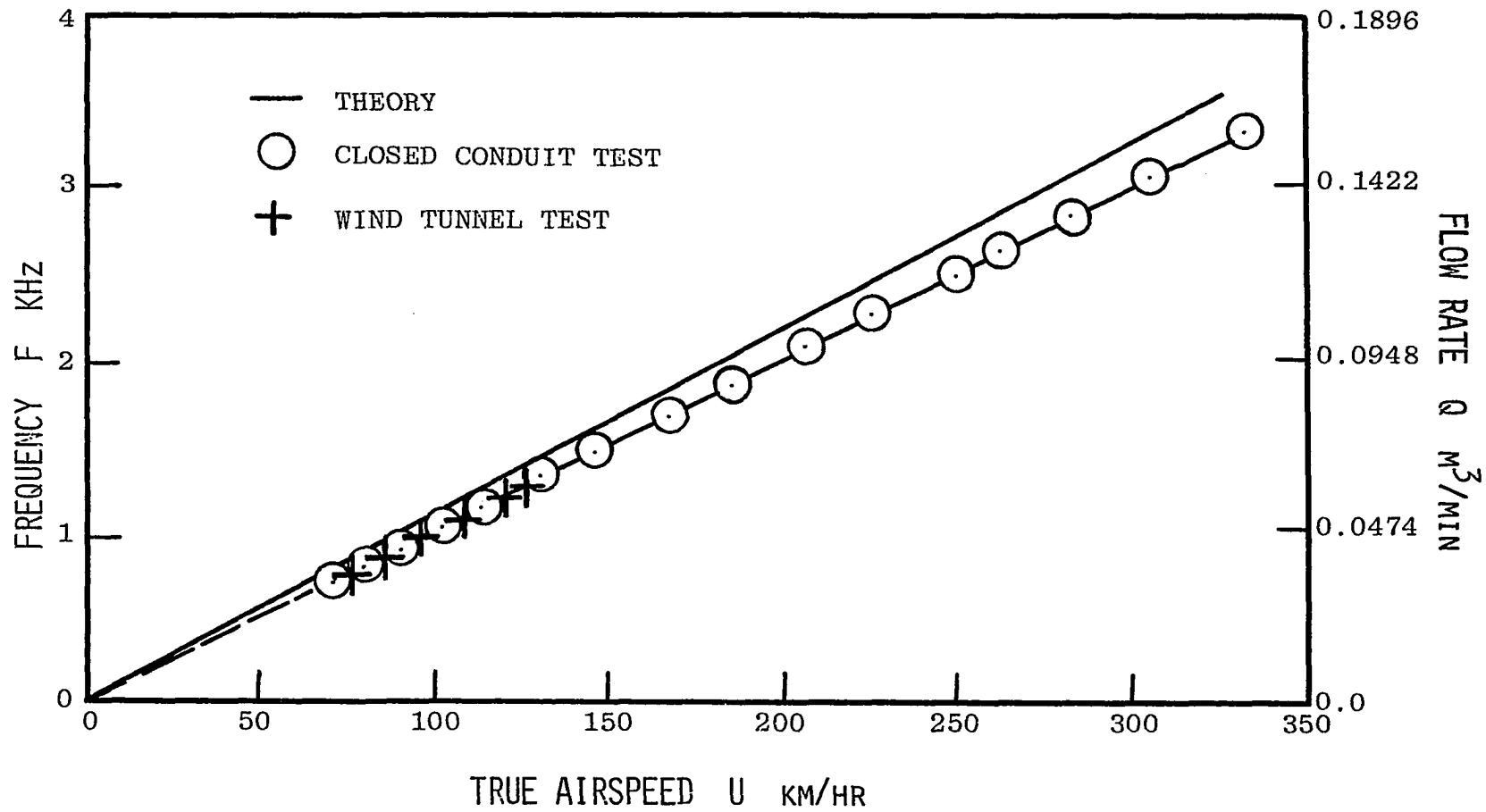


Fig. 78 The performance of Sensor 3 with swirler having four flutes and exit angle 45°.

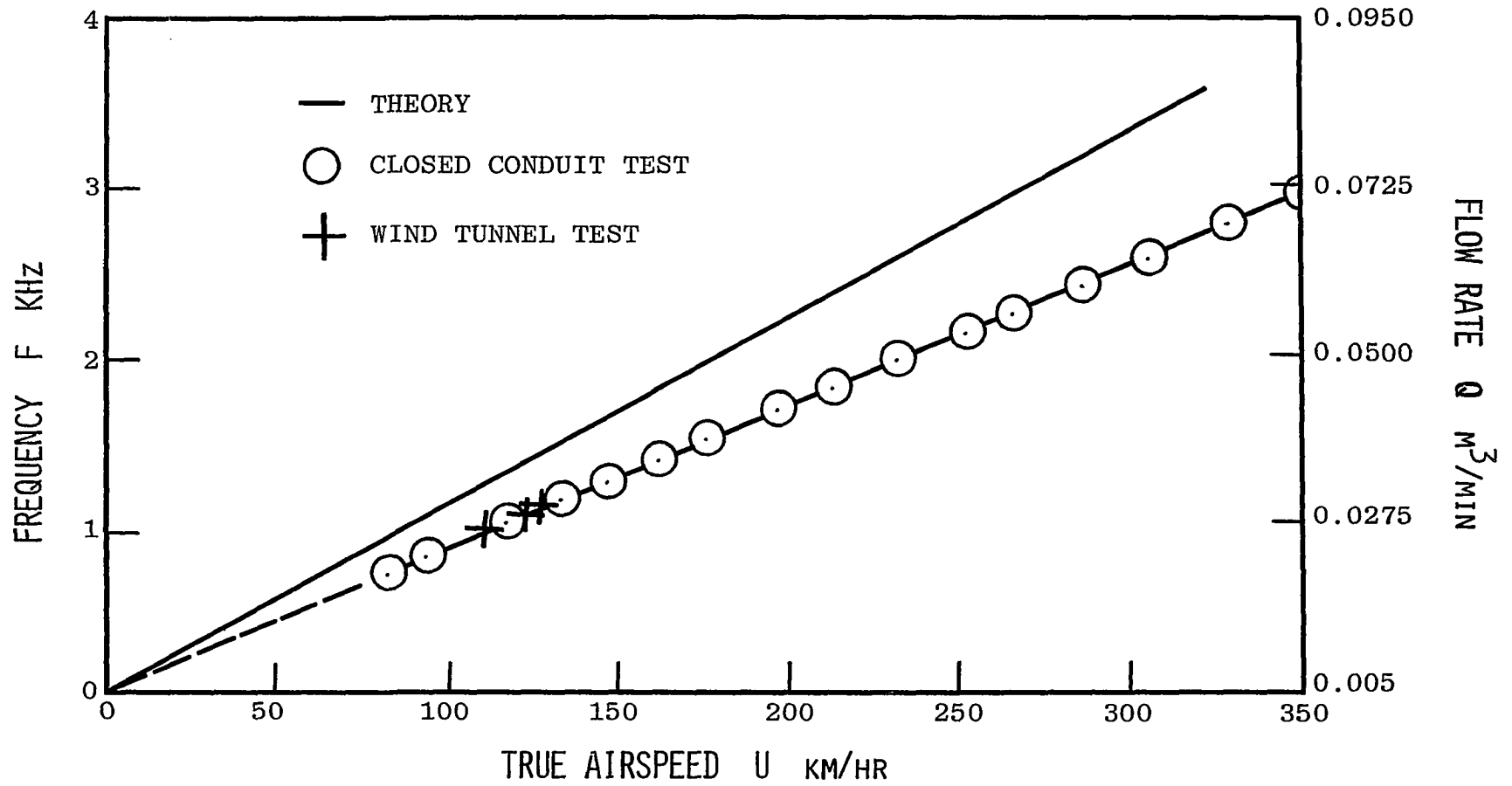


Fig. 79 The performance of Sensor 3 with swirler having four flutes and exit angle 60° .

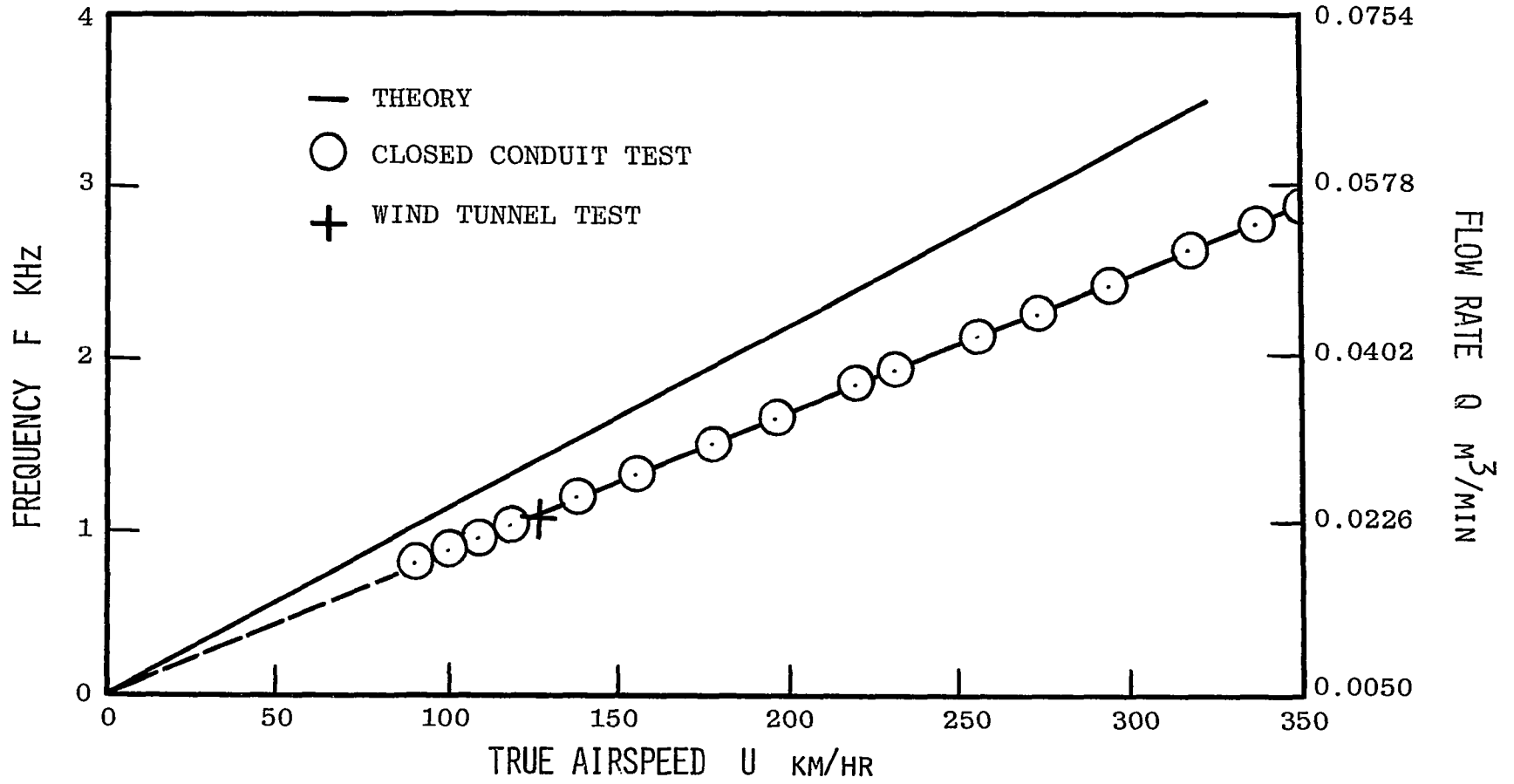


Fig. 80 The performance of Sensor 3 with swirler having four flutes and exit angle 75°.

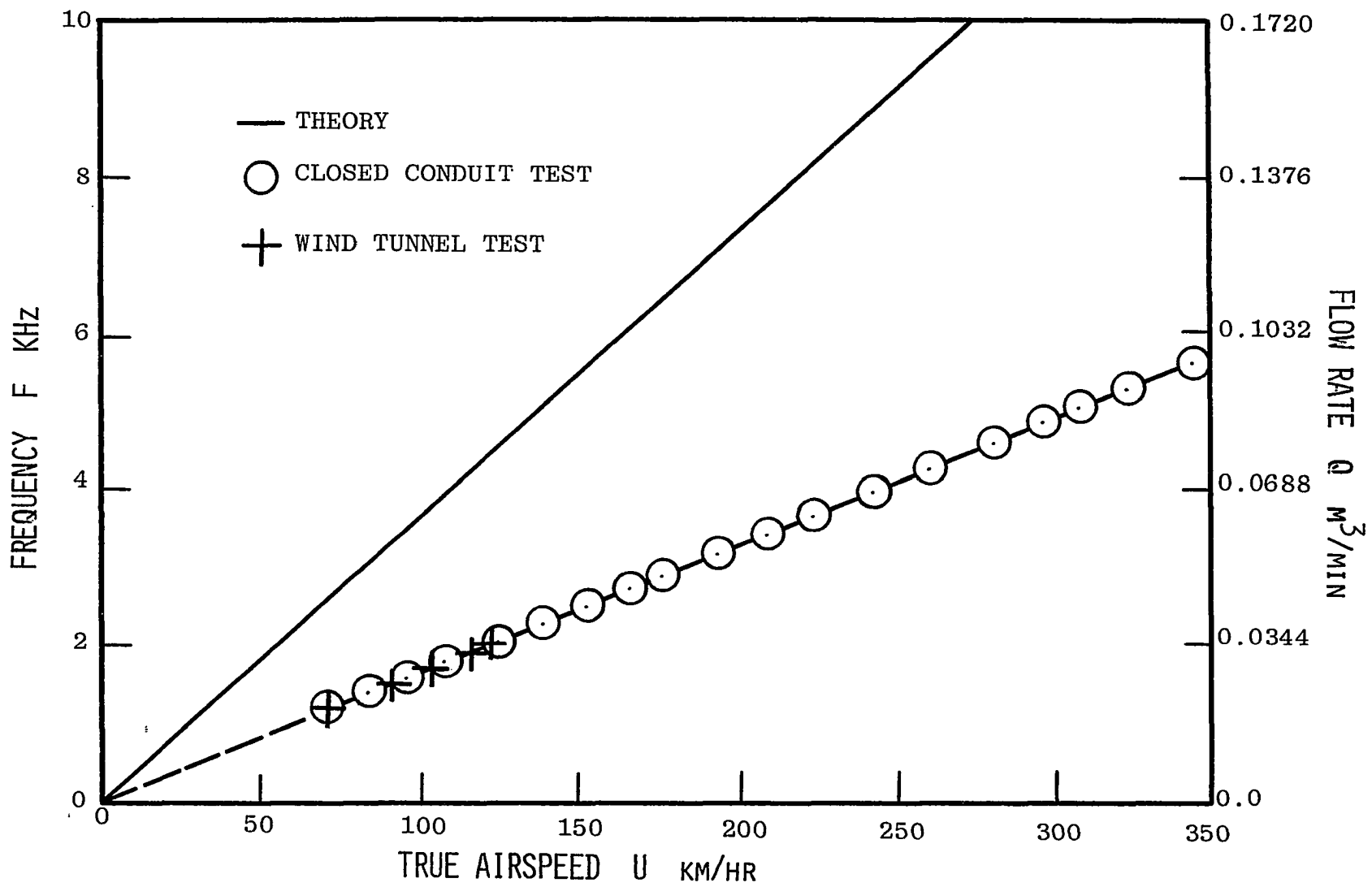


Fig. 81 The performance of Sensor 4 with swirler having four flutes and exit angle 45°.

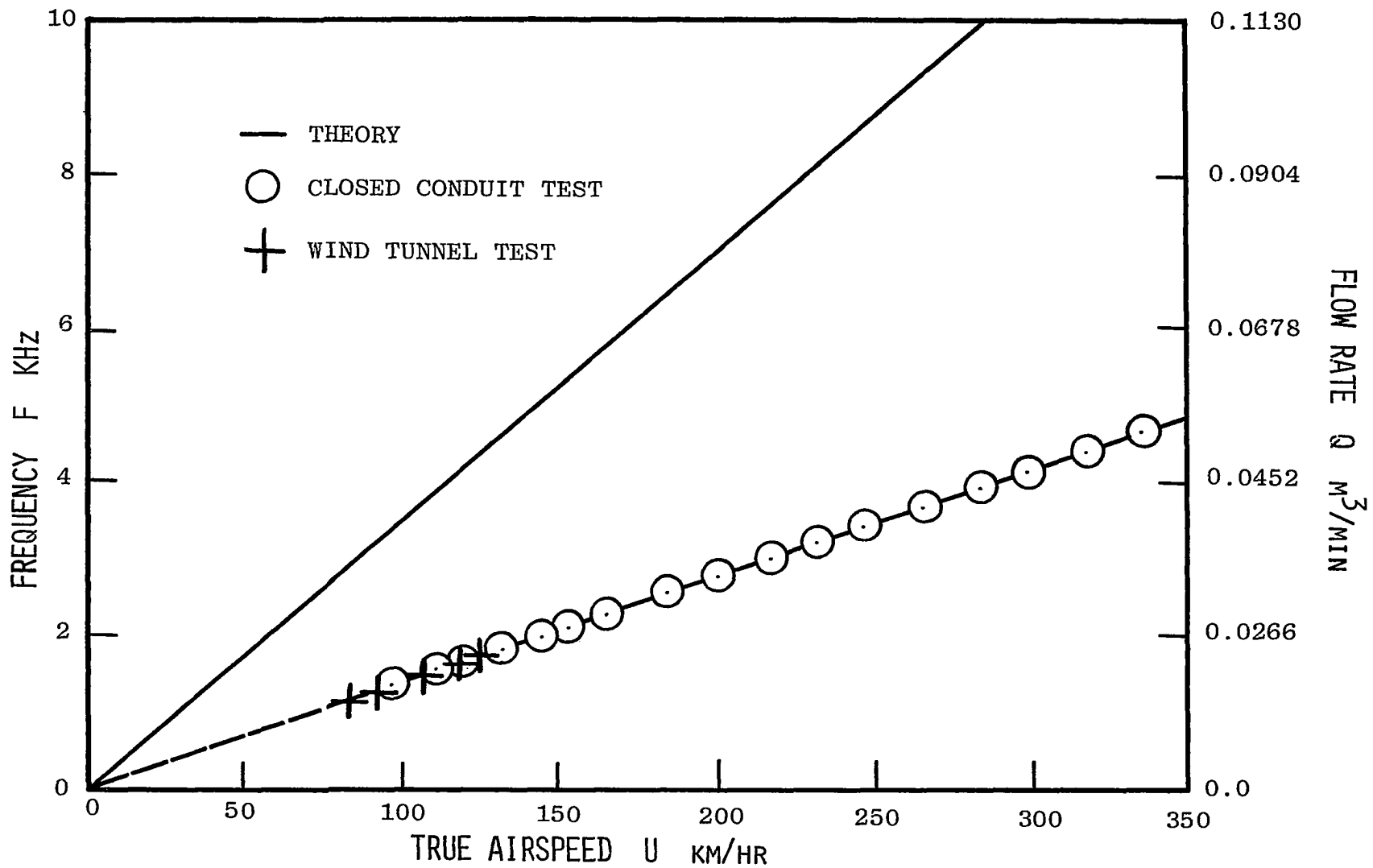


Fig. 82 The performance of Sensor 4 with swirler having four flutes and exit angle 60°.

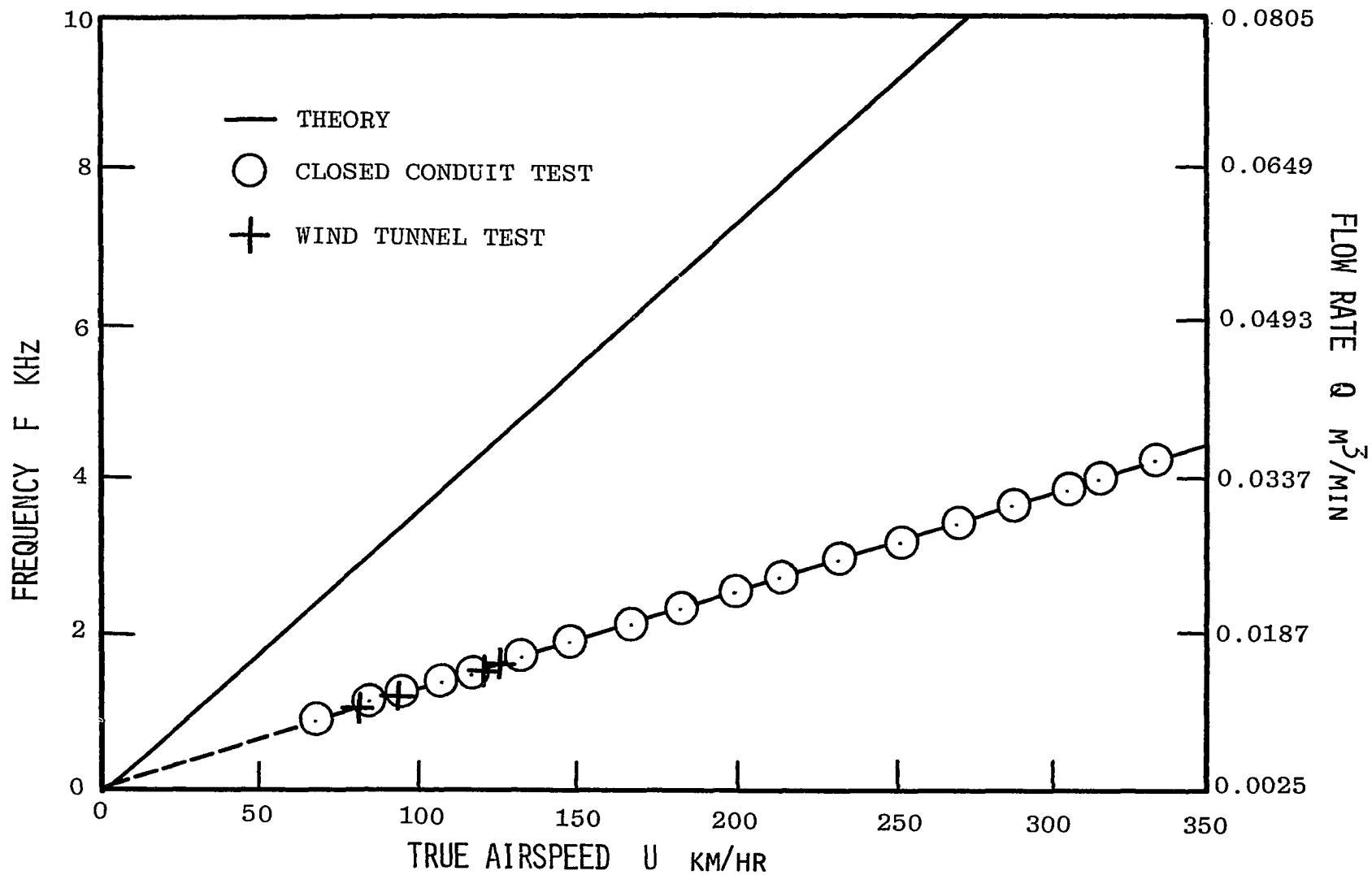


Fig. 83 The performance of Sensor 4 with swirler having four flutes and exit angle 75°.

swirler the working, linear range for the closed conduit test is also the working range for the wind tunnel test. It is noted that the frequency response is linearly proportional to the true airspeed. When the desired maximum airspeed 321.9 km/hr (200 mph) is reached, the frequency response is still within the linear range.

Figs. 72-83, the converted dimensional numerical results are plotted for comparison. The converted numerical results were obtained by multiplying the theoretical results by the area ratio shown in Fig. 65. To avoid any misunderstanding two comments should be mentioned. First, the numerical results were calculated using a number of simplifying assumptions. In reality, the viscous effects were, however, significant. Besides viscous effects, the disagreement might be due to compressibility effects or variable fluid properties. The deviations between the theory and experimental data are clearly evident, especially for Sensors 2 and 4, which had the smallest value of D_3 . Hence, another possible cause for this deviation between experiment and theory could be enhanced decay of the swirl velocity between the swirler and the entrance of the precessional flow region for sensors with smaller D_3 values. The second comment of significance is that the pitot tube position for measuring the airspeed in the wind tunnel test was not at the same location as in the numerical calculation. The actual airspeed at the entrance of the vortex tube was 1.84 times higher than that at the

point of the converging nozzle. The experimental results for Sensors 1 and 3 compare favorably with the numerical results when one follows the procedures and measurements recommended in this chapter. A definite conclusion reached was that the analytic and experimental results did prove that the frequency response was linearly proportional to the true airspeed, while quantitative agreement between theory and experiment is sufficiently good to allow theoretical prediction only for Sensors 1 and 3. The actual reason for the deviation between experiment and theory for Sensors 2 and 4 is not known for certain.

SUMMARY AND CONCLUSION

An analytic and experimental study of a true airspeed sensor has been undertaken. The results of the theoretical study proved to be successful, in that it was determined that the frequency response was linearly proportional to the airspeed. The performance was shown to be heavily dependent upon the design of the vortex tube and swirler geometries. The smaller the cross-sectional area in the precessional flow region, the more sensitive was the frequency response. The exit angle on the swirler also played a very important role in the performance of the sensor. The larger the exit swirler angle, the greater was the frequency response. It was also observed that as Reynolds number increased the Strouhal number remained constant. Moreover, it was noticed that the Strouhal numbers based on mean axial velocity were dependent only upon the exit swirler angles.

The experimental results revealed similar characteristics to those obtained through analysis. This true airspeed sensor has three unique characteristics: flow phenomenon-precession, vortex whistle, and no moving parts. It was also observed that the position of the

microphone was critical. When the microphone was located close to the inner wall, a nondesirable random signal was created. On the other hand when the microphone was placed too far from the inner wall the capability of picking up a signal was reduced. Thus, the best microphone position was achieved by adjusting the position until a stable signal was obtained. By such a procedure it became possible to make the necessary measurements. The working ranges of the sensors were beyond the maximum airspeed required for use on small private aircraft.

Due to the complexity of the problem, the analytic results are valid only for inviscid fluid flow. When compared with the experimental result, the deviations noted are believed to be due to either the viscous effects, variable fluid properties or compressibility effects. Under the arrangement described in Chapter 5, it was found that the experimental results were in agreement with the analytic results for Sensors 1 and 3. Although for this project the minimum airspeed was 70 km/hr (43.5 mph), the minimum airspeed achievable could be lowered by placing a modified convergent nozzle in front of the vortex tube. By such a modification a stable signal could be detected even at lower airspeeds.

In conclusion, it was found that this true airspeed sensor has the feature of having a linear relationship between frequency response and airspeed as well as being independent of altitude, temperature and density. The

sensor has proven to be reliable, capable of high accuracy, and to be one that could be easily fabricated and maintained. Such an instrument would be desirable in measuring true airspeeds and flow rates.

REFERENCES

1. Lighthill, M. J., "On Sound Generated Aerodynamically," Proceedings of the Royal Society, Vol. 211, March 1952, pp. 564-587.
2. Curle, N., "The Influence of Solid Boundaries upon Aerodynamic Sound," Proceedings of the Royal Society (London), Vol. 231, Sept. 1955, pp. 505-514.
3. Howe, M. S., "Attenuation of Sound in a Low Mach Number Nozzle Flow," Journal of Fluid Mechanics, Vol. 91, pt. 2, March 1979, pp. 209-229.
4. Roshko, A., "On the Development of Turbulent Wakes from Vortex Streets," NACA TN-2913, Report 1191, March 1953.
5. Blokhinstev, D. I. (Translated by Cooper, R. D.), "Excitation of Resonance by Air Flow," Zhurnal Tekhnicheskoi Fiziki, Vol. XV, 1945, pp. 63-70.
6. Powell, A., and Shulman, A., "On the Edgetone," Journal of the Acoustical Society of America, Vol. 33, No. 4, April 1961, pp. 395-409.
7. Powell, A., and Shulman, A., "Vortex Action in Edgetones," Journal of the Acoustical Society of America, Vol. 34, No. 2, Feb. 1962, pp. 163-166.

8. Powell, A., and Shulman, A., "Effects of Wire Resonance on Aerolian Tones," Journal of the Acoustical Society of America, Vol. 34, No. 8, Aug. 1962, pp. 1146-1147.
9. Wilson, T. A., Beavers, G. S., DeCoster, M. A., Holger, D. K., and Regenfuss, M. D., "Experiments on the Fluid Mechanics of Whistling," Journal of the Acoustical Society of America, Vol. 50, No. 1, pt. 2, July 1971, pp. 366-372.
10. Fineblum, S. S., "Vortex Diodes," Fluidic State-of-the-Art Symposium, Vol. 1, Sept. 1974, pp. 46-80.
11. Fink, R. M., "Prediction of Airfoil Tone Frequencies," Journal of Aircraft, Vol. 12, No. 2, Feb. 1975, pp. 118-120.
12. Cummings, A., "Sound Transmission at Sudden Area Expansions in Circular Ducts with Superimposed Mean Flow," Journal of Sound and Vibration, Vol. 38, No. 1, Jan. 1975, pp. 149-155.
13. Vonnegut, B., "A Vortex Whistle," Journal of the Acoustical Society of America, Vol. 26, No. 1, Jan. 1954, pp. 18-20.
14. Michelson, I., "Theory of Vortex Whistle," Journal of the Acoustical Society of America, Vol. 27, No. 5, Sept. 1955, pp. 930-931.
15. Nicklas, J. P., "Investigation of a Vortex Tube True Airspeed Sensor," Cornell Aeronautical Laboratories. Report 1H-942-P-2, May 1957.

16. Suzuki, M., "Theoretical and Experimental Studies on the Vortex-Tube," Scientific Papers of the Institute of Physical Chemistry Research, Tokyo, Vol. 54, No. 1, Jan. 1960, pp. 43-87.
17. Chanaud, R. C., "Experiments Concerning the Vortex Whistle," Journal of the Acoustical Society of America, Vol. 35, No. 7, July 1963, pp. 953-960.
18. Powell, A., "Theory of Vortex Sound," Journal of the Acoustical Society of America, Vol. 36, No. 1, Jan. 1964, pp. 177-195.
19. Chanaud, R. C., "Observations of Oscillatory Motion in Certain Swirling Flows," Journal of Fluid Mechanics, Vol. 21, pt. 1, Jan. 1965, pp. 111-127.
20. Talbot, L., "Laminar Swirling Pipe Flow," Journal of Applied Mechanics, March 1954, pp. 1-7.
21. Rodely, A. E., White, D. F., and Chanaud, R. C., "A Digital Flowmeter Without Moving Parts," ASME Paper No. 65-WA/FM-6.
22. Gore, R. W., and Ranz, W. E., "Backflows in Rotating Fluids Moving Axially through Expanding Cross Sections," American Institute of Chemical Engineers Journal. Vol. 10, No. 1, Jan. 1964, pp. 83-88.
23. Chanaud, R. C., "Aerodynamic Whistles," Scientific American, Vol. 222, No. 1, Jan. 1970, pp. 40-46.
24. Weissler, P., "Servicing the '79 Chrysler-Plymouth and Dodge Models," Popular Mechanics, Oct. 1978, pp. 40.

25. Kopp, J. G., "The Swirlmeter," Tenth CHEMPID Symposium, Toronto, May 1969.
26. Herzl, J. P., "The System Approach to High Performance Gas Flow Measurement with the Swirlmeter," FLOW: It's Measurement and Control in Science and Industry, Vol. 1, pt. 2, 1974, pp. 963-966.
27. White, D. F., Rodely, A. E., and McMurtrie, C. L., "The Vortex Shedding Flowmeter," FLOW: It's Measurement and Control in Science and Industry, Vol. 1, pt. 2, 1974, pp. 967-974.
28. Yamasaki, H., and Rubin, M., "The Vortex Flowmeter," FLOW: It's Measurement and Control in Science and Industry, Vol. 1, pt. 2, 1974, pp. 975-983.
29. Beale, R. B., and Lawler, M. T., "Development of a Wall-Attachment Fluidic Oscillator Applied to Volume Flow Metering," FLOW: It's Measurement and Control in Science and Industry, Vol. 1, pt. 2, 1974, pp. 989-996.
30. Kwok, C. K., Lee, P. M., and Lin, S., "An Analytical Investigation of a Vortex Flowmeter," Instrument Society of America Transactions, Vol. 14, No. 2, Sept. 1975, pp. 167-171.
31. Kirshner, J. M., and Katz, S., Design Theory of Fluidic Components, Academy Press, 1975.
32. DiPrima, R. C., "Stability of Nonrotationally Symmetric Disturbances for Viscous Flow Between Rotating Cylinders," The Physics of Fluids, Vol. 4, No. 6, June 1961, pp. 751-755.

33. Krueger, E. R., and DiPrima, R. C., "Stability of Non-rotationally Symmetric Disturbances for Inviscid Flow between Rotating Cylinders," The Physics of Fluids, Vol. 5, No. 11, Nov. 1961, pp. 1362-1367.
34. Sparrow, E. M., Munro, W. D., and Jonsson, V. K., "Instability of the Flow between Rotating Cylinders: the Wide-gap Problem," Journal of Fluid Mechanics, Vol. 20, pt. 1, Sept. 1964, pp. 35-46.
35. Schwarz, K. W., Springett, B. E., and Donnelly, R. J., "Modes of Instability in Spiral Flow between Rotating Cylinders," Journal of Fluid Mechanics, Vol. 20, pt. 2, Oct. 1964, pp. 281-289.
36. Mattingly, G. E., and Criminale, W. O., "The Stability of an Incompressible Two-dimensional Wake," Journal of Fluid Mechanics, Vol. 51, pt. 2, Jan. 1972, pp. 233-272.
37. Kubo, I., and Gouldin, F. C., "Numerical Calculations of Turbulent Swirling Flow," Journal of Fluids Engineering, Sept. 1975, pp. 310-315.
38. Morris, P. J., "The Spatial Viscous Instability of Axisymmetric Jets," Journal of Fluid Mechanics, Vol. 77, pt. 3, Oct. 1976, pp. 511-529.
39. Shen, Y. C., and Goglia, G. L., "Experimental and Analytic Studies in Fluidics: The Experimental Study of a True Airspeed Indicator," Progress Report: Old Dominion University, Norfolk, Virginia, June 1978.

40. Jenkins, M. A., and Traub, J. F., "A Three Stage Variable-Shift Iteration for Polynomial Zeros and Its Relation to Generalized Rayleigh Iteration," Numerische Mathematik, Vol. 14, July 1970, pp. 252-263.
41. Jenkins, M. A., and Traub, J. F., "A Three-Stage Algorithm for Real Polynomials using Quadratic Iteration," SIAM Journal on Numerical Analysis, Vol. 7, No. 4, Dec. 1970, pp. 545-566.

APPENDIX A

NUMERICAL ANALYSIS AND SOLUTIONS

Since equation (51) from Chapter 2 contains the precessional angular velocity ω , a complex number, and since the arguments of the Bessel functions are also complex, a quantitative solution of equation (51) in Chapter 2 is difficult to obtain. Therefore, an alternate method will be used to obtain the frequency response for a specified airspeed.

Throughout the following analysis, with the exception of one parameter of particular interest, all other system parameters will be assumed constant. Let ω_r and ω_i respectively represent the real and imaginary parts of the precessional angular velocity, such that $\omega = \omega_r + i\omega_i$. When substituted into equation (20) from Chapter 2, one obtains

$$e^{i(kz + n\theta - \omega t)} = e^{\omega_i t} \cdot e^{i(kz + n\theta - \omega_r t)} \quad (A1)$$

As evident, for ω_i values greater than zero, the perturbation amplitude increases as ω_i increases. The objective of this analysis is to find the maximum value of ω_i for a specified velocity, such that the corresponding ω_r will be

the precessional angular velocity (or frequency) response desired. Equation (50) from Chapter 2 can be written in the following form

$$\frac{J_{n-1}(RK)}{J_n(RK)} = \frac{n}{RK} \left(1 + \frac{2 \omega_o}{\omega - n \omega_o - k W_c} \right) \quad (A2)$$

In equation (A2), n will be assigned the value one. The justification for this assumption is based on observations in the present work and results of Chanaud's work. Chanaud [17] tested a vortex tube submerged in water. He injected air into the vortex tube to observe the air bubble flow pattern throughout. He noted the formation of a bubble line, and that the line did not assume a helical form. This can be interpreted to imply that the perturbations are constant along a simple helix, and this would be the case for n equated to one in equation (A2). Thus, providing parameters ω_o , W_c , k and R are known, equation (A2) becomes

$$\frac{J_o(RK)}{J_1(RK)} = \frac{1}{RK} \left(1 + \frac{2 \omega_o}{\omega - \omega_o - k W_c} \right) . \quad (A3)$$

However from equation (40) from Chapter 2 with $n = 1$, K can be written as

$$K = \frac{k \sqrt{4 \omega_o^2 - (\omega - \omega_o - k W_c)^2}}{\omega - \omega_o - k W_c} \quad (A4)$$

Substituting equation (A4) into equation (A3), the right hand side (R. H. S.) of equation (A3) becomes

$$\text{R. H. S.} = \frac{1}{\text{RK}} \frac{\omega - \omega_0 - k W_c}{\sqrt{4 \omega_0^2 - (\omega - \omega_0 - k W_c)^2}} \left(1 + \frac{2 \omega_0}{\omega - \omega_0 - k W_c} \right)$$

or

$$\text{R. H. S.} = \frac{1}{\text{RK}} \frac{\omega + \omega_0 - k W_c}{\sqrt{4 \omega_0^2 - (\omega - \omega_0 - k W_c)^2}} \quad (\text{A5})$$

Noting, however, that the left hand side (L. H. S.) of equation (A3) is

$$\text{L. H. S.} = \frac{J_0(\text{RK})}{J_1(\text{RK})}$$

and since

$$J_0(x) = 1 - \frac{x^2}{2^2(1!)^2} + \frac{x^4}{2^4(2!)^2} - \frac{x^6}{2^6(3!)^2} + \dots \quad (\text{A6})$$

and

$$J_1(x) = \frac{x}{2} - \frac{x^3}{2^3 \cdot 1! \cdot 2!} + \frac{x^5}{2^5 \cdot 2! \cdot 3!} - \frac{x^7}{2^7 \cdot 3! \cdot 4!} + \dots \quad (\text{A7})$$

the L. H. S. of equation (A3) can then be expressed approximately as

$$\text{L.H.S.} \approx \frac{1 - \frac{(RK)^2}{2^2(1!)^2} + \frac{(RK)^4}{2^4(2!)^2} - \frac{(RK)^6}{2^6(3!)^2}}{\frac{RK}{2} - \frac{(RK)^3}{2^3(1!)(2!)} + \frac{(RK)^5}{2^5(2!)(3!)}} \quad (\text{A8})$$

An analysis of the errors due to replacing the exact expression by equation (A8) may be found in Appendix D.

Substituting equation (A4) into equation (A8) and simplifying, one obtains

$$\begin{aligned} \text{L.H.S.} \approx & \{(\omega - \omega_0 - kW_c)^6 - \frac{R^2 K^2}{4} [4\omega_0^2 - (\omega - \omega_0 - kW_c)^2]\} (\omega - \omega_0 - kW_c)^4 + \frac{R^4 K^4}{64} [4\omega_0^2 - (\omega - \omega_0 - kW_c)^2]^2 (\omega - \omega_0 - kW_c)^2 - \frac{R^6 K^6}{2304} [4\omega_0^2 - (\omega - \omega_0 - kW_c)^2]^3 \} / \{ \frac{RK}{2} [4\omega_0^2 - (\omega - \omega_0 - kW_c)^2]^{\frac{1}{2}} (\omega - \omega_0 - kW_c)^5 - \frac{R^3 K^3}{16} [4\omega_0^2 - (\omega - \omega_0 - kW_c)^2]^{\frac{3}{2}} (\omega - \omega_0 - kW_c)^3 + \frac{R^5 K^5}{384} [4\omega_0^2 - (\omega - \omega_0 - kW_c)^2]^{\frac{5}{2}} (\omega - \omega_0 - kW_c) \} \quad (\text{A9}) \end{aligned}$$

By introducing the following coefficients:

$$\begin{aligned} C_0 &= \omega_0 + kW_c \\ C_1 &= 4\omega_0^2 - C_0^2 \\ C_2 &= RK/2 \end{aligned}$$

$$\begin{aligned}
C_3 &= R^2 K^2 / 4 = C_2^2 \\
C_4 &= R^3 K^3 / 16 = C_2^3 / 2 \\
C_5 &= R^4 K^4 / 64 = C_2^4 / 4 \\
C_6 &= R^5 K^5 / 384 = C_2^5 / 12 \\
C_7 &= R^6 K^6 / 2304 = C_2^6 / 36 \\
C_8 &= \omega_0 - k W_c
\end{aligned}
\tag{A10}$$

Equations (A9) and (A5) become respectively,

$$\begin{aligned}
\text{L.H.S.} &= \{(\omega - C_0)^6 - C_3(C_1 + 2C_0\omega - \omega^2)(\omega - C_0)^4 + \\
&C_5(C_1 + 2C_0\omega - \omega^2)^2(\omega - C_0)^2 - C_7(C_1 + 2C_0\omega - \\
&\omega^2)^3\} / \{C_2(\omega - C_0)^5(C_1 + 2C_0\omega - \omega^2)^{\frac{1}{2}} - \\
&C_4(\omega - C_0)^3(C_1 + 2C_0\omega - \omega^2)^{3/2} + C_6(\omega - C_0) \\
&(C_1 + 2C_0\omega - \omega^2)^{5/2}\} \quad , \tag{A11}
\end{aligned}$$

$$\text{R.H.S.} = \frac{1}{2C_2} \frac{\omega + C_8}{(C_1 + 2C_0\omega - \omega^2)^{\frac{1}{2}}} \tag{A12}$$

Equating equations (A11) and (A12), and multiplying both sides by $(C_1 + 2C_0\omega - \omega^2)^{\frac{1}{2}}$, one obtains

$$\frac{1}{2C_2} (\omega + C_8) = \{(\omega - C_0)^6 - C_3(C_1 + 2C_0\omega - \omega^2)(\omega -$$

$$\begin{aligned}
& C_0)^4 + C_5(C_1 + 2C_0 \omega - \omega^2)^2(\omega - C_0)^2 - C_7(C_1 + 2C_0\omega - \\
& \omega^2)^3 \} / \{ C_2(\omega - C_0)^5 - C_4(\omega - C_0)^3(C_1 + 2C_0\omega - \\
& \omega^2) + C_6(\omega - C_0)(C_1 + 2C_0\omega - \omega^2)^2 \}. \quad (A13)
\end{aligned}$$

Simplifying and rearranging according to the power of ω , one obtains

$$\begin{aligned}
F(\omega) &= C_{39} \omega^6 + C_{40} \omega^5 + C_{41} \omega^4 + C_{42} \omega^3 + C_{43} \omega^2 + \\
& C_{44} \omega + C_{45} = 0, \quad (A14)
\end{aligned}$$

where the intermediate C constants in the development are as follows.

$$\begin{aligned}
C_9 &= 9C_0^2 - C_1 \\
C_{10} &= 3C_0C_1 - 7C_0^3 \\
C_{11} &= 2C_0^4 - 3C_0^2C_1 \\
C_{12} &= 8C_0^2 - 2C_1 \\
C_{13} &= 4C_0C_1 - 4C_0^3 + 2C_1 \\
C_{14} &= C_1^2 - 4C_0^2C_1 \\
C_{15} &= 14C_0^2 - C_1 \\
C_{16} &= 4C_0C_1 - 16C_0^3 \\
C_{17} &= 9C_0^4 - 6C_0^2C_1
\end{aligned}$$

$$C_{18} = 4C_o^3C_1 - 2C_o^5$$

$$C_{19} = 9C_o^2 + 4C_o - 2C_1$$

$$C_{20} = 8C_oC_1 - 8C_o^2 - 4C_o^3$$

$$C_{21} = 4C_o^3 - 10C_o^2C_1 + C_1^2$$

$$C_{22} = 4C_o^3C_1 - 2C_oC_1^2$$

$$C_{23} = 12C_o^2 - 3C_1$$

$$C_{24} = 12C_oC_1 - 8C_o^3$$

$$C_{25} = 3C_1^2 - 12C_o^2C_1$$

$$C_{26} = C_2 + C_4 + C_6$$

$$C_{27} = 1 + C_3 + C_5 + C_7$$

$$C_{28} = 10C_o^2C_2 + C_4C_9 + C_6C_{12}$$

$$C_{29} = 15C_o^2 + C_3C_{15} + C_5C_{19} + C_7C_{23}$$

$$C_{30} = -10C_o^3C_2 + C_4C_{10} + C_6C_{13} + 10C_o^2C_2C_8 + C_4C_8C_9 + \\ C_6C_8C_{12}$$

$$C_{31} = 20C_o^3 - C_3C_{16} - C_5C_{20} - C_7C_{24}$$

$$C_{32} = 5C_o^4C_2 + C_4C_{11} + C_6C_{14} - 10C_o^3C_2C_8 + C_4C_8C_{10} + \\ C_6C_8C_{13}$$

$$C_{33} = C_3C_{17} - 15C_o^4 - C_5C_{21} - C_7C_{25}$$

$$C_{34} = C_o^4C_4 - C_1C_6$$

$$C_{341} = C_0^4 C_2 (5C_8 - C_0)$$

$$C_{35} = C_4 C_8 C_{11} + C_6 C_8 C_{14}$$

$$C_{36} = 6C_0^5 - C_3 C_{18} - C_5 C_{22} + 6C_0 C_1^2 C_7$$

$$C_{37} = C_0^2 C_4 - C_1 C_6$$

$$C_{38} = -C_0^4 + C_0^2 C_1 C_3 - C_1^2 C_5$$

$$CC = 1/C_2$$

$$C_{39} = \frac{CC}{2} C_{26} - C_{27}$$

$$C_{40} = \frac{CC}{2} C_{26} (C_8 - 5C_0) + 6C_0 C_{27}$$

$$C_{41} = \frac{CO}{2} C_{28} - 5C_0 C_8 C_{26} - C_{29}$$

$$C_{42} = \frac{CC}{2} C_{30} + C_{31}$$

$$C_{43} = \frac{CC}{2} C_{32} + C_{33}$$

$$C_{44} = \frac{CC}{2} (C_0 C_1 C_{34} + C_{341} + C_{35}) + C_{36}$$

$$C_{45} = \frac{CC}{2} (C_0 C_1 C_8 C_{37} - C_0^5 C_2 C_8) + C_0^2 C_{38} + C_1^3 C_7.$$

Equation (51) has therefore been transformed to equation (A14) a sixth order polynomial in ω having real coefficients C_{39} through C_{45} . As stated earlier for a specified air-speed, one desires the maximum value of ω_i among the six roots of the equation. The corresponding ω_r is the frequency response. The solution to equation (A14) will be obtained through use of computer program available at

National Aeronautics and Space Administration, Langley Research Center. The subroutine of this program, named RPOLY, is a simple program developed to determine the complex roots of an equation by a three-stage variable-shift technique [40, 41]. The distinct advantage of this subroutine is that it does not require any initial estimates of the roots.

The derivation of expressions for the upstream fluid angular velocity ω_0 and the constant mean axial flow velocity W_c is given in Appendix B. The computing procedure and sample programming are given in Appendix C.

APPENDIX B

THE DERIVATION OF THE UPSTREAM FLUID ANGULAR VELOCITY

ω_o AND THE CONSTANT MEAN AXIAL FLOW VELOCITY W_c

The values of the upstream fluid angular velocity ω_o and the downstream constant mean axial flow velocity W_c are strongly depended upon the design of both the vortex tube and swirler flow generator.

The derivation will be based on the parameters listed in Table 1 of Chapter 3. However, prior to the derivation each parameter will be discussed separately.

The combination of vortex tube and swirler used in the analysis is shown in the Fig. B.1. The cross-sectional view of A-A is shown in the Fig. B.2. The net fluid passage area as shown in Fig. B.2 is

$$A_{net} = \frac{\pi}{4} (D_1^2 - D_2^2) - n_1 h \frac{D_1 - D_2}{2} \quad (B1)$$

where n_1 is the number of flutes in the swirler, and h is the width of each flute. It is apparent that the net area at section B-B is

$$B_{net} = \frac{\pi D_3^2}{4} \quad (B2)$$

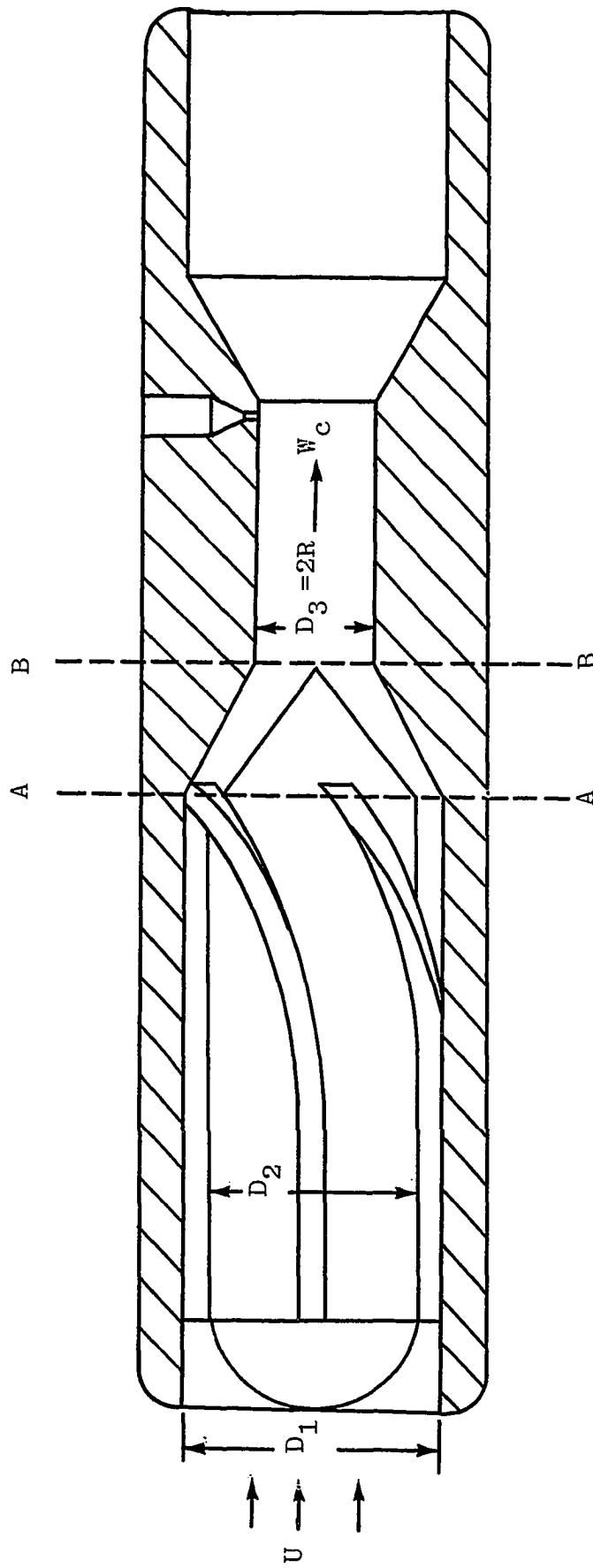


Fig. B.1 The description and cross-sectional view of vortex tube and swirler.

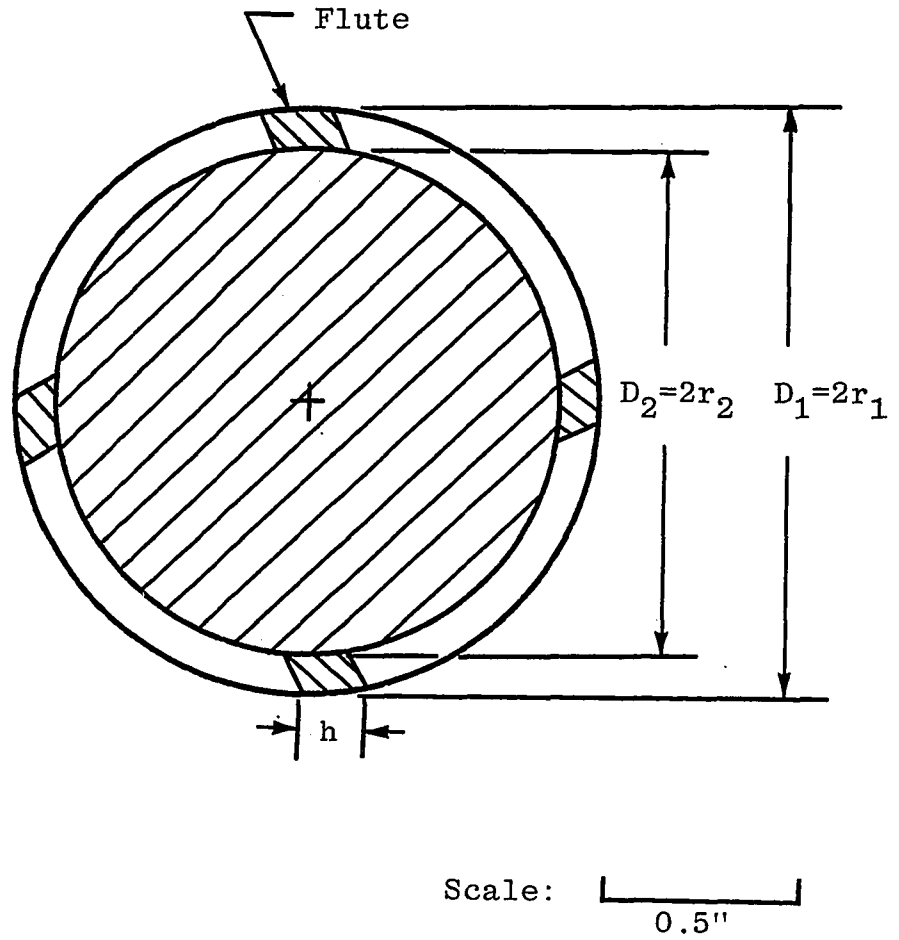


Fig. B.2 The cross-sectional view of section A-A.

The fluid velocity or airspeed U leaving section A-A at an angle of α , as shown below is separated into axial and tangential velocities U_a and U_t respectively.



Due to the complexity in geometry, an accurate analysis is very difficult to obtain. Thus, an approximation, which is close to reality will be derived.

Since the fluid passage or gap between the vortex tube wall and swirler is so small, it is assumed here that the net area, A_{net} , at section A-A be replaced by a circular ring with the same outside radius, r_1 , but different inside radius, named equivalent radius $r_{e,2}$ which is larger than the original radius r_2 . This equivalent radius $r_{e,2}$ will be determined first and then be used later as a lower limit in the calculation of conservation of angular momentum at section A-A. Hence this circular ring will not include the cross-section areas of flutes. Thus, one can find this equivalent radius $r_{e,2}$ by equating the net area A_{net} with this new circular ring area as

$$A_{net} = \pi (r_1^2 - r_{e,2}^2)$$

or

$$r_{e,2} = \sqrt{r_1^2 - \frac{A_{net}}{\pi}} \quad (B3)$$

where A_{net} was defined in equation (B1).

Due to the converging geometry between sections, the fluid angular velocity at section A-A is different than that at section B-B. The conservation of angular momentum can be expressed as

$$\int_{r_{e,2}}^{r_1} \omega_A r^2 dr = \int_0^R \omega_O r^2 dr \quad (B4)$$

where ω_A and ω_O are constant fluid angular velocities at section A-A and B-B respectively.

In the forced vortex flow the tangential velocity is equal to the product of the constant angular velocity and the radius. Since the spacing between the core of the swirler and inner wall of the vortex tube is extremely small, the radius will be considered to be the average of r_1 and $r_{e,2}$. Thus, the constant angular velocity ω_A can be written as

$$\omega_A = \frac{U_t}{\frac{r_1 + r_{e,2}}{2}}$$

or

$$\omega_A = \frac{2 U \sin\alpha}{r_1 + r_{e,2}} \quad (B5)$$

Note, however, that $U_t = U \sin \alpha$.

And therefore equation (B4) becomes

$$\int_{r_{e,2}}^{r_1} \frac{2 U \sin \alpha}{r_1 + r_{e,2}} r^2 dr = \int_0^R \omega_o r^2 dr . \quad (B6)$$

The value of the constant angular velocity ω_o , at section B-B, can then shown to be

$$\omega_o = \frac{2 U \sin \alpha}{R^3} \frac{r_1^3 - r_{e,2}^3}{r_1 + r_{e,2}} . \quad (B7)$$

Hence, for a given airspeed U and swirler geometry there is one value for ω_o .

The downstream constant mean axial velocity W_c is obtained by considering the continuity of mass for sections A-A and B-B. The conservation of mass requires, assuming constant ρ

$$U_a A_{net} = W_c B_{net}, \quad (B8)$$

where U_a is $U \cos \alpha$ and W_c is the constant mean axial velocity. Thus, the constant mean axial velocity W_c can be written as

$$W_c = U \cos \alpha \frac{A_{net}}{B_{net}} . \quad (B9)$$

APPENDIX C

COMPUTING PROCEDURE AND PROGRAMMING

Equation (A14) of Appendix A can be easily solved by use of the computer, and the step by step procedure is given below.

1. Input the physical parameters D_1 , D_2 , D_3 , n_1 , α and calculate equations (B1), (B2), (B3), (B7) and (B9) derived in Appendix B.
2. Set airspeed equal to zero kilometer per hour and calculate all the polynomial coefficients listed in Appendix A.
3. Find the roots of the polynomial by calling the subroutine RPOLY.
4. Separate the real and imaginary parts of the roots.
5. Find the maximum value of imaginary part of the root ω_i , which gives the maximum amplitude, and the corresponding real part of root ω_r .
6. Calculate the frequency response and Strouhal number, St .
7. Print out the airspeed and frequency response. Then increase the airspeed and repeat the procedure until the airspeed reaches 321.9 km/hr (or 200 mph).

8. Repeat the above procedure for different vortex tube configurations and swirler designs.

The flow diagram for the above procedure is shown in Fig. C.1. All the data were plotted by using NASA CDC 6000 series CalComp model 765 plotter. The NASA Langley subroutine INFOPLT was used to generate the plot for specified information. The flow diagram used in obtaining the plot is shown in Fig. C.2. The complete computer program is listed after Fig. C.2 on pages 149-156. The program only involved Sensor 4. For the other indicators, only D_2 and D_3 need to be changed.

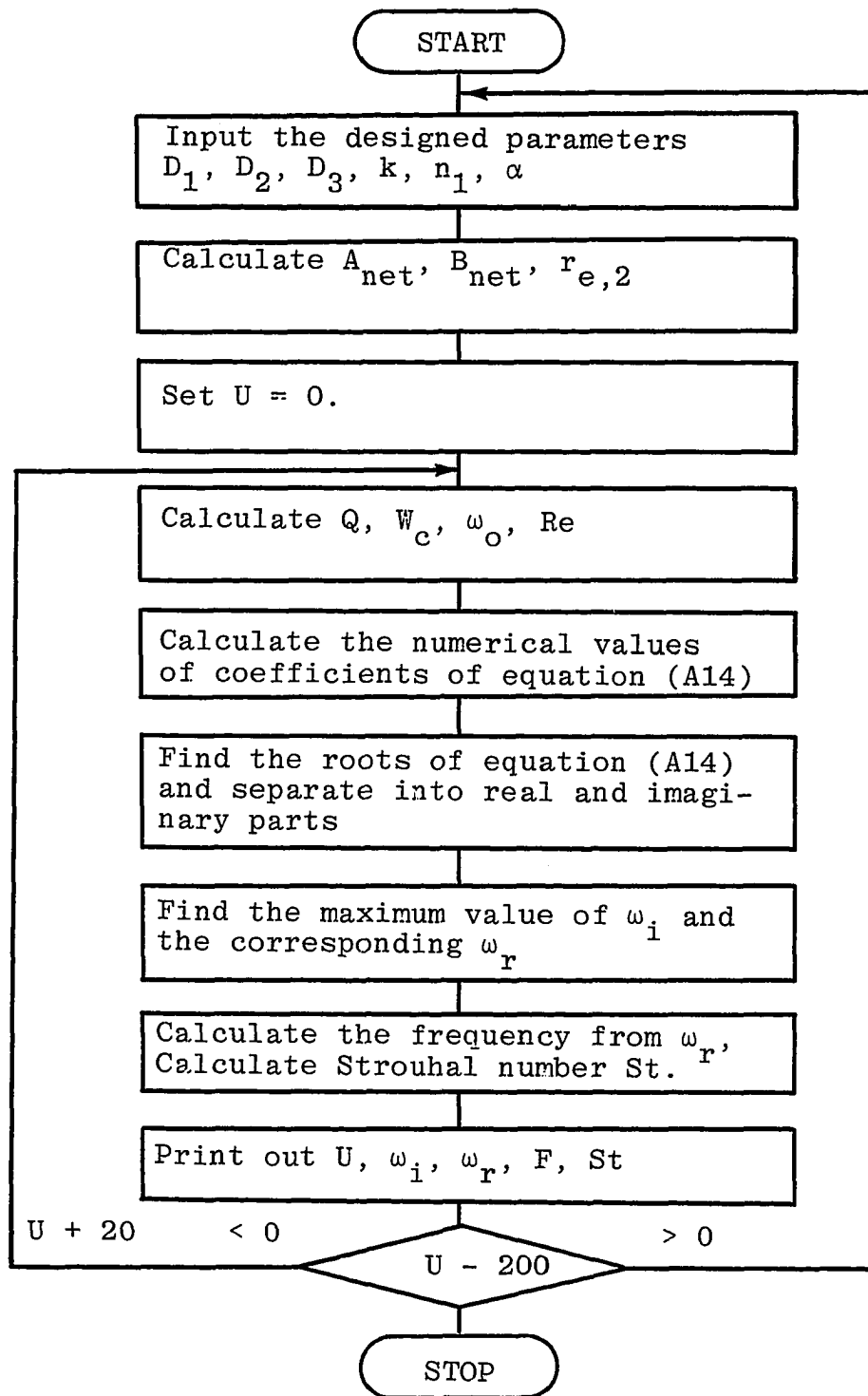


Fig. C.1 Flow diagram for calculating the frequency at various true airspeed.

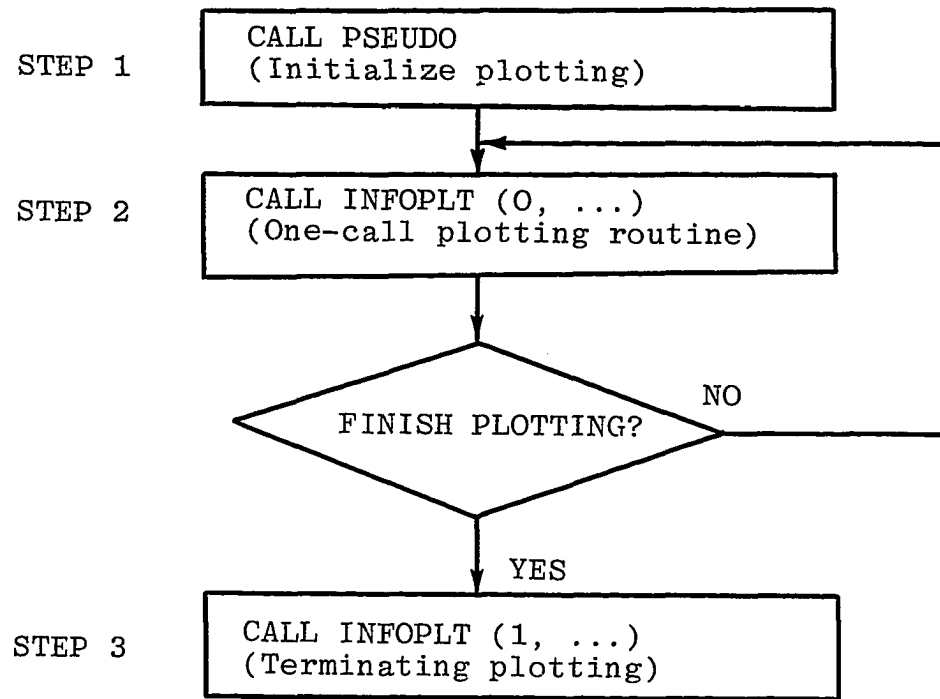


Fig. C. 2 Flow diagram for getting the plots.

```
PROGRAM WHISTL (INPUT,OUTPUT,TAPE5=INPUT,TAPE6=OUTPUT)
DIMENSION VEL(11),WC(11),RE(11),ST(11),UU(11),WCK(11)
DIMENSION ALPHAD(5),N1(5),FREQ(11),XO(11),U(11)
DIMENSION ROOT1(6,2)
DIMENSION COEFF(7)
COMPLEX ROOT(6)
C NUMBER OF POINTS TO BE CALCULATED
NN=11
C DEFINE WAVENUMBER K
CK=1.
C CHANGE THE VALUES OF K
DO 24 K=1,4
MM=6
WRITE(MM,1)
1 FORMAT(1H1)
C DEGREE OF THE POLYNOMIAL
IDEGRE=6
C DEFINE THE PARAMETERS FOR THE INDICATOR
D1=0.745/12.
D2=0.6/12.
D3=0.25/12.
R=D3/2.
H=0.1/12.
PI=3.1415927
XNU=160.OE-06
```

```

C   AN INTEGER REPRESENTS THE PERTURBATIONS ARE CONSTANT
C   ALONG A SIMPLE HELIX
      N=1
      DO 23 IJ=1,3
        XIJ=IJ+2
C   DESIGNED NUMBER OF FLUTES ON THE SWIRLER
      DO 22 II=1,3
        N1(II)=II+1
        CKW=CK/(2.*PI)
        WRITE(MM,2) CK,CKW
2   FORMAT(5X,*THE WAVENUMBER K=*,E10.3,10X,*THE WAVELENG
      1TH=K/(2.PI)=*,E10.3////)
C   DESIGNED EXIT ANGLES ON THE SWIRLER
      ALPHAD(IJ)=XIJ*15.
      ALPHA=ALPHAD(IJ)*PI/180.
      AREAA=PI/4.*(D1**2.-D2**2.)-N1(II)*H*(D1-D2)/2.
      AREAB=PI/4.*D3**2
C   EQ.(B3)
      RE2=SQRT((D1/2.)**2-(AREAA/PI))
      WRITE(MM,3)D1,D2,D3,H,N1(II),AREAA,AREAB
3   FORMAT(5X,*D1=*,F10.5/5X,*D2=*,F10.5/5X,*D3=*,F10.5//
      15X,*H=*,F10.5/5X,*HOW MANY FLUTES IN THE SWIRLER?*,I3
      2/5X,*NET AREA AT SECTION A-A=*,F10.5/5X,*NET AREA AT
      3SECTION B-B=*,F10.5//)
      WRITE(MM,4)N,ALPHAD(IJ)

```

```
4 FORMAT(5X,*N=*,I2/5X,*EXIT ANGLE OF SWIRLER=*,F5.1,2X,
1*DEGREES*//)
```

```
U(1)=0.0
```

```
C***** CHANGE VELOCITY*****
```

```
DO 21 J=1,11
```

```
C VELOCITY FOOT PER SECOND
```

```
VEL(J)=U(J)*5280./3600.
```

```
C VELOCITY KILOMETER PER HOUR
```

```
UU(J)=U(J)*1.60935
```

```
C AXIAL MEAN VELOCITY IN Z-DIRECTION(FT/SEC)
```

```
WC(J)=VEL(J)*COS(ALPHA)*AREAA/AREAB
```

```
C IN KILOMETER PER HOUR
```

```
WCK(J)=WC(J)*0.304801E-03*3600.
```

```
C REYNOLDS NUMBER BASED ON MEAN AXIAL VELOCITY
```

```
RE(J)=WC(J)*D3/XNU
```

```
C UPSTREAM ANGULAR VELOCITY AT SECTION AA AS DEFINED IN
```

```
C EQ(B7)
```

```
XO(J)=2.*VEL(J)*SIN(ALPHA)*((D1/2.)**3.-RE2**3.)/(R**
13.*(D1/2.+RE2))
```

```
WRITE(MM,5)U(J),VEL(J),UU(J),WC(J),WCK(J),RE(J),XO(J)
```

```
5 FORMAT(5X,*U=*,F7.1,2X,*MILES PER HOUR*,5X,*OR*,2X,F7
```

```
1.1,2X,*FOOT PER SECOND*,5X,*OR*,2X,F7.1,2X,*KILOMETER
```

```
2 PER HOUR*/5X,*WC=*,F7.1,2X,*FOOT PER SECOND*,5X,*OR*,
```

```
32X,F7.1,2X,*KILOMETER PER HOUR*/5X,*REYNOLDS NUMBER=*
```

```
4,F8.1/5X,*ANGULAR VELOCITY AT ENTRANCE=*,F8.1//)
```

```
CO=XO(J)+CK*WC(J)
```

```

C1=4.*XO(J)**2.-CO**2.
C2=R*CK/2.
C3=C2**2.
C4=C2**3./2.
C5=C2**4./4.
C6=C2**5./12.
C7=C2**6./36.
C8=XO(J)-CK*WC(J)
C9=9.*CO**2.-C1
C10=3.*CO*C1-7.*CO**3.
C11=2.*CO**4.-3.*CO**2.*C1
C12=8.*CO**2.-2.*C1
C13=4.*CO*C1-4.*CO**3.+2.*C1
C14=C1**2.-4.*CO**2.*C1
C15=14.*CO**2.-C1
C16=4.*CO*C1-16.*CO**3.
C17=9.*CO**4.-6.*CO**2.*C1
C18=4.*CO**3.*C1-2.*CO**5.
C19=9.*CO**2.+4.*CO-2.*C1
C20=8.*CO*C1-8.*CO**2.-4.*CO**3.
C21=4.*CO**3.-10.*CO**2.*C1+C1**2.
C22=4.*CO**3.*C1-2.*CO*C1**2.
C23=12.*CO**2.-3.*C1
C24=12.*CO*C1-8.*CO**3.
C25=3.*C1**2.-12.*C1*CO**2.
C26=C2+C4+C6

```

$$C27=1.+C3+C5+C7$$

$$C28=10.*CO**2.*C2+C4*C9+C6*C12$$

$$C29=15.*CO**2.+C3*C15+C5*C19+C7*C23$$

$$C30=-10.*CO**3.*C2+C4*C10+C6*C13+10.*CO**2.*C2*C8+C4*1C8*C9+C6*C8*C12$$

$$C31=20.*CO**3.-C3*C16-C5*C20-C7*C24$$

$$C32=5.*CO**4.*C2+C4*C11+C6*C14-10.*CO**3.*C2*C8+C4*C81*C10+C6*C8*C13$$

$$C33=C3*C17-15.*CO**4.-C5*C21-C7*C25$$

$$C34=CO**2.*C4-C1*C6$$

$$C341=CO**4.*C2*(5.*C8-CO)$$

$$C35=C4*C8*C11+C6*C8*C14$$

$$C36=6.*CO**5.-C3*C18-C5*C22+6.*CO*C1**2*C7$$

$$C37=CO**2.*C4-C1*C6$$

$$C38=-CO**4.+CO**2.*C1*C3-C1**2.*C5$$

$$CC=1./C2$$

$$C39=(CC*C26)/2.-C27$$

$$C40=(CC*C26/2.)*(C8-5.*CO)+6.*CO*C27$$

$$C41=CC/2.*C28-5.*CO*C8*C26)-C29$$

$$C42=CC*C30/2.+C31$$

$$C43=CC*C32/2.+C33$$

$$C44=CC/2.*(CO*C1*C34+C35+C341)+C36$$

$$C45=CC/2.*(CO*C1*C8*C37-CO**5.*C2*C8)+CO**2.*C38+C1**13.*C7$$

C COEFFICIENTS OF THE POLYNOMIAL

$$COEFF(1)=C39$$

```

      COEFF(2)=C40
      COEFF(3)=C41
      COEFF(4)=C42
      COEFF(5)=C43
      COEFF(6)=C44
      COEFF(7)=C45
      WRITE(MM,6) (COEFF(I),I=1,7)
6  FORMAT(5X,7(E12.5,2X)//)
C  FIND THE COMPLEX ROOTS OF THE POLYNOMIAL
      CALL RPOLY (IDEGRE,COEFF, ROOT, IERR)
      WRITE(MM,7) IERR, IDEGRE
7  FORMAT(5X,*IERR=*,I2,5X,I5//)
      WRITE(MM,8)
8  FORMAT(11X,*REAL PART OF ROOT*,3X,*IMAG PART OF ROOT*
1,11X,*ROOT NUMBER*/)
      DO 9 I=1,IDEGRE
9  WRITE(MM,10) ROOT(I),I
10 FORMAT(5X,2E20.5,I20)
C  SEPARATE THE REAL AND IMAGINARY PARTS OF ROOT
      DO 11 M=1,6
      ROOT1(M,1)=REAL(ROOT(M))
      ROOT1(M,2)=AIMAG(ROOT(M))
11 CONTINUE
C  FIND THE MAXIMUM IMAGINARY PART OF ROOT AMONG THOSE
C  ROOTS
      AMAX=ROOT1(1,2)

```

```

    IMAX=1
    DO 12 MN=2,6
    IF(ROOT1(MN,2).LE.AMAX) GO TO 12
    AMAX=ROOT1(MN,2)
    IMAX=MN
12 CONTINUE
C   DESIRED FREQUENCY RESPONSE
    FREQ(J)=ROOT1(IMAX,1)/(2.*PI)/1000.
    IF(J-1) 13,13,14
13 RK=0.
    GO TO 15
14 OMEGA=SQRT(AMAX**2.+ROOT1(IMAX,1)**2.)
    XK1=OMEGA-1.*XO(J)-CK*WC(J)
    XK2=SQRT(4.*XO(J)**2.-(XK1**2.))
    XK3=CK*XK2
    XK=XK3/XK1
    RK=R*XK
15 CONTINUE
    WRITE(MM,16) RK
16 FORMAT(5X,*THE ARGUMENT OF THE BESSEL FUNCTION =*,E12
    1.5//)
    IF(J-1) 17,17,18
17 ST(1)=0.0
    GO TO 19
C   CALCULATE THE CORRESPONDING STROUHAL NUMBER

```

```
18 ST(J)=FREQ(J)*1000.*D3/WC(J)
19 CONTINUE
    WRITE(MM,20) ROOT1(IMAX,1),ROOT1(IMAX,2),FREQ(J),ST(J)
20 FORMAT(5X,*THE DESIRED SOLUTIONS ARE*/5X,2E20.5/5X,*TH
    1E CORRESPONDING FREQUENCY AT THIS VELOCITY IS*,E15.5,2
    2X,*KHZ*/5X,*THE STROUHAL NUMBER IS*,E15.5/////))
    U(J+1)=U(J)+20.
21 CONTINUE
    WRITE(MM,1)
22 CONTINUE
23 CONTINUE
    CK=CK+2.
24 CONTINUE
    STOP
    END
```

APPENDIX D

ERROR ANALYSIS

In order to effectively compare the theoretical, numerical and experimental results an error analysis was undertaken. Throughout this research endeavor and in particular in the development of the theoretical aspects of the problem it became evident that certain simplifications would be necessary. As a result of these simplifications errors might have possibly been introduced.

The deviation of the theoretical from the experimental results, due to neglecting viscous effects, variable fluid properties or compressibility effects in the development of the theory, has already been discussed in Chapter 5. In the derivation of the upstream fluid angular velocity ω_o and the constant downstream mean axial velocity W_c as presented in Appendix B, the error introduced is considered insignificant. The complexity of the flow pattern between sections A-A and B-B rendered a quantitative error analysis virtually impossible. The derivations, however, were believed to be close enough to reality so that the errors could be considered extremely small compared with the overall performance features.

The most significant errors are found in the derivation of equation (A14), where the Bessel function J_0 and J_1 were evaluated on the basis of equation (A6) and (A7). It is, however, very difficult to solve the problem as both arguments of J_0 and J_1 are complex numbers. In equation (A8), J_0 took into consideration the first four terms of equation (A6) whereas J_1 took into consideration the first three terms of equation (A7). It is the purpose here to investigate the errors introduced from the elimination of the higher terms in the Bessel functions J_0 and J_1 . The actual values of J_0 and J_1 will be calculated by calling the subroutine COMBES provided by National Aeronautic and Space Administration at Langley Research Center. This subroutine COMBES is the only known source available for computing the Bessel functions $J_w(z)$ and $Y_w(z)$ for complex orders and arguments. Note that the convergence of equations (A6) and (A7) is premised on the requirement that the absolute value of the argument of the Bessel function must be less than one. The argument of the Bessel function will be derived first and its absolute value evaluated before proceeding with the derivation.

It is necessary to first determine the real and imaginary expressions for the argument RK. Rewrite equation (40) in Chapter 2 as

$$K = \frac{k \sqrt{4\omega_0^2 - (\omega - n\omega_0 - kW_c)^2}}{\omega - n\omega_0 - kW_c}, \quad (D1)$$

then the expression for RK becomes

$$RK = Rk \frac{\sqrt{4\omega_0^2 - (n\omega_0 + kW_c)^2 + 2(n\omega_0 + kW_c)\omega - \omega^2}}{\omega - (n\omega_0 + kW_c)} \quad (D2)$$

Let $A_1 = n\omega_0 + kW_c$, $A_2 = 4\omega_0^2 - A_1^2$ and $A_3 = Rk$, and substitute into equation (D2), which then becomes

$$RK = A_3 \frac{\sqrt{A_2 + 2A_1\omega - \omega^2}}{\omega - A_1} \quad (D3)$$

Now assume

$$\omega = \omega_r + i\omega_i \quad (D4)$$

where ω_r and ω_i are respectively the real and imaginary parts of precessional angular velocity.

Substituting equation (D4) into equation (D3) and let

$$A_4 = A_3 / [(\omega_r - A_1)^2 + \omega_i^2] \quad (D5)$$

$$A_5 = A_2 + 2A_1\omega_r - \omega_r^2 + \omega_i^2 \quad (D6)$$

$$A_6 = 2A_1\omega_i - 2\omega_r\omega_i \quad (D7)$$

$$A_7 = \omega_r - A_1 \quad (D8)$$

then one obtains

$$RK = A_4 [(A_7 - i\omega_i)(A_5 + iA_6)^{\frac{1}{2}}]. \quad (D9)$$

However, it is desirable to convert the expression $(A_5 + iA_6)^{\frac{1}{2}}$ into a simple $X + iY$ form, where X and Y are real numbers, so that the argument RK can be rearranged into a convenient form for later use.

Noting that Z^α can be expressed as

$$Z^\alpha = e^{\alpha \ln(Z)} = e^{\alpha \ln(Z)} = e^{\alpha [\ln(Z + i(\theta_1 + 2m\pi))]} \quad (D10)$$

where $Z = x + i y$, α is either a constant or a complex number, $|Z| = (x^2 + y^2)^{\frac{1}{2}}$, and θ_1 is the principle value of angle defined by $\theta_1 = \tan^{-1}(y/x)$. An appropriate selection of θ_1 allows $(A_5 + iA_6)^{\frac{1}{2}}$ to be written as

$$(A_5 + iA_6)^{\frac{1}{2}} = e^{\frac{1}{2}} [\ln(A_5^2 + A_6^2)^{\frac{1}{2}} + i \theta_1] \quad (D11)$$

where $\theta_1 = \tan^{-1}(A_6/A_5)$, or

$$(A_5 + iA_6)^{\frac{1}{2}} = (A_5^2 + A_6^2)^{\frac{1}{4}} (\cos \frac{\theta_1}{2} + i \sin \frac{\theta_1}{2}) \quad (D12)$$

Again let

$$A_8 = (A_5^2 + A_6^2)^{\frac{1}{4}} \quad (D13)$$

$$A_9 = A_7 \cos \frac{\theta_1}{2} + \omega_i \sin \frac{\theta_1}{2} \quad (D14)$$

$$A_{10} = A_7 \sin \frac{\theta_1}{2} - \omega_i \cos \frac{\theta_1}{2} \quad (D15)$$

$$A_{11} = A_4 A_8 A_9 \quad (D16)$$

$$A_{12} = A_4 A_8 A_{10} \quad (D17)$$

then equation (D9) becomes

$$RK = A_{11} + i A_{12} \quad (D18)$$

where the constant A_{11} and A_{12} are real and imaginary parts of the argument. The subroutine COMBES can then be used to evaluate the actual values of Bessel functions J_0 and J_1 for each argument of RK.

Now substituting equation (D18) into equations (A6) and (A7), one obtains

$$J_0(\text{RK}) \approx 1 - \frac{1}{4} (A_{11} + i A_{12})^2 + \frac{1}{64} (A_{11} + i A_{12})^4 - \frac{1}{2304} (A_{11} + i A_{12})^6 \quad (\text{D19})$$

and

$$J_1(\text{RK}) \approx \frac{1}{2} (A_{11} + i A_{12}) - \frac{1}{16} (A_{11} + i A_{12})^3 + \frac{1}{384} (A_{11} + i A_{12})^5 \quad (\text{D20})$$

Expanding the power series, simplifying and separating the real and imaginary parts, $J_0(\text{RK})$ becomes

$$J_0(\text{RK}) \approx [1 - \frac{1}{4} (A_{11}^2 - A_{12}^2) + \frac{1}{64} (A_{11}^4 - 6A_{11}^2 A_{12}^2 + A_{12}^4) - \frac{1}{2304} (A_{11}^6 - 15A_{11}^4 A_{12}^2 + 15A_{11}^2 A_{12}^4 - A_{12}^6)] + i [-\frac{1}{2} A_{11} A_{12} + \frac{1}{64} (4A_{11}^3 A_{12} - 4A_{11} A_{12}^3) - \frac{1}{2304} (6A_{11}^5 A_{12} - 20A_{11}^3 A_{12}^3 + 6A_{11} A_{12}^5)] \quad (\text{D21})$$

and $J_1(\text{RK})$ becomes

$$J_1(\text{RK}) \approx [\frac{1}{2} A_{11} - \frac{1}{16} (A_{11}^3 - 3A_{11} A_{12}^2) + \frac{1}{384} (A_{11}^5 - 10A_{11}^3 A_{12}^2 + 5A_{11} A_{12}^4)] + i [\frac{1}{2} A_{12} - \frac{1}{16} (3A_{11}^2 A_{12} - A_{12}^3) + \frac{1}{384} (5A_{11}^4 A_{12} - 10A_{11}^2 A_{12}^3 + A_{12}^5)] \quad (\text{D22})$$

Let

$$A_{13} = A_{11}^2 - A_{12}^2 \quad (\text{D23})$$

$$A_{14} = A_{11}^4 - 6A_{11}^2 A_{12}^2 + A_{12}^4 \quad (\text{D24})$$

$$A_{15} = A_{11}^6 - 15A_{11}^4 A_{12}^2 + 15A_{11}^2 A_{12}^4 - A_{12}^6 \quad (D25)$$

$$A_{16} = -\frac{1}{2}A_{11} A_{12} \quad (D26)$$

$$A_{17} = 4A_{11}^3 A_{12} - 4A_{11} A_{12}^3 \quad (D27)$$

$$A_{18} = 6A_{11}^5 A_{12} - 20A_{11}^3 A_{12}^3 + 6A_{11} A_{12}^5 \quad (D28)$$

$$A_{19} = 1 - A_{13} / 4 + A_{14} / 64 - A_{15} / 2304 , \quad (D29)$$

$$A_{20} = A_{16} + A_{17} / 64 - A_{18} / 2304 , \quad (D30)$$

then equation (D21) becomes

$$J_0(\text{RK}) = A_{19} + i A_{20} . \quad (D31)$$

Note that A_{19} and A_{20} are real constant numbers.

The Bessel function $J_1(\text{RK})$ is obtained in a similar manner to $J_0(\text{RK})$ by allowing

$$A_{21} = A_{11}^3 - 3A_{11} A_{12}^2 \quad (D32)$$

$$A_{22} = A_{11}^5 - 10A_{11}^3 A_{12}^2 + 5A_{11} A_{12}^4 \quad (D33)$$

$$A_{23} = 3A_{11}^2 A_{12} - A_{12}^3 \quad (D34)$$

$$A_{24} = 5A_{11}^4 A_{12} - 10A_{11}^2 A_{12}^3 + A_{12}^5 \quad (D35)$$

$$A_{25} = \frac{1}{2}A_{11} - A_{22}/16 + A_{24}/384 \quad (D36)$$

$$A_{26} = \frac{1}{2}A_{12} - A_{23}/16 + A_{24}/384 , \quad (D37)$$

then the Bessel function $J_1(\text{RK})$ can be written as

$$J_1(\text{RK}) = A_{25} + i A_{26} . \quad (D38)$$

Note that A_{25} and A_{26} are real constant numbers.

Equations (D31) and (D38) are the approximate solutions for values of Bessel functions J_0 and J_1 .

Thus far the expressions for the argument RK and approximate solutions for J_0 and J_1 have been established. The absolute values of the approximate Bessel functions J_0 and J_1 are obtained respectively from equations (D31) and (D38) as

$$E_0 = |J_0(\text{RK})| = (A_{19}^2 + A_{20}^2)^{\frac{1}{2}} \quad (\text{D39})$$

and

$$E_1 = |J_1(\text{RK})| = (A_{25} + A_{26})^{\frac{1}{2}} \quad (\text{D40})$$

The actual value of J_0 as obtained from the computer output is

$$J_0(\text{RK}) = \text{BJRE}(1) + i \text{BJIM}(1)$$

from which the absolute value is defined as

$$A_0 = |J_0(\text{RK})| = \{[\text{BJRE}(1)]^2 + [\text{BJIM}(1)]^2\}^{\frac{1}{2}} \quad (\text{D41})$$

Similarly the absolute value of $J_1(\text{RK})$ can be shown to be

$$A_1 = |J_1(\text{RK})| = \{[\text{BJRE}(2)]^2 + [\text{BJIM}(2)]^2\}^{\frac{1}{2}} \quad (\text{D42})$$

The difference between actual and estimated values of J_0 is defined as

$$D_0 = |A_0 - E_0| \quad (\text{D43})$$

Thus the error based on the actual value is then defined as

$$\text{Error \%} = \frac{|A_0 - E_0|}{A_0} \cdot 100\% \quad (\text{D44})$$

In a similar manner the error for J_1 is defined as

$$\text{Error \%} = \frac{|A_1 - E_1|}{A_1} \cdot 100\% \quad (\text{D45})$$

The procedure for determining the approximate and actual values of J_0 and J_1 is as following:

1. Determine the values of ω_r and ω_i from equation (A14) in Appendix A for a specified airspeed.
2. Substitute ω_r , ω_i and other relevant information into equation (D18) so as to obtain the values of the real and imaginary parts of the argument, i.e. A_{11} and A_{12} .
3. Input the values of A_{11} and A_{12} into the subroutine COMBES to determine the values of J_0 and J_1 and its absolute values.
4. Use the value of ω from step 1 to evaluate A_{19} and A_{20} and find the absolute approximate value for J_0 as in equation (D39).
5. Proceeding as instructed in step 4 and by calculating A_{25} and A_{26} one obtains the absolute approximate value for J_1 as in equation (D40).
6. The solutions from steps 3, 4 and 5 are then compared with the absolute actual values of J_0 and J_1 as in equations (D41) and (D42).
7. Calculate the error for J_0 and J_1 by using equations (D44) and (D45) respectively.

The flow diagram is shown in Fig. D.1, and the computer program appears on pages 167-175. A sample output appears on page 176.

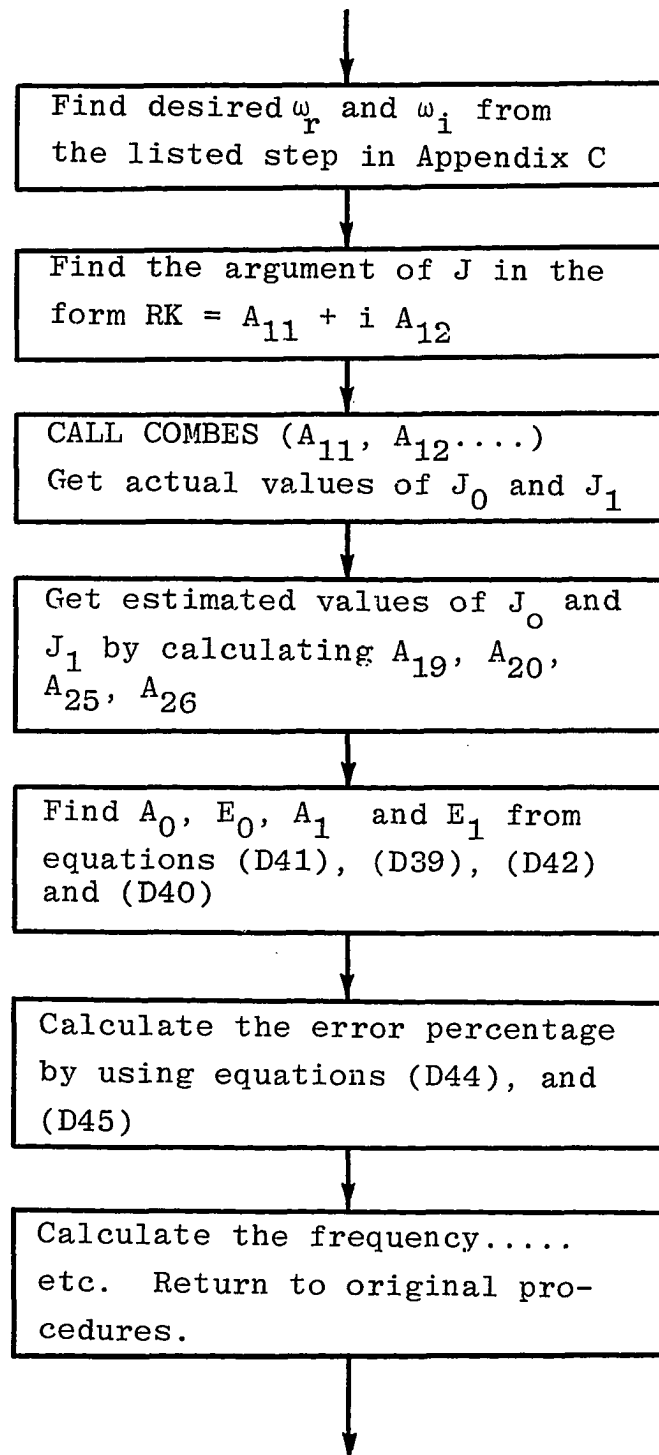


Fig. D.1 Flow diagram for the error analysis in the Bessel functions.

The computer output shows that the arguments of the Bessel functions are indeed less than one for each case shown. Therefore, since the procedure for deriving and calculating the numerical solutions satisfies this requirement, the solution procedure is correct. Furthermore, the error analysis reveals insignificant difference between the actual and estimated values of the Bessel functions. The errors based on equations (D44) and (D45) were 0.11×10^{-7} when J_0 had the value of 1, and 0.25×10^{-8} when J_1 had the value of 0.676×10^{-1} .

```
PROGRAM WHISTL (INPUT,OUTPUT,TAPE5=INPUT,TAPE6=OUTPUT)
DIMENSION VEL(11),WC(11),RE(11),ST(11),UU(11),WCK(11),
DIMENSION U(11)
DIMENSION ALPHAD(5),N1(5),FREQ(11),XO(11)
DIMENSION COEFF(7),ROOT1(6,2),Q(11),QQ(11)
DIMENSION BJRE(50),BJIM(50),YRE(10),YIM(10)
COMPLEX ROOT(6)
NN=11
CK=1
MM=6
WRITE(MM,1)
1 FORMAT(1H1)
  IDEGRE=6
  PI=3.1415927
  XNU=160.0E-06
  N=1
  LL=1
  D1=0.745/12.
  DO 25 LM=1,3
    IF(LM-2) 2,3,4
2 D2=0.625/12.
  GO TO 5
3 D2=0.6/12.
  GO TO 5
4 D2=0.375/12.
```

```

5 CONTINUE
   DO 24 NM=1,2
     IF(NM-1) 6,6,7
6 D3=0.375/12.
   GO TO 8
7 D3=0.25/12.
8 CONTINUE
   WRITE(MM,9) LL
9 FORMAT(5X,*FOR THE DEVICE *,I1/)
   R=D3/2.
   H=0.1/12.
   CKW=CK/(2.*PI)
   DO 23 IJ=1,3
     XIJ=IJ+2
     DO 22 II=1,3
       N1(II)=II+1
       ALPHAD(IJ)=XIJ*15.
       WRITE(MM,10) N1(II),ALPHAD(IJ)
10 FORMAT(5X,I1,*-*,F3.0.*DEGREE SWIRLER*//)
     ALPHA=ALPHAD(IJ)*PI/180.
     AREAA=PI/4.*(D1**2.-D2**2.)-N1(II)*H*(D1-D2)/2.
     AREAB=PI/4.*D3**2
     RE2=SQRT((D1/2.)**2-(AREAA/PI))
     WRITE(MM,11)
11 FORMAT(5X,*VEL*,11X,*RE J*,11X,*IM J*,8X,*ERROR %*,14X

```

1, *ARGUMENT OF J*/)

U(1)=0.0

C***** CHANGE VELOCITY *****

DO 21 J=1,11

VEL(J)=U(J)*5280./3600.

UU(J)=U(J)*1.60935

Q(J)=VEL(J)*COS(ALPHA)*AREAA*60.

QQ(J)=UU(J)*COS(ALPHA)*1000./60.*AREA*0.0929

WC(J)=VEL(J)*COS(ALPHA)*AREAA/AREAB

WCK(J)=WC(J)*0.304801E-03*3600.

RE(J)=WC(J)*D3/XNU

XO(J)=2.*VEL(J)*SIN(ALPHA)*((D1/2.)**3.-RE2**3.)/R**3

1.*(D1/2.+RE2))

CO=XO(J)+CK*WC(J)

C1=4.*XO(J)**2.-CO**2.

C2=R*CK/2.

C3=C2**2.

C4=C2**3./2.

C5=C2**4./4.

C6=C2**5./12.

C7=C2**6./36.

C8=XO(J)-CK*WC(J)

C9=9.*CO**2.-C1

C10=3.*CO*C1-7.*CO**3.

C11=2.*CO**4.-3.*CO**2*C1

C12=8.*CO**2.-2.*C1

$$\begin{aligned}
C13 &= 4 \cdot CO \cdot C1 - 4 \cdot CO^{**3} + 2 \cdot C1 \\
C14 &= C1^{**2} - 4 \cdot CO^{**2} \cdot C1 \\
C15 &= 14 \cdot CO^{**2} - C1 \\
C16 &= 4 \cdot CO \cdot C1 - 16 \cdot CO^{**3} \\
C17 &= 9 \cdot CO^{**4} - 6 \cdot CO^{**2} \cdot C1 \\
C18 &= 4 \cdot CO^{**3} \cdot C1 - 2 \cdot CO^{**5} \\
C19 &= 9 \cdot CO^{**2} + 4 \cdot CO - 2 \cdot C1 \\
C20 &= 8 \cdot CO \cdot C1 - 8 \cdot CO^{**2} - 4 \cdot CO^{**3} \\
C21 &= 4 \cdot CO^{**3} - 10 \cdot CO^{**2} \cdot C1 + C1^{**2} \\
C22 &= 4 \cdot CO^{**3} \cdot C1 - 2 \cdot CO \cdot C1^{**2} \\
C23 &= 12 \cdot CO^{**2} - 3 \cdot C1 \\
C24 &= 12 \cdot CO \cdot C1 - 8 \cdot CO^{**3} \\
C25 &= 3 \cdot C1^{**2} - 12 \cdot C1 \cdot CO^{**2} \\
C26 &= C2 + C4 + C6 \\
C27 &= 1 + C3 + C5 + C7 \\
C28 &= 10 \cdot CO^{**2} \cdot C2 + C4 \cdot C9 + C6 \cdot C12 \\
C29 &= 15 \cdot CO^{**2} + C3 \cdot C15 + C5 \cdot C19 + C7 \cdot C23 \\
C30 &= -10 \cdot CO^{**3} \cdot C2 + C4 \cdot C10 + C6 \cdot C13 + 10 \cdot CO^{**2} \cdot C2 \cdot C8 + C4 \cdot \\
&1C8 \cdot C9 + C6 \cdot C8 \cdot C12 \\
C31 &= 20 \cdot CO^{**3} - C3 \cdot C16 - C5 \cdot C20 - C7 \cdot C24 \\
C32 &= 5 \cdot CO^{**4} \cdot C2 + C4 \cdot C11 + C6 \cdot C14 - 10 \cdot CO^{**3} \cdot C2 \cdot C8 + C4 \cdot C8 \cdot \\
&1C10 + C6 \cdot C8 \cdot C13 \\
C33 &= C3 \cdot C17 - 15 \cdot CO^{**4} - C5 \cdot C21 - C7 \cdot C25 \\
C34 &= CO^{**2} \cdot C4 - C1 \cdot C6 \\
C341 &= CO^{**4} \cdot C2 \cdot (5 \cdot C8 - CO) \\
C35 &= C4 \cdot C8 \cdot C11 + C6 \cdot C8 \cdot C14
\end{aligned}$$

C36=6.*C0**5.-C3*C18-C5*C22+6.*CO*C1**2*C7

C37=CO**2.*C4-C1*C6

C38=-CO**4.*CO**2.*C1*C3-C1**2.*C5

CC=1./C2

C39=(CC*C26)/2.-C27

C40=(CC*C26/2.)*(C8-5.*CO)+6.*CO*C27

C41=CC/2.*(C28-5.*CO*C8*C26)-C29

C42=CC*C30/2.+C31

C43=CC*C32/2.+C33

C44=CC/2.*(CO*C1*C34+C35+C341)+C36

C45=CC/2.*(CO*C1*C8*C37-CO**5.*C2*C8)+CO**2.*C38+C1**3

1.*C7

COEFF(1)=C39

COEFF(2)=C40

COEFF(3)=C41

COEFF(4)=C42

COEFF(5)=C43

COEFF(6)=C44

COEFF(7)=C45

CALL RPOLY (IDEGRE , COEFF , ROOT , IERR)

DO 12 M=1,6

ROOT1(M,1)=REAL(ROOT(M))

ROOT1(M,2)=AIMAG(ROOT(M))

12 CONTINUE

AMAX=ROOT1(1,2)

IMAX=1

```

DO 13 MN=2,6
  IF(ROOT1(MN,2).LE.AMAX) GO TO 13
  AMAX=ROOT1(MN,2)
  IMAX=MN
13 CONTINUE
  FREQ(J)=ROOT1(IMAX,1)/(2.*PI)/1000.
C  NOW CALCULATE THE REAL AND IMAGINARY PART OF ARGUMENT
C  OF THE BESSEL FUNCTION
  ZR=ROOT1(IMAX,1)
  ZI=ROOT1(IMAX,2)
  A1=N*XO(J)+CK*WC(J)
  A2=4.*XO(J)**2-A1**2
  A3=R*CK
  A4=A3/( ( ZR-A1)**2+ZI**2)
  A5=A2+2.*A1*ZR-ZR**2+ZI**2
  A6=2.*A1*ZI-2.*ZR*ZI
  IF(J-1) 14,14,15
14 BJRE(1)=1.
  BJIM(1)=0.
  BJRE(2)=0.
  BJIM(2)=0.
  A19=1.
  A20=0.
  A25=0.
  A26=0.
  PEO=0.

```

```

PE1=0.
GO TO 16
15 CONTINUE
THETA1=ATAN2(A6,A5)
THETA=THETA1/2.
A7=ZR-A1
A8=(A5**2+A6**2)**0.25
A9=A7*COS(THETA)+ZI*SIN(THETA)
A10=A7*SIN(THETA)-ZI*COS(THETA)
A11=A4*A8*A9
A12=A4*A8*A10
C FIND THE ACTUAL VALUES OF THE BESSEL FUNCTIONS
CALL COMBES(A11,A12,0.,0.,1,BJRE,BJIM,YRE,YIM)
C FIND THE ESTIMATED VALUES OF BESSEL FUNCTION JO
A13=A11**2-A12**2
A14=A11**4-6.*A11**2*A12**2+A12**4
A15=A11**6-15.*A11**4*A12**2+15.*A11**2*A12**4-A12**6
A16=-0.5*A11*A12
A17=4.*A11**3*A12-4.*A11*A12**3
A18=6.*A11**5*A12-20.*A11**3*A12**3+6.*A11*A12**5
A19=1.-A13/4.+A14/64.-A15/2304.
A20=A16+A17/64.-A18/2304.
C FIND THE ESTIMATED VALUES OF BESSEL FUNCTION J1
A21=A11**3-3.*A11*A12**2
A22=A11**5-10.*A11**3*A12**2+5.*A11*A12**4
A23=3.*A11**2*A12-A12**3

```

```

A24=5.*A11**4*A12-10.*A11**2*A12**3+A12**5
A25=0.5*A11-A21/16.+A22/384.
A26=0.5*A12-A23/16.+A24/384.

C  ACTUAL VALUE OF JO
   CAO=SQRT(BJRE(1)**2+BJIM(1)**2)

C  ESTIMATED VALUE OF JO
   CEO=SQRT(A19**2+A20**2)

C  ACTUAL VALUE OF J1
   CA1=SQRT(BJRE(2)**2+BJIM(2)**2)

C  ESTIMATED VALUE OF J1
   CE1=SQRT(A25**2+A26**2)
   DCO=ABS(CAO-CEO)

C  ERROR PERCENTAGE OF JO
   PEO=DCO/CAO*100.
   DC1=ABS(CA1-CE1)

C  ERROR PERCENTAGE OF J1
   PE1=DC1/CA1*100.

16 CONTINUE
   WRITE(MM,17) U(J),BJRE(1),BJIM(1),A11,A12,A19,A20,PEO
1, BJRE(2),BJIM(2),A25,A26,PE1
17 FORMAT(5X,F4.0,2X,*(A) *,E13.7,2X,E13.7,15X,*(*,E13.7
1,* +I *,E13.7,*)*/11X,*(E) *,E13.7,2X,E13.7,2X,E11.5/
211X,*(A) *,E13.7,2X,E13.7/11X,*(E) *,E13.7,2X,E13.7,2
3X,E11.5/)
   IF(J-1) 18,18,19

18 ST(1)=0.0

```

```
GO TO 20
19 ST(J)=FREQ(J)*1000.*D3/WC(J)
20 CONTINUE
    U(J+1)=U(J)+20.
21 CONTINUE
22 CONTINUE
23 CONTINUE
    LL=LL+1
    WRITE(MM,1)
24 CONTINUE
25 CONTINUE
STOP
END
```


APPENDIX E

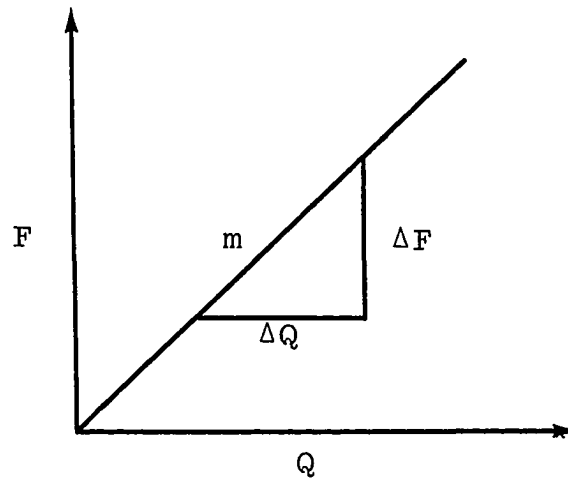
THE CONSTRUCTION OF FIGURES 72 THROUGH 83

The procedure for construction of the scales and data line is as follow:

1. Find the slope, m , of the data line in closed conduit test results.
2. (A) If the data line goes through the origin, as in (a) Fig. E.1, calculate the receiprocal of the slope, and obtain the scale for flow rate per unit frequency response, i.e., $(m^3/\text{min})/\text{KHz}$.
(B) If the data line does not go through the origin, as in (b) Fig. E.1, calculate the reciprocal of the slope, and obtain the scale for flow rate per unit frequency response. Then use the following form to mark the scale for flow rate.

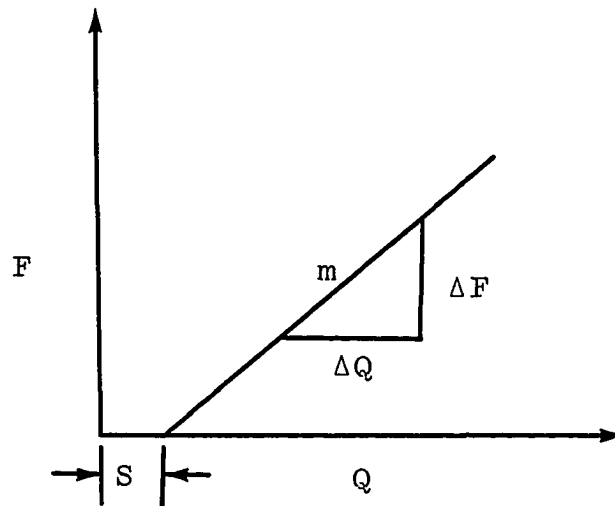
$$Q = \frac{1}{m} F + S \quad (\text{E1})$$

3. Mark the scale of the frequency response, F , on the left hand side of the figure. Also, mark the scale of the true airspeed, U , on the bottom of the figure as shown in Fig. E.2.
4. (A) If the data line as mentioned in step 2 goes through the origin, mark the scale of the flow



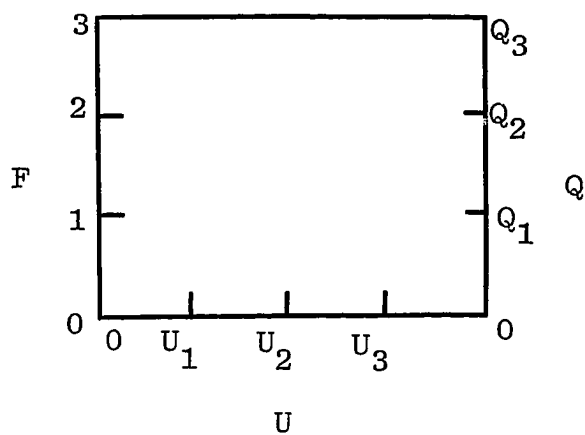
$$m = \Delta F / \Delta Q$$

(a)

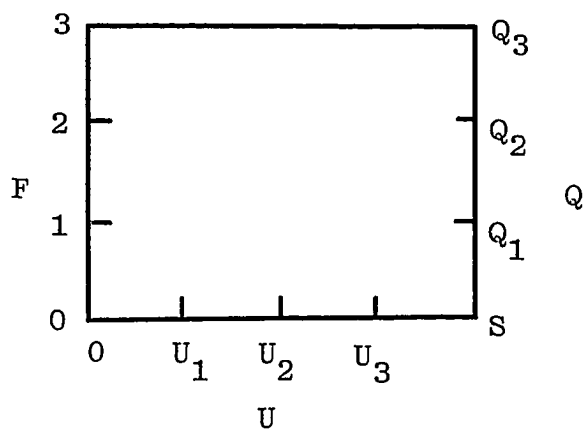


(b)

Fig. E.1 Types of data line taken at closed conduit test.



(a)



(b)

Fig. E.2 The scales for flow rate at right hand side.

rate on the right hand side of the figure with zero m^3/min at bottom line as in (a) Fig. E.2.

(B) If the data line as mentioned in step 2 does not go through the origin, mark the bottom line with the value of S, and the corresponding scales based on equation (E1) as in (b) Fig. E.2.

5. Find the slope of the data line taken from the wind tunnel test, then calculate the reciprocal of the slope to obtain the value of airspeed per unit frequency response, F_r .
6. Find the intersection of one KHz and the value F_r from step 5.
7. Draw the line which connected the origin and the intersection found in step 6. Hence this line represents the desired relationship among true airspeed, flow rate and frequency response as shown in Fig. E.3.

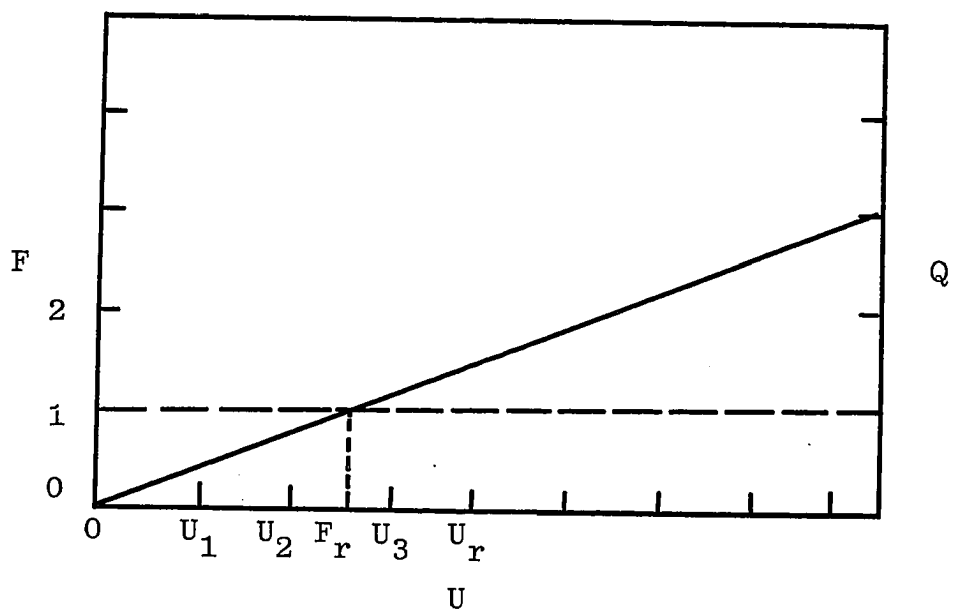


Fig. E.3 The performance line of a specific sensor.

BIOGRAPHY

Joseph Yao-Cheng Shen was born in Shanghai, China, on June 29, 1948. He was raised and educated in Taiwan, Republic of China. He graduated from the High School of National Taiwan Normal University in 1966. In June 1970, he received the Bachelor of Science degree in Mechanical Engineering from the Chung Yuan Christian College of Science and Engineering in Taiwan.

After graduation, he served one year in Armour Corps as a second lieutenant. He taught and trained people how to set up and maintain the telephone communication system at the division of Signal Corps. After departing the army, he received a position with the China Gulf Plastic Corporation as a Design Engineer. He remained in this position for one and one half years before coming to the United States to pursue an advanced degree. In August 1975, he received the Master of Engineering degree from Old Dominion University.

During the summers of 1973 and 1974, he worked at Gulf Oil Chemical Company, Orange, Texas as a trainee. He also has served as a graduate research assistant since 1973 at Old Dominion University. The research assistantship was funded through a grant provided by the National

Aeronautics and Space Administration. The responsibilities associated with this assistantship involved both analytical and experimental studies in the general area of fluidics. In 1977, he became a candidate for the doctor of Philosophy degree in Mechanical Engineering.

Presently he is a member of the American Society of Mechanical Engineers, a member of SIGMA XI, the Scientific Research Society, and a member of Virginia Academy of Science.